

Edited by
Volodymyr Korzhyk

THEORY AND PRACTICE OF PLASMA-DETONATION TECHNOLOGY OF SURFACE HARDENING METAL PRODUCTS

Monograph

UDC 621.785.5
BBK 34.65
K75

Published in 2021
by PC TECHNOLOGY CENTER
Shatylova dacha str., 4, Kharkiv, Ukraine, 61165

Approved by the Academic Council of E. O. Paton Electric Welding Institute of the National Academy of Sciences of Ukraine, Protocol No. 2 of 25.10.2021

Reviewers:

Valerii Lykhoshva, Doctor of Technical Sciences, Professor, Head of Department of Concentrated Energy Impacts, Physico-technological Institute of Metals and Alloys of National Academy of Sciences of Ukraine;
Yurii Kunitskii, Doctor of Physical and Mathematical Sciences, Professor, Researcher Consultant, Limited Liability Company "Foreign Economic Representation of Chinese-Ukrainian E. O. Paton Welding Institute".

K75

Authors:

Edited by **Volodymyr Korzhyk**

Volodymyr Korzhyk, Yuriy Tyurin, Oleg Kolisnichenko

Theory and Practice of Plasma-Detonation Technology of Surface Hardening Metal Products: monograph / V. Korzhyk, Yu. Tyurin, O. Kolisnichenko. — Kharkiv: PC TECHNOLOGY CENTER, 2021. — 244 p.

The book contains data on development of the technologies based on the use of non-stationary electric discharges in plasma jets. Formation of a plasma jet takes place under the effect of non-stationary detonation waves propagating between electrode units. In this case the energy parameters of the plasma can be controlled by a fuel mixture composition, electric potential and geometric characteristics of a device. As a result of interaction with plasma, the treated surface is subjected to pulsed electromagnetic, thermal and elastic-deformation influence. The results of studies of modified layers subjected to pulse plasma treatment are presented. The book describes technologies and equipment that are commercially applied for modification of working surfaces of machine parts and tools. Examples of application of the technologies in metallurgy, mining industry, wood working, machine building and other industrial sectors are given. For engineering and technical workers of machine-building enterprises and institutions specializing in the field of hardening processing of products.
Figures 130, Tables 29, References 322 items.

All rights reserved. No part of this book may be reprinted or reproduced or utilised in any form or by any electronic, mechanical, or other means, now known or hereafter invented, including photocopying and recording, or in any information storage or retrieval system, without permission in writing from the authors. This book contains information obtained from authentic and highly regarded sources. Reasonable efforts have been made to publish reliable data and information, but the author and publisher cannot assume responsibility for the validity of all materials or the consequences of their use. The authors and publishers have attempted to trace the copyright holders of all material reproduced in this publication and apologize to copyright holders if permission to publish in this form has not been obtained. If any copyright material has not been acknowledged please write and let us know so we may rectify in any future reprint. The publisher, the authors and the editors are safe to assume that the advice and information in this book are believed to be true and accurate at the date of publication. Neither the publisher nor the authors or the editors give a warranty, express or implied, with respect to the material contained herein or for any errors or omissions that may have been made.

Trademark Notice: Product or corporate names may be trademarks or registered trademarks, and are used only for identification and explanation without intent to infringe.


DOI: 10.15587/978-617-7319-46-6
ISBN 978-617-7319-46-6 (online)
ISBN 978-617-7319-41-1 (print)



Copyright © 2021 V. Korzhyk, Yu. Tyurin, O. Kolisnichenko
This is an open access paper under the Creative Commons CC BY license

AUTHORS

VOLODYMYR KORZHYK

Corresponding Member of National Academy of Sciences of Ukraine,
Doctor of Technical Sciences, Professor, Head of Department
Department of Electrothermal Processes of Materials Processing
E. O. Paton Electric Welding Institute of the National Academy of Sciences of Ukraine
 ORCID ID: <https://orcid.org/0000-0001-9106-8593>

YURIY TYURIN

Doctor of Technical Sciences, Senior Researcher
Department of New Physical and Chemical Ways of Welding
E. O. Paton Electric Welding Institute of the National Academy of Sciences of Ukraine
 ORCID ID: <https://orcid.org/0000-0002-7901-7395>

OLEG KOLISNICHENKO

PhD, Senior Researcher
Department of New Physical and Chemical Ways of Welding
E. O. Paton Electric Welding Institute of the National Academy of Sciences of Ukraine
 ORCID ID: <https://orcid.org/0000-0003-4507-9050>

ABSTRACT

The book contains data on development of the technologies based on the use of non-stationary electric discharges in plasma jets. Formation of a plasma jet takes place under the effect of non-stationary detonation waves propagating between electrode units. In this case the energy parameters of the plasma can be controlled by a fuel mixture composition, electric potential and geometric characteristics of a device. As a result of interaction with plasma, the treated surface is subjected to pulsed electromagnetic, thermal and elastic-deformation influence. The results of studies of modified layers subjected to pulse plasma treatment are presented.

The book describes technologies and equipment that are commercially applied for modification of working surfaces of machine parts and tools. Examples of application of the technologies in metallurgy, mining industry, wood working, machine building and other industrial sectors are given.

For engineering and technical workers of machine-building enterprises and institutions specializing in the field of hardening processing of products.

KEYWORDS

Plasma generator, equipment, pulsed plasma, surface modification, structural phase state, industrial application.

CONTENTS

List of Tables	ix
List of Figures	xi
Circle of readers and scope of application	xviii
Introduction	1
1 Technologies of processing of products by energy flows	4
1.1 Technologies based on concentrated energy sources	4
1.1.1 Laser technologies	4
1.1.2 Plasma technologies	5
1.1.3 Electron beam technologies	5
1.1.4 Ion implantation	6
1.1.5 Shock wave treatment	6
1.2 Application of high-energy density technologies	7
1.2.1 Heat hardening	7
1.2.2 Surface alloying	8
1.2.3 Hardening of tool alloys	9
1.2.4 Hardening of hard alloys	10
1.3 Requirements to modification technologies	12
1.3.1 Alloys and properties of alloying elements	12
1.3.2 Modification of high-speed steels	13
1.3.3 Acceleration of diffusion of alloying elements	14
1.3.4 Nitriding	16
1.4 Duplex and triplex modification technologies	17
1.5 Requirements to integrated plasma-detonation technology	18
2 Theory of plasma-detonation generation of plasma	20
2.1 Interaction of plasma with surface of a solid	20
2.1.1 Principle of laser plasma hardening	20
2.1.2 Deceleration of plasma jet on a solid surface	21
2.1.3 Surface heating	23
2.1.4 Determination of heat flow	25
2.2 Plasma-detonation generation of plasma	25
2.2.1 Problem statement and solution	25
2.2.2 Analysis of the solution results	34

3 Experimental study of pulsed plasma	38
3.1 Peculiarities of design of plasma-detonation generators	38
3.2 Procedure for investigation of pulsed plasma	42
3.3 Formation of plasma jet and its interaction with obstacle	42
3.4 Experimental studies of pulsed plasma	47
3.4.1 Energy characteristics of plasma generators	47
3.4.2 Spectroscopic examinations	56
4 Plasma-detonation equipment	58
4.1 Pulsed plasma generators	58
4.2 Technological modification systems	61
5 Plasma modification of surfaces of parts made from iron-base alloys	64
5.1 Alloys with 0.7–0.8 % C	64
5.1.1 PDT procedure	64
5.1.2 Efficiency of the effect on the surface by physical fields	64
5.1.3 Peculiarities of plasma-setonation treatment (PDT)	65
5.1.4 X-ray phase and diffraction analysis of alloy after PDT	69
5.1.5 Metallography and auger spectroscopy	72
5.2 Modification of medium-carbon alloys	75
5.3 Modification of surface of high-speed steels	82
5.3.1 PDT in air atmosphere	82
5.3.2 Treatment in nitrogen atmosphere	87
5.4 Hardening by plasma treatment	90
5.5 Generalisation of PDT and plasma treatment investigation results	93
6 Surface alloying	96
6.1 Mass transfer in pulsed treatment of metals	96
6.2 Interaction of pulsed plasma with solid surface	100
6.2.1 Modelling of processes occurring in the shock-compressed layer	100
6.2.2 Workpiece surface set as cathode	104
6.2.3 Workpiece surface set as anode	106
6.2.4 Surface of insulated workpiece	108
6.3 Thermal-physical characteristics of surface	109
6.3.1 Modelling	109
6.3.2 Temperature field in surface layers during PDT	110
6.4 Mass transfer in carbon steels	114
6.4.1 Steel 9KhS (0.9 % C, 1 % Cr, 1 % Si)	114

6.4.2	Modification of α -Fe samples	116
6.4.3	Modification of medium-carbon steel surface	118
7	Modification of surface by fusion	123
7.1	Description of treatment technology and its features	123
7.2	Modification of surface with metals by the PDT method	127
7.2.1	PDT conditions and investigation results	127
7.2.2	Modification of surface with copper and aluminium by PDT	129
7.2.3	Modification of surface with titanium and tungsten by PDT	130
7.2.4	Modification of surface of iron-graphite alloy	132
7.3	Modification of surface with alloying elements contained in coverings	134
7.3.1	Laser alloying	134
7.3.2	Modification by PDT using coverings	137
8	Surface hardening of various steels and alloys	139
8.1	Plasma treatment of high-strength cast iron	139
8.2	Plasma-detonation hardening of cast iron	142
8.3	Plasma-detonation hardening of die steel	147
8.4	Modification of surface of hard alloy	152
8.5	Modification of titanium base alloys	157
8.5.1	Alloy VT-22	157
8.5.2	Alloy VT-6	161
8.5.3	X-ray diffraction analysis	164
8.5.4	Formation of surface geometry	167
8.5.5	Laser hardening of titanium-base alloys	168
8.5.6	Microhardness titanium base alloys after PDT	169
9	Investigation of the fine structure of surface layers st. 40X after PDT. Analytical evaluation of the properties of plasticity and strength	171
9.1	Materials and methods of research	171
9.2	Results of metallographic studies and X-ray phase analysis	174
9.3	Transmission microdiffraction electron microscopy	176
9.4	Fractographic study of the fracture surface of the modified layer	178
9.5	Analytical assessment of the relationship between structural parameters in pulsed plasma treated layers and their mechanical properties	184
9.5.1	Assessment of the yield strength of the surface layers of steel 40X after PDT ..	185
9.5.2	Analytical assessment of plasticity properties	188
9.5.3	Calculation of local internal stresses (tin) according to the depth of products from steel 40X treated with pulsed plasma	189

10 Commercial application of surface modification	191
10.1 Hardening of metal cutting tools	192
10.2 PDT of blanking dies and punches	193
10.3 PDT of tools for hot treatment of metals.....	194
10.4 PDT of wood working knives, saws and mills.....	199
10.5 PDT of hard alloy tools	201
10.6 PDT of tools used in processing industry.....	202
10.7 PDT of car components.....	203
10.8 PDT of hydraulic drive and end seal components	203
10.9 PDT of printing machine parts.....	204
Conclusions	205
References	207

LIST OF TABLES

5.1	Ratio of integrated intensities of X-ray α -Fe and γ -Fe lines after PDT of steel 40X	77
5.2	Ratio of integrated intensities of X-ray α -Fe and γ -Fe lines after PDT of steel 45 (0.45 % C)	77
5.3	Estimation of amount of retained austenite in steel 40X (0.4 % C, 1 % Cr) after PDT using Mo electrode (numbers of samples correspond to those in Table 5.1)	79
5.4	Parameters of plasma-detonation treatment of samples (batch 1)	83
5.5	Parameters of plasma-detonation treatment of samples (batch 2)	83
5.6	Depth of the PDT hardened layer	85
5.7	Ratio of intensities of lines for different treatment conditions	86
5.8	Treatment parameters and properties of modified layer on steel R6M5	88
5.9	Hardening parameters and hardness of alloys [218]	90
5.10	Phase composition and parameters of crystalline lattice of deposited metal	92
6.1	Depths of penetration of atoms of t elements into alloy (Fe-Ni 30 %)	98
6.2	Absolute values of mass transfer of metal elements depending upon the impact method and surface temperature	98
6.3	Mass transfer coefficients in high-rate tension in pulsed magnetic field ($t_{pulse} = 105\text{--}110 \mu\text{s}$)	99
6.4	Mass transfer coefficients D , cm^2/s , in the case of pulsed electromagnetic compression at 300 K and $\epsilon = 1.7 \cdot 10^3 \text{ s}^{-1}$ [259]	99
6.5	Plasma parameters, heat flows and density of current to a workpiece depending upon the intensity of the electric current in the gap between electrodes	108
6.6	PDT parameters	116
7.1	PDT modification parameters and results	128
8.1	Properties of high-strength cast iron after plasma hardening	140
8.2	Conditions for modification of cast iron sample surfaces by PDT and investigation results	145
8.3	Parameters of treatment	147
8.4	Properties of hard alloys in the initial and hardened conditions	154
8.5	Hardness H_V and crack resistance of the surface of hard alloys in plasma hardening (values for treatment with fusion of the binder are given in numerator, and values for treatment without fusion are given in denominator)	156
8.6	Conditions of PDT in nitrogen atmosphere and characteristic of modified surface of alloy VT-6	163

8.7	Phase composition of alloy VT-6 after PDT	165
8.8	Microhardness of the surface of samples of titanium alloys	170
9.1	Changes in structural parameters and their contribution to hardening (σ_y) for steel 40X treated with pulsed plasma	187
9.2	Calculation of the stress intensity factor (K_{1C})	188
9.3	Calculation of internal stresses (τ_m) of steel 40X after PDT	190
10.1	Results of industrial tests of tools made from high-alloy and low-alloy steels after the duplex technology	198

LIST OF FIGURES

2.1	Schematic diagram of plasma-detonation device – plasma generator	26
2.2	Diagram for calculation of geometry of the plasma-detonation generator reaction chamber: $L=300$ mm, $r_{10}=40.5$ mm, $r_{20}=10.5$ mm, $r_{1k}=33$ mm, $r_{2k}=3$ mm	27
2.3	Temperature and Mach number of gas behind the front of the detonation wave depending upon the distance it passed for different values of electric field intensity E	36
2.4	Temperature of gas depending upon the intensity of the electric field, E_0 for different lengths of plasma generators, L : 1 – 100 mm; 2 – 200 mm; 3 – 300 mm	36
2.5	Velocity of gas, V/a_0 , depending upon the intensity of the electric field, E_0 , for different lengths of plasma generators, L : 1 – 100 mm; 2 – 200 mm; 3 – 300 mm	37
2.6	Dependencies of velocity V and temperature T of plasma flow upon cone angle α of gap between electrodes in plasma generator	37
3.1	Schematic of plasma-detonation unit operating with water electrolysis products	39
3.2	Schematic of design of cylindrical pulsed plasma generator	39
3.3	Pulsed plasma generator with conical reaction chamber	40
3.4	Pneumatic control circuit for the pulsed-plasma unit	41
3.5	Results of frame-by-frame filming (3,250 frame/s) of the plasma jet emitted from generator with cylindrical chamber: a – with obstacle; b – without obstacle (free jet)	43
3.6	Results of frame-by-frame filming (3,700 frame/s) of the plasma jet emitted from generator with a conical combustion chamber: a – free plasma jet; b – insulated obstacle extending to a distance of 30 mm; c – grounded obstacle extending to a distance of 30 mm	44
3.7	Time scans of glow of the plasma jet in different cross sections: a – near the exit section of the generator combustion chamber; b – at a distance of 5 mm from the exit section; c – at a distance of 10 mm from the exit section	44
3.8	Time scan of glow of the plasma jet: a – tracks of particles; b – traces of plasma jets; c – primary plasma jet	45
3.9	High-speed photography of interaction of the pulsed plasma jet with an obstacle	46
3.10	Appearance of the plasma barrier layer ahead of a solid obstacle	47
3.11	Appearance of free pulsed plasma jet	48
3.12	Time variations in electric current: 1 – current in the gap between electrodes; 2 – current between the central electrode and workpiece	50
3.13	Time diagram of electric current I (A) flowing between the consumable electrode tip and workpiece surface: 1 – $h=20$ mm, $H=40$ mm; 2 – $h=0$ mm, $H=70$ mm; 3 – $h=20$ mm, $H=70$ mm; 4 – $h=40$ mm, $H=70$ mm; 5 – $h=20$ mm, $H=100$ mm	51

3.14	Typical radiation spectrum of the pulsed plasma jet at a distance of 15 mm from the chamber exit section	52
4.1	Diagram of pulsed plasma generator with a conical reaction chamber: <i>a</i> – generator; <i>b</i> – variation of intensity of the electric field in gap between electrodes	58
4.2	Appearance of pulsed plasma generator	59
4.3	Pulsed plasma generator of a cylindrical shape	60
4.4	Pulsed plasma generators: <i>a</i> – for modification of surface properties; <i>b</i> – for deposition of coatings	60
4.5	Tool hardening system based on milling machine	61
4.6	System for pulsed-plasma treatment (coating) of large-size parts: metal cutters and mould plates	62
4.7	Automated system for hardening of workpiece surfaces and deposition of coatings	63
4.8	Appearance of system UN 138M: <i>a</i> – flow diagram; <i>b</i> – photo	63
5.1	Layer formed in pulsed plasma treatment: <i>a</i> – plasma has a stoichiometric composition; <i>b</i> – plasma has an increased oxygen content	66
5.2	Hardness of treated layer on samples of steel U8 (0.8 % C) using tungsten and molybdenum electrodes	67
5.3	Distribution of microhardness after laser treatment of metal alloys with a carbon content of 0.2, 0.45, 0.8, 1.0 and 1.2 %	67
5.4	X-ray pattern of the surface of alloy (0.3 % C) before and after PDT by the pulsed plasma containing: <i>a</i> – copper and aluminium; <i>b</i> – nitrogen and oxygen	68
5.5	X-ray pattern of the surface of the steel U8 (0.8 % C) samples (batch 1): <i>a</i> – sample after hardening in furnace; <i>b</i> – sample after PDT ($D=50$ mm, $h=15$ mm, $N=8$, Mo); <i>c</i> – sample after PDT ($D=50$ mm, $h=15$ mm, $N=8$, W)	70
5.6	Splitting of martensite line (211) for carbon steels depending upon the carbon content	71
5.7	Physical widening of X-ray lines of retained austenite in samples of alloy (0.8 % C) after PDT. Designation of points corresponds to numbers of samples in batch 1 (Table 5.1)	71
5.8	Auger spectra of the surfaces of samples 2–4 of steel 45 (0.45 % C) treated by plasma with an addition of Ti vapors ($D=40$ mm, $h=35$ mm)	73
5.9	Auger spectra of the surface of samples 2–4 of steel 45 (0.45 % C) treated by plasma with an addition of vapors of copper+zinc alloy ($D=40$ mm, $h=35$ mm)	73
5.10	Auger spectra of the surface of samples 2–4 of steel 45 (0.45 % C) treated by plasma with an addition of aluminium vapors ($D=40$ mm, $h=35$ mm)	73
5.11	Microstructure of transverse sections of samples of steel U8 (0.8 % C) (batch 2) after PDT with an addition of titanium to plasma ($D=60$ mm, $h=15$ mm, $N=5$). The photos are made using scanning electron microscope	74
5.12	Appearance of nano-crystalline layer formed on the surface of alloy (0.7 % C, 1 % Cr, 1 % Ni, 1 % Mo) sample after PDT by pulsed plasma (5 pulses)	75

5.13	Structure of layer in alloy 40X (0.4 % C, 1 % Cr) revealed by transmission electron microscopy: <i>a</i> – non-hardened alloy; <i>b</i> – alloy after PDT at $D=40$ mm, $h=15$ mm, $N=3$, Mo electrode	76
5.14	Results of examination of sample of alloy U8 (0.8 % C) after PDT ($D=50$ mm, $h=15$ mm, $N=8$, $C=800$ μ F, Mo electrode): <i>a</i> and <i>b</i> – fracture surface; <i>c</i> – cross section	76
5.15	Texture of steel U8A (0.8 % C) (batch 2) before and after PDT ($D=60$ mm, $h=35$ mm, $N=1$, $K=5$): <i>a</i> – steel in the as-rolled condition, texture $\langle 111 \rangle$; <i>b</i> , <i>c</i> and <i>d</i> – texture of a sample after PDT, texture of hardened steel is close to $\langle 001 \rangle$; <i>b</i> – Mo electrode; <i>c</i> – W electrode; <i>d</i> – Ti electrode	78
5.16	Sample of steel ShKh15 after PDT ($h=50$ mm, $D=30$ mm, $N=1$): <i>a</i> – appearance of surface after PDT with Mo vapors added to plasma; <i>b</i> – appearance of surface after PDT with stainless steel vapors added to plasma; <i>c</i> – transverse section of sample	80
5.17	Appearance of surface of steel 40X (0.4 % C) sample ($h=15$ mm, $D=40$ mm, $N=3$): <i>a</i> – X17, <i>b</i> – X250, <i>d</i> – X1000; $N=5$: <i>c</i> – X35, <i>g</i> – X100, <i>e</i> – X175. T–20 recording	81
5.18	Auger spectra of different regions of the surface of sample 6 in steel 40X (0.4 % C) after PDT ($h=30$ mm, $D=30$ mm, $N=5$, Cr18N9T electrode)	81
5.19	Appearance of the surface and Auger spectra of sample 5 of high-speed steel (R6M5) after PDT ($h=15$ mm, $D=50$ mm, $N=6$, molybdenum electrode)	84
5.20	Microstructure of the high-speed steel (R6M5) layer hardened by PDT (molybdenum electrode, 6 pulses)	84
5.21	Microstructure of hardened layer on PM high-speed steel (R6M5) after PDT, molybdenum electrode, 6 pulses	88
5.22	X-ray pattern of the sample surface after PDT in nitrogen atmosphere	89
5.23	Distribution of alloying elements, e.g. tungsten, in layer δ thick at a PDT distance equal to 40 mm. X-ray microanalysis measurement result	89
5.24	Microhardness of the surface layer on samples of alloy R6M5 after pulsed plasma treatment	90
6.1	Interaction between the pulsed plasma jet and solid substrate: <i>a</i> – photo of the shock-compressed plasma layer on the solid surface; <i>b</i> – calculation of energy parameters of the jet	101
6.2	Distribution of temperature through thickness of the surface layer at certain time moments t of heating: 1 – $t=4.5 \cdot 10^{-5}$ s; 2 – $t=7.5 \cdot 10^{-5}$ s; 3 – $t=1.5 \cdot 10^{-4}$ s; 4 – $t=3.0 \cdot 10^{-4}$ s; 5 – $t=4.5 \cdot 10^{-4}$ s; 6 – $t=6.0 \cdot 10^{-4}$ s	111
6.3	Temperature change in the surface layers at different depths: 1 – $z=0$ μ m; 2 – $z=20$ μ m; 3 – $z=40$ μ m; 4 – $z=60$ μ m; 5 – $z=100$ μ m	111
6.4	Cooling rate of surface layers at different depths: 1 – $z=0$ μ m; 2 – $z=20$ μ m; 3 – $z=40$ μ m; 4 – $z=60$ μ m; 5 – $z=100$ μ m	112

6.5	Variations in temperature through thickness of the heated layer depending upon the distance from the surface under a multiple effect by pulsed plasma in PDT: $a - z = 0 \text{ } \mu\text{m}$; $b - z = 20 \cdot 10^{-3} \text{ } \mu\text{m}$; $c - z = 60 \cdot 10^{-3} \text{ } \mu\text{m}$; $d - z = 80 \cdot 10^{-3} \text{ } \mu\text{m}$	113
6.6	Distribution of alloying elements through thickness of the layer depending upon the quantity of pulses: a – oxygen; b – nitrogen; 1 – 10 pulses; 2 – 20 pulses; 3 – 30 pulses	115
6.7	Morphology of the α -Fe sample surface after PDT	116
6.8	Energy spectrum of Rutherford ion backscattering for the α -Fe sample after PDT (10 pulses) recorded by using ^4He : a – determination of molybdenum concentration; b – determination of carbon	117
6.9	Energy spectrum of Rutherford ion backscattering recorded by the method of elastic resonance of protons with an energy of 1.745 MeV to determine the concentration of carbon and oxygen on the α -Fe sample after PDT (20 pulses)	117
6.10	Surface layer of the steel 45 (0.45 % C) sample after PDT (3 pulses)	118
6.11	Surface layer of the steel 45 (0.45 % C) sample after PDT (5 pulses)	119
6.12	Auger spectra of medium-carbon steel samples after PDT with titanium added to plasma	120
6.13	Microstructure of surface layer of the carbon steel sample after PDT using titanium electrode: a, b – sample 2–1 ($D=60 \text{ mm}$, $h=15 \text{ mm}$, $N=5$); c, d – sample 2–3 ($D=60 \text{ mm}$, $h=35 \text{ mm}$, $N=5$); e, f – sample 2–2 ($D=80 \text{ mm}$, $h=15 \text{ mm}$, $N=5$); g – sample 2–4 ($D=80 \text{ mm}$, $h=35 \text{ mm}$, $N=5$); a, c, e and g – light microscope images; b, d, f – scanning microscope images	121
6.14	X-ray pattern of samples after PDT with different plasma composition: a – sample 1–2 ($D=50 \text{ mm}$, $h=15 \text{ mm}$, $N=8$, 18 % Cr, 9 % Ni, 73 % Fe); b – sample 1–4 ($D=50 \text{ mm}$, $h=15 \text{ mm}$, $N=8$, Mo); c – sample 1–6 ($D=50 \text{ mm}$, $h=15 \text{ mm}$, $N=8$, W). Records made in $\text{FeK}\alpha$ radiation	122
7.1	Schematic of device for pulsed-plasma microsurfacing	124
7.2	Diagram of formation of the metal-containing plasma jet	124
7.3	Schematic of distribution of heat flows in formation of the shock-compressed layer	126
7.4	Section of the surface layer of steel (0.3 % C) after one-pulse microsurfacing: a – with copper; b – with aluminium	129
7.5	Appearance of section of the surface layer of steel (0.3 % C) after one-pulse microsurfacing: a – with titanium; b – with tungsten	130
7.6	Appearance of section of the surface layer of steel (0.3 %) after 5 plasma pulses containing: a – tungsten; b – titanium	131
7.7	Appearance of section of the surface layer of iron-graphite sample after treatment with one plasma pulse containing: a – titanium; b – tungsten	133
7.8	Appearance of section of the surface layer of iron-graphite sample after treatment with one plasma pulse containing: a – molybdenum; b – chromium	133

LIST OF FIGURES

7.9	Appearance of section of the surface layer of iron-graphite sample after treatment with plasma pulses containing no metal: <i>a</i> – one pulse; <i>b</i> – three pulses; <i>c</i> – five pulses	134
7.10	Microstructure of the steel 40X sample surface after PDT by fusion of the binary titanium-chromium carbide with the BF-2 adhesive binder	138
8.1	Microstructure of surface of the grey cast iron sample after PDT	142
8.2	Microstructure of surface of the high-strength cast iron sample with spherical graphite particle inclusions after PDT	143
8.3	Microstructure of surface of the high-strength cast iron sample after PDT	144
8.4	Auger spectrum and appearance of surface of the high-strength cast iron sample after plasma treatment by adding molybdenum to plasma (SEM photo)	144
8.5	Transverse section of modified layer on surface of the cast iron sample (SEM photo)	144
8.6	Modified surfaces of high-strength cast iron samples. PDT was performed using plasma generator with a molybdenum electrode (SEM photo)	146
8.7	Microsections of samples: <i>a</i> – No. 1; <i>b</i> – No. 2	148
8.8	Modified layer of the sample No. 3: <i>a</i> – layer image on the optical microscope; <i>b</i> – layer image on the SEM	148
8.9	X-ray surface analysis of the sample No. 3	149
8.10	Modified layer of the sample No. 4: <i>a</i> – layer image on the optical microscope; <i>b</i> – image of the analyzed zone on the TEM	149
8.11	Modified layer of the sample No. 5: <i>a</i> – layer image on the optical microscope; <i>b</i> – layer image on the SEM	150
8.12	X-ray surface analysis of the sample No. 5	151
8.13	Distribution of alloying elements through thickness of the modified layer	151
8.14	Characteristic microstructure of the layer modified by PDT (single-pulse treatment) on the surface of alloy VT-22	158
8.15	Characteristic microstructure of the surface of alloy VT-22 modified by PDT (treatment with three pulses)	158
8.16	Microhardness of the VT-22 sample surface modified by PDT	159
8.17	Diffraction pattern of alloy VT-22 before and after pulsed plasma treatment	160
8.18	Characteristic microstructure of the surface of alloy VT-6 modified by PDT with 20 pulses in nitrogen atmosphere	161
8.19	Microhardness of the surface of alloy VT-6 modified by PDT	161
8.20	Characteristic microstructure of the surface of alloy VT-6 modified by PDT with three pulses in nitrogen atmosphere at a distance of 40 mm	162
8.21	Characteristic microstructure of the surface of alloy VT-6 modified by PDT with three pulses in nitrogen atmosphere at a distance of 70 mm	162
8.22	Results in formation of a hardened layer 20–30 μm thick VT-6	163
8.23	Results of X-ray diffraction analysis of an angle lap of the surface of a titanium sample modified by PDT (SEM)	166

8.24	Appearance of the surface of a titanium sample modified by PDT with 2 pulses: <i>a</i> – alloy VT-23; <i>b</i> – alloy VT-1-0	168
9.1	Microstructure of the near-surface layer of steel 40X during pulsed plasma treatment	174
9.2	Steel 40X. Base metal. Processing: heating to 850 °C and quenching in oil	175
9.3	Changing the nature of the distribution of integral microhardness from the outer surface to be treated to the base metal	175
9.4	Fine structure of a surface treated by pulsed plasma of steel samples at a distance of 10 μm from the surface	177
9.5	Fine structure of the transition zone of a sample treated with pulsed plasma at a distance of 90 μm and 100 μm from the surface	177
9.6	Fine structure of the base metal of a steel 40X sample treated with pulsed plasma	178
9.7	View of the fracture surface: <i>a</i> – along the destruction zones; <i>b</i> – schematic illustration	179
9.8	Fragments of the fracture microstructure in the area of the treated surface at different magnifications	180
9.9	Fragments of the microstructure of the fracture in the adjacent area to the machined surface at different magnifications	181
9.10	Fragments of the microstructure of a fracture in the area of brittle fracture of surface layers at various magnifications	182
9.11	Fragments of the fracture microstructure in the region of the transition fracture zone at various magnifications	183
9.12	Fragments of the microstructure of a fracture in the area of destruction of the base metal at various magnifications	183
9.13	Change in the volume fraction (<i>V_{fr}</i> , %) of all types of fracture: brittle, quasi-brittle and viscous (pie diagrams) and characteristic parameters of the micro-relief of the fracture surface (histograms) – the size of the facets of the brittle and quasi-brittle type (D_F^{br} ; $D_F^{a/br}$); secondary microcracks (L_w); viscous fracture pits (D_p ; d_p – dispersed) along the fracture zones	184
9.14	Contribution of individual structural parameters to hardening along the layer depth	187
9.15	Total (integral) hardening due to the structural state and stress intensity factor K_{1C}	189
9.16	Diagram of the distribution of local internal stresses over the depth of a 40X sample treated with pulsed plasma	190
10.1	Hardened knives for cutting rolled stock: <i>a</i> – steel sheets; <i>b</i> – sections	193
10.2	Metal cutting tools hardened by PDT: <i>a</i> – flat broach; <i>b</i> – taps M4-M16	193
10.3	Appearance of hardened blanking die	194
10.4	Hardened die for hot forming of cleaning machine cutters	195
10.5	Hardened dies for hot forming of metal: <i>a</i> – blocks; <i>b</i> – punches	196
10.6	Hardened punch for hot forming of metal	197

LIST OF FIGURES

10.7	Hardened rollers for rolling of metal sections: <i>a</i> – made from hard alloy; <i>b</i> – made from cast iron	198
10.8	Hardened saw disk	199
10.9	Hardened knife for wood crushing	200
10.10	Hardened knife for wood working	200
10.11	Hardened circular saw	201
10.12	Hardened saw with hard alloy regions formed on its surface	202
10.13	Hardened knife for cutting of sugar beet	202
10.14	Hardened knife for cutting of tobacco leaves	202
10.15	The end seals subjected to PDT	204

CIRCLE OF READERS AND SCOPE OF APPLICATION

The monograph contains information on the theory of the formation of high-energy plasma pulses and the practice of using in industry a fundamentally new, pulse-plasma technology for modifying the working surface of machine parts and tools. Particular attention in the monograph is paid to the experience of using the developed technologies, which makes it valuable both for scientists, graduate students and engineers in industry. The main application of the developed technologies is aviation and general mechanical engineering, woodworking, agricultural engineering, in railway and other types of transport, metallurgy and other industries for strengthening machine parts and tools.

INTRODUCTION

Surface modification can be performed by different methods involving treatment with concentrated energy flows. These are laser, electron and ion beams, shock waves, as well as stationary and pulsed plasma flows. If the surface of the material treated is covered by thin films of a different material, the short-time effect by energy flows leads to mixing and re-distribution of elements contained in a film and substrate, in addition to phenomena of a hardening character. As a result, stable and meta-stable alloys and compounds are formed. Super-high cooling and heating rates combined with the effect of physical fields allow nano-, microcrystalline or amorphous layers to be produced on the surface. Properties of these layers may be substantially different from those of metals and alloys in the equilibrium state.

Modification of properties of the surface is based on the principle of formation of complex multi-layer surface structures, such as amorphous films, finely dispersed precipitates and sub-layers with a high dislocation density. This allows a targeted variation of service characteristics of metallic materials, including corrosion resistance, strength, wear resistance, fatigue strength under cyclic loads, electric-erosion resistance, etc.

It should be noted that, along with experience of employing laser and electron beam treatment, a large amount of experimental data has been accumulated on the use of the high-energy density methods for treatment of materials with ion and plasma jets. Their commercial application fields have been studied.

The book presents ingenious data on modification of surfaces using high-energy density plasma technologies and optimization of surface geometry.

Main premises for using high-energy density plasma technologies are as follows:

- high energy density within the treatment zone and possibility of regulating it;
- short time and locality of the effect limiting the heat-affected zone;
- simplicity of control of energy pulses and possibility of treating curvilinear surfaces by no-contact methods;
- low costs of equipment and technology;
- possibility of automating the treatment process;
- high factor of utilization of power consumed for hardening.

The surface of a workpiece is treated during the process of plasma modification by thermochemical and thermomechanical effects that stimulate plasma-chemical synthesis and formation of new compounds. This allows deposition of coatings with predictable properties.

In addition, this allows alloying of the workpiece surface and formation of nano-crystalline structures having high wear, heat and scoring resistance, combined with sufficient strength and toughness of an alloy used to make a part.

The book contains information on optimization of the surface geometry by vibration work-hardening, which provides the possibility of lubrication of rubbing surfaces. In this case the

hydrodynamic effect of lubrication works, thus enhancing the effect of surface modification and complementing the effect of treatment with highly concentrated plasma flows. Optimization of the surface geometry leads to multiple decrease of friction and wear coefficients in sliding friction pairs.

Treatment of the workpiece surface with an optimal geometry by using intensive energy beams offers an extra possibility of controlling properties of the surface. Integrated technologies of plasma surface modification, i.e. so-called "duplex" technologies, offer good results.

Optical quantum generators, i.e. lasers, and different types of plasma accelerators have been developed in the last decades and are commercially applied now for this purpose. Combined with the shock wave effect, heating and deformation, these devices can provide the radiation and electromagnetic effects on surfaces. Plasma accelerators have a number of advantages over lasers, such as a much higher efficiency, lower power consumption per unit surface being modified and high degree of absorption of radiation in any material.

Methods involving the shock effect on the surface by using explosives are also efficient. Explosives form plasma jets with a velocity of 5–20 km/s and temperature of 10,000–30,000 K. The density of plasma with these methods is higher than that of the atmosphere by a factor of 50. Plasma of the explosives is also employed for thermochemical treatment of surfaces. Work is progress on further development of methods for generating pulsed plasma by electric explosion of conductors (foils). Plasma of the electric discharge is a versatile tool. It is used for thermochemical treatment of workpiece surfaces under the layer of liquid and in air atmosphere. Dozens of pulsed plasma duplex technologies are available. These technologies combine the high-rate heat treatment and alloying of surfaces with plasma components, such as carbon or nitrogen. Analysis of the investigation results shows that the impact by pulsed plasma on solid surfaces is more efficient than treatment with stationary jets, which is the case, for example, of "laser plasma".

The book contains data on development of the technologies based on the use of non-stationary electric discharges in plasma jets. Formation of a plasma jet takes place under the effect of non-stationary detonation waves propagating between symmetric electrode units. In this case the energy parameters of the plasma can be controlled by a fuel mixture composition, electric potential and geometric characteristics of a device. Parameters of the pulsed plasma can be varied within the following ranges: energy – 1,000–10,000 J, frequency – 1–10 Hz, duration – $0.5 \cdot 10^{-3}$ – $5 \cdot 10^{-3}$ s, velocity – 2,000–8,000 m/s and temperature – 5,000–15,000 K. Electric current of up to 15 kA is fed to the workpiece surface via the plasma jet, thus forming the magnetic and acoustic fields.

We suggest affecting the workpiece surface by a high-energy flow of alloying elements. This results in rapid heating (heating time – 10^{-3} – 10^{-6} s) of the surface layer, followed by its intensive cooling through removing heat both into the bulk of metal and to the surrounding atmosphere. The heat effect here is combined with the alloying processes.

The high rate of heating and cooling (10^4 – 10^8 K/s) of the surface layer of metal leads to formation of nano-microcrystalline structure, high dislocation density and growth of the concentration of alloying elements.

The pulsed-plasma technology allows a simultaneous, in one treatment pulse, realization of different methods of affecting the workpiece surface: elasto-plastic deformation, impact by sound and pulsed magnetic field, heat and electric-pulse treatment, and deformation of metals and alloys during reversible ($\alpha + \gamma$) transformations.

High power density of the flow (up to 10^6 W/cm² at the point of contact with the workpiece surface) makes it possible to perform treatment in air atmosphere with no surface preparation.

Treatment with a high-energy density flow of alloying elements causes no changes in geometric sizes of workpieces. Therefore, it is suggested that it should be used as a finishing operation. Industrial verification shows that performance of tools and machine parts after modification of their working surfaces increases 3–5 times.

Depending upon the composition of the high-energy density flow, the surface layer can have high anti-friction properties, as well as high heat, wear and corrosion resistance. As proved experimentally, the friction coefficient after treatment with the high-energy density flow decreases 3–5 times, load to seizure increases 10 times, wear resistance under fretting grows 2–5 times, and heat resistance increases 6 times.

The technology allows using low alloys with high strength and ductility for the fabrication of parts. Along with reduction in cost of a workpiece material, this leads to reduction in machining and heat treatment costs.

The range of parts for plasma hardening can be conditionally subdivided into the following three groups. These are parts for which the known (baseline) hardening methods fail to increase strength to a required level, parts that should have a combination of high operating properties (hardness, wear resistance, resistance to fracture through cracking), and parts the strength of which cannot be increased by the known and commercially verified technologies, or for the treatment of which the available technologies and equipment are too expensive.

The book describes technologies and equipment that are commercially applied for modification of working surfaces of machine parts and tools. Examples of application of the technologies in metallurgy, mining industry, wood working, machine building and other industrial sectors are given.

ABSTRACT

Chapter contains an analysis of literature sources on high-energy processing methods with concentrated energy sources, which are used to modify the surface of products. Laser, electron-beam, shock-wave, plasma, and many other technologies are considered. Technologies provide a manifold increase in the performance of products used in a variety of conditions.

KEYWORDS

Concentrated energy sources, surface modification of products, serviceability, processing efficiency, metal alloys.

1.1 TECHNOLOGIES BASED ON CONCENTRATED ENERGY SOURCES**1.1.1 LASER TECHNOLOGIES**

Different types of technological systems based on optical quantum generators, i.e. lasers, are of considerable current use in industry and laboratories of research centers.

Thermochemical laser treatment (TCLT) enables improvement of physical-mechanical properties of the surfaces of alloys and provides their high wear and corrosion resistance. Impact by TCLT on the surface of metal parts includes rapid heating, diffusion alloying and cooling. In many applications TCLT is more economically attractive than traditional hardening technologies [1–21].

Modification of surfaces of metal parts used in engineering is performed typically with high-power (>1 kW) CO_2 -lasers. They are employed for heat hardening [1–6], alloying [7–10], glazing of deposited layer [10, 11], and hardening of hard-alloy [12] and ceramic [13] materials.

Methods and devices developed for laser treatment are many and varied. Of the highest interest are ingenious laser methods used for heat treatment. Among them are the methods where liquid nitrogen is fed to the surfaces irradiated by the laser beam, or where a part treated is immersed into the bath with a transparent hardening compound. Hardening can be performed simultaneously by several laser beams generated in a pulsed or stationary flow mode.

Pulsed, continuous-wave or quasi-continuous lasers are used for laser treatment of surfaces. Of interest for the hardening technology is propagation of the laser beam along a spiral line, at an angle to the surface, using convex lenses or special optical systems. These technologies make it possible to harden surfaces of different configurations. Available are laser methods of surface hardening

that involve lapping of the tempering zones, peaks of a regular micro geometry of the surface, or superposition of interference grating, ensuring coverage of up to 50 % of the nominal surface area.

The TCLT processes are performed using lasers with a radiation frequency of 10–100 Hz for a time of 10–60 s, gas atmosphere pressure of up to 22–25 kg/cm² and radiation power of 10⁶–10⁷ W/cm². TCLT can be employed to treat cold surfaces of parts or surfaces heated to 300–500 °C [14–21].

Ingenious methods were developed for hardening using laser plasma that consists of argon. The sufficient scientific-and-technical potential is available now for wide application of TCLT. However, the extensive use of the process is limited due to high cost of the equipment involved and low power utilization factor.

1.1.2 PLASMA TECHNOLOGIES

Investigations of the effect exerted by high energy plasma on metal surface show [22] that deceleration of the plasma flow caused by braking radiation leads to formation of a plume, which does not differ in its impact on metals from the laser plume. A shock-compressed plasma layer is formed on the surface.

Explosives are also used to form the shock-compressed plasma layer [23]. Explosives form plasma jets with a velocity of 5–20 km/s and temperature of 10,000–30,000 K. Plasma density in this case exceeds the atmospheric one by a factor of 50.

The surface modification technologies performed with the high-energy density flow of plasma generated by explosives are considered in reference [24]. Such flows can also be formed by an electric explosion of conductors (foils) using a special device [25]. These technologies can be applied for surface hardening as well [26].

Pulsed electric discharges are used for thermochemical treatment of parts, which is performed under a layer of liquid [27, 28] or in vacuum [29]. As opposed to these methods, available are methods and technological devices for plasma treatment in a chamber under a pressure of 30 kg/cm² [30] or using a plasma gun having a capillary channel [31]. There are also dozens of nitriding methods performed with the nitrogen-containing high-velocity plasma.

Plasma methods are not inferior in the efficiency of hardening of the metal surface of tools or machine parts to the laser ones. The plasma methods have higher power utilization factors, amounting to 80 %. They are carried out using equipment that is less expensive (tens of times) and characterized by a lower material and power consumption during operation.

1.1.3 ELECTRON BEAM TECHNOLOGIES

Electron beam methods also find commercial application for modification of surfaces of metal parts. Surface hardening is performed using a beam of relativistic electrons [32–35], which provide high heating and cooling rates.

Rapid hardening of the workpiece surface is provided by electron beam melting with a beam scanned on a spiral path [35–37], by preliminarily nitriding the surface and its subsequent glazing with the electron beam [38], or by heat treatment with no melting [39, 40] using special insulating screens [41].

Studies [42–44] generalize and compare advantages and disadvantages of the electron beam, laser and plasma technologies. They note similarity of the processes occurring under the effect on a material by the electron beam, laser beam, electric current, plasma and electric discharge. For example, Detroit Diesel Allison performs hardening of the surfaces of some automobile parts by the electron beam method [45]. Before, the Company employed laser hardening for this purpose. Labour consumption in electron beam treatment proved to be lower than in laser treatment.

11.4 ION IMPLANTATION

Ion implantation of the surface of metallic materials is the most extensively studied area of science and technology. This can be explained by the industrial demand and the need to investigate radiation damage of materials in space engineering and nuclear power generation. The implantation process comprises introduction of high-energy atoms (ions) of chemical elements into the surface of a solid. The elements are introduced through bombardment of the surface with beams of the corresponding accelerated ions [46–48].

Ion implantation is employed to improve performance of bearings, valves, components of engines, members of aerospace structures, precision tools, dies and moulds. Implantation makes it possible to introduce elements and deposit, for example, carbon coatings on metal cutting tools. The technology can be used for nitriding of the surfaces of dies, lead screws and gears. Ion implantation is employed for hardening of the surfaces of parts made from alloys of the type of 30KhSA [49], ShKh15 [50, 51], tool steels [52, 53], and cobalt-base anti-friction alloys [54]. More information about the efficiency of ion implantation and its role in improving mechanical properties of parts can be found in articles and books [35, 55–59].

11.5 SHOCK WAVE TREATMENT

Shock wave treatment is one of the most efficient methods for affecting the workpiece surfaces. Some methods involving the shock wave effect have been studied in terms of the possibility of alloying the workpiece surfaces. Shock wave treatment is employed to increase corrosion [60] and wear resistance. Alloying of the surfaces is performed by using the explosive plasma to introduce chromium and graphite powders, nitrogen and vapors of different metals. In this case modification is carried out using the pulsed plasma and shock waves. Shock waves are formed using the pulsed magnetic fields [61, 62], explosives, electric discharges and energy generated by the electric explosion of conductors [35].

1.2 APPLICATION OF HIGH-ENERGY DENSITY TECHNOLOGIES

1.2.1 HEAT HARDENING

Further progress in the surface modification technology is related to the possibility of formation of hard nano- and microcrystalline structures. Formation of such structures is provided by heat treatment of surfaces using high-energy density methods. Technological continuous-wave lasers with a power of 3–50 kW are used for heat hardening of workpiece surfaces. Such lasers have received the widest acceptance in automotive industry and engine construction.

The Hamilton Standard (USA) unit is the most typical and widely applied machine for laser treatment of surfaces of parts. The unit has a modular design, and its radiation power ranges from 1.5 to 6 kW. The power consumption can be varied from 40 to 270 kW (efficiency – from 1.5 to 4 %) [63, 64]. Laser hardening is applied for treatment of bearing fillets of engine crankshafts, teeth and end faces of spiral gear wheels, piston ring grooves and metal cutting tools. AVCOE Everett (USA) together with General Motors developed a technology and equipment for hardening of automobile and aircraft components [65]. Available are the technology and equipment for hardening of the inside surfaces of aircraft engine cylinders (time of treatment is 1.5 min) and cast iron engine valve seats (time of treatment is 5 s).

United Technologies Research Center (USA) developed equipment for hardening of diesel cylinder sleeves [66]. Power of the laser used for this purpose is 5 kW. The scanning speed is 21–60 mm/min. The sleeves are made from grey cast iron. Hardness after the treatment is HRC 60.

Continuous-wave CO₂-lasers with a power of up to 1 kW are also applied for heat hardening [67–70]. The maximum depth of hardening with no melting of the surface (steel with 0.45 % C) is 0.33 mm, the scanning speed being 20–22 mm/min. Hardness of the surface after the treatment is $H_{50}=7500$ MPa.

The Joint Stock Company "Kirovsky Zavod" has experience in using the LTU-2 laser for hardening of cutting tools and fixture components. Performance of the tools, dies and other components treated increases by a factor of 2–3 [71–73]. Hardening of metal cutting tools with the pulsed laser provides improvement of 2.5–5 times in their performance [74].

The CW laser LG-702 (KARDAMON) is applied for hardening of cast iron parts [75, 76]. It provides increase in surface hardness of up to 9000 MPa. The developed technology is efficient for hardening of automobile engine sleeves, end faces of water pump bodies and piston rings. Performance of parts increases in this case by a factor of 2–3.

Reviews [77–81] provide systematized description of the equipment and technologies used for hardening, as well as the test results on the hardened parts. Reported is the spread of data on microhardness (up to 40 %) through thickness of the hardened layer, taking place even under identical laser treatment conditions. This is explained by a non-uniform distribution of energy density in the laser beam, and by an inhomogeneous reflectivity of the surface hardened.

There are publications on the application of laser treatment in automotive industry [82–86], machine-building [87–90], machine tool construction [91–93] and mining industry [94, 95].

Applicability of laser treatment was studied for various industries and on various materials, such as steels (0.45 % C) [96, 97], (0.45 % C, 1 % Cr) [98], (1 % C) [99], (1 % C, 18 % W) [100], hard alloys (88 % WC, 12 % Co) [101–103] and ceramic materials [104, 105], for hardening of machine tool parts [91], axial bearings of turbo-drills [106] and working surfaces of plane-parallel gauge blocks [107]. In all cases the application of laser hardening provided a multiple increase in wear resistance and improvement of reliability of parts at a simultaneous reduction in working hours of manufacture.

Reported are the studies of the effect exerted by the radiation energy density and pulse duration on structure and hardness of high-speed alloys [35, 108, 109], steel (1 % C, 1 % Cr, 1 % V, 1 % Mn) [110] and cast iron [111, 112]. As a rule, all the alloys prior to hardening were subjected to heat treatment by the standard technology. Laser hardening results in formation of structures having hardness equal to H_{μ} 11,200–11,500 MPa, and containing almost no retained austenite.

Treatment of the surfaces of parts with the pulsed laser beam leads to formation of a system of hardened spots, which affect residual stresses [113]. Distribution of residual stresses along the line of laser hardening using the pulsed laser "Quant-10" depends upon the coefficient of coverage of the hardened spots. The regions of both compressive and tensile stresses may be formed at a coverage coefficient of 25 %. The efficiency of laser treatment is reported in many publications, giving recommendations on its commercial application [114–123].

1.2.2 SURFACE ALLOYING

Melting of the surface layer and its super rapid solidification (10^6 – 10^9 °C/s) allows formation of oversaturated solid solutions on the surface. Composition of the surface may change due to alloying with elements that are components of the coating or elements added to the molten layer.

Experiments on adding extra alloying elements (C, W, Co, Ti, WC, TiC) to local regions of a high-speed alloy (1 % C, 18 % W) were conducted using quasi-stationary radiation of the ruby laser. The experimental procedure was as follows: paint of a micro powder with a binder in the form of liquid glass (sodium silicate) was deposited on the surface to be hardened. Upon solidification, the paint layer was melted by the laser beam together with the workpiece surface [80].

Graphite and micro powders of hard alloys were used to make the paint. Treatment with the laser beam led to evaporation of the binder, but had no effect on microstructure of the substrate material. For example, this treatment using graphite leads to increase in the amount of carbon in the surface layer of metal to 3.3 %. The use of tungsten increases its amount in the substrate by a factor of 1.7 (up to 30 %).

Laser treatment of the surface with a preliminarily deposited thin layer of graphite powder provides the effect of surface alloying with carbon. Carbonization in laser treatment is possible both by surface melting and high-rate heating without melting [81]. The presence of activators in paints

containing graphite (ammonium chloride, borax) enhances the carbonization effect. In the case of surface melting the depth of the carbonized layer may be 100–150 μm . It is reported [114] that the use of carbon coverings prior to laser heating increases the carbon content of the surface layer to 1.3–1.4 %.

Surface properties were studied [124–129] and the technology for laser alloying with Ni, Cr, B, Si, Al, etc. was optimized. Technological approaches of laser alloying are almost the same in all cases: first a layer of alloying elements or their mixture is deposited, and then this layer is melted together with the workpiece surface.

Of high practical interest is the method of plasma diffusion alloying with chromium [130]. This method is realized by using the electric current flowing through the plasma jet, or by repeated heating of the surface to the solidus-liquidus temperature followed by annealing at a temperature of 873–973 K [131]. As shown by economic analysis [132], power consumption in plasma treatment is lower than in laser treatment using the "Quant-16" laser.

Boride layers were subjected to laser treatment [133]. In this case the treatment decreases their brittleness (by a factor of 10–15) and allows expansion of the application field for borated steels. Technologies are available for producing boride coatings on iron- and titanium-base [134–136] alloys. These technologies involve the use of paints based on the BF-2 adhesive. The paints are dried on the workpiece surface at a temperature of 50 °C for 30 min, and after drying the surface is treated with the "Quant-16" laser beam, the pulse energy being 520 J. As a result, the boride layers 50–100 μm thick with hardness of up to 21,000 MPa are formed on the surface.

Studies were conducted to investigate displacement of nitrogen in the metal melt, and numerical relationships were derived to estimate the efficiency of absorption of nitrogen by the metal melt within the laser treatment zone [137, 138]. This allows prediction of results of the energy effect and selection of the treatment conditions for specific workpiece surfaces.

1.2.3 HARDENING OF TOOL ALLOYS

Efforts on surface hardening of parts made from tool alloys are of a high engineering interest. The method which has been most extensively studied up to now is laser hardening of tool materials. As shown by the studies, any type of laser treatment of tool alloys leads to the effect of phase hardening and martensitic transformations occurring in an alloy. Under certain conditions, increase in microhardness in local zones may amount to 22,000 MPa, which cannot be explained in terms of the commonly accepted theory.

Treatment with the pulsed laser beam provides the rates of surface heating amounting to 10^6 °C/s and thickness of a heated layer equal to 100–150 μm . Then follow a high-rate cooling, transformations, homogenization of solid and liquid solutions and formation of heterogeneous intermediate systems. Resulting layers are characterized by good wear resistance, although their corrosion resistance does not grow. Reportedly, the maximal hardening effect can be achieved

in the case of partial dissolution of initial carbides and formation of a large number of zones with micro chemical heterogeneity of solid solutions in the irradiated layer. Duration of a treatment pulse and structural state prior to irradiation have a special impact. The shorter the irradiation time and the higher the degree of dispersion of the soluble phase, the higher the hardening effect [139, 140].

Characteristic peculiarity of structure of the workpiece surface layer after pulsed hardening is that it is capable of retaining hardness in heating during the friction process. This phenomenon is attributable to the formation of regions having the form of thin plates during the rapid solidification process, the regions being in an amorphous or nano-crystalline state.

For implementation of the modification technology, the optimal value of the radiation power density is chosen on the basis of structure of a material in the hardened layer, which should be a martensite and carbide mixture. This mixture is formed as a result of secondary hardening occurring under the effect of an energy pulse [141, 142].

Deviation from the optimal hardening parameters leads to weakening and deterioration of the performance of parts. Duration of the radiation impact is found to influence the amount of retained austenite. So, at a treatment time of $t=1.5$ and 8 ms, the amount of the α -phase detected in structure is 15 % [141]. The structure contains secondary carbides, the amount of which increases with increase in time.

Irradiation of the preliminarily quenched samples of a tool alloy (of the type of 1 % C, 6 % W, 5 % Mo) was performed without melting [108, 109, 141–145]. The time of exposure of the alloy to radiation was 3 ms, and strength of the metal cutting tools increased 3–5 times. The maximal amount of secondary carbides is shown to form at $We=320$ J/cm².

Martensite with an increased content of carbon and alloying elements is formed on the surface of tool materials after secondary hardening. This is caused by saturation of solid solution at a partial dissolution of carbides. Increase in hardness and wear resistance of the treated layer occurs only in the case where the pulse power density is in a range of $1 < Wp < 5 \cdot 10^5$ W/cm² and the exposure time is $t=5 \cdot 10^{-3}$ s. The highest effect is achieved at a power density of $5 \cdot 10^5$ W/cm², which provides the ultimate temperature of the surface close to the melting point of the alloy [145–148].

Deviation from optimal parameters may lead to deterioration of the performance of the alloys. The efficiency of hardening of the tools was checked on cutters made from a high-speed alloy (1 % C, 9 % W, 5 % Mo) [144, 145]. The experiments were conducted by turning cylindrical samples of high alloys. Rear faces of the cutters were hardened in one pulse using the "Quant-16" unit. Wear resistance of the cutters after hardening increased 3–5 times.

12.4 HARDENING OF HARD ALLOYS

To develop technologies for modification of hard alloys, it is necessary to study the mechanism of their fracture. Wear resistance of different grades of hard alloys over a wide range of cutting speeds cannot be explained in terms of only the mechanism of fracture of carbides [149–154].

Strength of carbides (W, Ti, Ta)C and (W, Ti)C is much lower than that of WC. Therefore, the given mechanism is inapplicable for substantiation of a higher strength of the TK grade alloys (Ti/C/Co) compared with the VK (W/C/Co) and TTK (Ti/Ta/C/Co) grade ones. Oil quenching of hard alloys from temperatures of 1100–1200 °C leads to increase in bending strength (20 %), impact toughness (15–20 %) and durability under cyclic loading (2–6 times). However, improvement in these characteristics, providing no increase in strength of the cutters in turning of steels at high cutting speeds, causes even some decrease in wear resistance.

It is a known fact that interaction of surfaces of base and tool materials results in formation of a stable adhesive bond. This bond is not violated by cutting, thus inducing the adhesion and fatigue wear mechanisms. The evidence of this fact is a smooth profile of mating surfaces on the front and rear faces of a cutter. No traces of separation of individual carbide grains or their conglomerates are found. The tungsten carbide grains in contact with steel are strongly smoothed out, and the binary titanium-tungsten carbide grains project to some extent over the profile of the WC grains.

Presumably, there are two processes that lead to smoothing out of the tungsten carbide grains. The first process involves diffusion dissolution of carbides in alloys treated, resulting in smoothing out of the WC grains in contact with steel. And the second process is based on fracture of the tungsten carbide grains and drag-out of sub-particles from their surfaces. Size of the sub-particles is much smaller than size of the grain proper, which is responsible for a very smooth surface of a hard alloy. Consider three processes leading to wear of the hard alloy tools used for processing of steels [149–152]:

1. Dissociation of tungsten carbide and dissolution of WC grains in iron-carbon alloys.
2. Micro fracture of carbide grains.
3. Weakening of the binding cobalt phase by iron and drag-out of the partially dissolved tungsten carbides and non-dissolved grains (W, Ti)C with moving volumes of the alloy treated.

The cause of smoothing out of carbides is their diffusion dissolution. In this case the intensive dissolution and smoothing of the WC grains seems more logical, compared with the (W, Ti)C grains, as the temperature of dissociation of carbide (W, Ti)C is much higher than that of carbide WC [150–153].

Some principles of variations in mechanical characteristics of hard alloys depending upon their structure and structural components are given in [154]. These principles can be employed to develop and practically apply plasma methods for hardening of hard alloy parts.

Consider the known methods used for hardening of hard alloys. One of them is explosion hardening [152]. Physical-mechanical properties of alloy VK16 changed but insignificantly as a result of hardening. Only an increase in hardness is indicative of a change in state of the binding phase. The cause of a doubled service life in this case can be an increased tungsten and carbon content of cobalt. This increase is attributable to changes in ductile characteristics of a hard alloy.

The process of plasma-chemical synthesis and deposition of coatings is performed, as a rule, in vacuum. It results in thin strong nitride, carbide and oxide films formed on the surface. And it is these films that take up the fracture load applied to the hard alloy. Versatility of the process allows selection of a coating composition depending upon the operational requirements.

Impact by the concentrated flows of light energy is also used for hardening. As a result of this treatment, the heat-affected zone (HAZ) 30–60 μm deep is formed in the surface layer. This zone is characterized by a higher microhardness, compared with the initial material. Substantial decrease in content of the cobalt binder and refinement of the carbide grains in HAZ were detected in the samples treated by the light flows. New phases WC and W_2C are formed in hard alloys based on tungsten carbide. At the same time, no new phases were detected in hard alloys based on TiC.

HAZ in the hardened samples is characterized by refining of carbide grains, dissolution of tungsten carbides in cobalt binder and increased porosity within the recrystallization zone. Formation of pores in the treated layer is attributed to burning out and re-distribution of the cobalt binder. Porosity in HAZ depends upon the time of the effect on a sample by the light flow. The melting zone grows with the duration of this effect. The depth of HAZ in alloys (98 % WC, 2 % Co) and (80 % WC, 20 % Co) is 1.5–2.0 times larger than in alloys (TiC, Co) and (TiC, TaC, Co). This depends upon the difference in the coefficients of thermal conductivity of the WC and TiC base hard alloys.

Of high interest is hardening of tungsten carbide and cobalt base hard alloys with laser radiation. Microhardness of the surface layer after hardening increases to 35,000 MPa. This is attributable to the formation of carbides of the W_2C type, which have higher hardness than WC (by 10,000–14,000 MPa). Also, this leads to changes in fine structure and composition of the binding alloy.

If the energy density does not exceed 80 J/cm^2 , the binder becomes saturated with the products of destruction of monocarbide WC. Complex carbides $\text{Co}_3\text{W}_3\text{C}$ are formed at an energy density of 80–100 J/cm^2 , leading to weakening of the alloy due to decrease in the metal cobalt content of the binder. Complex carbides with a violated stoichiometry (of the type of $\text{Co}_x\text{W}_y\text{C}_z$) are formed in the binding layer, and the content of semi-carbides W_2C and cubic carbide WC markedly increases at an energy density of 140–280 J/cm^2 .

To increase wear resistance of hard alloys containing 3–6 % Co, the energy density should not exceed 80 J/cm^2 . For alloys containing 6–8 % Co this value should be 100 J/cm^2 , and for those with 10 % Co – 120 J/cm^2 . The aggregate state of an alloy hardly changes under irradiation with a low-energy density.

It was found that sensitivity of a hard alloy to cracking depends to a considerable degree upon the amount of the cobalt binder and possibility of refining of the carbide grains. The products of dissociation of monocarbide WC are fcc carbides WC, binary carbides W_2C , etc. They enrich the binding layer (Co) and have a negative effect on strength of an alloy.

1.3 REQUIREMENTS TO MODIFICATION TECHNOLOGIES

1.3.1 ALLOYS AND PROPERTIES OF ALLOYING ELEMENTS

Modification of surfaces of parts made from low alloys is of a high industrial interest. These alloys have high strength and are relatively inexpensive. Owing to alloying with chromium (0.2–0.7 %),

vanadium (0.15–0.30 %) and tungsten (0.5–0.8 %), low tool alloys are characterized by higher stability in heating and higher wear resistance, compared with carbon alloys.

Critical machine parts and wood-working knives are made primarily from alloys with a chromium content of up to 6 %. These alloys are additionally alloyed with vanadium, tungsten or molybdenum, as well as nickel and titanium. It is a known fact that chromium even in small amounts causes increase in abrasive wear resistance of the alloys. Alloy (1 % C, 6 % Cr, 4 % V, 1 % Mo) is the best among this group of the alloys.

High-speed alloys (1 % C, 6 % W), (1 % C, 6 % W, 5 % Mo) and (1 % C, 6 % W, 5 % Mo, 3 % V) are used mostly for the manufacture of tools operating under conditions of heavy loading and heating of the working surfaces. High cutting properties of the tools are provided through alloying with strong carbide-forming elements, such as tungsten, molybdenum and vanadium. The chromium content of all high-speed steels is 3–4.5 %.

Alloys employed for the manufacture of dies for hot forming of machine parts can be conditionally sub-divided into three groups: alloys containing up to 2–6 % W, alloys containing 6–9 % W, and alloys with 12–18 % W.

Tungsten has a different effect on heat and fire crack resistance of die steels. Increase of the tungsten content in an alloy to 7–8 % causes an almost proportional increase in its heat resistance. Further increase in the tungsten content (up to 12 %) hardly increases heat resistance of the alloy. The presence of chromium in complex carbide (MeC) favours its dissolution, increases the degree of alloying of solid solution and improves heat resistance of the tungsten alloy. The chromium content of more than 5 % has a negative effect on heat resistance of the alloy.

The element that effectively improves properties of die steels is molybdenum. Unlike chromium, molybdenum improves toughness with no deterioration to heat resistance of the alloy surfaces, and increases fire crack resistance. Molybdenum alloys (5–6 % Mo) are very sensitive to decarburization. Therefore, the molybdenum content of more than 3 % is permitted for alloys heated for hardening in controlled environments. Molybdenum has a positive effect on alloys containing 2–3 % nickel. Nickel is added to increase toughness and hardenability of an alloy.

This minimum of the information is necessary to get an adequate understanding of the plasma technology used for modification of surfaces of metal alloys.

1.3.2 MODIFICATION OF HIGH-SPEED STEELS

High-speed alloys belong to the special class of materials intended for operation under conditions of high contact loads and temperatures. Of interest is further improvement of surface properties parts made from these alloys, with no changes into their bulk properties.

Investigations of the mechanism of surface modification were conducted on alloys containing no tungsten (1.1 % C, 4 % Mo, 2 % V, 1 % Al, 1 % Cu) and on alloy (1 % C, 6 % W, 5 % Mo). Surface modification was performed using laser plasma [147, 148]. The investigations showed

a considerable increase in the content of retained austenite, amounting to about 60 % (45 % in alloy 1 % C, 6 % W, 5 % Mo) after laser treatment with no surface melting. The shape of profiles of diffraction lines is indicative of a substantial heterogeneity of solid solution as to the carbon content. This is caused by high heating and cooling rates achieved in laser heat treatment.

The results of studies on the efficiency of pulsed-plasma laser treatment are of a similar character [153, 154]. Treatment of the surface of the 1% C, 6 % W, 5 % Mo alloy sample with the flow of plasma (radiation energy density $I=34 \text{ MJ/m}^2$) provides increase in hardness, grain refining, fragmentation of structure and elimination of clusters of coarse carbide particles.

The maximal values of surface hardness are provided by the pulsed treatment, which is associated with formation of a dislocation structure of metal having an increased density of defects, high degree of dispersion of blocks and concentration heterogeneity, which are higher by an order of magnitude than those of the quenched steels.

Surface treatment with the high-energy density plasma jets is effective for hardening of both carbon and alloyed steels. Further improvement of surface properties of parts can be achieved through alloying the surface with appropriate elements. Complex alloying of the part surfaces provides increase in wear, heat, corrosion, erosion resistance, etc.

1.3.3 ACCELERATION OF DIFFUSION OF ALLOYING ELEMENTS

The efficiency of modification is achieved owing to the effects of abnormal mass transfer of alloying elements. The effect of abnormal mass transfer in solids is a physical phenomenon that shows up only under pulsed loads. This phenomenon takes place only under non-equilibrium conditions and is fundamentally different from diffusion occurring under stationary hardening conditions.

Wide acceptance has been gained lately by methods of impact magnetic compression, treatment with the pulsed magnetic field, laser and explosion treatment, hydro-electropulse treatment, ultrasonic peening (UP) and deformation of metals and alloys during the process of reversible martensitic transformations.

Technology sophistication and simultaneous application of several types of the pulsed effect to the surface lead to the non-additive character of acceleration of diffusion [155–158]. The abnormal mass transfer cannot be described in terms of classical diffusion.

It is a known fact that an increase in temperature of crystalline solid bodies is accompanied by increase in mobility of atoms, but there is no way so far of achieving the value corresponding to that of the coefficient of diffusion of intrinsic atoms in liquid metal ($\sim 10^{-6} \text{ cm}^2/\text{s}$) under conventional conditions. Migration of atoms can be increased through increasing defectiveness of the crystalline structure as a result of irradiation, phase transformation and plastic deformation. In this case the diffusion coefficient grows, which is attributable to increase in the mean concentration of vacancies [155].

In addition, the high-rate deformation results in a dramatic increase in the quantity of spot-like defects in crystals. The process of generation of defects is faster than dynamic recrystallization,

which causes acceleration of diffusion [156, 157]. Diffusion of atoms in this case is realized through moving dislocations, and duration of the deformation effect influences the mass transfer coefficient [159–161]. So, as shown in study [155], under the shock effect (deformation time $t=4\cdot10^{-3}$ s) and at a temperature in the contact zone equal to 800 °C, the presence of iron atoms in titanium is fixed at a depth of 200 μm . The diffusion coefficient in this case is $D=8.3\cdot10^{-3}$ cm^2/s , which by two orders of magnitude higher than in liquid metal.

Dramatic increase in mass transfer is reported to take place in ultrasonic peening. Investigations of structural changes in metal after ultrasonic peening show that grain refining takes place and grain boundaries acquire a wavy shape after the multiple shock effect ($n\sim 30$ kHz) [154]. This results in the process of dynamic recrystallization. Recrystallization after each loading event occurs simultaneously with subsequent events. Therefore, displacement of the grain boundaries is superimposed on the transfer of atoms deep into metal, taking place during ultrasonic peening [157–162]. Under the effect of ultrasound, in addition to multiplication of dislocations the quantity of spot-type defects grows to values characteristic of those seen at high temperatures.

Intensification of mass transfer can be attributed also to the processes resulting from $\alpha>\gamma$ transformations. Substantial stresses are induced during the process of growth of the martensite crystal ($\alpha>\gamma$ transformation). Relaxation of these stresses leads to deformation of metal in micro volumes and growth of defectiveness of the structure. The reverse $\gamma>\alpha$ transformation maintains boundaries of the phases formed in direct transformation. In addition, an increase in temperature from 300 K to the diffusion annealing temperature is accompanied by partial decomposition of martensite and formation of carbides, which also favours increase in length of the phase boundaries. Each next event of $\alpha>\gamma$ transformation leads to increase in the dislocation density, as well as length of the boundaries between the phases and grains in the structure, which are the ways of accelerated diffusion [155–160].

Therefore, intensification of mass transfer is a complex process caused by a combination of high-rate transformations in structure of an alloy. Kinetics of mass transfer in surface melting using the laser beam was studied on samples made from the iron-base alloy with a carbon content of 0.3 % [163]. Al, Cr and Ni coatings 10–80 μm thick were deposited on the sample surfaces. Then the surfaces were penetrated by the 5 kW laser LT-1 to a depth of 0.3–1.0 mm. As shown by the studies, mass transfer in laser melting takes place primarily due to the thermocapillary effect. Treatment with the pulsed plasma raises the rate of deformation of the contact zone to values of 10–100 s^{-1} . In turn, this results in development of the diffusion zone with a value of 0.01–0.001 s. The length of this zone can be described at a diffusion coefficient value of about 0.01–0.001 cm^2/s . This value is by several orders of magnitude higher than in the liquid state.

Treatment of samples using the ultrasonic radiation source oscillating at an increased frequency caused growth of the diffusion coefficient by more than 30 orders of magnitude [161]. The treatment was performed at room temperature.

The coefficients of mass transfer substantially grow at high-rate tension in the pulsed magnetic field ($T_p=105\text{--}110$ μs) [155]. Migration of atoms is affected also by energy of a magnetic

field pulse. The coefficients of mass transfer in the case of pulsed compression at 300 K amount to $D=50-8.3 \cdot 10^{-3} \text{ cm}^2/\text{s}$.

Brief review presented in the book shows that activation of mass transfer can be achieved by different methods of the pulsed effect realized in pulsed-plasma treatment.

1.3.4 NITRIDING

The technology of alloying with nitrogen (nitriding) is widely applied in industry, and upgrading of this process is of a high industrial importance. The work is in progress to study laser and plasma nitriding.

Investigations are conducted to study alloying of surfaces of some alloys with the jet of nitrogen gas fed together with the laser beam via a nozzle 1–4 mm in diameter [163]. The distance between the exit section of the nozzle and surface treated is 2 mm. Duration of the laser beam pulse is 0.002 s. The investigations show that repeated application of the laser beam pulses resulted in an increase in depth of the nitrided zone and its microhardness by 20–30 %. Formation of the nitrided layer to a depth of 80 μm was observed after the complex nitrogen treatment of tool alloy (1 % C, 18 % W), stainless alloy (0.2 % C, 13 % Cr) and medium-alloyed alloy (0.38 % C, 1 % Cr, 1 % Mo, 1 % Al), which, in terms of the classical diffusion theory, can be achieved only after the treatment with nitrogen for 34 h at a temperature of $T=813 \text{ K}$.

It is assumed in further considerations and calculations that variations in the content of carbon and nitrogen in the surface layer of metal alloy are proportional to the flow of particles in a direction to the surface. At a short time of the process the reverse flow of atoms from the melt is ignored. The concentration of gas dissolved in the melt is characterized by an extreme dependence upon its pressure. After affecting a sample of alloy VT-9 by the plane shock wave having a pressure of 2–12 GPa, the rate of the nitriding process grew 2–3 times. And the process could be realized at low temperatures [161]. The alloying process was performed under the shock-pulsed effect by the nitrogen containing plasma. Elastic disturbances caused by the shock-pulse effect propagated outside the directly deformed layer.

Four modes of the pulsed effect of nitrogen on the chromium sample surface were studied [164]. The layer-by-layer X-ray diffraction analysis of a nitrided chromium sample showed that the zone of high hardness was an oversaturated solid solution of nitrogen, the grain size of this solution being by an order of magnitude smaller than that of the initial element. The dispersed inclusions of nitride Cr_2N , few in number, were revealed along the boundaries of small grains. Formation of the oversaturated solid solution of N in Cr during diffusion interaction was proved to be the autocatalytic process. Diffusion of N into Cr leads to formation of the excess defects in the crystalline lattice, and nitrogen atoms segregating on them increase the concentration of solid solution up to the values that are higher than solubility limit of nitrogen in equilibrium structures.

1.4 DUPLEX AND TRIPLEX MODIFICATION TECHNOLOGIES

Among the known methods used for modification of surface layers the most efficient ones are those which are based on the simultaneous or successive combination of two (duplex) or three (triplex) technologies. These technologies provide the surface layer containing compounds that are characterized by unique properties, which cannot be provided by using any technology taken separately [165–176]. The positive effect of applying the duplex technologies is determined in many respects by the metallurgical compatibility of materials utilized.

The list of some duplex technologies is given below:

1. Nitriding, carburization or alloying from the salt melts can be followed by deposition of hard coatings by galvanic, vacuum-plasma or thermal spraying methods.
2. Nitriding of workpiece surfaces after heat hardening, alloying from the salt melts and/or thermal spraying of coatings.
3. Heat hardening of the surface after deposition of thermal spray coatings, borating, vanadium plating, chromium plating or nitriding.
4. Machining of the surface after heat hardening, carburization, nitriding or thermal spraying.
5. Simultaneous melting of the workpiece surface and special paints of alloying elements (coverings) and coatings after thermal spraying.

The first group of the technologies includes processes of thermochemical treatment of the surface layer after plasma-chemical synthesis and subsequent deposition of a material synthesized. This group also includes passivation of the surface prior to deposition of galvanic coatings.

Technologies of the second groups are applied to decrease wear. They are performed by alloying with nitrogen after preliminary hardening of workpieces. This provides deposition of the nitride coatings, which are important in terms of tribology. These technologies are also employed in a combination with melting and alloying of the surface layer of light metal parts. In addition, they make it possible to increase wear resistance of the surface layer formed by thermal spraying of hard alloy powders.

The third group of the technologies includes the combined processes, which are intended for optimization of properties of the surface layers of coated parts through their subsequent heat hardening. This combination provides good adhesion of the hard surface layer to the substrate.

Of interest also is machining of the surfaces of parts preliminarily hardened by thermochemical methods. This leads to formation of extra compressive stresses and substantial improvement of contact fatigue. This combination of the technologies provides stability of the shape and increase in fatigue strength of a part.

Glazing of thermal spray coatings of powders favours increase in their adhesion strength. The "thermal spraying – melting" combination is used also for alloying of the surface layer.

The "nitriding – deposition of hard alloy coating" technology combination is employed to harden metal cutting tools, hot and cold forming dies and heavy-loaded machine parts. Depending upon the technology conditions, thickness of the nitrided layer may be varied from 10 to 500 μm . Nitriding

with formation of a corrosion-resistant protective layer is used only in the cases of increased requirements for corrosion resistance of parts.

The continuous process of nitriding and coating proved advantageous for producing thin hardened layers, which is required, for example, for cutting tools. At present such technologies are implemented using the PVD (physical vapor deposition) units. The coatings are formed by deposition from the vapor or gas phase. This is the operation of formation of a substrate for subsequent deposition of thin hard surface layers.

The above analysis shows that the most common technologies are as follows: hardening of the surface layer of nitrided parts, hardening of the surface layer of parts after borating and parts with a hard material coating, hardening and melting of the surface of grey cast iron parts followed by nitriding, and heat hardening of the surface layer followed by nitriding.

In addition, the analysis shows that almost all of these technologies can be implemented using the pulsed-plasma technology, the requirements to which will be presented in the next section of the book.

1.5 REQUIREMENTS TO INTEGRATED PLASMA-DETONATION TECHNOLOGY

Analysis of literature sources on high-energy density treatment methods used to modify surfaces of parts shows that they, as a rule, provide a multiple increase in performance of the parts operating under the most diverse conditions. Investigations prove the high efficiency of treatment using the high-energy density heat sources for almost all known iron-, titanium-, cobalt-, nickel-, aluminium- and copper-base alloys.

Of special interest is the application of the pulsed plasma treatment methods, which are not inferior and sometimes even superior in their efficiency to laser, electron beam, electric-discharge and other treatment methods.

The studies conducted by the authors to investigate the magnetic-gas-dynamic flow of products of combustion of fuel mixtures in annular channels showed the possibility of the formation of plasma with energy parameters required for surface modification. These parameters are achieved in the gas-detonation systems operating in a compressed mode of combustion of gas mixtures.

The compressed mode is the mode of detonation combustion of fuel gas mixtures in the electrostatic field. The energy parameters of plasma are adjusted through the composition of the fuel gas mixture, electric potential and geometric characteristics of the device. The parameters can be varied within the following ranges: energy 1,000–10,000 J, frequency 1–10 Hz, duration $0.5 \cdot 10^{-3}$ – $5 \cdot 10^{-3}$ s, speed 2,000–8,000 m/s and temperature 5,000–20,000 K. The electric current pulses of 1–15 kA are passed through the plasma jet. The pulsed magnetic field is formed, corresponding to the amperage. The integrated simultaneous impact on the surface being modified leads to the abnormal effects of heat and mass transfer, as well as the effects of formation of nano-crystalline structures, formation of new chemical compounds, meta-stable and multilayer structures.

It seems appropriate that further development of the modification technologies should be based on the integrated impact on the surface of metal parts by physical fields, which are induced by the electric current passing via the pulsed plasma jet.

The surfaces are affected most efficiently by a set of physical phenomena: shock waves, magnetic fields, kinetic energy of particles, high-rate heating of small regions on the surface, ion implantation, fast heating with electron beams, plasma-chemical synthesis and deposition of films.

By interacting with metals and alloys, each of the above physical phenomena intensifies martensitic transformations, increases the dislocation density, provides synthesis of carbides or nitrides in the form of films, forms amorphous coatings or layers on the surface, etc.

The maximal effect is achieved in the case of the integrated effect on the surfaces of metals and alloys by all of the above physical factors. It is necessary to combine in one treatment cycle such processes as fast heating and cooling, saturation of surface with elements (N, C, W, Mo, Ti, Ni, Cr, etc.), treatment with a pulsed magnetic field and high-power shock wave, and deposition of films of the plasma-chemical synthesis products. Flow of the electric current via the plasma jet to the surface being modified increases the efficiency of impact on the surface. This provides realization of the effects of abnormal diffusion of elements (forming the plasma) into the surface layers. Plasma-detonation treatment (PDT) we offer comprises the entire set of duplex technologies.

Plasma-detonation generators of the pulsed plasma were developed for PDT. Design of these generators is based on adjustment of basic energy parameters of the plasma jet.

PDT provides:

- solid-phase alloying of the surface with elements that comprise the plasma (C, N, W, Mo, Cr, Ni, Ti, etc.) or alloying from molten paints (coverings);
- formation of a thin layer (up to 100 μm thick) with nano-crystalline structure on the surface of parts;
- pulsed-magnetic treatment of the part surfaces;
- formation of a thin coatings of metals and alloys, oxides, carbides, nitrides, etc. by condensation of metal vapors and their interaction with the main components of plasma.

The field of application of the high-energy density modification technologies are components of drives of tractors, harvesters, excavating machines and cars, as well as thrust bearings, disks, supports of pumps and hydraulic machines, rings of synchronisers, cams and axles of camshafts, and rings of screw wheels. Also efficient is hardening of internal surfaces of cylinders of engines and pumps, channels and journal boxes, jack hammers and perforators, and locations of gear box bearings. These technologies are employed for modification of properties of the surfaces of transmission gears and gear pumps, cams, piston rings, etc.

Worthy of notice also is the high efficiency of hardening of metal cutting and wood working tools, dies, moulds, punches, matrices, etc. Industrial tests showed a 3–5 times increase in performance of the tools after hardening.

ABSTRACT

A brief theory of plasma-detonation generation of pulsed plasma is considered. The result of the simulation allows to optimize the geometric dimensions of plasma-detonation devices. These devices are designed to generate highly concentrated pulsed plasma jets for surface modification of products.

KEYWORDS

Theory of pulsed plasma generation, pulsed plasma jet generator.

2.1 INTERACTION OF PLASMA WITH SURFACE OF A SOLID**2.1.1 PRINCIPLE OF LASER PLASMA HARDENING**

Physical principle of hardening by the laser beam is that hardening of the surface is performed by the "laser" plasma, rather than by the electromagnetic radiation (light beam) [177]. The laser pulse falling on the workpiece surface causes evaporation of dielectric material of the coating, which efficiently absorbs radiation. This material is either available already or specially deposited on the workpiece surface. The vapor region screens the workpiece, resulting in formation of a strong shock wave in it and ionization of gas adjoining the workpiece behind the wave front. The light radiation absorption coefficient dramatically grows, the gas becomes overheated and transforms into plasma. The laser beam meets with the electromagnetic radiation absorption wave, which heats and ionises the gas.

There are publications [177–181] dedicated to study of the effect of gas and composition of laser plasma on surface hardening. The concentration of elements dissolved in metal, e.g. nitrogen, and microhardness of the surface being hardened can be controlled through varying the composition, pressure and power density of the plasma flow. The high-density gas jet restrains scattering of plasma, thus extending the time of its interaction with the surface.

It is a known fact that the rate of heating of the exposed surface having no absorbing coating, when subjected to pulsed-periodic irradiation in the oxidising environment, can be several times higher than in continuous treatment of the coated surface. This is caused by formation of a layer of oxides on the workpiece surface, where the oxides act as absorbing materials for the energy of subsequent pulses. Summation of the thermal energy takes place at a pulse repetition frequency equal to microseconds (100 Hz) and low heating (to 100 °C) per pulse [182].

2.1.2 DECELERATION OF PLASMA JET ON A SOLID SURFACE

Based on analysis of the above information, laser treatment can be regarded as treatment with a stationary or pulsed plasma jet generated and maintained by electromagnetic radiation, i.e., the concentrated light beam.

Let's consider processes of deceleration of the pulsed plasma jet on a fixed surface [181–185]. Enthalpy of this jet can be determined from the following equation:

$$h = \frac{5}{2}kT(1+i) + iJ + \frac{mv^2}{2}, \quad (2.1)$$

where T – the temperature in the decelerated plasma layer, K; i – the degree of ionization of plasma; J – the ionization energy; m – the mass of plasma; v – the velocity of the plasma flow at deceleration $v=0$.

Analysis of the equation shows that the main contribution to the heat content of the plasma jet is made by the kinetic energy of the jet. The enthalpy depends upon the velocity of the plasma flow, mass and temperature.

The enthalpy of deceleration on a fixed wall at $v=0$ is as follows:

$$h^* = \frac{5}{2}kT^*(1+i^*) + i^*J, \quad (2.2)$$

where T^* – the temperature of the decelerated plasma; i^* – the degree of ionization of the decelerated plasma.

The main mechanisms of heat transfer in the decelerated plasma are convective and radiant heat transfers. In the case where plasma flows over the workpiece surface, the convective heat transfer is determined as follows:

$$g_e = k \cdot \text{grad}T, \quad (2.3)$$

where g_e – the value of the convective flow; k – the thermal conductivity coefficient for a mixture of molecules, atoms, ions and electrons; T – the temperature gradient near the surface of a body flowed about by plasma.

The coefficient of thermal conductivity for a mixture of gases can be written down as follows:

$$k = k_e + k_{ma}, \quad (2.4)$$

where k_e – the coefficient of thermal conductivity by electrons; k_{ma} – the coefficient of thermal conductivity for the atom-molecule mixture.

At a substantial ionization in the decelerated (shock-compressed) plasma layer the heat transfer to a body hardened occurs by electrons (thermal conductivity by electrons takes place). Thermal

conductivity by electrons is much higher than that by ions, as at close temperatures T_i and T_e the thermal velocity of electrons is m_i/m_e times higher than that of ions.

The coefficient of thermal conductivity of the atom-molecule mixture can be written down as follows:

$$k_{ma} = k_a \times \frac{(0.7 \times L + 1.28)}{(1 + i)};$$

$$k_a = 8.4 \times 10^{-7} \times T^{4/5}, \quad (2.5)$$

where k_a – the coefficient of thermal conductivity by atoms.

After substitution of constants to the formulae and transformations, the coefficient of thermal conductivity by electrons can be written down as follows:

$$k_e = 9.34 \cdot 10^{-12} \frac{\sqrt{T_e^5}}{iL}, \quad (2.6)$$

where T_e – the electron temperature; L – the Coulomb logarithm; i – the ionization degree.

Under conditions of a low-voltage electric discharge, the value of the coefficient of heat transfer, k , is determined by the total contribution made by electrons, ions, atoms and molecules. In pulsed-plasma treatment the shock-compressed (decelerated) plasma layer is up to 1 mm thick. The temperature gradient in this layer amounts to $4 \cdot 10^7$ K/m.

At a temperature of more than 15,000 K the process of dissociation is completed, as the energy of dissociation is normally lower than the ionization energy. The presence of free electrons is required for formation of continuous radiation.

The heat radiation flow from an absolutely black body is determined by the following relationship [184]:

$$g_i = \sigma T^4, \quad (2.7)$$

where σ – the Stefan-Boltzmann constant; T – the temperature of the black body.

Analysis of equation (2.7) shows that the sufficient number of electrons for the electron mechanism of thermal conductivity is achieved already at a temperature of 10,000 K. The complete radiation density within a temperature range of $0 \rightarrow \infty$ is equal to:

$$U_{(0, \infty, T)} = U_{(T)} = \sigma T^4 = 5.67 \cdot 10^{-8} \cdot T^4, \text{ W/m}^2. \quad (2.8)$$

The pulsed-plasma jet causes continuous radiation on the workpiece surface, induced by free-free and bound-free transitions, as well as linear radiation induced by bound-bound transitions [185].

To calculate density of the radiation flow from a shock plasma layer formed near the surface, one should take into account that air absorbs electromagnetic radiation with a wavelength from 2000 Å to ∞ :

$$U_{(v_1, v_2, T)} = 5.67 \cdot 10^{-8} \cdot T^4 |Q_1(x_1) - Q_1(x_2)|. \quad (2.9)$$

The values of $Q_1(x)$ can be found from tables [186].

It is known that the heat radiation flow absorbed by the metal surface under the effect of the supersonic jet, where a shock-compressed plasma layer is formed near the surface, is calculated in a forward-backward approximation [182]. The radiant heat flow is calculated allowing for the emissivity factor of plasma (0.65–0.95). The temperature of the metal surface is calculated with allowance for the radiation absorption coefficient, which is equal to 0.3–0.5 for surfaces of different metals.

The main condition for formation of a radiant flow is that the shock region of plasma confined between the outgoing shock wave and surface of an obstacle should be present near the surface of a body. The jump-like increase in temperature, density and pressure of the incident flow occurs in this region. Optically dense plasma regions are formed at a high flow rate, i.e. where the deceleration enthalpy is high.

Decrease in the velocity of the plasma jet and, therefore, in the deceleration enthalpy leads to decrease in the temperature of plasma in the shock-compressed region. The radiant heat flow decreases in proportion to decrease in temperature with the fourth power. The role of the convective electron flow decreases, and the convective atom-molecule heat flow increases accordingly.

Decrease in the jet energy to 200 J leads to decrease in the temperature of plasma in the shock-compressed layer to 8,000 K, and the emissivity factor of plasma falls to 0.65. The convective mechanism of heat transfer acquires a decisive importance.

Theoretical analysis of physical processes occurring in the shock-compressed plasma layer allows calculation and prediction of basic thermal-physical characteristics of the plasma jet necessary for surface modification.

2.1.3 SURFACE HEATING

In pulsed-plasma treatment the region to be hardened is heated from the surface, and the propagation of heat in depth takes place due to thermal conductivity. Cooling of the surface after heating occurs mainly due to the heat capacity of the cold layers of metal.

It is assumed in our further considerations that the maximum permissible temperature of the workpiece surface allowing structural transformations is the solidus temperature of a given alloy, T_{pl} .

The permissible specific heat flow q absorbed by the surface can be determined subject to the absence of surface melting [187]:

$$q = \sqrt{\pi} \cdot \frac{\Delta_{pl}\beta}{2\sqrt{\tau_n}}, \quad (2.10)$$

where Δ_{pl} – the increment in temperature to melting, $\Delta_{pl}=T_{pl}-T_0$; β – the coefficient of accumulation of heat by the workpiece material, kcal/m²; τ_n – the time of irradiation of surface by the plasma jet, s.

Specific power of the plasma flow absorbed by the workpiece surface is determined from the following formula:

$$N_o = 6.183 \cdot 10^{-8} \frac{\Delta_{pl}\beta}{\sqrt{\tau}}, \text{ KW/m}^2. \quad (2.11)$$

After discontinuation of irradiation, cooling of the workpiece surface begins. However, the layers of metal located beneath the surface still continue to be heated for some time. These layers receive energy from the surface and are heated to a certain maximum temperature T_{max} , and only after that they begin to cool down.

By transforming (2.11), reduce it to the dependence of thickness of the hardened layer upon the radiation time and thermal-physical characteristics of an alloy treated:

$$x_s = 2\beta\sqrt{(a \cdot \tau_n)}, \quad (2.12)$$

where α – the coefficient of thermal diffusivity.

Effects of short plasma pulses on the surface of a solid are compared, by analogy, with the surface explosion, at which the calorific power of an explosive is equal to Q/M^* , where M^* is the mass of a material energized during the time of the effect by a plasma pulse.

Surface $i=0$ subjected to a short-time impact by plasma with time t_o should be small, compared with thickness of the absorbing layer divided by the velocity of sound. After impact by the plasma jet, the layer that absorbed its energy scatters at an initial velocity of $v = \sqrt{Q/M^*}$, while the shock wave propagates through a quiescent body (gas).

As follows from the solutions of equations of gas dynamics in the automodel form, 89 % of mass introduced into motion is contained between the shock wave front and point $x=0$, corresponding to the initial position of a body, the outburst being only 11 %.

To estimate thickness of the layer heated by the mechanism of electron thermal conductivity, consider displacement of the front of the heat wave occurring in accordance with the following law: $cp_o x^2 \approx x_e(T)t$, $cp_q^2 x \equiv \Delta$ at $t > t_o$, and heat capacity of a unit volume can be considered constant. The thermal conductivity coefficient is $x_e = bT^{5/2}$, and the law of movement of the heat wave front has the form of $x = DT^{2/9}$ [182]. The law of variation in mean temperature with time is $T = kt^{2/9}$, where

$$D = \Delta^{2/3} B^{2/9} (cp_o)^{-7/9}, \quad K = (\Delta / t_o)^{4/9} (Bcp_o). \quad (2.13)$$

The mass of a material, M^* , heated by the heat wave for time t_o equals:

$$M^* = c^{-1} (Bc\rho t_o)^{2/9} \Delta^{5/9}. \quad (2.14)$$

2.1.4 DETERMINATION OF HEAT FLOW

The following formula for engineering calculations of increase in surface heating temperature was derived on the basis of simplified mathematical models [72, 184, 188]:

$$\Delta = \frac{q\sqrt{a}}{\lambda\pi\sqrt{t}}, \quad (2.15)$$

where q – the specific heat flow, W/cm²; λ – the thermal conductivity, W/cm-deg.

This relationship is valid for time $t > 10^{-5}$ s of interaction of the plasma flow with surface, and provides a sufficiently accurate description of the reality at $t_i = 10^{-3}$ s.

As the heat flow depends upon the power of the plasma jet, it is of interest to estimate it also from the standpoint of ensuring structural transformations at a certain depth under the surface:

$$\Theta = \lambda(T_p - T_s) / x_s, \quad (2.16)$$

where Θ – the heat flow, W; T_p – the melting point of the workpiece surface (solidus temperature); T_s – the temperature of structural transformations (hardening); x_s – the hardened layer thickness.

Analysis of these relationships shows that it is necessary to increase the time of interaction of plasma with the surface in order to provide layers of a sufficient thickness. In the pulsed treatment mode, it can be done by irradiating one and the same location at a high frequency. This treatment provides the thermal cycling conditions and maintains the high rates of heating and cooling of the surface layer, which is characteristic of the pulsed treatment.

As shown by the experiments conducted with pulsed technological lasers, heat is accumulated in the surface, and thick hardened layers are formed at a frequency of 100 Hz, the rate of variations in temperature being 10^3 – 10^7 °C [189].

2.2 PLASMA-DETONATION GENERATION OF PLASMA

2.2.1 PROBLEM STATEMENT AND SOLUTION

Modern engineering industry requires development of cost-effective and efficient technologies and equipment to ensure modification of surfaces of metal parts and tools. This encourages development of the treatment methods based on electromagnetic principles of acceleration and heating

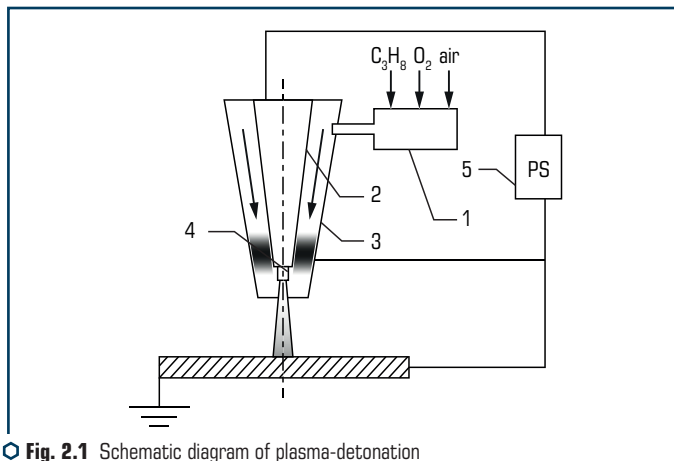
of a gas (plasma) jet [190–207]. In electromagnetic devices of the type of rail drivers (railtrons), acceleration and heating of a working gas are performed through interaction of ponderomotive forces induced by the electric current flowing through the rails and a current-conducting gas layer. The velocity of gas is proportional to the amperage. The latter should be 150 kA to achieve the velocity equal to 2–4 km/s. The time of the acceleration process in this case is 120 μ s and the temperature of gas amounts to 20,000 °C.

The more advantageous type of the "railtron" is suggested in monograph [191]. This axial "railtron" provides velocity of the plasma "piston" equal to 10 km/s at a current of 20 kA. As a result, the outlet velocity the plasma jet amounts to 4 km/s.

Localization of the arc in the plasma "piston" and its fixation to the electrode (rail) surfaces cause erosion and fracture of the rails. As a result, this limits the application fields of the electromagnetic systems. In addition, such plasma generation systems should be equipped with sophisticated devices for switching of the electric current (20–150 kA) at a frequency of 2–10 Hz, which has a negative effect on their performance.

The efficient method for generation of the high-energy plasma jet is detonation of a fuel mixture in the electromagnetic field induced between two coaxial electrodes in a reaction chamber (RC). Energy parameters of the non-stationary detonation combustion (pulsed plasma jet) products were determined by solving the known 2-dimentional non-stationary problem of propagation of the detonation wave in the electric field between two coaxial electrodes. The pulsed plasmatron (**Fig. 2.1**) was designed on the basis of the obtained data.

It consists of device 1 for mixing of fuel gases and initiation of the detonation combustion of fuel gas mixtures, central anode electrode 2, conical cathode electrode 3, evaporated electrode 4, and electric current supply 5.



○ **Fig. 2.1** Schematic diagram of plasma-detonation device – plasma generator

At the moment of the detonation initiation, the combustion products enter into a gap between electrodes and close the electric circuit of a capacitor-discharge power supply. This results in formation of the electrically conducting layer of the combustion products. This gaseous layer is accelerated under the effect of the gas-dynamic and electromagnetic forces. When the pulsed plasma jet is ejected from the plasmatron, it switches the electric circuit between the anode electrode and cathode workpiece surface. As a result of the electric current flowing through this jet, plasma is heated due to release of Joule heat $Q = \sigma E_2^2 \text{ W/m}^3$. Tip of the anode consumable electrode is overheated and evaporated, which provides addition of alloying elements into the plasma jet.

The high-energy jet of gas, falling on the workpiece surface, forms a shock-compressed layer (SCL) on it. The electric current flowing through the plasma jet (PJ) causes extra heating of SCL and intensification of diffusion processes.

To develop the method for design of the pulsed plasma generator, consider propagation of the detonation wave (DW) between two coaxial bodies of revolution used as electrodes. Behind the detonation wave, the gaseous combustion products become current-conducting because of a dramatic increase in temperature. Connecting the electrodes to the power supply induces electric field E in a gap between the electrodes. The electric current flow is initiated behind the detonation wave, an extra ponderomotive force is generated, and an additional energy input to gas is caused by Joule heat dissipation, which leads to a substantial acceleration of DW [192–205].

Fig. 2.2 shows schematic of the pulsed plasma-detonation device reaction chamber.

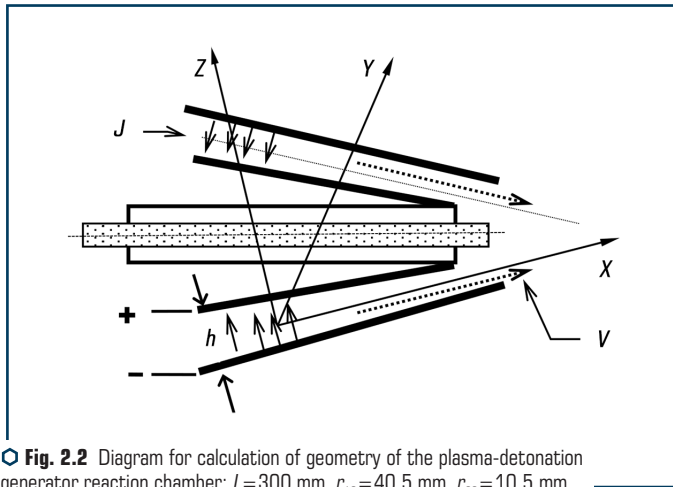


Fig. 2.2 Diagram for calculation of geometry of the plasma-detonation generator reaction chamber: $L=300 \text{ mm}$, $r_{10}=40.5 \text{ mm}$, $r_{20}=10.5 \text{ mm}$, $r_{1k}=33 \text{ mm}$, $r_{2k}=3 \text{ mm}$

As the problem has an axial geometry, vectors of electric field intensity $\vec{E} = (E_r, 0, E_x)$, current density $\vec{J} = (J_r, 0, J_x)$ and velocity $\vec{V} = (V, 0, U)$ lie in a meridian plane, and vector of magnetic

induction has only azimuthal component $B = (0, B, 0)$. In an assumption of homogeneous and isotropic conductivity, equations of magnetic dynamics of gases, which describe the gas flow behind DW, have the following form:

$$\frac{\partial \rho}{\partial t} + \frac{\partial \rho u}{\partial x} + \frac{1}{r} \frac{\partial \rho v r}{\partial r} = 0; \quad (2.17)$$

$$\rho \left(\frac{\partial u}{\partial t} + u \frac{\partial u}{\partial x} + v \frac{\partial u}{\partial r} \right) + \frac{\partial \rho}{\partial x} = \frac{1}{c} j_r B; \quad (2.18)$$

$$\rho \left(\frac{\partial v}{\partial t} + u \frac{\partial v}{\partial x} + v \frac{\partial v}{\partial r} \right) + \frac{\partial \rho}{\partial r} = -\frac{1}{c} j_x B; \quad (2.19)$$

$$\rho \left(\frac{\partial c_v T}{\partial t} + u \frac{\partial c_v T}{\partial x} + v \frac{\partial c_v T}{\partial r} \right) + \rho \left(\frac{\partial u}{\partial x} + \frac{1}{r} \frac{\partial v r}{\partial r} \right) = \frac{1}{\sigma} j^2; \quad (2.20)$$

$$\begin{aligned} \frac{\partial B}{\partial t} + u \frac{\partial B}{\partial x} + v \frac{\partial B}{\partial r} = & -B \left(\frac{\partial u}{\partial x} + \frac{\partial v}{\partial r} \right) + \\ & + v_m \left(\frac{\partial^2 B}{\partial x^2} + \frac{1}{r} \frac{\partial}{\partial r} \left(r \frac{\partial B}{\partial r} \right) - \frac{\partial B}{\partial x} \frac{\partial I_n \sigma}{\partial x} - \frac{1}{r} \frac{\partial B_r}{\partial r} \frac{\partial I_n \sigma}{\partial r} \right); \end{aligned} \quad (2.21)$$

$$j_x = \frac{c}{4\pi r} \frac{\partial B_r}{\partial r}, \quad (2.22)$$

$$j_r = -\frac{c}{4\pi} \frac{\partial B}{\partial x}, \quad (2.23)$$

$$j_x = \sigma \left(E_x + \frac{vB}{c} \right), \quad (2.24)$$

$$j_r = \sigma \left(E_r - \frac{uB}{c} \right), \quad (2.25)$$

where c_v – the heat capacity of the reaction products at a constant volume; σ – the conductivity; c is the velocity of sound in vacuum; $v_m = c^2/4\pi\sigma$ – the magnetic viscosity.

It is assumed that the Hall effect, velocity of the lateral motion of ions and displacement current are insignificant and can be neglected, compared with the conduction current. Equations (2.17–2.25) did not allow for thermal conductivity and viscosity of gas in thin boundary layers near the electrode walls. Thickness of a boundary layer is small compared with width of an annular gap between the electrodes, and is ignored in calculations [191].

The system of equations (2.17–2.25) is completed with the equation of state of a perfect gas:

$$P = \rho RT, \quad (2.26)$$

and determination of dependencies for c_v , R and σ upon parameters of state of the combustion products, allowing for the degree of their dissociation and ionization.

Consider the detonation wave to be an infinite thin discontinuity surface, where vectors \vec{E} and \vec{B} are continuous, and where the gas parameters experience an abrupt change according to ordinary relationships at DW, which can be written down as follows:

$$\frac{\rho_o}{\rho} = \frac{\gamma}{\gamma+1} - \frac{1}{\gamma+1} \sqrt{1 - M_\sigma^2 / M_D^2}, \quad (2.27)$$

$$v_n = a_o M_D \left(1 - \frac{\rho_o}{\rho} \right), \quad (2.28)$$

$$P = \gamma P_o M_D^2 \left(1 - \frac{\rho_o}{\rho} \right). \quad (2.29)$$

In these formulae zero designates the gas parameters ahead of DW:

- v_n – the component of velocity of the detonation products normal to the DW front;
- $M_D = D/a_o$ – the Mach number of DW;
- $M_j = \min M_D$ – the Mach number of the stationary Chapman-Jouguet detonation wave, which is the fuel mixture characteristic and determines the amount of heat released in combustion of a unit mass of the initial mixture;
- γ – the adiabatic exponent of the reaction products, i.e. $\gamma = \gamma(M_D)$.

It is assumed that $\sigma=0$ ahead of DW. $M_D/M_j \gg 1$ was used to derive (2.27–2.29). Consider boundary conditions on side walls of the channel. Assume that the walls act as barriers for gas and are solid electrodes, at which tangent component \vec{E} is equal to zero, $E_r=0$, accordingly $j_r=0$ or $\partial B_r / \partial n = 0$. Condition $j_x=0$ or $\partial B_r / \partial r = 0$ is met for a non-conducting device end corresponding to section $x=0$.

To complete the statement of the problem, current $I(t)$ should be either assigned or calculated using characteristics of the external electric circuit.

After DW leaves the channel, the electric current will flow not only in a gap between the electrodes, $0 \leq x \leq L$, but also outside the nozzle exit section of the plasmatron reaction chamber, $x > L$, thus leading to an additional acceleration of the plasma jet outside the plasmatron in a distance between the surface treated and nozzle exit section.

As the initial conditions ($t=0$) for the problem stated, assume that

$$x_D(0) = 0; M_D(0) = M_j; k(0) = 0. \quad (2.30)$$

The above stated 2-dimensional non-stationary problem is very difficult to solve. The situation becomes even more difficult because of the necessity to calculate the equilibrium composition of products of the detonation combustion of fuel gas mixtures and the degree of scattering of electrons at ions and neutral particles.

To derive engineering solutions, which would allow for basic physical mechanisms of the phenomenon and could be applied to design technological plasma devices, make some simplifying assumption in the initial problem.

Ignore variability of C_v and R both at DW and in a flow behind it, considering a gas to be perfect with constant adiabatic exponent γ . This assumption is related to ignoring the energies of dissociation and ionization of molecules behind DW, compared with energy input from the electromagnetic field and chemical energy released at DW. Assume that behind DW the conductivity is of an electron character and determined by the following formula [204]:

$$\sigma = \frac{e^2 n_e}{m_e v_e}, \quad (2.31)$$

where e – the electron charge; m_e – the electron mass; n_e – the concentration of electrons in unit volume; v_e – the frequency of collisions of electrons with heavy particles (ions, atoms and molecules).

Formula (2.31) can be applied in a case where the concentration of ions, n_i , in gas is not too high compared with concentration n_e . $n_i/n_e \leq 10^4 - 10^5$. The situation at which $n_i/n_e \leq 10^4 - 10^5$ takes place where the neutral molecules and atoms contained in gas have a high degree of affinity for electrons, and the degree of ionization of gas is insufficiently high. As regions with the combustion products, where the degree of ionization is low as yet, are characterized by weak interaction with the electromagnetic field, formula (2.31) is useful for describing amplification of DW due to this field.

The following formula is valid for determination of v_e in an assumption of the full thermodynamic equilibrium:

$$v_e = \sqrt{\frac{8kT}{xm_e} \sum_{k=1}^N n_k \delta_k}, \quad (2.32)$$

where k – the Boltzmann's constant; δ_k – the cross-section of scattering of electrons at heavy particles (ions, atoms and molecules) of the k -th kind; $k=1, 2, \dots, N$; n_k – the concentration of particles of the k -th kind.

For example, when DW propagates in a fuel mixture, the flow of the combustion products behind DW will contain ions H^+ , H^- , O^+ , O^- , O_2^+ , O_2^- , ... and neutral particles O , H , O_2 , H_2 , OH , H_2O , ...

As shown by experiments and calculations, the cross-section of scattering of electrons at neutral particles is by 4–6 orders of magnitude smaller than that at ions [207]. In an assumption of a rather high degree of ionization, this allows ignoring the summand in (2.32) responsible for scattering of electrons at neutral particles. To determine the cross-section of scattering of electrons at ions, use expressions corresponding to elastic scattering at which the quantum state of a heavy particle does not change [207]:

$$\delta_k = \pi \left(\frac{eZ_k}{kT} \right)^2 \ln \Lambda, \quad (2.33)$$

where Z_k – the value of charge of the k -th ion; $\ln \Lambda$ – the so-called Coulomb logarithm, the value of which depends upon the temperature and degree of ionization, although this dependence is very weak. Normally, it is assumed in calculations that $\ln \Lambda = 10$.

According to (2.33), the value of δ_k is determined by the ion charge. Considering that all ions have single ionization, $|Z_k| = e$, and ignoring total concentration of negative ions compared with total concentration of positive ions, we will have that $n_e = n_i$. Hence, using (2.31–2.33) yields:

$$\delta = c \frac{(kT)^{3/2}}{e^2 \ln \Lambda \sqrt{8\pi m_e}}, \quad (2.34)$$

where c – the dimensionless constant, the emergence of which is related to the fact that (2.33) is accurate up to a constant factor. Its value should be estimated from comparison with experimental data or calculated theoretically allowing for the specific character of each kind of ion.

The gas-dynamic flow in the electric field under consideration is not unidimensional: the values of vectors of the electric field intensity and electromagnetic induction grow in a direction to the symmetry axis. Joule heat dissipation and velocity of the detonation products simultaneously grow. To further simplify the problem, use a hydraulic approach, which provides for averaging of parameters of the flow in each section of the channel. The hydraulic approach allows evaluation of the distribution of average values of hydrodynamic and electrodynamic values along the channel, ignoring their distribution in sections.

Entering geometric and energy parameters averaged over the width of the gap between the electrode (**Fig. 2.2**) allows their calculation from the following formula:

$$\langle X \rangle = \frac{1}{h} \int_0^h X dh, \quad (2.35)$$

where X – takes the values of B, E, j, w, \dots ; h – the width of the annular gap; B – the magnetic induction; E – the electric field; j – the value of the electric current; w – the velocity of the plasma flow.

Integration is performed with respect to normal to the electrode surfaces. Calculation parameters depend only upon the time and distance along the generating line to the point of initiation of the detonation wave, which is designated as l . The length of the reaction chamber channel is designated as L . In the assumption made, position of the DW front is characterized by function $l = l_D(t)$ and velocity of DW – by equality $D = dl_D/dt$.

To derive relations at DW, use equation (2.35) assuming that $M_D = D/a_0 = (dl_D/dt)/a_0$. The surface of the DW front will consist of sections normal to the electrodes.

Assume that vectors of current $\langle j \rangle$ and intensity $\langle E \rangle$ are normal and vector of velocity of the plasma jet $\langle w \rangle$ is parallel to the generating line of the electrodes. The ground is the equality of tangent component of vectors \vec{j} and \vec{E} , as well as the normal component of vector \vec{v} ,

respectively, to zero at the electrodes, as well as the narrowness of the annular gap between the electrodes ($h=6-8$ mm).

The flow of gas in the channel behind DW can be described by the system of differential equations allowing for the above assumptions:

$$\frac{\partial \rho}{\partial t} + \frac{1}{A} \cdot \frac{\partial}{\partial l} \cdot (\rho w A) = 0; \quad (2.36)$$

$$\rho \left(\frac{\partial w}{\partial t} + w \frac{\partial w}{\partial l} \right) + \frac{\partial \rho}{\partial l} = \frac{1}{c} j_n B; \quad (2.37)$$

$$\frac{\partial \rho}{\partial t} + w \frac{\partial \rho}{\partial l} + \gamma \rho \frac{\partial w}{\partial l} = \frac{\gamma - 1}{\sigma} j_n^2; \quad (2.38)$$

$$\frac{\partial B}{\partial t} + \frac{\partial w B}{\partial l} = v_m \left(\frac{\partial^2 B}{\partial l^2} + \frac{1}{L-l} \frac{\partial B}{\partial l} + \frac{\partial \ln \sigma}{\partial l} \left(\frac{B}{L-l} - \frac{\partial B}{\partial l} \right) \right); \quad (2.39)$$

$$j_n = -\frac{c}{4\pi} \left(\frac{\partial B}{\partial l} - \sin \alpha \frac{B}{L-l} \right); \quad (2.40)$$

$$j_n = \sigma \left(E_n - \frac{w B}{c} \right). \quad (2.41)$$

The system of equations (2.36–2.41) was formulated for the average values, where the angle brackets were omitted for simplicity.

In these equations w is the average value of the velocity of gas for DW in a direction of axis l :

- $A=A(l)$ – the total surface area of section of the annular gap normal to axis l ;
- β – the angle of half-opening of conical generating lines of the channel;
- $\beta=0$ – for a cylindrical channel.

Formulae (2.39–2.41) are derived at the above-mentioned limitations on vectors \vec{E} , \vec{j} and \vec{v} and, in an assumption that all values depend only upon l .

The last assumption is equivalent to application of the operation of averaging for equations (2.17–2.25) with an assumption that average of the product of values is equal to the product of averages, which is made approximately.

In the hydraulic approximation, use equation (2.28) to derive relations at DW, assuming in them that:

$$M_D = \frac{D}{\alpha_o} = \frac{(dl_D/dt)}{\alpha_o}. \quad (2.42)$$

The flow of gas in the channel behind DW can be described by the system of differential equations in partial derivatives, allowing for geometric parameters of the reaction chamber (length – L , section area of the annular gap – A , and angle of half-opening of generating lines of the electrodes – β).

To calculate parameters at DW as function of the distance it passed, l , use the Whitham's method [208].

The Mach number of the detonation wave, $MD=MD(l)$, is the solution of the differential equation allowing for a constant (acoustic characteristic $c+$), overtaking DW and gas-dynamic parameters at DW expressed in terms of MD. Combination of equations of the gas-dynamic sub-system yields relation in the $c+$ characteristic:

$$\begin{aligned} \frac{dp}{dl} + \rho a \frac{dw}{dl} &= \frac{j_h}{w+a} \left(\frac{\gamma-1}{\sigma} j_h + \frac{a}{c} B \right) - \frac{\gamma p w}{w+a} \frac{1}{A} \frac{dA}{dl}, \\ (w+a) \frac{d}{dl} &= \frac{\partial}{\partial t} + (w+a) \frac{\partial}{\partial l}, \end{aligned} \quad (2.43)$$

where γ – the adiabatic exponent of the combustion products; p and ρ are the pressure and density; w – the average value of the velocity of gas behind DW in a direction of axis of the combustion chamber; α – the increase in the velocity of gas behind DW due to the electromagnetic energy input; j_h – the electric current; σ – the conductivity of plasma; c – the dimensionless constant related to total concentration of positive ions; τ – the time; l – the current length of the channel.

Allowing for the relations at DW, insert the following values in the equations:

$$B=0 \text{ and } j_h = \sigma E_0,$$

where E_0 – the averaged vector of intensity of the electric field ahead of DW, equal to the difference in potentials at the electrodes divided by the width of the annular gap.

Insert new dimensionless values Z and ξ instead of MS and l according to the following formulae:

$$\xi = \frac{l}{L}. \quad (2.44)$$

$$Z = \sqrt{1 - \frac{M_j^2}{M_D^2}}.$$

According to the known value of $Z=Z(x)$, the velocity of DW, gas-dynamic parameters behind it: detonation Mach number D , pressure P density ρ , total velocity U , and temperature of plasma before and after introduction of the electromagnetic field, T and T_0 , respectively, can be determined from the following formulae:

$$D = \frac{a_0 M_j}{\sqrt{(1-Z^2)}}; \quad (2.45)$$

$$P = \frac{P_0 M_j^2 \gamma}{(\gamma+1)(1-Z)}; \quad (2.46)$$

$$\rho = \frac{\rho_o(\gamma + 1)}{(\gamma - Z)}; \quad (2.47)$$

$$w = \frac{M_j a_o}{\gamma + 1} \sqrt{\frac{1 + Z}{1 - Z}}; \quad (2.48)$$

$$\alpha = \frac{M_j \alpha_o}{\gamma + 1} \sqrt{\frac{\gamma(\gamma - Z)}{(1 - Z)}}. \quad (2.49)$$

Function $Z(\xi)$ is determined by solving an ordinary differential equation, which can be integrated by elementary functions:

$$\begin{aligned} & \left(1 + \sqrt{\frac{\gamma}{(\gamma - z)(1 + z)}} \right) \left(1 + z + \sqrt{\gamma(\gamma - z)(1 + z)} \right) \frac{dz}{d\xi} = \\ & = k(1 - z)^2 \sqrt{1 - z^2} - \gamma(1 - z^2) \frac{1}{A} \frac{dA}{d\xi}. \end{aligned} \quad (2.50)$$

By representing solution $Z(\xi)$ in the implicit form, make numeric integration of the ordinary differential equation at the assigned initial conditions of $Z(\xi)=0$. Ignore variability of $\ln \Delta$ in the calculations, assuming that $\ln \Delta = 10$, $k = k_o(\gamma - Z)^{3/2}/(1 - Z)^{3/2}$.

Numeric integration of ordinary differential equation (2.50) was performed at the assigned initial conditions of $Z(0)=0$. The tentative calculation was made at the following values of main parameters of the problem (for simplification, all dimensional values are given in the absolute Gaussian system of units (CGS):

- $\gamma - 1.2$ is the adiabatic exponent of the combustion products;
- $M_j - 5.0$ is the Mach number of the detonation wave propagating through a fuel mixture under the Chapman-Jouguet conditions;
- $P_o - 10^6$ dyne/cm² is the initial pressure of the fuel gas mixture;
- $\rho_o - 10^3$ g/cm³ is the initial density of the combustion products;
- $m - 18$ g/mole is the molar density of the combustion products;
- $E_o - \text{statV/cm}$ is the intensity of the electric field in the annular gap between the electrodes of the plasma detonation device.

Geometry of the gap is shown in **Fig. 2.2**.

2.2.2 ANALYSIS OF THE SOLUTION RESULTS

At $E_o=0$, acceleration of the detonation wave, increase in temperature and velocity of gas behind it occur only due to decrease in the section surface area of the channel. The effect for this geometry of the channel is very insignificant.

With increase in E_o , the second factor is involved into acceleration of DW: Joule heat input. In this case the acceleration of the wave is accompanied by growth of temperature, which in turn leads to increase in conductivity.

Assume that conductivity behind DW becomes of an electron character. This assumption is acceptable in the case where the concentration of ions in gas is commensurable with the concentration of electrons. Again, the acceleration of the wave is accompanied by growth of temperature, which leads to increase in the velocity and density of the plasma flow.

In a case of $dA/dx=0$, parameter k is the parameter of the scale similarity. $A=A(l)$ is the total section surface area of the annular gap normal to the axis of the plasma device.

Then

$$k = \frac{\delta E_o^2 (\gamma - 1)(\gamma + 1)^2 L}{\gamma a_o \rho_o M_j^3}, \quad (2.51)$$

$$\delta = c \frac{(KT)^{3/2}}{e^2 \ln \Delta \sqrt{8\pi m_e}}, \quad (2.52)$$

where K – the Boltzmann's constant; T – the temperature; m_e and e – the mass and charge of an electron; $\ln \Delta$ – the Coulomb logarithm the value of which depends upon the temperature and degree of ionization. In numeric integration, variability of $\ln D$ was ignored, and it was assumed that $\ln \Delta = 10$. Also, it was assumed that the section of the annular gap does not vary or that $dA/dx=0$.

Correct quantitative allowance for this factor requires knowledge of empirical constant C in the law of temperature dependence of conductivity (2.41). It was assumed in the calculations that $C=0.75$. Conductivity along the length of the channel varied by an order of magnitude from $\sigma=0.2252 \cdot 10^{12} \text{ s}^{-1}$ in the initial section to $\sigma=3.957 \cdot 10^{12} \text{ s}^{-1}$ in the exit section of the plasma device.

Analysis of formulae shows that temperature, velocity and density of the pulsed plasma jet can be varied within wide ranges, depending upon the length of the plasmatron, cone angle, size of the gap between the electrodes and intensity of the electric field in the reaction chamber of the plasma-detonation device. **Fig 2.3** shows temperature and Mach number of gas directly behind the detonation wave depending upon the distance it passed in the combustion chamber for different values of E_o .

The most efficient parameter affecting energy characteristics of the pulsed plasma flow was selected to simplify calculations and design. This is the length of the plasmatron, L . **Fig. 2.4, 2.5** show plots for temperature and velocity of plasma at the exit section of the plasma device combustion chamber depending upon the intensity of the electric field in the gap between the electrodes.

The following technological characteristics of the pulsed plasma can be achieved by varying length of the reaction chamber: plasma jet power density in a range from 10^3 to 10^7 W/cm^2 , plasma temperature from $2 \cdot 10^3$ to $3 \cdot 10^4 \text{ K}$, velocity from 600 to 8000 m/s.

The maximal values correspond to the length of the reaction chamber equal to 500 mm. Dependencies of variations in the velocity of the plasma jet vary but very slightly in a range of lengths of the combustion chamber from 300 to 500 mm. This was allowed for in optimization of sizes of the plasmatron. Software for computer modelling of plasma-detonation devices was developed as a result of the conducted theoretic studies. These devices are intended for generation of high-concentration pulsed plasma jets.

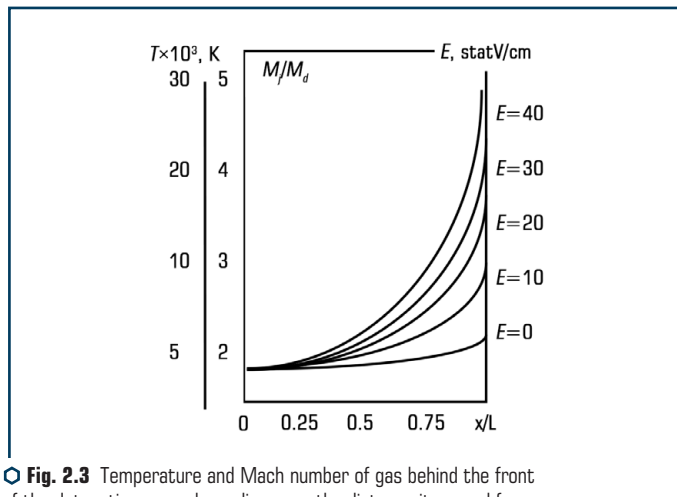


Fig. 2.3 Temperature and Mach number of gas behind the front of the detonation wave depending upon the distance it passed for different values of electric field intensity E

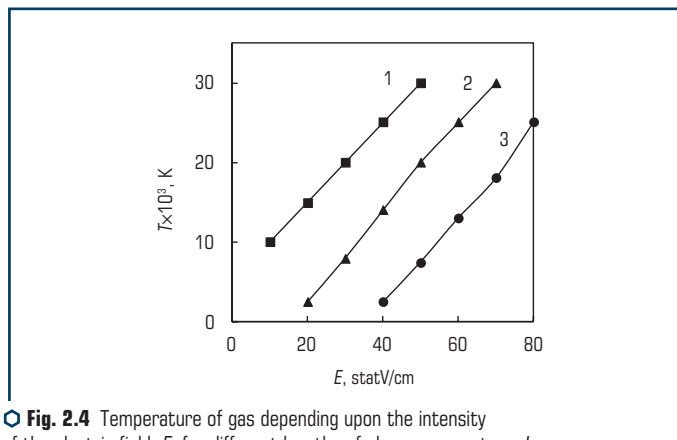


Fig. 2.4 Temperature of gas depending upon the intensity of the electric field, E , for different lengths of plasma generators, L : 1 – 100 mm; 2 – 200 mm; 3 – 300 mm

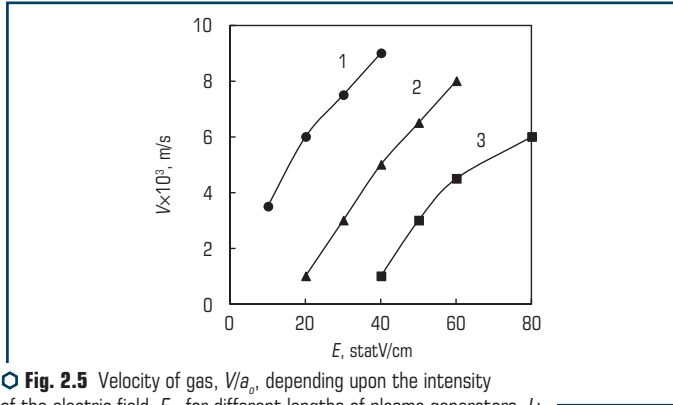


Fig. 2.5 Velocity of gas, V/a_0 , depending upon the intensity of the electric field, E_0 , for different lengths of plasma generators, L : 1 – 100 mm; 2 – 200 mm; 3 – 300 mm

The result of modelling is optimization of geometric parameters of the plasma generator reaction chamber. Temperature, velocity and density of the pulsed plasma jet can be increased tens of times, depending upon the length, cone angle and size of the gap of the reaction chamber.

Here it is possible to see almost linear, steeply growing dependence of energy characteristics upon the electric field intensity (Fig. 2.4, 2.5). The cone angle of the chamber has a slight effect on temperature and velocity of plasma (Fig. 2.6).

Pressure in the plasma flow has a linear dependence upon the cone angle of the chamber and increases with increase in its length. The work performed allows optimization of geometric sizes of the plasma-detonation devices intended for generation of pulsed plasma jet depending upon the designed technology requirements.

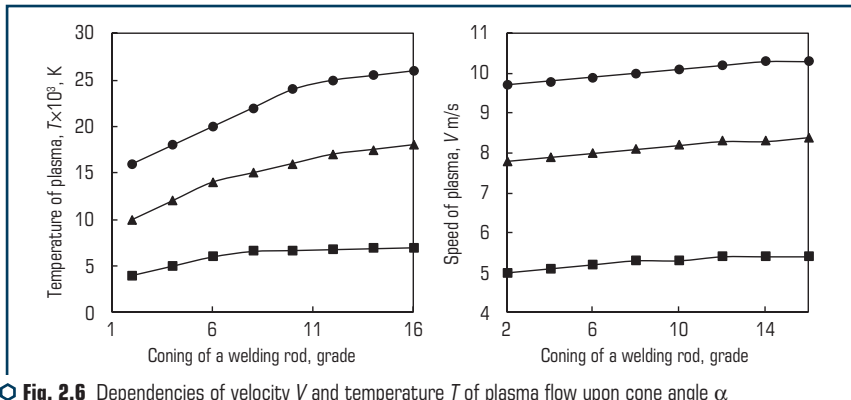


Fig. 2.6 Dependencies of velocity V and temperature T of plasma flow upon cone angle α of gap between electrodes in plasma generator

ABSTRACT

Some design features of plasma generators and the results of their study are shown. Experimental work on the study of pulsed plasma jets was carried out in laboratory and industrial installations. Experimental work and calculations have shown that generators with a conical reaction chamber are the most efficient.

KEYWORDS

Magnetogasdynamic regime, detonation combustion of combustible gas mixtures in an electrostatic field, pressure, velocity of plasma jets, plasma temperature.

3.1 PECULIARITIES OF DESIGN OF PLASMA-DETONATION GENERATORS

Solutions of equations modelling magnetic-gas-dynamic conditions of compression of detonation combustion of a fuel gas mixture in electrostatic field were reduced to the engineering form. Geometry and size of plasma generator reaction chambers were optimized on the basis of these solutions, which allowed a series of their typical designs to be developed.

Chapter 3 describes some peculiarities of design of plasma generators and presents results of investigation of the pulsed plasma jets. Experiments to study the pulsed plasma jets were conducted using laboratory and industrial units. The laboratory unit (**Fig. 3.1**) comprises pulsed-plasma generator 1, mating channel 2 of the detonation gun and spark plug 3. A piece to be hardened is fixed in the holder of manipulator 4, which is installed inside a cabinet with noise-proof walls 5. Gas to the detonation gun is fed via pipes 6 from collecting tanks 7 and 8 housed in electrolytic cell 9. Electrodes 10 connected to d-c power supply 11 are located inside the tanks. The electromagnetic field intensifying combustion is supplied from pulse capacitors 12 charged from converter 13.

The plasma generator (**Fig. 3.2**) comprises channel (reaction chamber) 1, jackets 2 and 3 for water cooling, coaxial cylindrical electrode 4, assembly 5 to feed a coolant, copper busbars 6 to supply the electric current, insulator 7 and small-size detonation gun 8 with a spark plug, and gas mixing chamber 9.

The detonation gun channel is tangentially connected to the plasma generator reaction chamber. The electrode is fixed along the axis of the reaction chamber using an insulator. The tip of the chamber has a special extension piece to focus the plasma jet. The fuel gas mixture is fed to the detonation gun channel and reaction chamber in the form of water electrolysis products or in the

form of a fuel gas+oxygen mixture. The fuel mixture is ignited with the spark plug (of the type used in cars) with a frequency of 2–6 Hz.

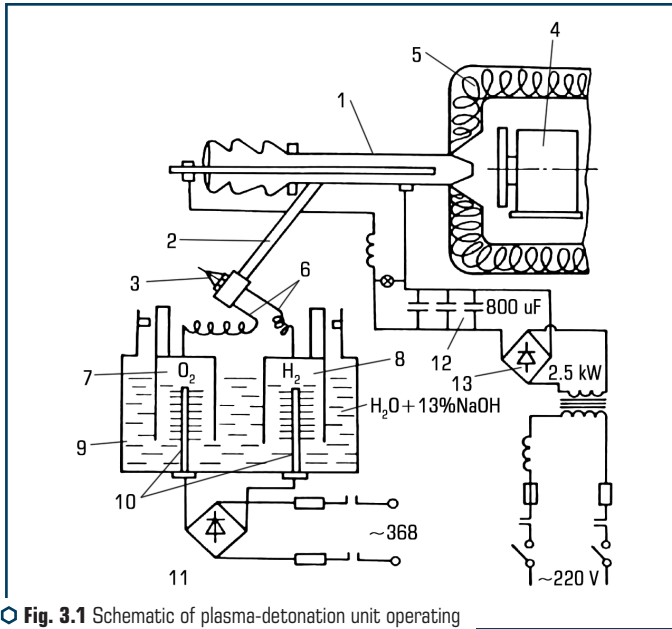


Fig. 3.1 Schematic of plasma-detonation unit operating with water electrolysis products

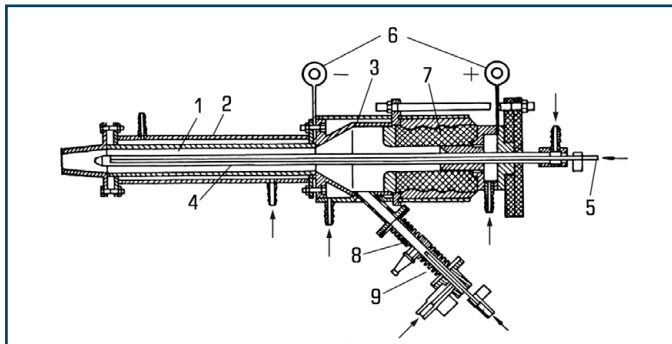


Fig. 3.2 Schematic of design of cylindrical pulsed plasma generator

The cylindrical generator operates on the stoichiometric mixture of hydrogen and oxygen with an addition of up to 50 % of air. Also, it can operate on a mixture of propane-butane

and oxygen. The electric current converter in this device comprises pulse capacitors with a total capacitance of 800 μF .

Geometry of the generator was optimized, and the industrial pulsed plasma generator with a conical reaction combustion chamber was manufactured (**Fig. 3.3**).

In this generator, walls of the reaction chamber, i.e. cathode, and central electrode, i.e. anode, are connected into the electric circuit.

Combustion products from the detonation gun are introduced into the gap between the electrodes to switch the electric current. Plasma is formed as a result of extra heating of the combustion products in chamber gap 1, the chamber is confined with wall (cathode) 2 and water-cooled jacket 3. The conical surface of the chamber (cathode) has open outlet 4. Conical gaps 5 and 6, as well as insulators 7 are made in the closed part of the chamber.

Conical electrode (anode) 8 is mounted on these insulators, and rod 9 of alloying materials is placed along the electrode axis. Busbars 11 used to supply the electric potential are connected to external surface 10 of the chamber and central electrode. The central electrode is cooled with air through nipple 12. Small-size detonation gun 13 is connected through nozzle 14 to mixing chamber 15 housing spark plug 16. Components of the fuel mixture are fed to the mixing chamber via nipples 17.

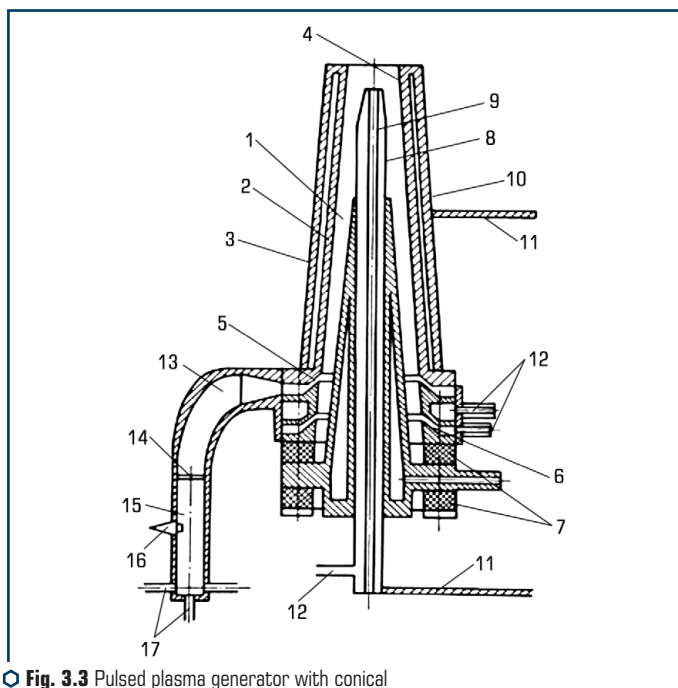


Fig. 3.3 Pulsed plasma generator with conical reaction chamber

The plasma generator reaction chamber has the form of a conical cavity formed by the electrodes, so that the tip of anode 9 extends from the plane of cathode edge 4 to a value of its exit diameter.

The sequence of operation of the generator is as follows. The reaction chamber is filled with the fuel gas mixture. The detonation combustion mode is initiated in the mixture. As a result, a layer of the combustion products having high electrical conductivity is formed in the reaction chamber. The electric current in the dissipation mode is passed through this layer between the electrodes. As a result, the stationary mode of the detonation combustion changes into the compressed mode, and then into the magnetic-gas-dynamic one. The high-energy plasma jet formed between the electrodes is directed to the surface of a piece being hardened, which is connected to the circuit as cathode.

The plasma generator operates on the fuel mixture of propane-butane and air (ratio 5:1:8). Capacitance of the capacitors in the electric converter is 400–1200 μF , voltage is 3.5 kV, and inductance of the current-conducting wires is 50 μH . This generator is characterized by the presence of consumable electrode 9, which enables alloying elements to be added to plasma.

In addition, feeding of a reaction gas to the gap between the electrodes, as well as oxidation protection and cooling of the surface being modified, are provided owing to the possibility of scavenging the reaction chamber with gases. In this case the plasma jet is focused through a gas-dynamic compression at cone 5 and due to ponderomotive forces induced by the electric current flowing between the consumable electrode tip and internal surface of the cone.

Pneumatic control circuit for the plasma-detonation unit is shown in **Fig. 3.4**.

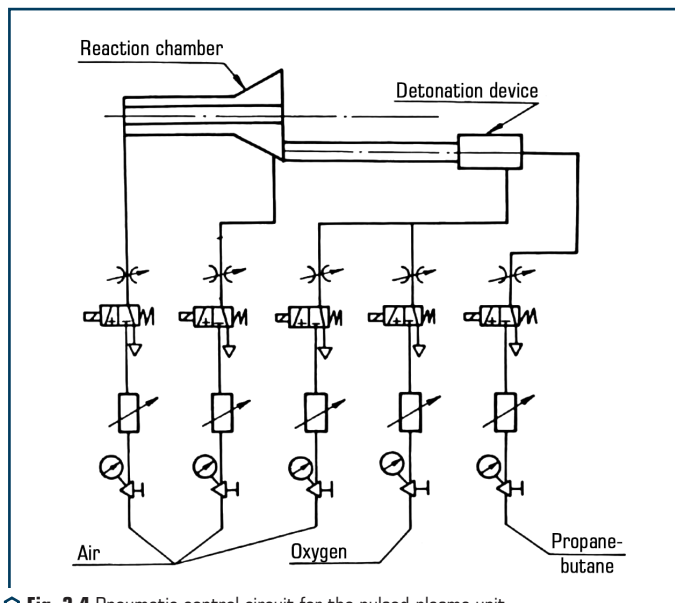


Fig. 3.4 Pneumatic control circuit for the pulsed-plasma unit

The circuit comprises controllers and indicators used to control the flow rates of oxygen, propane-butane and air.

3.2 PROCEDURE FOR INVESTIGATION OF PULSED PLASMA

Experiments to study evolution of space and time structures of plasma jets were conducted using a special rig. This rig is equipped with systems for high-speed photography of the flows of plasma and registration of spectral characteristics of its radiation.

Frame-by-frame photography allows visual examination of the process of formation of the plasma jet and its interaction with a solid obstacle. Continuous recording on a moving film makes it possible to estimate velocity of the jet at different stages of the pulsed discharge. Variants of filming of different sections of the jet regions enable tracing of the dynamics of the jet glow in a selected section.

Investigations were performed using camera SKS-1M, which permitted frame-by-frame registration of images of an object with a frequency of 4000 frames per second and continuous scanning of images with time resolution of up to 10^{-5} s.

Spectroscopy of the plasma jets was performed using a diffraction attachment to the high-speed photographic registration device VFU-1. The diffraction grating included into the attachment had 600 slits per millimeter of the surface. Reduced images of the plasma jet were projected to a slit of the spectral attachment.

The diffraction grating slit was up to 20 mm wide, which made it possible to achieve spectral resolution of 0.2 nm at a dispersion of 810 nm/mm. The spectral range of registration was from 380 to 700 nm.

The spectra were registered at two orientations of the spectrograph slit relative to the plasma jet axis: normal to the axis (transverse spectra) and parallel to the axis (longitudinal spectra). Transverse spectra were registered at different distances from the exit section of the generator nozzle, and longitudinal spectra were registered only at the central (axial) part of the jet. Variations in the radiation spectra of a free jet and jet falling on the metal obstacle (target) placed at a distance of 20–30 mm from the exit section of the plasma generator nozzle were examined. The registered spectra were of an integrated character, i.e. registration of each spectrum was performed within the time of one or several plasma pulses.

3.3 FORMATION OF PLASMA JET AND ITS INTERACTION WITH OBSTACLE

Analysis of the investigation results allows the following description of the process of formation of the plasma jet (**Fig. 3.5**).

Upon initiation of detonation in a fuel gas mixture, at first, we see its glow. The heated combustion products arrive to the gap between the electrodes (discharge gap) to form a luminous

plume consisting mostly of the electrode erosion products. After 0.25 ms, the plume reaches its maximal length. This stage lasts approximately 0.3–0.5 ms, after which the intensity of glow of the plasma jet dramatically falls.

The reduction of glow is caused by decrease in the jet temperature. The presence of particles (electrode erosion products) is detected in the jet. In some cases the registered duration of this phase is 7 μs (**Fig. 3.5, a**).

When the plasma jet interacts with an obstacle, its location goes on glowing. After the active phase of a pulse is completed, continuation of this glow is caused both by heating of the obstacle and its illumination with the combustion products in the plasma generator chamber. The continuing process of after-burning is evidenced by irregular fluctuations of brightness of a luminous spot on the obstacle surface (**Fig. 3.5, b**).

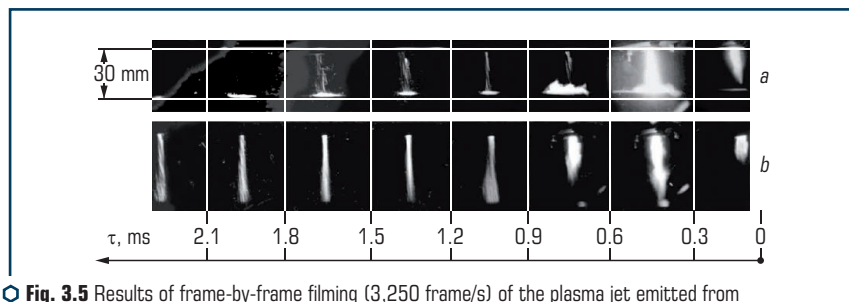
Modification of plasma generator with a conical chamber is characterized by a high energy input to the plasma pulse. This shows up in behavior of the jet during the discharge. In this case the jet has a more stable shape (**Fig. 3.6**).

The initial phase of operation of the generator begins with formation of a high-velocity jet preceding the electric discharge. Beginning of the discharge is characterized by emergence of an intensive glow of the jet. Its shape is stable. This is attributable to a higher velocity of the combustion products (**Fig. 3.6, a**). Changes in working conditions of the generator, i.e. free jet, presence of an insulated obstacle (**Fig. 3.6, b**) or grounded obstacle (**Fig. 3.6, c**), have a strong effect on shape and luminescence of the plasma jet.

It should be noted that the frame-by-frame filming results in a time integrated exposure of distribution of the intensity of radiation of the jet. The exposure of one frame was 0.25 μs .

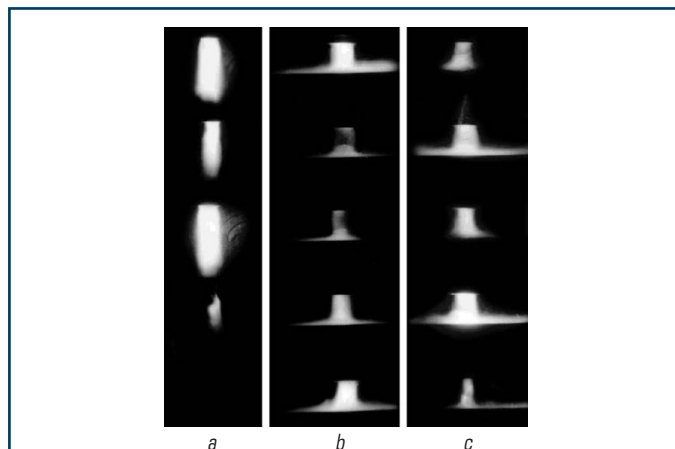
Good reproducibility of shape of the jet in this case is indicative of the fact that image of each frame is a result of sufficient averaging of faster processes. An indirect proof of this is the transverse structure of the jet seen in some frames, as well as the periodic changes in brightness of some frames relating to one pulse.

At the same time, the transverse size of the plume for the major part of the discharge is determined by the diameter of the plasma generator outlet nozzle.

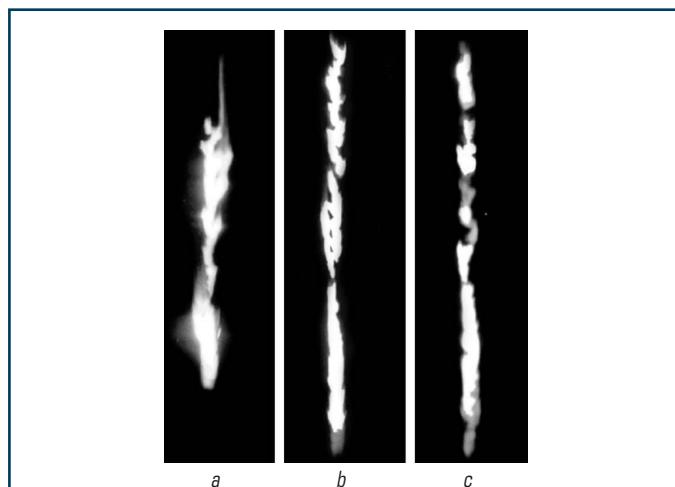


○ **Fig. 3.5** Results of frame-by-frame filming (3,250 frame/s) of the plasma jet emitted from generator with cylindrical chamber: *a* – with obstacle; *b* – without obstacle (free jet)

The space-time structure of the plasma jet was examined also by using a photo registration device. The results are shown in **Fig. 3.7**.



⬢ **Fig. 3.6** Results of frame-by-frame filming (3,700 frame/s) of the plasma jet emitted from generator with a conical combustion chamber: *a* – free plasma jet; *b* – insulated obstacle extending to a distance of 30 mm; *c* – grounded obstacle extending to a distance of 30 mm



⬢ **Fig. 3.7** Time scans of glow of the plasma jet in different cross sections: *a* – near the exit section of the generator combustion chamber; *b* – at a distance of 5 mm from the exit section; *c* – at a distance of 10 mm from the exit section

Time resolution in this case was $15\text{ }\mu\text{m}$. Time scans of the glow at a distance from the exit section of the plasma generator nozzle show a complex character of luminescence of the plasma jet. This is caused by changes in the discharge current, turbulence of the outgoing flow and processes occurring on the electrode surfaces.

The glow of the jet can be subdivided into two large-scale phases: initial phase characterized by a comparatively high brightness and constituting about 40 % ($0.4\text{ }\mu\text{s}$) of the time of existence of the jet (**Fig. 3.6, b**), and subsequent phase characterized by a higher space-time instability (**Fig. 3.7, c**). In addition, up to five medium-scale fluctuations of the glow intensity (mean period – $0.2\text{ }\mu\text{s}$) occur during the time of existence of the plume. The initial part of the discharge features a comparatively good stability. This can be explained by the fact that the initial phase occurs in a flow of the combustion products at cold electrodes. The subsequent phase of the discharge is characterized by a comparative complexity. Here we can see two types of the jets forming the plume. Erosion jets caused by the processes taking place on a heated surface of electrodes are dominant in this phase. At any time, moment these jets can take a random position in space, although they are located within the limits of the plasma plume. Several jets of this type may exist simultaneously.

The equipment used in the experiment allowed detection of the components at a frequency of up to 50 kHz with a maximum of about 20 kHz. Along with the chaotically formed jets, there are also jets that are characterized by high space stability. These jets are located mostly in the periphery of the plasma plume. Their high space stability allows a conclusion that they are not related to the processes occurring at the electrodes.

It will be shown below using the spectroscopy methods that the peripheral part of the plasma jet is formed by hot gas flows with a relatively low content of vapors and electrode material erosion products.

Study of the space-time structure of the plasma jet was conducted using the SKS-1M camera in the high-speed photo registration mode. It can be seen from the time scans that the plume of the pulsed discharge is a complex formation varying in space and time (**Fig. 3.8**).

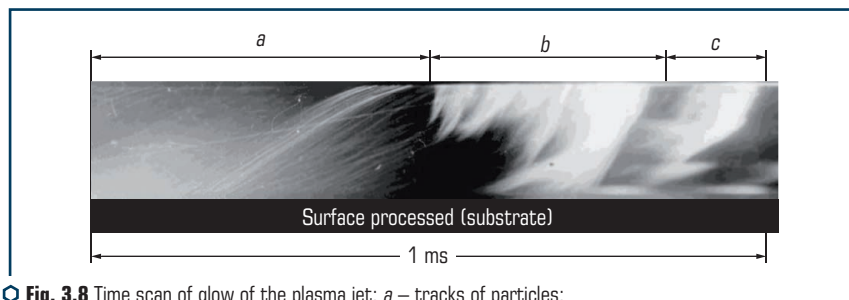


Fig. 3.8 Time scan of glow of the plasma jet: *a* – tracks of particles; *b* – traces of plasma jets; *c* – primary plasma jet

Length of the plume corresponds to the value of the electric current for this type of the discharges. The time of existence of the plume correlates with the calculated duration of the

electric discharge. However, behavior of the plume has certain peculiarities. In particular, there are individual jets characterized by a high velocity, wide range of variations in the intensity of glow of the plume and presence of heated luminous particles (**Fig. 3.8, a**), which are formed in the second half of the discharge and carried away with the gas jet after completion of the electric discharge. These particles are the result of erosion of electrodes. They change the qualitative composition of plasma and character of the impact by the plasma jet on an obstacle (workpiece).

Interaction of the plasma jet with the obstacle is of a typical character (**Fig. 3.9**).

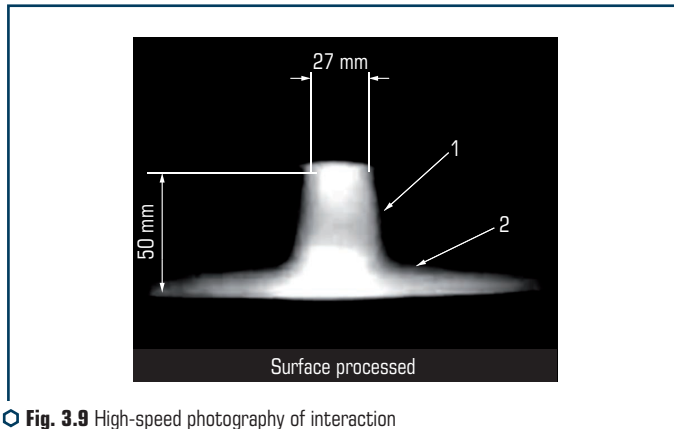


Fig. 3.9 High-speed photography of interaction of the pulsed plasma jet with an obstacle

After beginning of the discharge, the erosion jet is ejected from the generator nozzle and moves in a direction to the obstacle. Upon reaching the obstacle, the jet starts spreading over its surface at a velocity of about 100 m/s. After the end of the electric discharge, the obstacle is still affected by the gas jet and flow of the erosion products. As distance between the nozzle exit section and obstacle decreases, the time of impact by the jet on the surface increases, thus leading to increase in energy density and efficiency of the energy transfer process.

In the generator with a conical combustion chamber, the plasma jet has a higher space stability and power level per unit surface. In this case the velocity of spread of plasma over the obstacle surface is 300 m/s. The efficiency of interaction of the plasma jet with a solid obstacle (workpiece surface) strongly depends upon its grounding. For the case of a grounded obstacle the plasma jet glow is more intensive, and the plasma layer spreading over the obstacle surface has a larger volume and higher temperature (**Fig. 3.6, c**).

The interaction efficiency depends also upon the value of the electric potential between the obstacle (workpiece) surface and anode electrode. The barrier layer causing a dramatic decrease in the efficiency of impact of the plasma jet is formed ahead of the electrically neutral obstacle (**Fig. 3.10**).

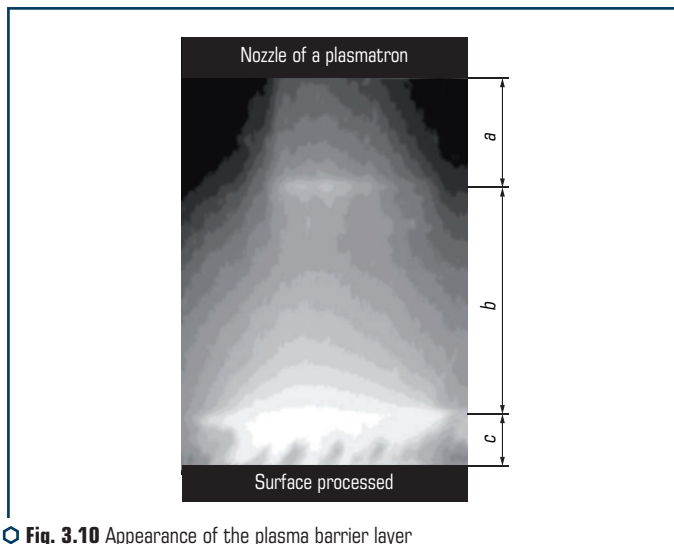


Fig. 3.10 Appearance of the plasma barrier layer ahead of a solid obstacle

Connection of a workpiece to the electric circuit as cathode introduces the following changes into the process: contraction of the plasma jet (pinch-effect) due to the electric current flowing between the anode and cathode, and enhancement of the efficiency of impact by the electron flow (electric current).

Experimental measurements of temperature of the plasma flow show that it rapidly lowers with increase in distance from the plasma generator to the workpiece surface. The composition of plasma also changes. With distance from the exit section of the chamber, the heavy atoms of metals catch up with a lighter component (atoms and molecules of nitrogen, oxygen, hydrogen and carbon). Structure of the jet becomes more uniform, its mean temperature lowering by 30–40 %.

Utilization of an extra energy source forming a control electric current on the obstacle surface leads to a substantial increase in the efficiency of impact on the metal surface by the plasma jet.

3.4 EXPERIMENTAL STUDIES OF PULSED PLASMA

3.4.1 ENERGY CHARACTERISTICS OF PLASMA GENERATORS

As shown by experimental studies of short high-power pulsed discharges [22], all types of hydrodynamic instabilities can be found in them. Energy of the discharge is consumed for heating of electrodes, melting, evaporation and transmitting a directed motion to the vapors, as well as

for ionization and radiation. Reportedly [22], velocity of movement of the discharge plume depends upon the material and polarity of the electrodes. For example, for a copper electrode the velocity is 6 km/s, and for an aluminium electrode it is 8.5 km/s. This is attributable to differences in thermal-physical characteristics of metals and differences in the rate of their ablation. To stabilize the discharge, it is suggested that its length and time of energy input should be increased.

Characteristics of the plasma jet in the plasma-detonation generator depend primarily upon the length of the gap between the electrodes and electric field intensity (**Fig. 2.4**). Plasma has a temperature of 20,000 K and velocity of 6 km/s at a reaction chamber length $L=200$ mm and electric field intensity of 400–500 kV/m (**Fig. 2.6**). The temperature and velocity of plasma were evaluated experimentally from the high-speed filming results and spectrograms. The temperature of the plasma jet, averaged over its existence time, was determined from the relative intensity of iron lines. Analysis of the plasma radiation spectra integrated with respect to time shows that the plasma temperature is 15,000–20,000 K.

Examination of the high-speed photo scans of the plasma jet shows that they contain shock waves and abrupt changes of the periodic structure (**Fig. 3.11**).

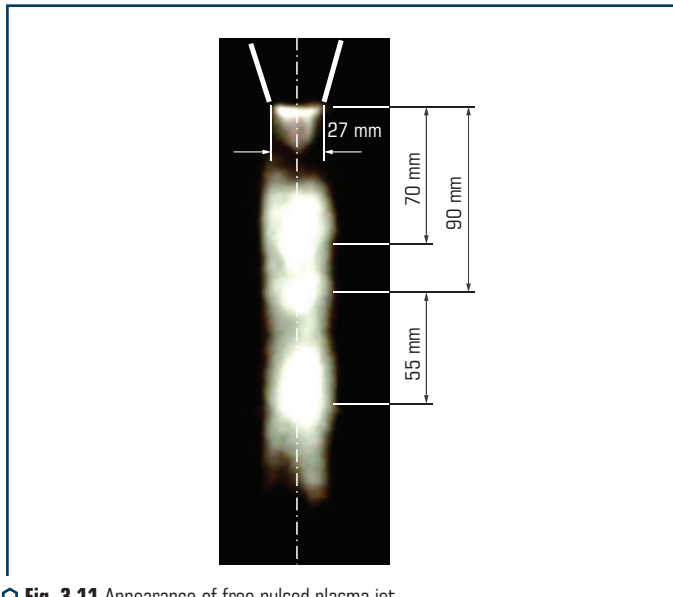


Fig. 3.11 Appearance of free pulsed plasma jet

As can be seen in the photo scans, the first shock wave in the plasma jet consists practically of two shock waves, which can be explained by a non-uniformity of the plasma jet consisting of different-velocity jets. Velocity of the jet, V , is calculated from the following formula (3.1) [209]:

$$L_w = 1.3d_g \sqrt{M^2 - 1}$$

or

$$V = \sqrt{\left(\frac{L_w}{1.3d_g}\right)^2 + 1} \cdot a_0, \quad (3.1)$$

where $d_g=0.027$ m – the diameter of the plasmatron nozzle; $M=V/a_0$ – the Mach number; $Lw_1=70$ mm and $Lw_2=90$ mm – the periodic structure wavelengths (**Fig. 3.11**); a_0 – the velocity of sound determined from the following formula:

$$a_0 = \sqrt{\gamma RT}, \quad (3.2)$$

where in our case, $\gamma=1.3$ – the adiabatic constant; $R=300$ J/(kg·K) – the gas constant; $T=15,000$ K – the jet temperature.

Substitution of (3.2) to (3.1) yields the velocities of the plasma jet – $V_1=5.4$ km/s and $V_2=6.7$ km/s, which is in agreement with the theoretically derived data. Structure of the plasma jet shown in **Fig. 3.11** is characteristic of a supersonic jet in the under-expansion mode, which corresponds to the explosive character of operation of the plasmatron, where the pressure inside the chamber may substantially exceed the ambient one. The picture of interaction of plasma jet 1 with the obstacle is characterized by the presence of a region of shock-compressed layer (SCL) 2, which is very typical (**Fig. 3.9**).

After break-down of SCL, the electric current flows through plasma jet 1 from the central electrode in the plasmatron to the workpiece surface. Density of the electric current in the plasma jet is $J=(1-7) \cdot 10^3$ A/cm² and temperature is 20,000–30,000 K. The heat flow to a workpiece depends upon the current density and varies within a range of $(0.1-5) \cdot 10^6$ W/cm². The heat flows were estimated on the basis of theoretical analysis of a non-stationary heat conduction equation from geometric characteristics of hardened layers of the martensitic steel grades.

Energy characteristics of a plasma pulse are controlled through varying capacitance C of the capacitors (200–1200 μ F), voltage U_{charge} at the capacitor bank plates (2.5–3.5 kV), inductance L in the discharge circuit (20–60 μ H), distance H to the workpiece surface (30–120 mm) and change in size of the spot of interaction with the surface (8–30 mm). Measurements of time variations of the electric current in the gap between the electrodes, as well as between the central electrode and surface of a solid, were made using the Rogowski belts [210]. The Rogowski belt was connected to the measurement circuit as current transformer. Two identical coils with the following parameters: $n=146$ turns, $h=7 \cdot 10^{-3}$ m, $r_1=22 \cdot 10^{-3}$ m, $r_2=50 \cdot 10^{-3}$ m and $R_0=0.9$ Ohm, were used to make the measurements.

The design inductance was $2.45 \cdot 10^{-5}$ H. Signals from each separate coil of the measurement system arrive to input of the double-beam oscillograph S8-17. Then, after registration and conversion, they are fixed in the form of a curve describing the time dependence of the current (shape and duration of a current pulse) (**Fig. 3.12**).

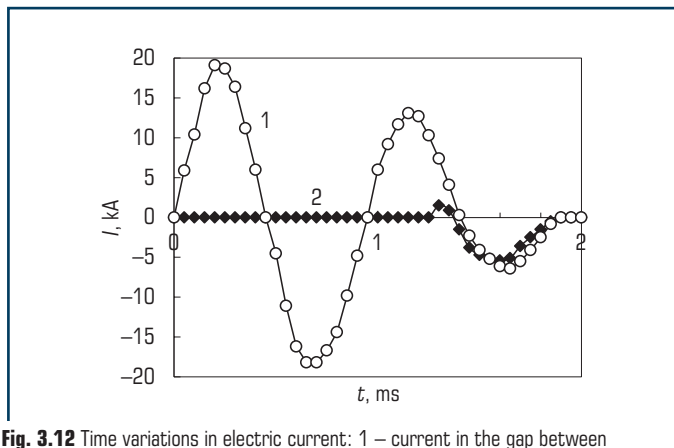


Fig. 3.12 Time variations in electric current: 1 – current in the gap between electrodes; 2 – current between the central electrode and workpiece

The curves plotted with the oscillograph were integrated using the Mathcad-7 mathematical editor program. Inductance of the discharge circuit did not change and equaled approximately $20 \mu\text{H}$. In operation within a frequency range of up to 10 Hz, the capacitor banks have enough time to be fully charged in an interval between two pulses. Therefore, in operation at a frequency of 2 Hz, the factor of the effect of frequency on a current pulse was ignored.

As shown by preliminary experiments, variations in a flow rate of plasma gases C_3H_8 , O_2 and air in a range of $0.24\text{--}0.48 \text{ m}^3/\text{h}$ and $1\text{--}2 \text{ m}^3/\text{h}$, respectively, exert an insignificant effect on the current. The following values were varied during the measurements: capacitance of the capacitor bank – $C=600\text{--}1200 \mu\text{F}$, distance from the nozzle exit section to a workpiece – $H=40\text{--}100 \text{ mm}$, and distance from the central electrode tip to nozzle exit section – $h=0\text{--}40 \text{ mm}$.

Analysis of time distribution of currents shows (**Fig. 3.12**) that break-down of the compressed layer occurs only after 1.2 ms. Capacitors are re-charged during this time, and a consumable electrode acts as cathode for 0.1 ms, and then again as anode for 0.4–0.5 ms. Accordingly, the surface of a solid is also re-charged.

The amplitude values of the current decrease with increase in distance to the surface, H . But even at a distance of $70\text{--}100 \text{ mm}$ (characteristic of the coating spraying technology) the values of the current are $1000\text{--}3000 \text{ A}$.

The maximal values of the electric current along the plasma jet between the central electrode and surface of a solid at different distances from the central electrode tip to nozzle exit section, h , are shown in **Fig. 3.13**. Current density on the surface of a solid decreases with increase in h and H . This is attributable to the screening effect of the plasmatron cathode and decrease in conductivity of the plasma jet.

As proved by the experiments, the surface of a solid experiences at the first moment an elastic-deformation interaction with a shock wave and a pulsed plasma jet, and then it is subjected to the

impact by the electric current. The amplitude value of the current is up to 7 kA. This results in formation of the pulsed magnetic field with an intensity of up to 2000 Oe. Plasma and electrode erosion products flow onto the surface almost simultaneously. This forms the shock-compressed layer.

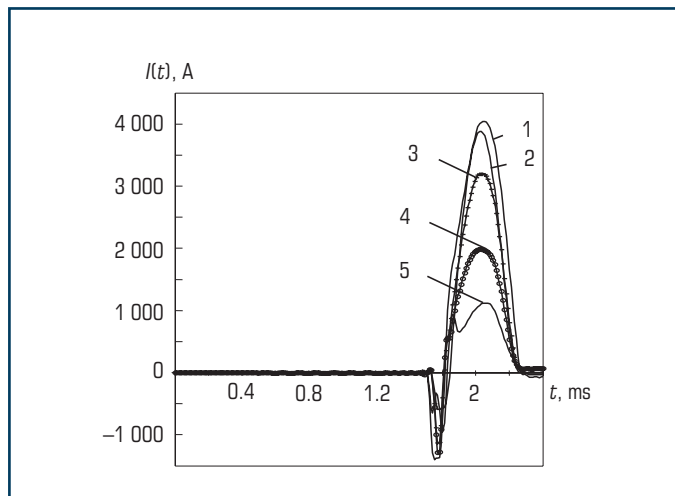


Fig. 3.13 Time diagram of electric current I (A) flowing between the consumable electrode tip and workpiece surface: 1 – $h=20$ mm, $H=40$ mm; 2 – $h=0$ mm, $H=70$ mm; 3 – $h=20$ mm, $H=70$ mm; 4 – $h=40$ mm, $H=70$ mm; 5 – $h=20$ mm, $H=100$ mm

Analysis of time distribution of the currents shows that the shock-compressed layer (SCL) formed by the plasma flowing onto the workpiece surface has a much higher electrical resistance than the discharge gap between coaxial electrodes. Break-down of SCL occurs only after 1.2 ms. Capacitors are re-charged during this time, and a consumable electrode acts as cathode for 0.2 ms, and then again as anode for 0.4–0.6 ms. Parameters of the electric converter are as follows: capacitance $C=1000$ mF, voltage $U_{charge}=3500$ V and inductance $L=3 \cdot 10^{-5}$ H.

In plasma-detonation treatment the workpiece surface is subjected at the first moment to interaction with a shock wave and a pulsed plasma jet. Then, at break-down of SCL, the surface is subjected to the impact by the electric current. The amplitude value of the current is 5 kA.

As a result, the pulsed magnetic field with an intensity of up to 2000 Oe is formed. Then the combustion and electrode erosion products flow onto the surface for a time of 3–5 ms.

The radiation spectrum of plasma consists mostly of the intensive lines of iron and copper (Fig. 3.14). These elements enter the plasma jet because of erosion of metal (consumable) electrodes. A continuous intensive glow of these lines belonging to ions of nitrogen, oxygen and carbon with an excitation potential of 20 to 30 eV is seen in all the spectrograms.

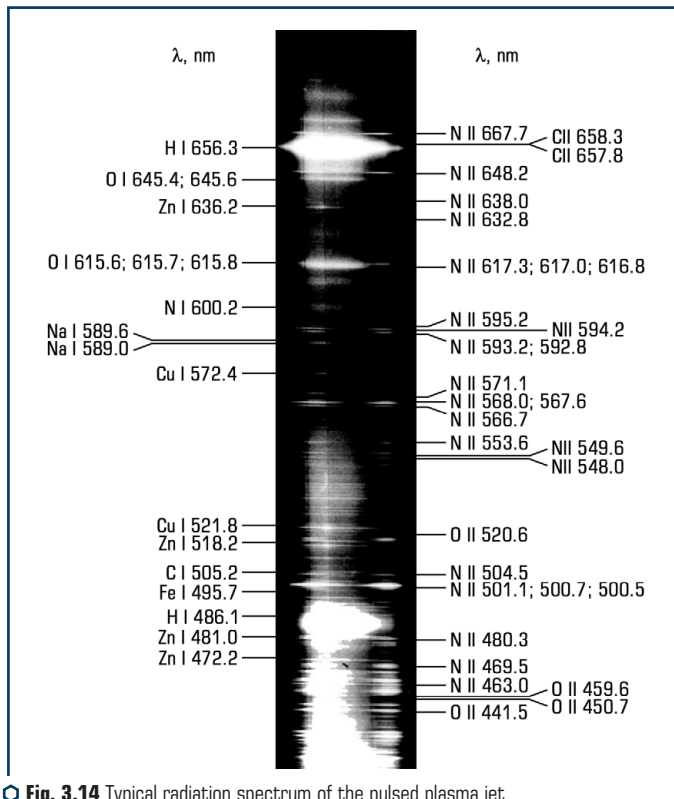


Fig. 3.14 Typical radiation spectrum of the pulsed plasma jet at a distance of 15 mm from the chamber exit section

The longitudinal spectra of plasma in SCL show a marked increase in the intensity of line and continuous radiation near the sample surface. The temperature and concentration of electrons in plasma, averaged for the time of existence of the plasma jet, as well as the distribution of temperature along the jet length, were estimated from the longitudinal and transverse spectra. The temperature of plasma was calculated from the relative intensity of the Fe_I lines using the following formula [211–215]:

$$\frac{I_1}{I_2} = \frac{A_1 g_1 \lambda_1}{A_2 g_2 \lambda_2} \exp\left(-\frac{E_1 - E_2}{kT}\right), \quad (3.3)$$

where I – the line intensity; A – the probability of transition; g – the statistical weight of the upper level; E – the energy of excitation of the upper level; λ – the wavelength of the selected line;

k – the Boltzmann's constant; T – the plasma temperature (index 1 refers to the first line, and index 2 – to the second line).

This method allows determination of plasma temperature not knowing the density of particles. The larger the difference in energies of upper levels of the selected lines, the higher the accuracy of the method. Transformation of formula (3.3) yields:

$$\frac{\Delta T}{t} = \frac{kT}{(E_1 - E_2)} \frac{\Delta(T_1/T_2)}{T_1/T_2}. \quad (3.4)$$

Lines $\text{Fe}_1 - \lambda = 640.0 \text{ nm}$ and $\lambda = 639.3 \text{ nm}$ with a difference of 1.2 eV in the upper level energies were selected for the diagnostics. The intensity was measured following the rules of photo spectroscopy, where the values of blackening fixed by the micro photometer are converted into the intensities according to the characteristic curve of photographic emulsion.

The transition probability values necessary for the calculation of temperature were taken from book [211]. Distribution of the temperature of plasma along the length of the jet evaluated from the longitudinal radiation spectra of a free jet from the generator with a cylindrical chamber shows that the temperature drops from 8000 to 6000 K in a distance of 40 mm.

Concentration of electrons in the plasma jet was determined from the half-width of lines H_α using the following relationship [212]:

$$N_e = C(N_e, T) \sqrt{(\Delta\lambda)^3}, \quad (3.5)$$

where N_e – the concentration of electrons; λ – the half-width of a line; $C(N_e, T)$ – the coefficient calculated using the tabular data [212–214].

The values of N_e calculated from the above relationship are equal to $(0.7\text{--}1.0) \cdot 10^{17} \text{ cm}^3$, depending upon the discharge conditions.

The following conclusions can be made from analysis of the investigation results. The process of a pulsed discharge in the pulsed-plasma generator can be conditionally subdivided into three stages. At the first stage the primary explosion takes place, and the capacitor bank starts to discharge. These processes occur in the reaction chamber, and duration of this stage is 0.5–1.0 ms. The processes are detected from glow of the plasmatron combustion chamber channel, which lasts to the moment of ejection of plasma jets from the nozzle. This can be seen in the first frames of photo scans.

The second stage, the time of which is 1ms, is an ejection of plasma flows in the form of individual plasma jets. This stage of the discharge is characterized by periodicity of growth and attenuation of brightness of plasma formations with a frequency of $(1\text{--}4) \cdot 10^4 \text{ Hz}$, and by a small-scale pulsation with a frequency of up to 10^6 Hz , associated with ejection of individual plasma jets.

The third stage with duration of up to 7–10 ms is characterized by a slightly glowing flow of heated gas, which is probably caused by after-burning of the fuel gas mixture.

The second stage of the discharge is of the highest practical interest, as formation and further evolution of the plasma flow takes place at this stage. Analysis of high-speed photo scans shows that the generated pulsed plasma flow has a clearly defined structure consisting of individual plasma jets. This multiple-jet mode is characterized by a relatively uniform stochastic distribution of plasma formations in the bulk of the plasma flow for a time comparable with duration of the discharge current flow (1 ms).

According to the existing notions, this mode is characteristic of cases where the external ring electrode is used as a cathode. Distinctive feature of the plasma-detonation method is a low divergence of the plasma jet. In the generator with a conical combustion chamber the plasma flow is convergent, which is caused by the effect of the ponderomotive forces, as well as by the geometric convergence of a heated gas flow at the outlet.

Examination of the high-speed photo scans shows the presence of shock waves and periodic structure. This structure is characteristic of the supersonic jets in the under-expansion mode. It agrees with the explosive character of operation of the generator, at which a substantial increase in pressure inside the reaction chamber is possible.

Connecting a workpiece into the electric circuit as cathode makes considerable changes in the process. Contraction of the plasma jet (pinch-effect) caused by the electric current flowing between anode and cathode takes place.

Experimental measurements of temperature of the plasma flow show that it rapidly falls with increase in distance from the plasma generator to the workpiece surface. The composition of plasma also changes. With distance from the exit section of the chamber, heavy atoms of metals catch up with a lighter component (atoms and molecules of nitrogen, oxygen, hydrogen and carbon). Structure of the jet becomes more uniform, but its mean temperature lowers by 30–40 %.

The use of an extra energy source inducing a control electric current on the workpiece surface increases the efficiency of the plasma jet impact to a substantial degree.

The investigations conducted allow the following mechanism of formation of the plasma jet to be considered. The current-conducting medium is formed at the initial time moment after explosion of the fuel gas mixture. The gas ionized in explosion (current layer), through which the electric current starts flowing, moves in the reaction chamber at an almost constant speed. Plasma jets moving at a higher velocity (from 3 to 8 km/s) are formed after tens of microseconds. During a time of 10^{-5} s these jets catch up with the current layer movement front and are decelerated in it to form fixed structures looking like the shock-compressed layer. In particular, this explains the presence of the plasma jets, almost fixed or even moving in a reverse direction, in a continuous photo scan. Along with the plasma jets, also the characteristic tracks caused by movement of macro particles in a flow are seen here. These are the molten particles (erosion products) detached from the electrode.

The presence of the periodic structure in a flow of gas and plasma allows determination of some of its parameters. Empirical relationships, which are valid, strictly speaking, only for a heated gas, can be used for preliminary estimations [209]:

$$L = 0.9d \sqrt{\frac{P_1 - 1.9P_2}{P_2}}, \quad (3.6)$$

where L – the wavelength of the periodic structure of the supersonic jet in a fixed environment; d – the diameter of the outlet nozzle; P_1 – the pressure at the nozzle outlet; P_2 – the pressure in the environment.

Similar relationship between the wavelength of the periodic structure, L , and Mach number M has the following form:

$$L = 1.3d \sqrt{M^2 - 1}. \quad (3.7)$$

Assuming that $L = 10$ mm, pressure in the reaction chamber of the generator is $P_1 = 2.5$ atm. Almost over the entire time of generation of the plasma jets (electric current flow) L hardly changes. Estimation of the Mach number for this case from formula (3.5) yields $M = 1.1$. In principle, having these data, it is possible to determine the temperature of the plasma flow using the following expression [211]:

$$C_s = \sqrt{\frac{k\gamma(T_i + ZT_e)}{M_i}}, \quad (3.8)$$

where C_s – the velocity of sound in plasma; k – the Boltzmann's constant; T_i and T_e – the temperatures of ions and electrons, respectively; Z – the ion charge; M_i – the ion mass; γ – the adiabatic exponent.

Analysis of the data shows that the values of γ for a wide range of the composition of plasma vary within a narrow range ($\gamma = 1.2 - 1.6$). It is known to decrease with increase in the ionization degree [227]. Assume for the calculations a minimal value of $\gamma = 1.2$, as well as a mean value of $M_i = 3.7 \cdot 10^{-23}$ g. This corresponds to the presence of iron and nitrogen in a ratio of 2:1 in plasma. Assume also that a single equilibrium temperature $T_i = T_e = T$ is established in plasma at a flow velocity of $V = 3$ km/s. Thus, the mean temperature of the flow of plasma at the exit section of the cylindrical generator nozzle will be $T = 8000$ K.

As indicated by investigations, the periodic structure is formed in the plasma flow. Estimations made using formulae (3.4) and (3.6) show that in the initial phase of the discharge the pressure at outlet of the generator nozzle is about 4.5 atm, and the Mach number is 1.3. According to the spectroscopy data, the composition of jets is determined mostly by gas components (N, O, H, C). In this case M_i can be assumed to be equal approximately to $2.3 \cdot 10^{-23}$ g. The resulting value of the velocity of plasma jets in the initial phase of the electric discharge is about 8 km/s.

Investigations show that the composition of plasma is determined by the excited components of gaseous combustion products (H, O, C, N). In particular, this is the case of the initial phase of the discharge. Pressure in the reaction chamber varied over a wide range from 3 to 8 atm,

velocity of the plasma jets varied, accordingly, to 10 km/s, and temperature, which theoretically may amount to 30,000 K, was fixed to be 25,000 K under the experiment conditions.

3.4.2 SPECTROSCOPIC EXAMINATIONS

Composition of the plasma jet was studied from longitudinal and transverse radiation spectra. Identification of the spectra was done using a measurement microscope. Radiation spectrum of the experimental generator consists primarily of the intensive iron lines with an excitation potential of 3.2 to 6.4 eV. The spectrum also contains low-intensity copper lines and a yellow doublet of sodium atom, $\lambda=290$ nm.

These elements enter into the plasma jet because of erosion of the metal (consumable) electrode. In addition to metal lines, the spectrum also contains the lines of hydrogen atoms H-1, H-11 and H-111, as well as diffusion lines of oxygen and nitrogen atoms in a field of 600 nm. A very intensive continuous spectrum is seen against the line radiation spectrum. **Fig. 3.14** shows identification of a transverse spectrum fixed at a distance of 15 mm from the exit section of the generator reaction chamber.

Analysis of transverse spectrograms recorded at different distances from the nozzle exit section indicates that the composition of spectrum undergoes no qualitative changes at a distance of 15 and 30 mm from the exit section. Some spectrograms fixed near the nozzle exit section show traces of the most intensive Fe_{II} line with an excitation potential of 5.82 eV (ionization potential of iron atom is 7.9 eV). When the plasma jet falls on the obstacle placed at a distance of 30 mm from the exit section, the transverse (light) diameter of the jet increases markedly from 30 to 60 mm.

Glow of the jet caused by Fe , Cu and Na , attenuates at a distance of 70 mm from the exit section. The intensity of radiation of gaseous components H , O , and C , decreases at a distance of 30 mm. The periodic structure along the length of the jet, as well as decrease and increase in the intensity, can be seen in some spectrograms. This shows up in the Fe and H lines. This structure is attributable to the presence of shock waves in the jet. Experiments and calculations show that the most efficient generators are those that have a conical reaction chamber. The plasma jet from such a generator emits much more energy at the almost identical electric power. Composition and space distribution of emitting components are totally different from those measured with the generator equipped with a cylindrical combustion chamber. Hydrogen, oxygen, nitrogen and carbon atoms are emitted from the central part of the jets. An intensive continuous radiation can be seen in all spectrograms. The spectra contain the intensive lines of zinc and copper atoms, which are caused by the presence of a consumable brass electrode (62 % Cu, 38 % Zn). The iron lines can be seen only as traces of the most intensive lines. Peculiarity of these radiation spectra of the plasma jet from the generator is the presence of lines belonging to nitrogen, oxygen and carbon with an excitation potential of 20 to 30 eV.

Composition of the emitting components remains unchanged with distance from the exit section, but only to a distance of 15 mm. In the transverse spectra fixed at a distance of 30 mm,

the N_{II} , O_{II} and C_{II} lines are present only in the form of traces. The longitudinal radiation spectra of a free plasma jet and jet falling on the obstacle placed at a distance of 25 mm from the exit section show a marked increase in the intensity of both line and continuous radiation near the sample surface. The obstacle is made from copper and connected to the generator cathode via a copper busbar.

The central part of the jet with a light diameter of 18 mm emits mostly H_I , N_I , O_I and C_I , and it is more stable in its spatial position. The jet has high-temperature fragments (N_{II} , C_{II} and O_{II}) formed as individual jets with a diameter of up to 10 mm, located about a central nucleus. The atoms of iron, zinc and copper are distributed more uniformly across the jet.

Comparison of spectrograms with space-time scans suggests that the ejection of the central nucleus of plasma emitting H_I , O_I , N_I and C_I occurs at the first stage of the electric pulse. Then follows the ejection of metal erosion plasma and high-temperature cathode jets N_{II} , O_{II} and C_{II} . Therefore, the integrated radiation spectra of the plasma jet are formed of its individual components at different time moments.

4 PLASMA-DETONATION EQUIPMENT

ABSTRACT

The description of plasma-detonation equipment is given. The equipment, as a rule, consists of a plasma generator, standard product manipulator and an electric power source. The workroom is equipped with supply and exhaust ventilation and protection systems. The unit is controlled remotely from the control panel.

KEYWORDS

Equipment, specialized premises, work safety.

4.1 PULSED PLASMA GENERATORS

Basic technological equipment for generation of pulsed plasma is generator with a conical reaction chamber having a cone angle of 6° and length of 300 mm.

The generator (**Fig. 4.1**) consists of detonation gun 1, spark plug 2 for detonation initiation, conical cathode 3 and anode electrode 4 installed along the axis of the reaction chamber on post insulators 5. Cylindrical channel 6 designed for acceleration and heating of powders is secured to the end of the reaction chamber.

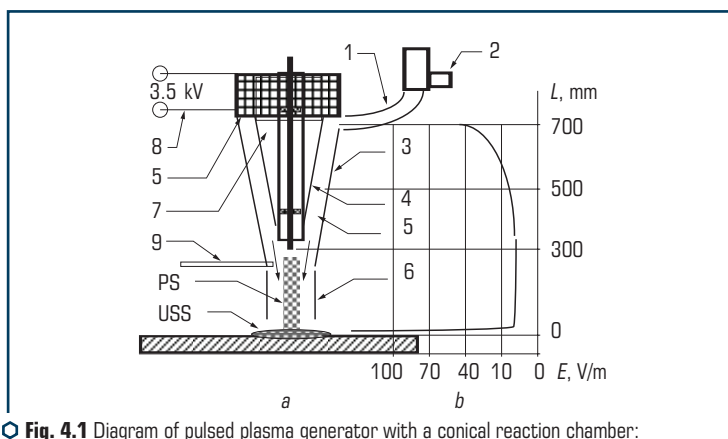


Fig. 4.1 Diagram of pulsed plasma generator with a conical reaction chamber:
a – generator; b – variation of intensity of the electric field in gap between electrodes

All active elements of the generator are cooled by running water circulating through chambers 7. Electric potential is supplied to the anode and cathode from high-voltage current source 8. A spray material in the form of a powdered alloy is fed via pipe 9 to channel 6. Plasma generators are of two standard types. Reaction chamber of a lower-power conical generator (**Fig. 4.2**) is 100 mm long. Reaction chamber of this device has a cylindrical annular and conoidal volume with a cone angle of 12° . The generator consists of external cathode electrode 1, which is fixed with fixing device 2 and cooled using a water chamber. The internal anode electrode is cooled by water and has a hollow channel along its axis, where the consumable electrode is installed.

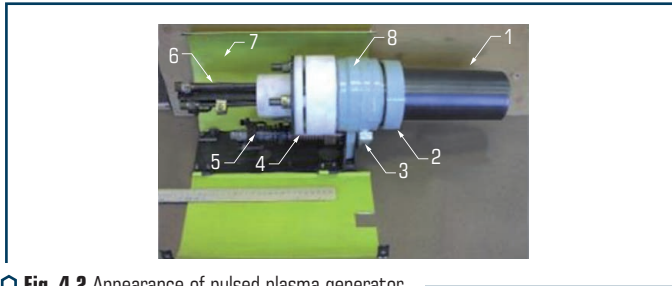


Fig. 4.2 Appearance of pulsed plasma generator

The anode is fixed with insulators 4. Components of a fuel gas mixture are fed to small-size detonation gun 5, where they are mixed and detonated from the electric discharge excited by the car-type ignition system. Reaction gas is fed to the generator through union 3.

Water that cools the generator is fed in and out and the electric potential is supplied through hollow pins 6. Peculiarity of this generator is the presence of a consumable electrode, which allows alloying elements to be fed to plasma. In addition, purging the electrode with gases provides feeding of a reaction gas to the gap between the electrodes, as well as oxidation protection and cooling of the surface being modified. Focusing of the plasma jet here is provided by a gas-dynamic compression at the cone and ponderomotive forces induced by the electric current flowing between the consumable electrode tip and internal surface of the cone. Therefore, power density of the jet can be varied due to extension of the electrode tip from the end of the conical part of the chamber.

The thermal spraying technology is realized using generators with cylindrical reaction chambers 300 and 500 mm long (**Fig. 4.3**).

These generators are fundamentally different in design from conical generators. They comprise external cylindrical electrode 1 made of standard steel tubes, internal electrode 2 made of 3/8" tube and fluoroplastic insulator 3, which fixes these electrodes using pins 4. Like in the above devices, water cooling is done via pipes 5 and water jackets 6. Detonation gun 7 is intended for mixing of a fuel gas mixture and initiation of its detonation.

Fig. 4.4 shows appearance of pulsed plasma generators for surface modification (**Fig. 4.4, a**) and deposition of coatings of a powdered material (**Fig. 4.4, b**).

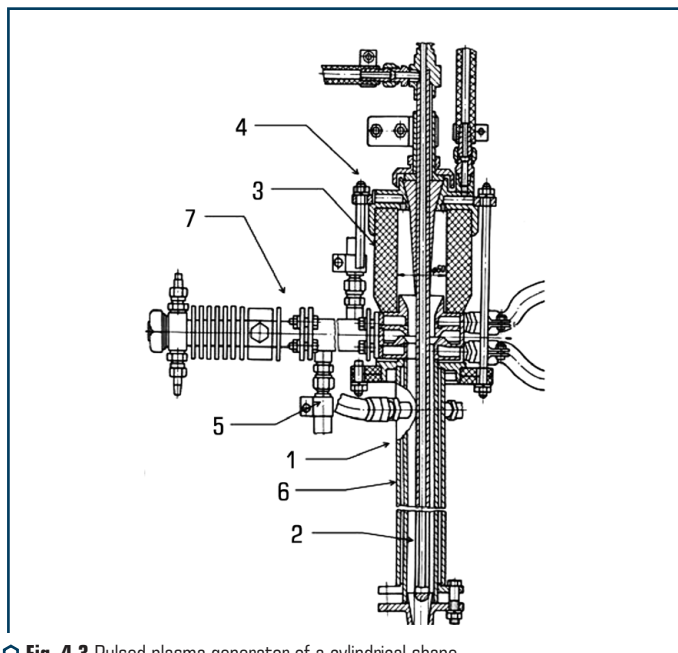


Fig. 4.3 Pulsed plasma generator of a cylindrical shape

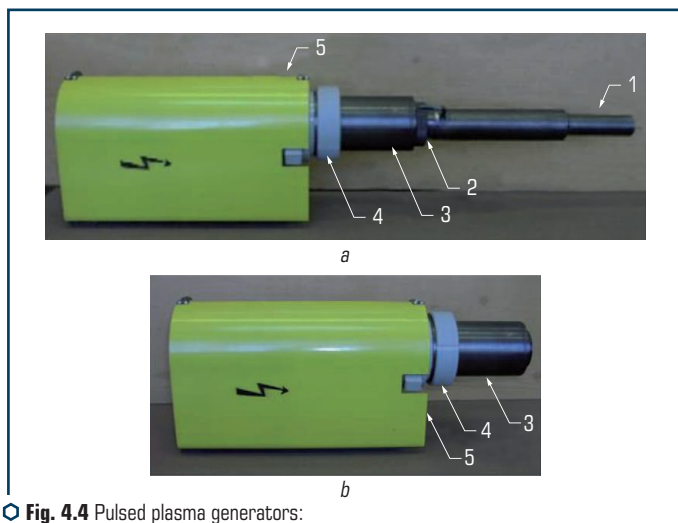


Fig. 4.4 Pulsed plasma generators:
a – for modification of surface properties; *b* – for deposition of coatings

The main difference between them is the presence of channel 1, which is used for acceleration and heating of powders. The channel is connected to the reaction chamber through connecting unit 2. Depending upon the process conditions, reaction chamber 3 can be replaced using connecting unit 4. The detonation device, connecting pipes and insulator are closed by jacket 5.

4.2 TECHNOLOGICAL MODIFICATION SYSTEMS

Different versions of systems were developed and manufactured for plasma-detonation treatment of parts. One of the simplest technological systems is the pulsed-plasma generator mounted on a metal-working machine tool, e.g. horizontal milling machine (**Fig. 4.5**).

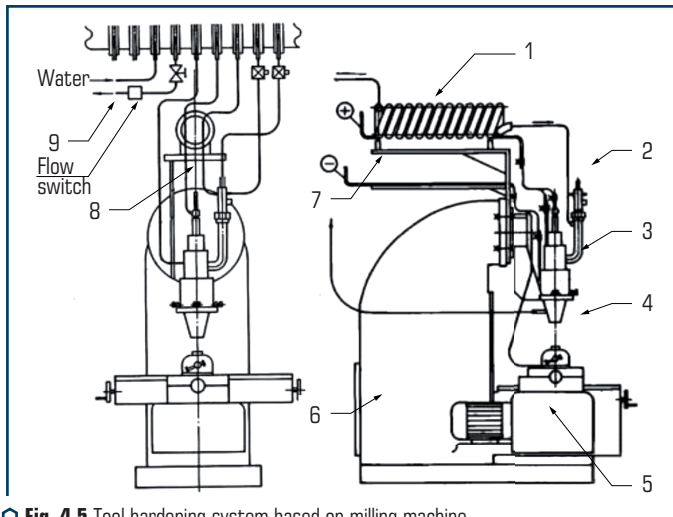


Fig. 4.5 Tool hardening system based on milling machine

Induction-capacitance energy integrator 1, detonation device 2 and pulsed-plasma generator 3 are mounted on the machine frame. Workpiece 4 is mounted on machine support 5. Frame 6 of the machine is an assembly element, which provides strength and accuracy of joining of the system components. The electric current is fed to the plasmatron via copper busbars 7 and inductor 1, while gases and a coolant are fed via pipes 8 and 9.

System UN-143 is applied for deposition of coatings and hardening of large-size parts in wood working and metallurgical industries. This system can provide hardening of parts up to 2000 mm long (**Fig. 4.6**).

The system is equipped with a workpiece manipulator, which allows coating and hardening of rollers, rolls, cutting disks and saws with a diameter of up to 1500 mm. System UN-143 is installed

in a noise-proof room. The room is fitted with plenum-exhaust ventilation and remote control. The process capacity can be increased through installing several plasma generators, which can be oriented to one point on the workpiece surface. This raises energy density, improves quality and increases productivity of the treatment process.

The system (**Fig. 4.6**) comprises plasma generator 1, control panel 2, gas distribution panel 3, device 4 for mechanised movement of the generator, electric energy converter 5, frame 6, and support 7 with device 8 for rotation of workpieces. This system is intended for hardening and designed with a possibility of moving and rotating parts up to 2 meters long and up to 1000 kg in weight.

The system is controlled from a remote panel located in a control room. The system is switched off by a command from the limit switch installed in the machine carriage or by an operator.

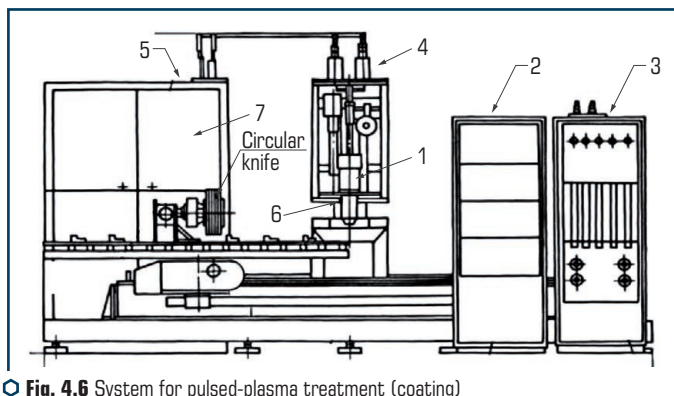
The system with a possibility of pre-programmed movement of plasma generator in an automated mode was developed and manufactured for plasma-detonation treatment of parts.

The system is placed in a noise-proof room (**Fig. 4.7**). Pulsed plasma generator 2 is mounted on manipulator 3 with three axes of freedom. Special manipulator 1 for rotation of workpieces is installed under the generator nozzle. This manipulator can change the angle of the rotation axis and has a current collector (up to 1000 A) at the spindle.

The room has a double noise-proof door and observation window 5. The room door is equipped with retaining contacts. Gas distribution panel 8 and electromechanical system control panel 7 are located in the operator's room in front of the observation window.

The room is fitted with the noise and electromagnetic radiation neutralisation systems and plenum-exhaust ventilation. The electric energy converter is placed in the operator's room, and the high-voltage wire through a passage in the room wall connects it to the induction-capacitance energy integrator. The electromechanical system is driven using a special program, which provides treatment of large-size complex-configuration parts in the automated mode.

Fig. 4.8 shows a flow diagram and photo of the technological system UN 138M.



○ **Fig. 4.6** System for pulsed-plasma treatment (coating) of large-size parts: metal cutters and mould plates

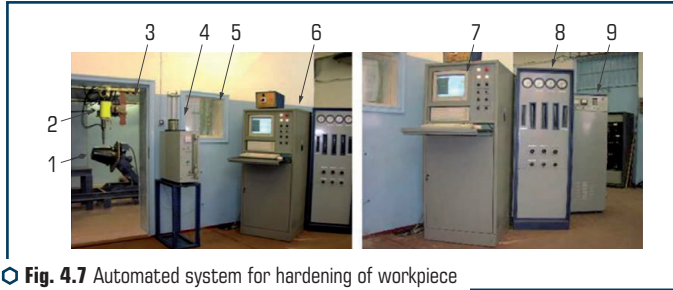


Fig. 4.7 Automated system for hardening of workpiece surfaces and deposition of coatings

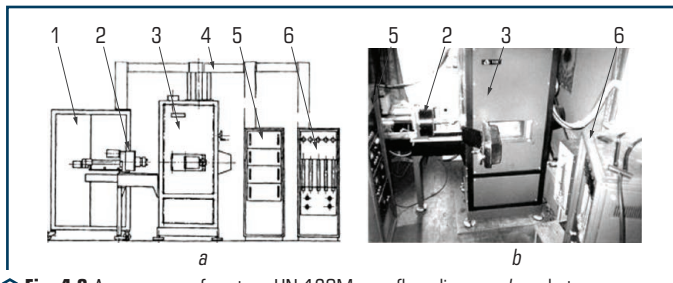


Fig. 4.8 Appearance of system UN 138M: *a* – flow diagram; *b* – photo

This system is designed for operation in a workshop. It has a built-in chamber with noise-proof walls and systems for neutralisation of electromagnetic radiation. The system is completed with electric power unit 1 (of the VV-114 type), manipulator 2 for a workpiece to be hardened; process unit 3, connecting pipes 4, cabinet 5 with control and technology automation systems and gas preparation unit 6. The process unit of the system has built-in noise-proof chamber and pulsed plasma generator. This system in its baseline version is designed for hardening (coating) of parts up to 300 mm long and up to 150 mm in diameter. These could be sets of mills, broaches, shafts, sets of piston rings, knives, pistons and other parts. If necessary, the system can be upgraded and used to harden parts up to 2000 mm long. This could be done by replacing the manipulator and lateral caps of the process unit.

Realization of the plasma-detonation technology is accompanied by formation of a sound field up to 150 dB. Therefore, all the equipment is located in a special room having double noise-proof walls and observation window. As a rule, the equipment consists of a plasmatron, standard workpiece manipulator and power supply. The room is equipped with plenum-exhaust ventilation and systems for protection from electromagnetic radiation and noise. Pipes for gases are fitted with electromagnetic stop valves, and a water pipe has a flow relay. The system is controlled from the remote panel located outside the room, or from a computer. Operational safety is ensured by the fuel gas feed, ignition switching and high-voltage electric potential locking systems. Locking responds to operation of the ventilation, feeding of the coolant, closing of the retaining contacts on the door, in the room and in cabinets with electrical equipment.

ABSTRACT

The results of investigations of pulse-plasma modification of the products surface made of tool steels are presented. The processes occurring in the surface layers during short-term pulsed plasma exposure are described. Their structures and properties have been studied.

KEYWORDS

Metallography, scanning electron microscopy, X-ray phase analysis. structural condition.

5.1 ALLOYS WITH 0.7–0.8 % C

5.1.1 PDT PROCEDURE

Efficiency of plasma-detonation treatment (PDT) of surfaces of parts made from iron-base alloys was studied on samples 19 mm in diameter and 4 mm thick. The samples were made of steel U8 (0.7 % C) in the as-received state (high-temperature drawing, no extra heat treatment).

The treatment was performed using machine UN-138M (**Fig. 4.8**). During the hardening process the high-energy jet (power density – 10^5 – 10^6 W/cm²) falling on the sample surface forms a shock-compressed layer (SCL). The electric current with almost no losses flows through the plasma jet to SCL to release heat.

Evaporating electrodes, i.e. rods of Mo, Ti, W, NiCr and alloy consisting of 18 % Cr, 9 % Ni, 1 % Ti and 72 % Fe, were used to introduce metallic alloying elements into plasma. Distance from the plasma generator reaction chamber end to a sample was set at $D=50$ mm, and distance to the evaporating electrode – at $h=15$ mm. PDT was performed with 3 and 8 pulses.

5.1.2 EFFICIENCY OF THE EFFECT ON THE SURFACE BY PHYSICAL FIELDS

It is well known that the process of treatment of the surface layer of metal with concentrated energy sources results in its rapid heating and subsequent intensive cooling. Heat is removed both into the bulk of metal and into the environment. High rates of heating and cooling of the surface metal layer (10^4 – 10^8 K/s) lead to formation of a dispersed crystalline structure, high dislocation density and variations in the concentration of alloying elements, including carbon and nitrogen [216–221].

Results of studies [222–226] show that in pulsed treatment of the metal surface the coefficient of mass transfer of alloying elements grows and hardly depends upon the size of grains. Increase in the number of pulses is accompanied by a monotonous decrease in the coefficient of mass transfer. What is most interesting is that the simultaneous effect on the workpiece surface by different types of pulsed treatment provides a significant increase in the coefficient of mass transfer, and that this increase is of a synergetic character. To conduct experiments, let's use plasma-detonation devices described in Chapters 2 and 3 [227–229].

The experiments show that the pulsed plasma ejected from the reaction chamber of the plasma-detonation generator closes the electric circuit between the anode electrode and cathode workpiece surface. Plasma is heated due to Joule heat $Q = \sigma E^2 W/m^3$ released as a result of the electric current flowing through this jet. At the initial moment the workpiece surface experiences an elastic deformation interaction with the shock wave and pulsed plasma jet. Then, at break-down of the shock-compressed layer of plasma, the surface is affected by the electric current. The current amplitude value is 5–10 kA. This results in the formation of a pulsed magnetic field with an intensity of up to $4 \cdot 10^5$ A/m). Then, for the next 3–5 ms, the surface is influenced by the electrode combustion and erosion products.

The pulsed surface treatment methods are characterized by the lack of time for occurrence and completion of structural changes, which leads to suppression of the processes of diffusion of alloying and interstitial elements. This results in "fixation" of highly heterogeneous and non-equilibrium structures, i.e. clusters, formed in heating. Hence, this leads to the probability of formation of structureless martensite – hardenite. The latter inherits the fine-grained structure and heterogeneous chemical composition of austenite formed at the moment of completion of heating. Higher hardness of the layer consisting mostly of hardenite, despite the presence of a considerable amount of retained austenite (about 20 %), is related to a high dislocation density, fine-grained structure and chemical and structural heterogeneity [67–70, 230, 231].

PDT is performed under conditions of high-rate heat treatment [228], which leads to decrease in retained austenite and disordering of carbon atoms in the martensite lattice. It is known that application of a magnetic field during laser treatment increases the value of microhardness, but exerts no effect on formation of a defective structure [222]. It is characteristic that under conditions of pulsed laser heating of iron-base alloys the process of dissolution of carbide phases and redistribution of carbon and alloying elements does not have time to develop either, and α - γ transformations occur within the initial ferrite-carbide structure. 1220–1270 °C is a temperature of α -solid solution of annealed steel R18. Hardening of the surface layers of annealed steel R18 can be related only to microplastic deformation and increase in the density of defects in α - γ transformations taking place during the heating process.

5.1.3 PECULIARITIES OF PLASMA-DETONATION TREATMENT (PDT)

Investigation results on the efficiency of PDT of iron-base alloy parts show that a sub micro-crystalline alloyed layer is formed on the surface (**Fig. 5.1**). Parameters of the pulsed plasma used

for the treatment are given above. The presence of visible defects in the layer depends upon the plasma composition and quantity of the treatment pulses.

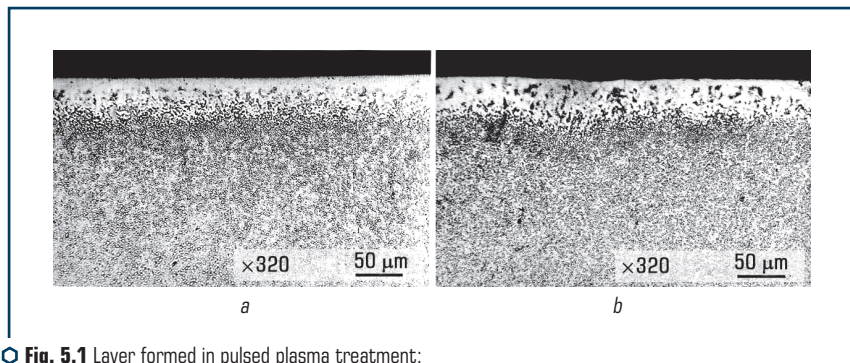


Fig. 5.1 Layer formed in pulsed plasma treatment:

a – plasma has a stoichiometric composition; *b* – plasma has an increased oxygen content

For example, treatment by plasma with an increased oxygen content at $\alpha > 1$ leads to formation of visible oxide inclusions in the layer (Fig. 5.1, *b*). No oxides are detected after the same treatment but at $\alpha < 0.8$ (Fig. 5.1, *a*).

$\alpha = \chi/\chi^0$ is the coefficient of excess oxidizer, which is the generalizing characteristic of composition of the combustion products making the base of the plasma jet, where $\chi^0 = \nu(\text{O}_2)/\nu(\text{C}_n\text{H}_m)$ is the molar stoichiometric coefficient, and χ is the actual proportion of components.

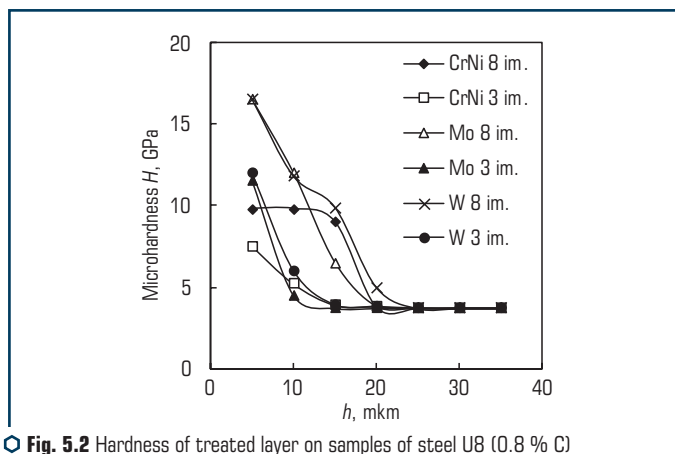
$\chi^0 = 5$ for a mixture of oxygen+propane. In addition to the above technological parameters, the value of microhardness of the surface is affected also by the quantity of plasma pulses (thermal cycles of treatment). Increase in the quantity of pulses leads to increase in thickness of the hardened layer and its uniformity.

The highest hardness of the treated layer on samples of steel U8 (subjected to quenching and high tempering) was achieved in PDT using tungsten and molybdenum electrodes (Fig. 5.2).

The treatment was performed with no fusion of the surface at a specific power of the jet equal to 10^6 W/cm^2 . Hardness was measured on transverse sections using the PMT-3 hardness meter.

Measurements were made with the Knoop diamond pyramid. Load on the pyramid was $P = 0.1 \text{ N}$. The use of the Knoop pyramid made it possible to approach to the surface to a distance of $5 \mu\text{m}$. Not less than 5 measurements were made at the same distance from the surface.

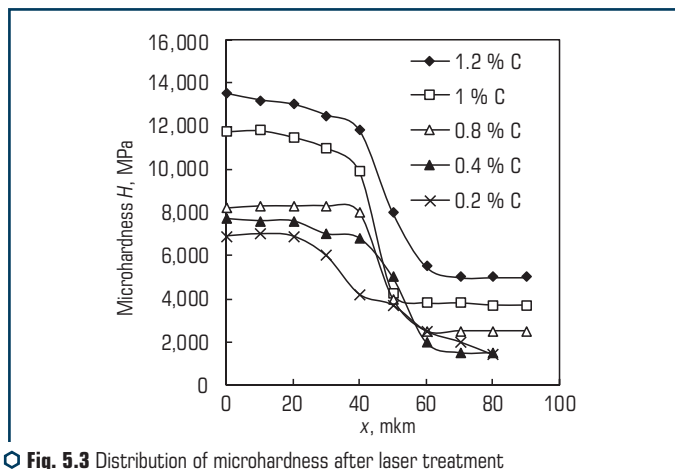
X-ray phase analysis of layers hardened by PDT [232–234] fixes widening of the α -Fe lines and appearance of the Fe retained austenite lines. Increase in the quantity of the PDT pulses leads to further widening of the α -Fe lines and decrease in their intensity, as well as increase in a relative intensity of the γ -Fe lines. Judging from the ratio of intensities of the retained austenite to ferrite lines, the largest amount of austenite under identical treatment conditions is seen in the case of using a tungsten electrode.



○ Fig. 5.2 Hardness of treated layer on samples of steel U8 (0.8 % C) using tungsten and molybdenum electrodes

X-ray spectrum analysis performed with the electron probe with a diameter of about $2\text{ }\mu\text{m}$ shows that the consumable electrode material penetrates into the hardened layer of a part treated. For example, in the case of using a tungsten consumable electrode, tungsten was fixed in the hardened layer at a depth of $20\text{ }\mu\text{m}$ [235].

The plasma formation method is also important. Reportedly [22], the laser beam forms plasma that is less efficient than plasma of the electric discharge [236]. Hardness of the surface after laser treatment depends primarily upon the amount of carbon in an alloy (Fig. 5.3).



○ Fig. 5.3 Distribution of microhardness after laser treatment of metal alloys with a carbon content of 0.2, 0.45, 0.8, 1.0 and 1.2 %

The character of interaction of pulsed plasma with the workpiece surface in PDT is more complicated than in laser treatment.

PDT results in rapid heating of local regions on the surface of a massive sample, which provides a strain rate of $\epsilon = 10^{-3} \text{ s}^{-1}$. In addition to a high strain rate, PDT forms an electromagnetic pulse and induced the magnetic field with an intensity of up to 1000 Oe. Such pulsed effects are known to substantially accelerate diffusion of elements in metal alloys. The simultaneous impact by several types of the pulsed effect leads to substantial acceleration of mass transfer of elements.

As shown by the experiments [228, 232–235], PDT provides maximal value of hardness of the surface layer. This is caused by formation of a special dislocation structure of metal with an increased density of defects, high degree of dispersion of blocks and concentration heterogeneity. Surface treatment by the high-energy plasma jets is effective for hardening of both carbon and alloyed steels. Further improvement of properties of the workpiece surface can be achieved through alloying it with appropriate elements. Complex alloying of the surface provides resistance to wear, heat, corrosion, fire cracks, etc. The following distribution of alloying elements (electrode erosion products) is seen through thickness of the modified layer. **Fig. 5.4** a shows X-ray pattern of the surface of sample of steel 3 (0.3 % C) before and after treatment with the pulsed plasma containing copper or aluminium.

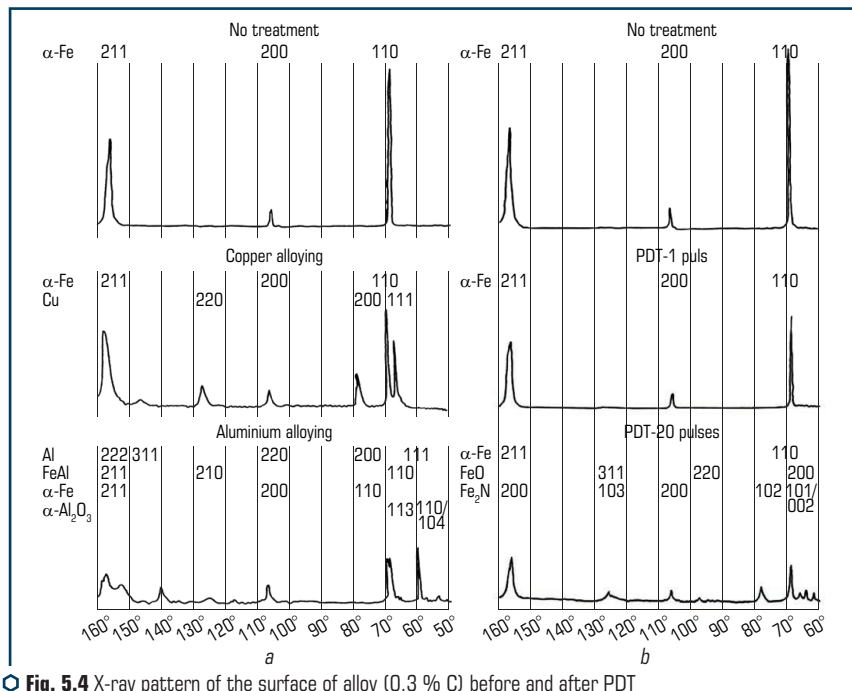


Fig. 5.4 X-ray pattern of the surface of alloy (0.3 % C) before and after PDT by the pulsed plasma containing: a – copper and aluminium; b – nitrogen and oxygen

Metals in the form of corresponding rods were introduced to the plasmatron, where they were evaporated to enrich plasma.

Thus, alloying of the modified surface and formation of new chemical compounds (aluminides, nitrides, carbides, oxides) can be provided in it by adding vapors of metals, e.g. copper or aluminium, to the plasma. PDT also enriches the surface with gaseous components of the plasma: nitrogen, carbon and oxygen. Increasing the quantity of pulses leads to a change in the surface state (**Fig. 5.4, b**). Iron oxides and nitrides are formed in the surface layer.

5.1.4 X-RAY PHASE AND DIFFRACTION ANALYSIS OF ALLOY AFTER PDT

PDT was performed under the following conditions: distance to the sample surface – $D=50$ mm, depth of immersion of an eroding electrode into the reaction chamber – $h=15$ mm. Only the plasma composition was changed through introducing electrodes of tungsten, molybdenum and alloy (18 % Cr, 9 % Ni, 1 % Ti, 72 % Fe) to the plasmatron.

Distinctive feature of X-ray patterns of the surface of hardened steel U8 (0.8 % C) is splitting of line of the α -phase caused probably by a tetragonal structure of surface quenching martensite. This splitting is especially pronounced for lines (110)- α and (211)- α . The surface layer of a sample treated by plasma containing vapors of alloy (18 % Cr, 9 % Ni, 1 % Ti, 72 % Fe) (**Fig. 5.5, c**) is characterized by wide split lines superimposed on narrow non-split ones. Height of the left peak is much lower than that of the right one. Analysis of the alloy surface in the initial state shows that lines of the α -phase are very narrow (**Fig. 5.5, a**). It should be noted that after standard hardening in furnace the α -phase line is widened to such a high extent that it masks splitting of other lines (**Fig. 5.5, b**).

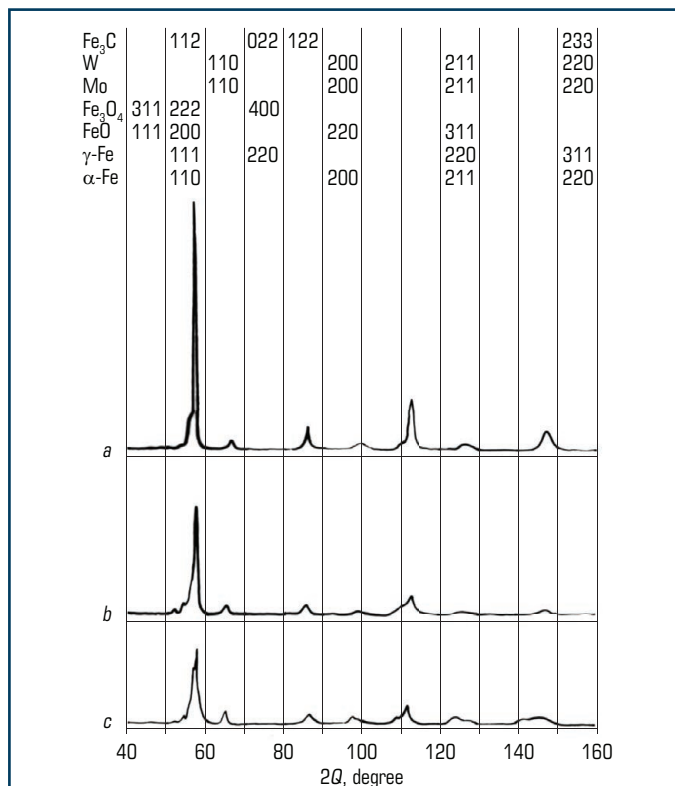
The amount of carbon contained in martensite is evaluated from splitting of its lines. Parameters a and c of the martensite lattice depend upon the weight percent of carbon, P , as follows [233]: $C=0.2866+0.0118 P \cdot \text{nm}$, $a=0.2866+0.0015 P \cdot \text{nm}$.

Bragg angle in the tetragonal lattice for lines (hkl) is equal to $\sin^2 Q = \gamma^2/4a^2 \cdot (h^2 + k^2 + l^2 \cdot a^2/c^2)$, where γ is the X-ray wavelength.

Fig. 5.6 shows the calculation result for line (211). Estimation of the lattice parameters of the alloy after furnace hardening (**Fig. 5.5, b**) showed (**Fig. 5.6**) that in this case $\delta(2Q)=2.5^\circ$. This corresponds to a carbon content of $P=0.75$ wt %. Splitting of line (211)- α after PDT with Mo and W electrodes is $\delta(2Q)=3^\circ$, which corresponds to $P=0.8$ wt %. This value is lower than the carbon content of the alloy, but higher than that of the hardened sample.

Given that the time of dwelling of the surface layer at a treatment temperature is extremely short, a higher carbon content of martensite after PDT is likely to be caused by extra absorption of carbon from the plasma jet.

Analysis of the austenite intensity lines shows that the amount of austenite is lowest in the case of PDT using electrode of alloy Kh18N9T (18 % Cr, 9 % Ni, 1 % Ti, 72 % Fe), and highest in the case of adding tungsten vapors to plasma.



○ **Fig. 5.5** X-ray pattern of the surface of the steel U8 (0.8 % C) samples (batch 1): *a* – sample after hardening in furnace; *b* – sample after PDT ($D=50$ mm, $h=15$ mm, $N=8$, Mo); *c* – sample after PDT ($D=50$ mm, $h=15$ mm, $N=8$, W)

This proves that the surface is heated to a higher temperature in the case of treatment with pulsed plasma containing the electrode material with a higher atomic number.

X-ray pattern of the initial sample (**Fig. 5.5, a**) shows weak lines of cementite, which almost vanish after PDT.

Physical widening of lines of retained austenite of the alloy (0.8 % C) (**Fig. 5.7**) is identical to that of carbon steels. This is in agreement with a conclusion that this widening is independent of the carbon content of the alloy.

X-ray patterns of the surface of the alloy (0.8 % C) sample after PDT with a titanium electrode were recorded using the DRON-3M diffractometer with a graphite monochromator. This allowed increasing resolution of the method. Thus, lines of cementite Fe_3C can be seen in X-ray pattern of

the initial sample. The lines of cementite persisted after PDT under the low intensity conditions, and two very strong lines appeared in a region of low reflection angles ($Q=7.2^\circ$, $d=0.714$ nm and $Q=14.5^\circ$, $d=0.244$ nm). The last line is a strong line of titanium nitride TiN.

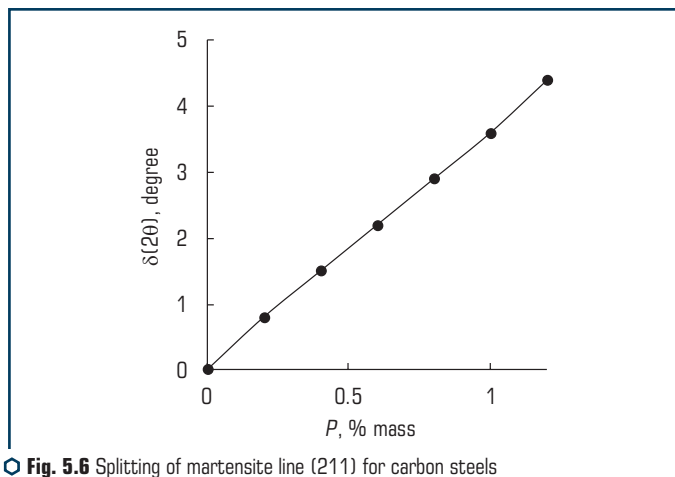


Fig. 5.6 Splitting of martensite line (211) for carbon steels depending upon the carbon content

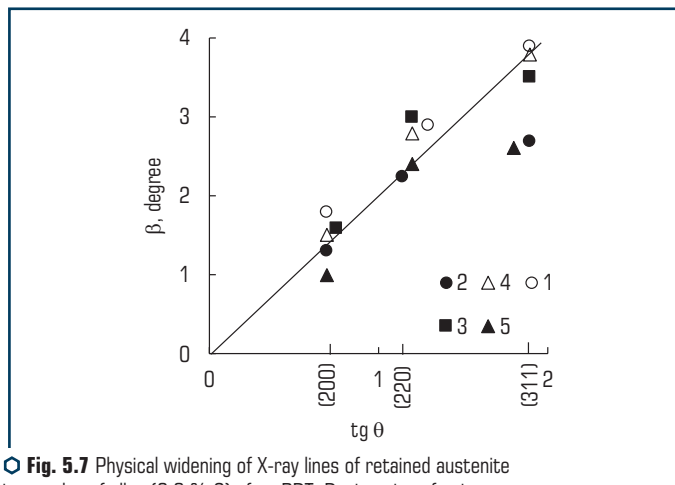


Fig. 5.7 Physical widening of X-ray lines of retained austenite in samples of alloy (0.8 % C) after PDT. Designation of points corresponds to numbers of samples in batch 1 (Table 5.1)

Then follows a strong line of TiN with $d=0.714$ nm, $Q=14.5^\circ$ and $d=0.357$ nm, as well as a weak line with $Q=21.5$ and $d=0.244$ nm. The last line is a strong line of titanium nitride TiN.

The next strong line of TiN ($d=0.2116$ nm and $Q=25.4^\circ$) is superimposed on the Fe_3C line ($d=0.2104$ nm) and cannot be unambiguously distinguished. This sample contains no retained austenite. The strong line at $Q=14.5^\circ$ may correspond to anatase, i.e. modification of titanium oxide TiO_2 ($d=0.352$ nm).

Austenite appears after more intensive PDT. The Fe_3C lines vanish, lines of Fe_3O_4 , O_2 and Fe are formed, and a weak line of titanium nitride persists at $Q=21.3^\circ$.

Persistence of radiation of TiN with $d=0.244$ nm in MoK- α suggests that TiN penetrates to a depth of more than 1 μm .

X-ray phase analysis of the surface layers of carbon steel samples hardened by the pulsed plasma fixes widening of the α -Fe lines and formation of the Fe retained austenite lines. Increasing the quantity of pulses leads to further widening of the α -Fe lines with decrease in their intensity, as well as to increase in the relative intensity of the γ -Fe lines. Judging from the ratio of the retained austenite and ferrite lines, the amount of austenite under the same treatment conditions is maximal in the case of using the tungsten electrode. X-ray diffraction examinations show that the consumable electrode material penetrates into the hardened layer of a workpiece. For example, in a case of using the titanium consumable electrode, titanium was detected in the hardened layer at a depth of 20 μm .

X-ray phase analysis shows that after solid-state treatment of parts by the pulsed plasma the modified layer exhibits a high intensity of the austenite lines, which grows with intensification of treatment. Examination of widening of X-ray diffraction lines indicates that widening of both α -Fe and γ -Fe lines after plasma treatment can be considered proportional to $\text{tg}Q$ (**Fig. 5.7**), which proves that a dominating contribution to widening is made by heterogeneous elastic distortions of the lattice [232, 233].

These distortions can be related both to elastic strains caused by dislocations and/or coherent bond between particles of different phases, as well as to heterogeneous distribution of alloying elements, such as titanium, nitrogen and carbon.

5.1.5 METALLOGRAPHY AND AUGER SPECTROSCOPY

Auger spectra were fixed in SET and COMPO modes, and characteristic Auger spectra of different regions of the sample surface were analysed to determine chemical composition of the surface layer of a sample after PDT.

Hardening of samples by PDT was performed under conditions given in Section 5.1.4. To illustrate, **Fig. 5.8** shows one Auger spectrum of the surface of a sample after PDT using the titanium electrode. After PDT using different electrodes, except for the titanium electrode, it can be seen from the Auger spectra of all the regions that the most intensive peaks are those of oxygen and carbon.

This is characteristic of treatment using electrodes of copper + zinc alloy (**Fig. 5.9**) or aluminium (**Fig. 5.10**).

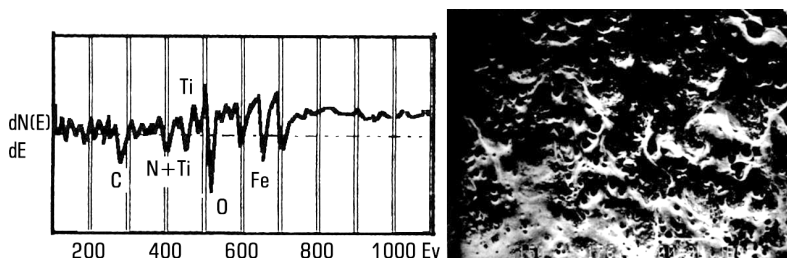


Fig. 5.8 Auger spectra of the surfaces of samples 2–4 of steel 45 (0.45 % C) treated by plasma with an addition of Ti vapors ($D=40$ mm, $h=35$ mm)

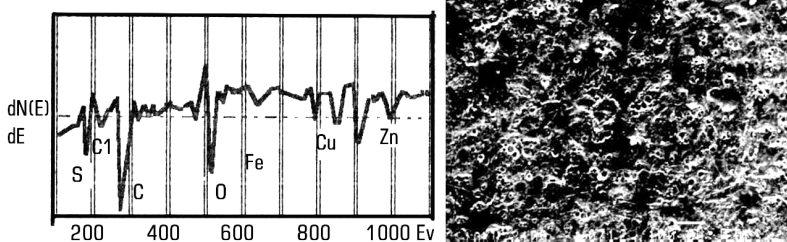


Fig. 5.9 Auger spectra of the surface of samples 2–4 of steel 45 (0.45 % C) treated by plasma with an addition of vapors of copper+zinc alloy ($D=40$ mm, $h=35$ mm)

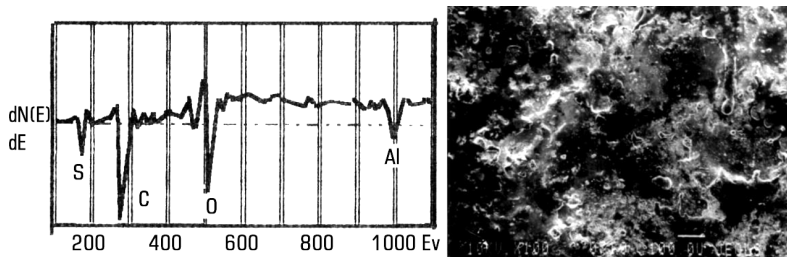


Fig. 5.10 Auger spectra of the surface of samples 2–4 of steel 45 (0.45 % C) treated by plasma with an addition of aluminium vapors ($D=40$ mm, $h=35$ mm)

Carbon peaks are especially intensive in dark regions of the COMPO image (spectrum 2) for samples subjected to PDT by introducing an eroding electrode of alloy Kh18N9T (18 % Cr, 9 % Ni, 1 % Ti, 72 % Fe) to the plasmatron. Also, there are regions with almost no iron and with a weak oxygen peak.

Analysis of the surface of samples after PDT with a molybdenum electrode introduced to the plasmatron indicates a bright light phase present on the surface, which is molybdenum heavily saturated with carbon and oxygen and slightly saturated with nitrogen. Molybdenum is present in this sample in a combination with iron. X-ray spectroscopy using the "Superprobe" unit showed approximately 5 at. % of molybdenum present in the sample matrix at a depth of a few microns.

After PDT of steel U8A (0.8 % C) by plasma with titanium vapors at $h=15$ mm, the Auger spectra of different surface regions show the presence of titanium and nitrogen peaks. It can be seen that titanium is always present in a combination with iron.

Intensity of iron peaks is decreased and intensity of carbon peaks is increased in dark regions of the sample surface (**Fig. 5.8**).

In Auger spectra of the surface of sample treated by plasma with titanium vapors at $h=35$ mm the carbon peak is most intensive, the titanium and nitrogen peaks are markedly weaker and are seen not in all the regions, and the dark spots consist almost entirely of carbon.

Therefore, preferential deposition of titanium and nitrogen on the sample surface, compared with carbon, is seen only in PDT with $h=15$ mm. It can be assumed that a deeper immersion of the eroding electrode into the reaction chamber of the plasmatron makes titanium atoms leave behind lighter carbon atoms in a shock wave in PDT. Microstructure of transverse sections is shown in **Fig. 5.11**.

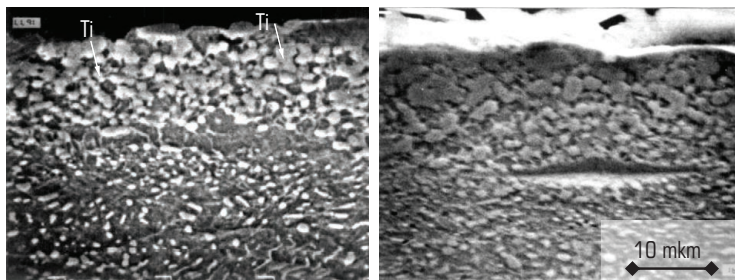


Fig. 5.11 Microstructure of transverse sections of samples of steel U8 (0.8 % C) (batch 2) after PDT with an addition of titanium to plasma ($D=60$ mm, $h=15$ mm, $N=5$).

The photos are made using scanning electron microscope

The examination results obtained using the light microscope "Neophot-2" and scanning electron microscope T-20 fully coincide. It can be seen that the sub-surface layer is characterized by the presence of a large amount of white globular formations up to $3.5 \mu\text{m}$ in size.

The samples hardened at a distance of 60 mm are characterized by the presence of globular formations of a large size and the widest region of their propagation through thickness. Increasing the distance leads to decrease in thickness of the layer and reduction in size of the globules. The sample treated at minimum possible intensities contains almost no globular structure. Structure

of this sample hardly differs from that of the matrix. A thin film of deposited material, i.e. products of plasma-chemical synthesis of the plasma material, is seen on the surface of the hardened structure. In PDT of steel U7 (0.7 % C) a nano-crystalline layer (white, non-etchable) with microhardness of 5800 to 8500 MPa is formed on the sample surface (**Fig. 5.12**). As the quantity of pulses is increased (from 5 to 15), thickness of this nano-crystalline layer grows to 25 μm . The white layer is followed by the heat-affected zone with microhardness of 4800 to 2500 MPa.

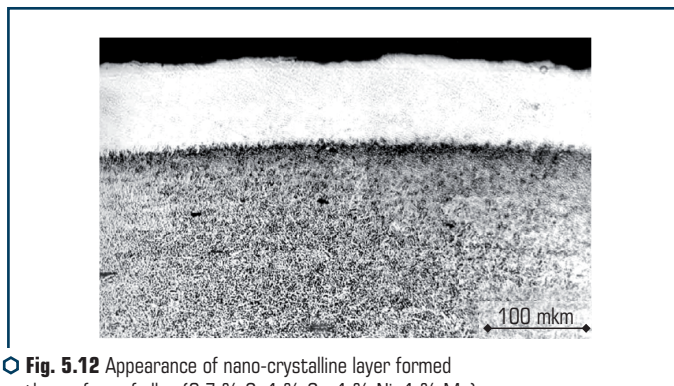


Fig. 5.12 Appearance of nano-crystalline layer formed on the surface of alloy (0.7 % C, 1 % Cr, 1 % Ni, 1 % Mo) sample after PDT by pulsed plasma (5 pulses)

Microhardness of the substrate at a depth of more than 120 μm is 1800 MPa. Formation of the nano-crystalline layer is especially pronounced on the samples of carbon alloy U10 (0.10 % C), which were subjected to PDT with an addition of tungsten vapors at 1, 5 and 10 plasma pulses. Uniform non-etchable "white" layers 23, 32 and 43 μm thick, respectively, are formed on the sample surfaces.

X-ray microanalysis of the sample surfaces using the "Cameca-546" device was performed to identify the hardened layer. The following conclusions can be made from the analysis results: after treatment with one pulse a thin layer of pure tungsten (consumable electrode material) is formed on the surface of the hardened layer, and there is another layer (up to 10 μm thick) of solid solution of tungsten in iron. The multi-pulse plasma treatment results in full dissolution of tungsten in the upper layer of the sample to form a new alloy with a tungsten content of 10–18 %.

5.2 MODIFICATION OF MEDIUM-CARBON ALLOYS

Experimental verification of the efficiency of modification was performed on alloys with a carbon content of up to 0.4 %. As shown by analysis, the acicular structure persists in the initial state of alloy 40X (0.4 % C, 1.0 % Cr) and its structure after PDT (**Fig. 5.13, a**). After PDT the

general character of structure remains fine-acicular and banded (**Fig. 5.13, b**), while both types of the structures have dark marks of carbide precipitates.

Pulsed-plasma hardening is provided by super rapid cooling of the workpiece surface alloyed in the melt. Smearing of the boundaries of clusters and their "freezing" through overcooling lead to formation of meta-stable structures with extremely intensive refining of structural element. This is demonstrated both by transmission electron microscopy and examination of the type of fracture (**Fig. 5.14**).

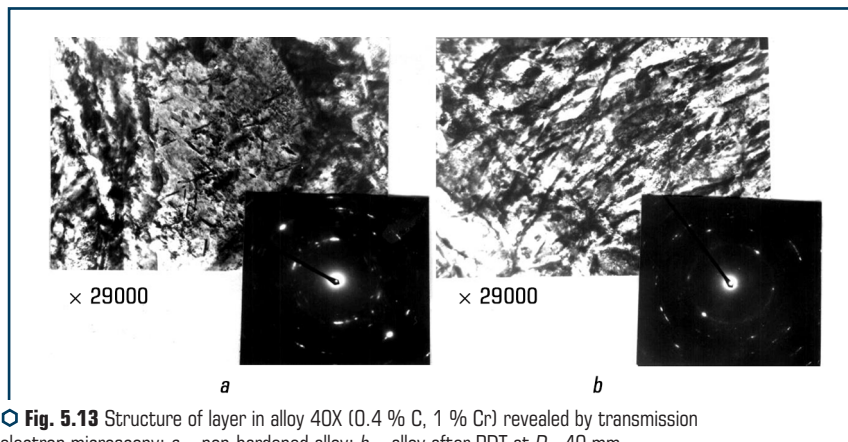


Fig. 5.13 Structure of layer in alloy 40X (0.4 % C, 1 % Cr) revealed by transmission electron microscopy: *a* – non-hardened alloy; *b* – alloy after PDT at $D=40$ mm, $h=15$ mm, $N=3$, Mo electrode

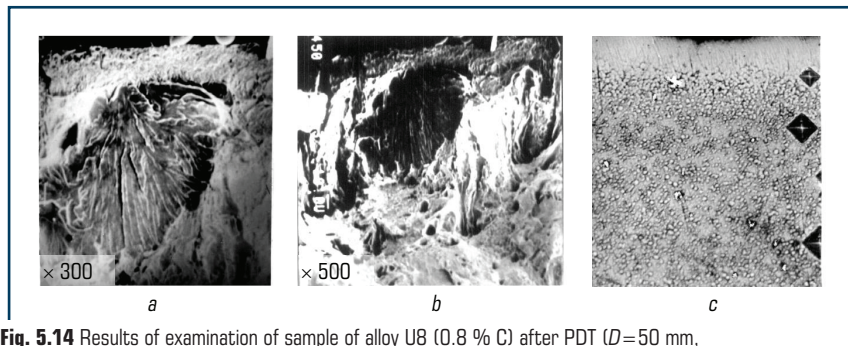


Fig. 5.14 Results of examination of sample of alloy U8 (0.8 % C) after PDT ($D=50$ mm, $h=15$ mm, $N=8$, $C=800$ μ F, Mo electrode): *a* and *b* – fracture surface; *c* – cross section

The samples were quenched prior to hardening, which provided dispersed structure of the alloy (**Fig. 5.13, c**). Analysis of the type of fracture of a sample hardened by PDT shows (**Fig. 5.14, a, b**) that the fractured hardened layer has a fine-crystalline structure with a coarse-grained cleavage located under the layer along the crystal boundaries of base metal. The fracture is of a tough character.

Refining of structure after PDT to a nano-crystalline state is evidenced by formation in the electron diffraction pattern of an almost continuous thin ring corresponding to the α -Fe reflexes (110) (**Fig. 5.13, c**).

X-ray phase analysis reveals retained austenite in the modified layer (**Tables 5.1, 5.2**). As seen from the Tables, the intensity of the austenite lines grows with intensification of PDT, and in the case of using the Mo electrode the growth is somewhat higher than in the case of using the stainless steel electrode. Radiography revealed another interesting phenomenon – dramatic decrease in the ratio of the intensities of the α -Fe lines (110) compared with those of the α -Fe lines (200) (**Tables 5.1, 5.2**).

● **Table 5.1** Ratio of integrated intensities of X-ray α -Fe and γ -Fe lines after PDT of steel 40X

No.	Electrode material	N, pulse	$I_{(110)\alpha}$	$I_{(200)\alpha}$	$I_{(211)\alpha}$	$I_{(220)\alpha}$	$I_{(111)\gamma}$	$I_{(200)\gamma}$	$I_{(220)\gamma}$	$I_{(311)\gamma}$	$I_{(110)\alpha}/I_{(200)\alpha}$	$I_{(220)\gamma}/I_{(200)\alpha}$
1	18 % Cr, 9 % Ni, 72 % Fe	3	50.1	4.3	10.3	3.5	6.4	1.7	1.2	0.9	11.6	0.40
2		8	23.3	2.1	4.7	1.4	3.3	1.2	0.1	0.6	11.1	1.75
3	Mo	3	95.1	5.9	18.6	7.1	2.9	0.6	0.3	0.3	16.1	0.1
4		8	21	2.1	3.7	1.2	11.4	2.1	0.9	0.9	10.0	1
5	W	3	61.5	6.2	11.4	3.4	5.2	1.4	0.6	0.6	9.92	0.22
6		8	15.2	20	3.7	1.2	11.7	3.8	1.3	1.2	4.11	1.90
7	Quenched	–	2.12	1.7	3.7	1.2	–	0.9	0.3	0.5	12.4	0.53
8	Initial	–	100	5.1	14.7	7.3	–	–	–	–	19.6	–

● **Table 5.2** Ratio of integrated intensities of X-ray α -Fe and γ -Fe lines after PDT of steel 45 (0.45 % C)

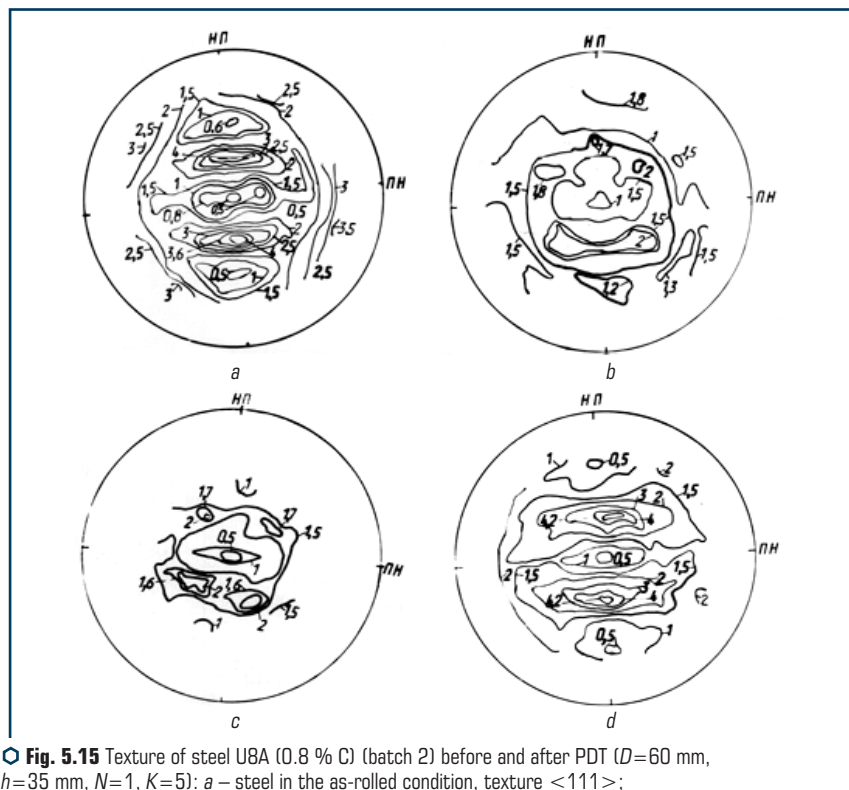
Sample No.	Electrode material	N, pulse	D, mm	H, mm	$I_{(110)\alpha}$	$I_{(220)\alpha}$	$I_{(200)\alpha}$	$I_{(110)\alpha}/I_{(220)\alpha}$	$I_{(200)\alpha}/I_{(220)\alpha}$
1	Titanium	1	60	15	69.5	8.8	0	7.9	0
2			40		53.3	7.0	1.2	7.6	0.17
3			20		51.8	10.6	1.3	4.9	0.12
4		5	60		70.0	10.4	1.7	6.7	0.16
5			40		48.3	8.0	4.2	6.0	0.52
6			20		38.7	7.2	7.5	5.4	1.54
7	Initial	–	–	–	83.8	9.6	0	8.7	0

Initial – alloy base, untreated

It is known that evolution of the crystallographic texture occurs in phase recrystallization under the rapid cooling conditions and at the presence of a high temperature gradient. It is also known

that preferred orientation of boundaries $\langle 001 \rangle$ along the temperature gradient takes place under these conditions for crystalline materials with a cubic lattice, which shows up as a relative growth of the (200) line intensities.

Quenched – sample after volumetric thermal quenching, without subsequent treatment. Initial – alloy base, without treatment. Formation of such a texture was proved by recording of straight pole figures (Fig. 5.15).



○ Fig. 5.15 Texture of steel U8A (0.8 % C) (batch 2) before and after PDT ($D=60$ mm, $h=35$ mm, $N=1$, $K=5$): *a* – steel in the as-rolled condition, texture $\langle 111 \rangle$; *b*, *c* and *d* – texture of a sample after PDT, texture of hardened steel is close to $\langle 001 \rangle$; *b* – Mo electrode; *c* – W electrode; *d* – Ti electrode

It can be seen by an example of steel U8 (0.8 % C) how dramatic is the change in the crystallographic texture of the sub-surface layer after PDT. The formed texture exhibits symmetry of the 4th order in location of maxima of the poled density, which is characteristic of the $\langle 001 \rangle$ orientation along the normal to the surface. For alloy α -Fe without texture, the intensity ratio I_{110}/I_{200} is 6.34. In the initial samples of steels 40X (0.4 % C, 1 % Cr) and 45 (0.45 % C) (polished

surface) the intensity ratio is a bit higher (about 9) because of the possible contribution by texture $\langle 110 \rangle$ formed both in drawing and polishing. After PDT it falls approximately to 3.

Preferred orientation of the same type is formed also in austenite of the modified layer. This shows up as a dramatic decrease in the intensity of line (111), compared with line (200). It is likely that this phenomenon should introduce a substantial error into the amount of retained austenite estimated from the X-ray data, for which the intensities of lines (110) and (111) are normally used.

Because of the identical character of texture, the ratio of the intensities of lines (220) and (220) given in **Tables 5.1, 5.2** must be more informative. Volume fraction of retained austenite, $V\alpha$, should be estimated from this ratio using the following formula:

$$V\alpha = 3I_{200}\gamma / (3I_{200}\gamma + 5I_{200}\alpha).$$

Table 5.3 gives estimates of the amount of retained austenite for steel 40X (0.4 % C, 1 % Cr) after PDT with molybdenum added to plasma. It can be seen that the content of austenite in the surface layer after PDT may amount to 50 %, which is much higher than in the sample after hardening in furnace. This is likely to be caused by a higher heating temperature, as well as by a probable stabilization of austenite with alloying elements added to plasma.

● **Table 5.3** Estimation of amount of retained austenite in steel 40X (0.4 % C, 1 % Cr) after PDT using Mo electrode (numbers of samples correspond to those in **Table 5.1**)

Sample No.	$V\alpha = 3I_{200}\gamma / (3I_{200}\gamma + 5I_{200}\alpha)$
3	9
4	38
7 – quenched	14
Quenched – sample after volume thermal quenching without subsequent treatment	

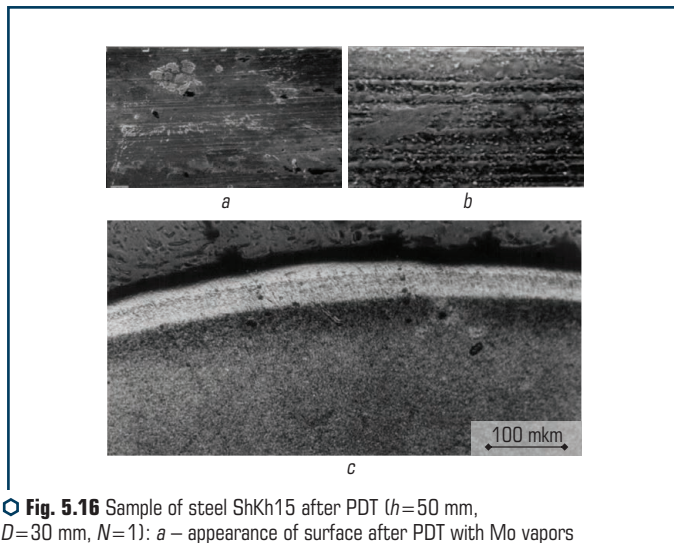
X-ray phase analysis after the intensive PDT conditions revealed, in addition to austenite, also the lines of iron oxides FeO and Fe₃O₄. But they are always much weaker than the α -Fe and γ -Fe lines. The lines of titanium nitride were detected in samples of steels treated with the Ti electrode (**Fig. 5.8**). The lines of copper and zinc were detected in the case of bronze added to plasma (**Fig. 5.9**), and the lines of aluminium were revealed in the case of aluminium added to plasma (**Fig. 5.10**).

Analysis of the sample after PDT shows that the metal phase is non-uniformly distributed over the surface after one plasma pulse. Increase in the quantity of pulses provides a uniform distribution of alloying elements in the surface layer of the sample.

As shown by investigation of physical widening of the X-ray diffraction lines, widening of both α -Fe and γ -Fe lines after intensive PDT can be considered proportional, which is indicative of the dominating contribution to widening by heterogeneous elastic distortions of the $\Delta a/a$ lattice. These distortions can be related both to elastic strains caused by dislocations and/or coherent

bond of particles of different phases, and to a non-uniform distribution of alloying elements, and carbon in particular. It is impossible to distinguish contributions made by these defects from the experimental data.

Scanning electron microscopy was performed to examine the surface of the hardened samples (**Fig. 5.16**). Analysis of appearance of sample surfaces shows that under comparatively soft conditions of PDT ($D=50$ mm, $h=30$ mm, $C=800$ μ F, 3 pulses) the surface roughness is uniformly fused in the case of the molybdenum electrode introduced to the plasmatron and is not fused in the case of the stainless steel electrode. Clearly defined grinding grooves persist on the surface (**Fig. 5.16, b**).



○ **Fig. 5.16** Sample of steel ShKh15 after PDT ($h=50$ mm, $D=30$ mm, $N=1$): *a* – appearance of surface after PDT with Mo vapors added to plasma; *b* – appearance of surface after PDT with stainless steel vapors added to plasma; *c* – transverse section of sample

This proves the fact that the plasma pulse energy substantially grows with an addition of heavy metals (W, Mo). Analysis of the transverse section (**Fig. 5.16, b**) indicates that the hardened layer is characterized by the presence of three lines of structural changes, which seem to correspond to three heat flows during the pulsed treatment process.

Enhancement of the pulse energy in PDT is caused by the fact that the process grooves due to abrasive treatment vanish, while drops, pores and a small amount of cracks are present on the surface (**Fig. 5.16**).

Individual drops consisting of the electrode material are also formed on the surface under the softest PDT conditions. The amount of the electrode material increases with growth of the PDT intensity. Metal spreads over the surface (**Fig. 5.17**).

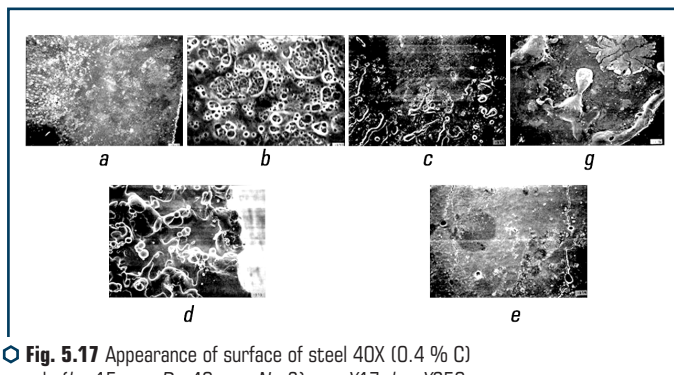


Fig. 5.17 Appearance of surface of steel 40X (0.4 % C) sample ($h=15$ mm, $D=40$ mm, $N=3$): *a* – X17, *b* – X250, *d* – X1000; $N=5$: *c* – X35, *g* – X100, *e* – X175. T-20 recording

It is seen that carbon is concentrated in pores. Intensification of treatment of the surface provides periodical deposition of the electrode material and its propagation into the sample surface being hardened. Cracks are formed along the boundaries of the fused layer (Fig. 5.17), which confirms an assumption of deformation of alloy during solidification.

Auger spectroscopy of transverse sections proves increase in the concentration of carbon in pores between alloying metal drops in the modified layer (Fig. 5.18).

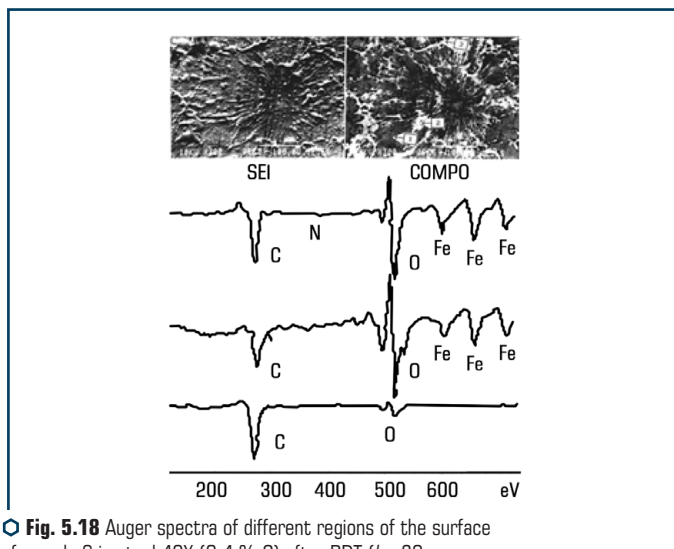


Fig. 5.18 Auger spectra of different regions of the surface of sample 6 in steel 40X (0.4 % C) after PDT ($h=30$ mm, $D=30$ mm, $N=5$, Cr18N9T electrode)

5.3 MODIFICATION OF SURFACE OF HIGH-SPEED STEELS

5.3.1 PDT IN AIR ATMOSPHERE

High-speed tool alloys have an extensive engineering application. These alloys are used to manufacture cutting tools and critical machine parts. Numerous studies on optimization of chemical composition of these alloys provided high performance of parts made from them.

Given that performance of the majority of parts is limited by physical-mechanical properties of the surface, surface modification using PDT is of high practical interest.

Investigation into the mechanism of modification of surfaces of high-speed steels was carried out on tungsten-free alloys 11M4F2YuD (1.1 % C, 4 % Cu, 2 % V, 1 % Al) and alloy R6M5 (0.85 % C, 6 % W, 5 % Mo, 4 % Cr, 2 % V) [74, 143–148, 236–238]. It was shown that laser treatment of an alloy without surface fusion led to a substantial growth of the content of retained austenite, amounting to 60 % (45 % in alloy R6M5). Profiles of the diffraction lines are indicative of a considerable heterogeneity of solid solution as to the content of carbon. This is caused by high heating and cooling rates characteristic of laser treatment.

The optimal value of the radiation power density is selected on the basis of structure of a material in the irradiated zone, which should be a martensite and carbide mixture formed as a result of secondary hardening occurring under the energy pulse effect.

Deviation from optimal parameters leads to loss in strength and deterioration of service properties of parts made from tool alloys. The time of exposure to radiation was found to affect the amount of retained austenite. Thus, at $t=1.5$ and 8 ms the amount of the α -phase detected in structure is 15 %. The structure also contains secondary carbides, the amount of which increases with time.

Preliminarily quenched samples of an alloy were subjected to radiation without fusion. The time of exposure was 3 ms. Tests of the tools hardened by this technology showed a 3–5 times increase in their performance. At a given energy density of the treatment no fusion of the surface was seen, but the formation of a maximal amount of secondary carbides was detected.

Secondary hardening results in the formation of martensite with an increased content of carbon and alloying elements. The cause is saturation of solid solution and partial dissolution of carbides. Increase in hardness and wear resistance of an alloy occurs only in the cases where the pulse power density is in a range of $1 < Wp < 5 \cdot 10^5$ W/cm² at an exposure time of $t=3-5 \cdot 10^{-3}$ s. The highest effect is achieved at a power density of $5 \cdot 10^5$ W/cm², providing the limiting surface temperature close to the melting point.

Deviation from optimal parameters may result in loss in strength and deterioration of service properties. The efficiency of hardening of tools was checked on cutters made from alloy R6M5. The experiment was conducted by turning cylindrical samples of a medium alloy. Rear edges of the cutters were hardened with one pulse using the "Kvant 16" unit. Their wear resistance increased from 3 to 5 times.

Characteristic peculiarity of structure of the workpiece surface after pulsed hardening is its capability of retaining hardness in heating during the friction process.

Analysis of the investigation results on laser treatment indicates that treatment of the preliminarily hardened samples of alloy R6M5 (0.85 % C, 6 % W, 5 % Mo, 4 % Cr, 2 % V) increases strength of the tools from 3 to 5 times. PDT of the samples was performed in air without surface fusion. Studies were conducted on the following batches of the samples. Batch 1 (**Table 5.4**) was treated by pulsed plasma with an addition of alloying metals from eroding electrodes: stainless steel Kh18N9 and molybdenum. The distance from the plasmatron to a sample, D , and immersion of electrode, h , for all the samples were identical and equal to 50 and 15 mm, respectively.

In PDT of the samples (batch 1) the visible diameter of a treatment spot was 15 mm. Treatment was performed by rotating a sample. Fourteen treatment pulses were made per revolution of a sample. Frequency of the treatment was 1.6 Hz. Duration of a treatment pulse was about 10^{-3} s. Diameter of a sample was 40 mm.

Prior to PDT, all the samples were subjected to standard heat treatment (quenching + tempering) and then abrasive treatment (grinding). Grinding provided removal of a defective layer formed after heat treatment from the surface. After that the sample surfaces were subjected to PDT under different process conditions. Sample 8 was used as a reference. It was not subjected to PDT.

Samples of batch 2 were treated by adding titanium to plasma and by changing the distance to the sample surface, increasing immersion of the electrode and varying the number of pulses (**Table 5.5**).

To illustrate, **Fig. 5.10** shows appearance of the surface of sample 5 and its Auger spectra.

● **Table 5.4** Parameters of plasma-detonation treatment of samples (batch 1)

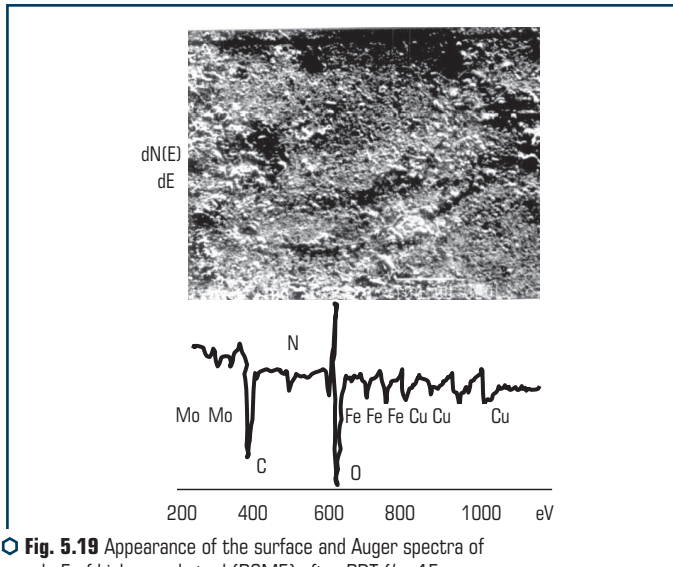
Sample No.	<i>D</i> , mm	<i>h</i> , mm	Q-ty of pulses	Q-ty of revolutions	Electrode material	Notes
2	50	15	14	1	Cr18Ni9	Without rotation
13			40	3		With rotation
4			14	1	Mo	
5			40	3		
8			Reference (quenching + tempering, grinding after heat treatment)			

● **Table 5.5** Parameters of plasma-detonation treatment of samples (batch 2)

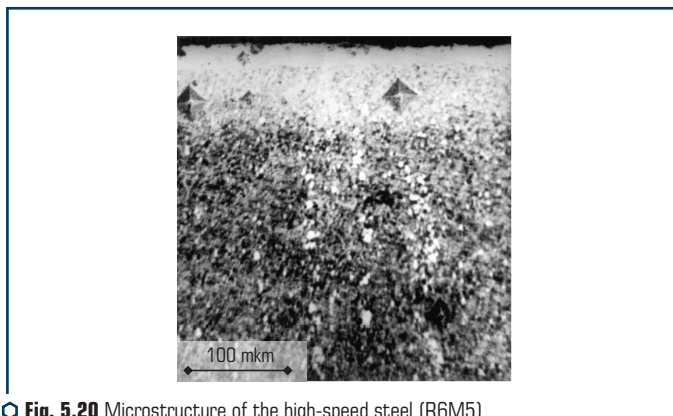
Sample No.	Distance to sample, mm	Immersion of electrode	Electrode material	Overlapping coefficient
10	30	15	Ti	5
11	60	35		10
12	10			

The surface of sample 13 after PDT (Cr18Ni9 electrode, $H=50$ mm, $h=15$ mm, 3 turns) is rough, i.e. it is characterized by the presence of traces of primary treatment (grinding), whereas the surface of sample 5 (molybdenum electrode, 3 turns, $D=50$ mm, $h=15$ mm) has no traces of primary treatment.

This is indicative of the fact that the intensity of PDT of the surface of sample 13 was lower. As seen from the Auger spectra, the surface of sample 13 exhibits, in addition to iron, carbon and oxygen, also a small amount of copper and zinc. Molybdenum, nitrogen and copper can be seen in spectrum of sample 5, in addition to iron, carbon and oxygen (**Fig. 5.19**). Microstructure of the hardened layer was examined on transverse sections after etching (**Fig. 5.20**).



◉ **Fig. 5.19** Appearance of the surface and Auger spectra of sample 5 of high-speed steel (R6M5) after PDT ($h=15$ mm, $D=50$ mm, $N=6$, molybdenum electrode)



◉ **Fig. 5.20** Microstructure of the high-speed steel (R6M5) layer hardened by PDT (molybdenum electrode, 6 pulses)

Structure of the surface after PDT consists of a poorly etchable light layer (PDT with stainless steel electrode) or unetchable white layer (PDT with titanium electrode). Structure of the surface layer after PDT with the molybdenum electrode may consist of two layers: the first layer directly adjoining the surface is the unetchable white layer, and the second layer is the poorly etchable one. Depths of the modified layer after PDT are given in **Table 5.6**.

● **Table 5.6** Depth of the PDT hardened layer

Sample No.	2	13	4	5	10	11	12
Layer depth, μm	27	27	27	30	14	23	40

Of notice is heterogeneity of the hardened layer through thickness, and even the absolute absence of this layer in some regions of the samples, sometimes even in the cases where a sample was treated with a 10-fold overlapping (sample 11) at a distance to it equal to 95 mm. The electrode was titanium. In the case of treatment with the molybdenum electrode at its distance to a sample equal to 60 mm, heterogeneity of the treated layer depends upon the overlapping factor. In the case where the overlapping factor is 3, the hardened layer is present on the entire sample surface. As the overlapping factor increases, the layer becomes more homogeneous through thickness. Maximal thickness of the hardened layer hardly depends upon the overlapping factor.

Samples were examined in MoK α radiation using the X-ray device DRON-3M. Identification of the X-ray patterns showed that plasma-detonation treatment causes the following changes in phase composition of the hardened layer: (a) the amount of austenite grows (samples 5, 10, 11, 12). This amount can be determined from the ratio of height of the α -Fe peak (002) to that of the peak which is superposition of lines 110 and 111 for the MoK α radiation, or from the ratio of surface areas of these peaks:

(a) the amount of carbides Mo₆C grows (samples 4, 5);

(b) iron oxide Fe₃O₄ is formed (samples 2, 13, 4, 10);

(c) after intensive treatment by plasma with an addition of titanium, the lines of titanium nitride TiN and titanium carbide TiC can be seen in the X-ray patterns. Also, titanium deposited in a small amount can be seen (sample 12).

The depth of penetration of X-rays for MoK α and CoK α radiation was calculated. For different reflection angles in MoK α radiation it ranges from about 4 μm for angles close to reflection of 222 γ -Fe, and from about 6.5 μm for angles close to reflection of 110 iron to about 13 μm for angle close to reflection of 220 γ -Fe in CoK α radiation. As the lines of different phases used for approximate quantitative analysis are located near 110 α -Fe, we may say that the quantitative ratios given in **Table 5.7** reflect the proportion of phases in a layer lying at a distance of 0 to 5 μm from the surface.

Microhardness was determined using the Knoop hardness meter (load 20 g, as well as using the Vickers hardness meter (load 50 g). Measurements were made on transverse sections

after etching. Regions in which the depth of the treated layer was maximal were selected for measurement of microhardness. Samples treated with an overlapping factor of 3 and higher exhibit increase in microhardness to 10.5–11.2 GPa, the initial microhardness being 9.2 GPa. For samples treated by plasma with an addition of stainless steel and molybdenum and with an overlapping factor of 3, the initial hardness values were reached at a distance of 75–120 μm from the surface. In samples treated with the molybdenum electrode and an overlapping factor of 3, at a distance of 5 mm from the surface there was a decrease in microhardness below the initial value, i.e. to about 7.2–7.8 GPa, despite a substantial growth of the amount of carbide phases in this layer (**Table 5.7**). Samples treated with the titanium electrode exhibit increase in hardness in the sub-surface layer to about 11.1–11.25 GPa.

● **Table 5.7** Ratio of intensities of lines for different treatment conditions

Sample numbers						
2	13	4	5	10	11	12
Composition of electrode and its extension from the reaction chamber, mm						
18 % Cr, 9 % Ni, 73 % Fe, $h=15$		Mo, $h=15$		Ti, $h=15$	Ti, $h=35$	
Plasma treatment distance, mm						
50				30	60	
Quantity of treatment pulses						
3		1	3	5	10	10
$\text{MoK}\alpha, h_{002\gamma}/(h_{110\alpha}+h_{111\gamma})$						
0.05	0.03	0.02	0.18	0.11	0.11	0.01
$\text{CoK}\alpha, S_{111\gamma}/S_{110\alpha}$						
—	0.08	—	0.42	1.6	0.12	0.13–0.63
$\text{XoK}\alpha, S_{\text{MoC } (d=2.12)}/S_{110\alpha}$						
—	0.02	—	0.62	0.14	0.43	0.35–0.54
$\text{CoK}\alpha, S_{\text{Fe304 } (d=2.966)}/S_{110\alpha}$						
—	0	—	0.15	0	0.19	0.05–0.09
$\text{CoK}\alpha, S_{\text{TiN } (d=2.44)}/S_{110\alpha}$						
—	0	—	0	0.40	0.05	0.07
$\text{CoK}\alpha, S_{\text{TiC } (d=2.18)}/S_{110\alpha}$						
0	0	0	0	0.11	0	0
$\text{CoK}\alpha, S_{\text{Mo2C+Mo2N+VC } (d=2.38-2.41)}/S_{110\alpha}$						
0	0	0	0.16	0	0	0
$\text{CoK}\alpha, S_{\text{FeCrMo } (d=2.13)}/S_{110\alpha}$						
0	0	0	0.13	0	0	0

In addition, in sample 10 treated under the most intensive PDT conditions the maximal hardness was achieved at a distance of 20 μm from the surface. At a distance of 5 mm from the surface the value of hardness decreased. Nevertheless, in contrast to samples treated with the molybdenum electrode it remained a bit higher than the initial one.

In sample 11 hardened under more moderate conditions, compared with sample 10, the maximal value of hardness, i.e. 11.25 GPa, is achieved near the surface (at a distance of 5 μm). Upon reaching the maximum, hardness of the samples treated by plasma with an addition of titanium falls in a wavy manner and reaches initial values at a distance of 60–70 μm from the surface. Maximal hardness of sample 11 corresponds to the following phase proportion: comparatively low amount of austenite (line intensity ratio 0.12) and substantial increase in carbide M_6C (line intensity ratio 0.43). Sample 10 that exhibited decrease in hardness at a distance of 5–15 μm from the surface contains very much austenite, i.e. more than ferrite (line intensity ratio 1.6) at a substantial amount of nitride and carbide phases (line intensity ratios 0.40 and 0.14).

Therefore, along with the hardening processes, also the processes leading to decrease in hardness and loss in strength are developed under intensive treatment conditions.

Decrease in hardness and loss in strength may be caused by decrease in the content of carbon in solid solution resulting from its consumption for formation of carbides, as well as by a large amount of austenite.

It is likely that increase in the intensity of treatment accelerates diffusion, which favours formation of carbide (M_6C) and a large amount of austenite, thus leading to loss of strength. Formation of carbide (M_6C) under optimal treatment conditions occurs probably due to diffusion of carbon from plasma.

No loss of strength in a layer 5 μm deep takes place in a sample after PDT with the titanium electrode. This is attributable to the fact that titanium actively combines with nitrogen to form titanium nitride (TiN) and absorbs less carbon from solid solution than molybdenum.

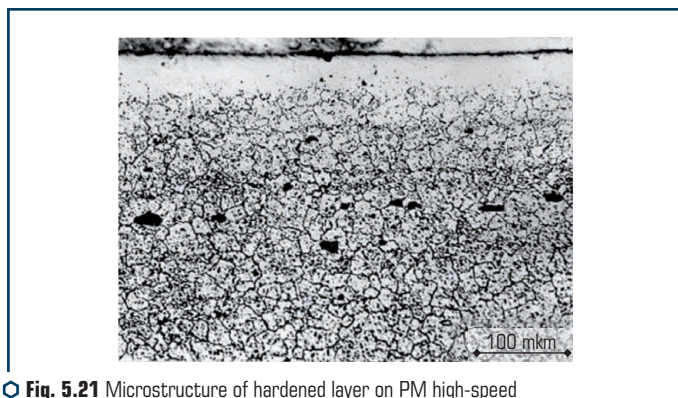
5.3.2 TREATMENT IN NITROGEN ATMOSPHERE

Samples of steel R6M5 (0.85 % C, 6 % W, 5 % Mo, 4 % Cr, 2 % V) were subjected to PDT in nitrogen atmosphere. Initial structure of the high-speed alloy was a fine-grained ferrite – carbide mixture. Fine grains of ferrite alternate with dispersed carbides of complex composition. Mean microhardness of the alloy is 6.0–6.5 GPa. According to the X-ray phase analysis data, the alloy contains a small amount the $\gamma\text{-Fe}$ phase (**Table 5.8**).

Microstructure of surface layers of the samples changed as a result of the pulsed-plasma treatment in nitrogen atmosphere. Non-etchable or poorly etchable layer, or both, can be seen on the surface (**Fig. 5.21**). Thickness of the layers with a changed structure is 20–30 μm and mean microhardness is 5.25–5.80 GPa.

● **Table 5.8** Treatment parameters and properties of modified layer on steel R6M5

Sample No.	Distance D, mm	Quantity of pulses, N	Thickness, μm	Hardness, GPa	Phase composition of modified layer
13	40	3	20	5.59	Fe- α , Fe- γ , M_0C , $\gamma\text{-Fe}_2\text{O}_3$, Fe_3O_4 , Fe_2O_3 , Fe_2N
15	70	15	20–30	5.25	Fe- α , Fe- γ , M_0C , Fe_2N
14	90	20	20–30	5.42	Fe- α , Fe- γ , M_0C , Fe_2N , $\gamma\text{-Fe}_2\text{O}_3$, Fe_3O_4 , Fe_2O_3
16	110	15	20	5.8	Fe- α , Fe- γ , M_0C , Fe_2N , $\gamma\text{-Fe}_2\text{O}_3$, Fe_3O_4 , Fe_2O_3



○ **Fig. 5.21** Microstructure of hardened layer on PM high-speed steel (R6M5) after PDT, molybdenum electrode, 6 pulses

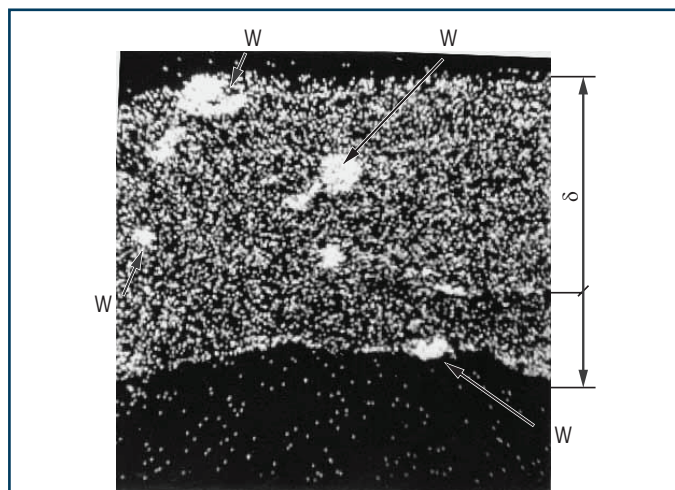
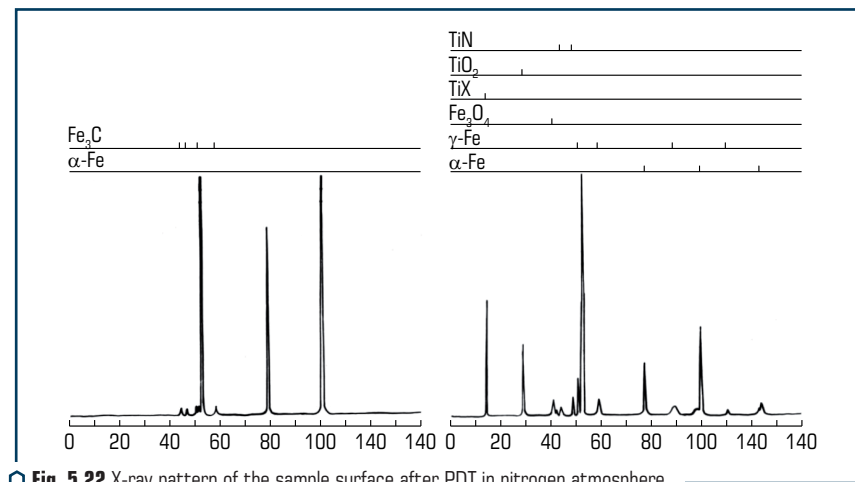
In PDT at a distance of 40 mm the molten layer 20 μm thick is formed on the surface. This layer solidifies to form structure of the martensitic type, and the amount of retained austenite in the layer grows. Also, small amounts of oxides and iron nitride Fe_2N can be seen on the surface. Mean microhardness of the layer is 5.59 GPa (**Fig. 5.22**).

According to the X-ray microanalysis, regions with an increased W content are revealed in the modified layer after PDT with the tungsten electrode (distance – 40 mm) (**Fig. 5.23**).

Also regions with partial dissolution of complex carbides (MoC) of steel R6M5 are detected. In this case the amount of W and Mo in matrix of the molten region increases from 3.54 to 4.95 and from 3.47 to 4.92 at. %, respectively.

The layers up to 30 μm thick are also formed on the surface with increase in the treatment distance to 70–90 mm (at 15 and 20 pulses, respectively), but their phase composition differs from the previous one. The main phase is nitrous austenite, despite the fact that PDT at a distance of 70 mm led to fusion of the surface, and at a distance of 90 mm the surface was not fused. Nitrogen (atmosphere), being a strong austeniser, does affect. Small amounts of iron oxides and nitrides (complex oxide FeWO_4 , Fe_2N) are formed on the surface. Microhardness of layers with a modified structure is shown in **Fig. 5.24**. PDT conditions are given in **Table 5.8**.

Increasing the distance to 110 mm (15 pulses) leads only to a partial modification of structure. It becomes less etchable, and partial dissociation of carbides takes place. Thickness of the modified layer is about 20 μm , and its microhardness is 5.8 GPa. The main phase is $\alpha\text{-Fe}$, and the $\gamma\text{-Fe}$ content is larger than in the base metal. A considerable amount of iron oxides is revealed on the surface. It is likely that oxygen from air has access to the treatment zone.



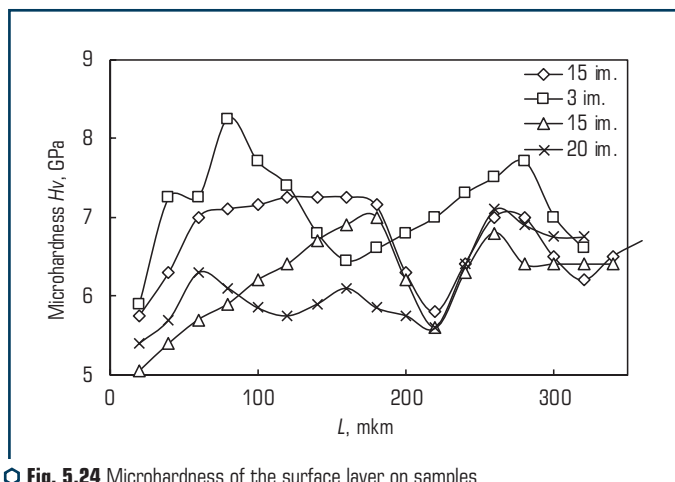


Fig. 5.24 Microhardness of the surface layer on samples of alloy R6M5 after pulsed plasma treatment

According to the X-ray microanalysis, the surface layer contains an increased amount of *N* and *W*. The content of carbon in carbides decreases to some extent because of their partial dissociation.

5.4 HARDENING BY PLASMA TREATMENT

Plasma hardening has found wide application recently for tool alloys. Reported [218, 239–243] are studies of peculiarities of phase and structural transformations taking place in different alloys during plasma hardening. Structural and low tool alloys were investigated. Initial state of the alloys was the as-received (normalized) one. Parameters of plasma hardening were selected by calculations followed by experimental optimization of the technology (Table 5.9).

Table 5.9 Hardening parameters and hardness of alloys [218]

Alloy	Hardening parameters (PT) parameters*				Hardness, HV		
	$T_h, ^\circ\text{C}$	Environment	I, A	$V, 10^{-3} \text{ m/s}$	Initial	After hardening	After PT
0.45 % C	850	Water	420	5.6	165–180	620–635	805–815
0.5 % C, 1 % Cr, 1 % Ni	850	Oil	400	5.6	195–210	665–680	840–855
0.65 % C, 1 % Mn,	850			7.0	200–225	690–705	835–850
0.8 % C	800			7.0	205–220	740–755	865–885
0.9 % C, 1 % Cr, 1 % V	850			7.0	235–260	750–765	880–900

*Variations in $U=f(I)$ correspond to volt-ampere characteristic of the plasmatron [218]

Electric arc and electroslag cladding of tool alloys are widely applied now for repair of industrial equipment. These alloys are also utilized for repair of tools. Below we give information on plasma hardening treatment of deposited alloys for rolling mill rolls and metallurgical equipment components [239, 240].

Reconditioning of some types of hot rolls and other rolling equipment components is performed by depositing a layer of alloyed steel 30KhGSA (0.3 % C, 1 % Cr, 1 % Si, 1 % Mn) [241–243] (type A according to the IIV classification). As proved, plasma hardening causes changes in structure and performance of deposited metal. Its wear resistance doubles. The deposited metal is subjected to volume and surface hardening by plasma, involving fusion of the surface. At the same time, because of the absence of carbide-forming elements in alloy composition and, thus, absence of a hardening carbide phase in structure, heat resistance of the deposited metal even in the hardened state is low.

As applied to hot rolls, alloys of the martensite-carbide grade, i.e. Cr-W-V and Cr-Mo-V, categorized as *H* type according to the IIV classification, provide a good combination of service properties. Alloy of the Kh5MF type (1 % C, 5 % Cr, 1 % Mo, 1 % V) has a sufficiently high wear and heat resistance (up to a temperature of 500 °C) and high toughness. In this connection, of current importance is the technology that comprises cladding of a working layer and its subsequent plasma hardening.

Experimental verification of the efficiency of plasma treatment was performed on specimens measuring 10·10·55 mm, which were cut from the deposited plates. Part of the specimens was subjected to plasma treatment without fusion. The treatment parameters were as follows: specific thermal power of the plasma jet – $1.2 \cdot 10^5$ W/cm², diameter of the nozzle opening – 6 mm, treatment speed – $(5.6\text{--}7.0) \cdot 10^{-3}$ m/s.

The amount of retained austenite – Θ_v , actual physical widening of the diffraction line of α -iron – β_{110} , type and content of the carbide phase, parameter of the crystalline lattice of martensite – a , degree of tetragonality of the martensite lattice – c/a , carbon content of martensite – p , micro distortions of the lattice – $\Delta a/a$, size of mosaic blocks (coherent expansion regions) – D , and dislocation density – ρ were determined [241]. Results of the studies are given in **Table 5.10**.

Results of X-ray diffraction analysis show that alloy 18Kh6GMFS deposited on the workpiece surface has an initial structure of tempered martensite. Plasma treatment causes a complete phase recrystallization of the alloy and high-rate quenching to form a martensitic structure with an increased content of retained austenite. Almost complete dissolution of the cementite phase and a major part of carbides takes place, which results in oversaturation of solid solution with carbon and alloying elements. In addition, the carbon content of martensite, crystalline lattice parameter and tetragonality degree grow. Extra factors that cause hardening of the martensitic structure of the alloy as a result of plasma treatment are micro distortions of the crystalline lattice, refining of the mosaic blocks and more than by an order of magnitude increase in the dislocation density.

The alloy after plasma treatment has a higher level of properties compared with the initial state. It has increased hardness, impact toughness (from 0.42 to 0.48 MJ/m²), dynamic crack resistance K_{ID} (from 28.2 to 32.5 MPa·m^{1/2}) and high-temperature stability. Hardness at a level

of HV 500 persists in heating to 550 °C. In heating to higher temperatures, hardness decreases insignificantly, still remaining higher than that of a non-hardened metal of basic composition.

● **Table 5.10** Phase composition and parameters of crystalline lattice of deposited metal

Characteristic of crystalline lattice of alloy: 0.18 % C, 6 % Cr, 1 % Mn, 1 % Mo, 1 % V	In initial state	After plasma treatment
Amount of retained austenite, θ_r , %	Up to 2.0	7.2
Actual physical widening of diffraction line of α -iron, β_{r10} , radian	0.0027	0.0032
Carbide phase	Fe_3C (~10 %) $Me_{23}C_6$ (~5 %)	Fe_3C < 1 % $Me_{23}C_6$ (~2 %)
Parameter of crystalline lattice of martensite, a , Å	2.8731	2.8992
Carbon content of martensite, p , wt. %	0.147	0.195
Degree of tetragonality of martensite lattice, c/a	1.0077	1.0109
Micro distortions of crystalline lattice, $\Delta a/a \cdot 10^{-2}$	0.47	1.18
Dislocation density, ρ , 10^{-16} , m^{-2}	1.7	24.7
Size of mosaic blocks, D , 10^{-7} , m	1.57	0.43
Hardness, H_V	380–410	520–530

It was concluded on the basis of the studies that a significant contribution to hardening in plasma treatment is made by the dispersion mechanism. A special role in dispersion hardening is played by a highly dispersed martensite of lath morphology and its high dislocation density. The positive effect on performance of the hardened alloy, and on fracture toughness in particular, is exerted also by an increased content of retained austenite. This is attributable to refining of structure of the γ -phase in high-rate heating, short holding time, heterogeneity of solid solution and high cooling rate. Retained austenite is present primarily in interlayers between the martensite laths, which allows this structure to be regarded as composite (lamellar) to a certain extent.

Fracture in the plasma hardened zone occurs by the micro tough mechanism. The main advantage of plasma treatment is a simultaneous increase in hardness and fracture toughness of the surface layer.

Increase in energy intensity of fracture of metal in the hardened zone, compared with the initial one, is promoted also by increase in the degree of dispersion of martensite. Plasma hardening provides refining of structure of the deposited metal, i.e. the degree of dispersion of the martensite packs is almost by an order of magnitude higher compared with the initial state.

In addition to refining of martensite, dislocation and dispersion hardening, increase in crack resistance of the alloy is affected also by an increase in the amount of retained austenite, as well as by the fact that it has the form of thin interlayers located between martensite crystals. Because of a relatively low carbon content and saturation with alloying elements, this austenite is resistant to α - γ transformations during the deformation process. The austenite interlayers persist in

fracture and serve for Localization of internal stresses, i.e. along with the dispersed precipitates they compensate for brittleness of martensite.

The effect of laser, pulsed-plasma and plasma treatment on structure and properties of the deposited metal alloyed with chromium (5–5 %), manganese, molybdenum and vanadium (up to 1 %) was comprehensively studied in [239–247]. In terms of composition optimization, the studies were also conducted on alloy Cr-Mo-V with decreased chromium content (2 %), increased molybdenum content and nickel addition.

5.5 GENERALISATION OF PDT AND PLASMA TREATMENT INVESTIGATION RESULTS

The most important peculiarity of surface hardening using concentrated energy sources is a high rate of heating and cooling. This causes grain refining, shift in a stage of α - γ transformations towards higher temperatures and inheritance of the initial structure defects. At high heating rates, because of inertia of the processes of redistribution of the dislocation structure, polygonization has no time to take place on a full scale. Decrease in internal stresses occurs by recrystallization, leading to refining of ferrite grains. Subsequent α - γ transformations result in formation of fine-grained austenitic structure, which after cooling yields a highly dispersed martensite having increased mechanical properties.

Alloys with additions of Cr, Mo, V, Mn and Si, subjected to plasma treatment, are characterized by formation of not only twinned martensite but also packed martensite. Packed lath martensite is another basic structural component of the hardened layer, the laths first grow in size to some extent with growth of the concentration of C, Cr, Mo and V in an alloy (i.e. with growth of carbon equivalent) and then remain unchanged. However, even in structure of the alloy with 5 % Cr and 0.18 % C we can clearly see individual relatively coarse plates of acicular twinned martensite, the content of which is about 15 %, and with growth of the alloying degree it increases to 40 % for an alloy with 7 % Cr and 0.35 % C.

Formation of highly dispersed twinned martensite in low-carbon alloy Cr-Mo-V can be explained as follows. Morphology of the formed martensite depends upon the ratio of critical tangential stresses in austenite causing slip and twinning. Decrease in temperature of the alloy is accompanied by a rapid growth of its slip resistance, and starting from a certain temperature the twinning resistance becomes higher. Therefore, formation of plate martensite is more probable at low temperatures of martensite transformations, and formation of packed martensite is more probable at higher temperatures. Peculiarity of plasma hardening is formation of heterogeneous austenite. As a result of high-rate cooling, volumes of the alloy with a different carbon concentration are hardened in a different way, and the range of temperatures within which the martensite transformations occur becomes substantially wider. Growth of the concentration of carbon and alloying elements in solid solution of the Cr-Mo-V alloy is accompanied by decrease in temperature of the martensite transformations. Austenite crystals, which are most saturated with carbon, are

hardened at a temperature of about 100 °C to form plate twinned martensite. Formation of heterogeneous (in structure and composition) martensite in the hardened zone has a favourable effect on improvement of performance of the alloy.

The considered modification mechanism is valid also for pulsed-plasma treatment (PDT). Higher temperature gradients and simultaneous treatment with high-energy physical fields aggravate the situation and widen the martensite transformation temperature range. As a result of PDT, practically all the alloys have abnormally high values of hardness of the surface layer (**Fig. 5.2**). Under the PDT conditions, which are comparable in power, increase in the quantity of pulses leads to increase in microhardness and thickness of the hardened layer. The highest hardness (21 GPa) and maximal thickness of the hardened layer (50 µm) were achieved in the case of using tungsten and molybdenum electrodes. To compare, the level of hardness of carbon steels achieved after laser plasma is 7.0–14.5 GPa (**Fig. 5.4**).

Auger spectroscopy shows that PDT leads to alloying of the surface layer with W, Mo, Ti, Cr, Cu, Ni and other elements added to plasma, in addition to mass transfer of nitrogen and carbon. For example, the light phase was detected on the sample surface in alloying with molybdenum. This phase is molybdenum highly saturated with carbon and oxygen, and very slightly with nitrogen. Molybdenum, combined with iron, was also fixed in the surface layer of matrix.

After treatment by plasma containing tungsten, the formation of a new high alloy was seen on the sample surface. Auger spectroscopy of cross section of this layer, the electron probe diameter being about 2 µm, showed the presence of about 18 at. % of tungsten at a depth of 20 µm in the surface layer of a sample treated.

Detection of molybdenum and tungsten by X-ray spectral analysis proves their penetration into the sub-surface layer to a depth close to that of penetration of X-rays, i.e. several microns.

Fracture of a sample after PDT, occurring normal to the treated surface, demonstrates extremely strong splitting of structural elements in the sub-surface layer (**Fig. 5.11**). Thickness of this layer is about 10 µm. Radiography showed decrease in the intensity of lines (110) and growth of the intensity of lines (200) with intensification of the PDT conditions. This is the result of phenomenon of preferred orientation of crystallographic lattices along the temperature gradients. Crystallization or recrystallization of material under rapid cooling conditions is accompanied by growth of stresses (**Fig. 5.14**). Preferred orientation $\langle 001 \rangle$ takes place under these conditions for crystalline materials with a cubic lattice.

X-ray patterns of treated steel U8 are characterized by splitting of lines of the α -phase, which is caused by tetragonality of martensite in surface hardening. This is especially pronounced for lines (110) and (211). X-ray phase analysis fixes widening of the α -Fe lines and formation of lines of retained austenite of Fe in the surface layer. Increase in the number of the PDT pulses involves further widening of the α -Fe lines and reduction in their intensity, as well as increase in the relative intensity of the γ -Fe lines.

Physical widening is almost proportional to tangent of the reflection angle, i.e. the main contribution to widening is made by heterogeneous distortions of the crystalline lattice. This could be

caused both by phase hardening and chemical heterogeneity of an alloy resulting from alloying of the surface layer in heterogeneous physical fields.

It should be noted that with a much higher hardness of the surface layer of steel U8 the widening of line (220) in it is much smaller than in steel 40X. Therefore, the presence of splitting of lines of the α -phase due to tetragonality of martensite is indicative of a higher hardening than in the presence of widening of lines of a symmetric character.

It was established that modification of surfaces in PDT is achieved through partial dissolution of initial carbides and formation of a large amount of zones with microchemical heterogeneity of solid solutions in the irradiated layer. The special effect is exerted by duration of a plasma pulse and structural state prior to irradiation. The shorter the time of irradiation and the higher the dispersion of a dissolved phase, the higher the effect of hardening.

Characteristic peculiarity of structure after pulsed plasma hardening is its capability of retaining hardness in heating during the friction process. This is attributable to formation of nanocrystalline structures and amorphized regions in the form of thin plates during the rapid solidification process.

The optimal value of power density of plasma radiation pulses should be chosen on the basis of structure of alloy in the irradiated zone, which should be a martensite-carbide mixture formed as a result of secondary hardening, which occurs under the effect of a plasma pulse. An additional factor for stabilization of the amount of austenite is absorption of alloying elements and carbon during the PDT process. It is likely that this is the results of "abnormal" processes of mass transfer of alloying elements from the plasma jet during PDT, as well as a short time of dwelling of a material at high temperature.

6 SURFACE ALLOYING

ABSTRACT

Alloying of surface layers is one of the main factors of surface hardening during pulsed plasma treatment. The complex effect on the surface makes it possible to accelerate the processes of heat and mass transfer. The chapter deals with the interaction of shock-compressed plasma with the surface and alloying processes during PDT.

KEYWORDS

Impulse action, deformation, recrystallization, movement of dislocations, coefficient of mass transfer.

6.1 MASS TRANSFER IN PULSED TREATMENT OF METALS

Temperature is one of the main parameters that determine mobility of atoms under conventional stationary conditions of isothermal annealing of metals and alloys. Increasing the temperature of crystalline solid bodies is accompanied by increase in the mobility of atoms. However, the attempts to practically achieve values corresponding to the value of the coefficient of diffusion of proper atoms in liquid metal ($\approx 10^{-6} \text{ cm}^2/\text{s}$) under conventional conditions have failed as yet. Migration of atoms can be increased through increasing defectiveness of the crystalline structure, which is caused by irradiation, phase transformation and plastic deformation [248–250]. Abundant information has been accumulated on the effect of plastic deformation on diffusion in a range of $\varepsilon = 10^{-7} - 10^{-3} \text{ s}^{-1}$. The coefficient of diffusion grows within this range of strain rates, which is attributable to increase in the mean concentration of vacancies, exceeding the equilibrium one [155–158]. The rate of plastic strain is determined as follows:

$$\varepsilon = \frac{\Delta h / h}{\tau},$$

where Δh – the variations of samples in height; h – the initial height of a sample; τ – time of strain.

At $\varepsilon = 10^{-3} - 10^{-1} \text{ s}^{-1}$ there is a decrease in the diffusion coefficient, which is caused by dynamic recrystallization [163].

Under conditions of high-rate plastic deformation of crystalline bodies ($\varepsilon \geq 20 \text{ s}^{-1}$) the velocity of migration of atoms in them exceeds that of diffusion transfer in liquid metal. The wide acceptance in industry has been received lately by such treatment methods as impact mechanical compression,

treatment with pulsed magnetic field, laser, explosion, electric, hydraulic and pulse treatment, ultrasonic peening and deformation of metals and alloys during the reversible martensitic transformation processes.

Distinctive feature of high-rate deformation of alloys is a dramatic increase in the number of spot-like defects (vacancies) in a crystal. The process of generation of defects in this case is faster than dynamic recrystallization, which leads, in the opinion of the authors of studies [250–252], to acceleration of mass transfer. Velocities of dislocations, V , during the shock loading process, even at low temperatures, amount to substantial values. For example, for molybdenum deformed at temperatures of 77 and 300 K, the velocities of screw dislocations are $10\text{--}10^3$ cm/s at stresses in an alloy equal to more than $300\text{--}700$ N/cm². Decrease in the time of the effect is accompanied by increase in the dislocation velocities. It is the opinion of the authors of study [253] that diffusion of alloying atoms into an alloy occurs with moving dislocations. Therefore, the time of the effect exerts a strong influence on the coefficient of mass transfer. For example, as shown in study [253], the shock effect (deformation time is $t=4\cdot 10^{-3}$ s, temperature within the contact zone is 800 °C) causes the presence of iron atoms in titanium at a depth of 200 μm . In this case the diffusion coefficient is $D=8.3\cdot 10^{-3}$ cm²/s, which is by two orders of magnitude higher than in liquid metal.

The pulsed plasma treatment leads to a dramatic heterogeneous deformation of metal, which is indicative of the formation of a dislocation structure. Pulses in this case normally last for milliseconds. The depth of the layer with an increased dislocation density grows from 15–20 (1 cycle) to 30–35 μm (10 cycles). The authors of [252–256] consider dependence of the dislocation density upon the depth as a result of superposition of two surface treatment processes, i.e. thermal and mechanical. The dislocation density in an alloy treated grows from $4\cdot 10^7$ to $5\cdot 10^9$ cm⁻² under the effect of the millisecond plasma pulses.

Study [257] gives results of investigations of multiple radiation impacts on the iron surface, which has a radioactive caesium layer deposited on it. The investigations show that the rate of mass transfer in iron depends upon the interlayer material. Thus, it is $D=2.4\cdot 10^{-5}$ cm²/s in irradiation through the copper interlayer, and $D=6.7\cdot 10^{-5}$ cm²/s in irradiation through the molybdenum interlayer. The ratio of the coefficients of mass transfer of copper and molybdenum is in inverse proportion to the ratio of their coefficients of thermal conductivity. This can be explained by the fact that increased thermal conductivity of copper leads to a faster transfer of the energy of plasma into the heat oscillations of the lattice, whereas the lower thermal conductivity of molybdenum caused their higher losses.

Investigation of structural changes of metal after ultrasonic peening shows that grain is refined and boundaries take a wavy shape as a result of multiple impacts ($n\sim 30$ kHz) [258]. This is indicative of occurrence of the process of dynamic recrystallization in an alloy treated. Recrystallization of the alloy after each loading event occurs simultaneously with the deformation events. Therefore, movement of the grain boundaries superimposes on the transfer of atoms deep into metal, which occurs in ultrasonic peening. Thus, ultrasonic peening causes atoms of aluminium to penetrate into copper to a depth of 150 μm (force – $F=150\text{--}200$ N, pulse frequency – $n=18$ kHz,

treatment time – $t=10$ s, temperature within the contact zone – $T=300$ K, plastic strain rate – $\varepsilon=5 \cdot 10^5$ s $^{-1}$) [252]. In addition to dislocation multiplication, ultrasonic peening causes increase in the number of spot-like defects up to the values characteristic of high temperatures.

The method was developed to study mass transfer through deformation of metals and alloys during reversible martensitic transformations. Growth of a martensite crystal ($\alpha \rightarrow \gamma$ transformation) induces substantial stresses, the relaxation of which leads to deformation of metal in micro volumes and increase in defectiveness of structure. Reverse $\gamma \rightarrow \alpha$ transformation maintains most of the boundaries of the α - and γ -phases formed in direct transformation. In addition, increase in temperature from 300 K to a temperature of diffusion annealing results in partial decomposition of martensite to form carbides, which also favours increase in length of the inter-phase boundaries. Each next event of the $\alpha \rightarrow \gamma$ transformation leads to increase in the dislocation density, as well as in the length of inter-phase and grain boundaries, which are the ways of accelerated diffusion. It is possible to achieve superposition of strains on phase transformations by placing samples in massive mandrels. The strain rate in this case is $\varepsilon=10^{-3}$ s $^{-1}$. The depths of alloying, depending upon the combined effect by plastic deformation and martensitic transformation, are given in **Tables 6.1, 6.2** [254].

● **Table 6.1** Depths of penetration of atoms of elements into alloy (Fe-Ni30 %)

Impact method	Depth of mass transfer of elements, mm							
	Co	Fe	Ni	Cu	C	N	Ti	Cr
Deformation ($\varepsilon = 10^{-3}$ s $^{-1}$)	12	12	8	4.5	3	3	2	1.5
$\gamma \rightarrow \alpha$ transformation	35	26	21	11	8.5	7	4	3.5
$\alpha \rightarrow \gamma$ transformation and resulting deformation	60	44	35	24	16	15	10	7

● **Table 6.2** Absolute values of mass transfer of metal elements depending upon the impact method and surface temperature

Temperature, K	Impact method	Depth of mass transfer of elements, mm							
		Co	Fe	Ni	Cu	C	N	Ti	Cr
233–173	Deformation	11	5.8	3.5	0.9	0.74	0.6	0.37	0.10
	$\alpha \rightarrow \gamma$ transformation	34	15	11	4.5	2.4	1.5	0.97	0.93
	$\alpha \rightarrow \gamma$ transformation	99	40	25	9.2	8.5	5.0	2.0	1.8
553–613	Deformation	17	8.9	6.3	2.4	1.9	1.4	1.0	–
	$\alpha \rightarrow \gamma$ transformation	72	30	31	14	7.1	5.8	4.6	–
	$\alpha \rightarrow \gamma$ transformation	150	50	41	27	23	15	8.2	–

As proved by the experiments, the coefficient of mass transfer in the alloy (Fe-Ni 30 %) subjected to high-rate loading in different temperature ranges is $D=10\text{--}10$ cm 2 /s.

It should be noted that differences in the coefficients of mass transfer in deformation under the martensitic transformation conditions are much smaller than under stationary conditions. In isothermal annealing and at a temperature of 613 K (temperature of the end of $\alpha \rightarrow \gamma$ transformation) the diffusion coefficient of carbon atoms is $1 \cdot 10^{-11}$ and that of iron and nickel atoms is $1 \cdot 10^{-21}$ and $5 \cdot 10^{-21}$ cm^2/s , respectively.

Investigation of the effect of the strain rate on mass transfer at high-rate tension in the pulsed magnetic field is described in [249–254]. With these treatment methods $\epsilon = 10^{-3} - 50 \text{ s}^{-1}$ (**Table 6.3**).

● **Table 6.3** Mass transfer coefficients in high-rate tension in pulsed magnetic field ($t_{\text{pulse}} = 105 - 110 \text{ } \mu\text{s}$)

$\epsilon, \text{ s}^{-1}$	Alloying element	Sample material	$D, \text{ cm}^2/\text{s}$
$3 \cdot 10^{-3}$	Ni	Cu	$2 \cdot 10^{-11}$
40	Cu	Ni	$8 \cdot 10^{-12}$
	Ni	Cu	$2 \cdot 10^{-5}$

In addition to plastic deformation, the migration of atoms is greatly affected by the pulse energy of the electromagnetic field (**Table 6.4**).

● **Table 6.4** Mass transfer coefficients $D, \text{ cm}^2/\text{s}$, in the case of pulsed electromagnetic compression at 300 K and $\epsilon = 1.7 \cdot 10^3 \text{ s}^{-1}$ [259]

Electromagnetic pulse energy, kJ	Mass transfer coefficient $D, \text{ cm}^2/\text{s}$			
	Cu	Ni	Al	Fe
6	$8.2 \cdot 10^{-5}$	$6.5 \cdot 10^{-5}$	$4.1 \cdot 10^{-5}$	$4.8 \cdot 10^{-5}$
12	$5.1 \cdot 10^{-4}$	$4.5 \cdot 10^{-4}$	$5.1 \cdot 10^{-4}$	$7.0 \cdot 10^{-4}$
23	$9.5 \cdot 10^{-3}$	$7.8 \cdot 10^{-3}$	$2.0 \cdot 10^{-2}$	$1.1 \cdot 10^{-2}$

It should be noted that with any pulsed treatment method the coefficient of mass transfer hardly depends upon the size of grains. It monotonously decreases with increase in the quantity of pulses. The simultaneous impact by several types of the pulse effect leads to a substantial acceleration of diffusion, this acceleration being of a non-additive character.

It can be suggested on the basis of modern notions that there are more than 12 mechanisms of diffusion of atoms in metal [255]. These are an interchange of locations of atoms, circular interchange, direct and indirect interstitial displacement of atoms, interstitial configuration displacement of atoms, diffusion via dislocation tubes, along grain boundaries, along phase boundaries and other mechanisms. None of the known mechanisms, taken separately, can give a satisfactory description of such high coefficients of mass transfer which we have with the pulsed treatment of materials. Therefore, the question of the atomic mechanism of diffusion in the case of the pulsed treatment of metals and alloys is still open.

6.2 INTERACTION OF PULSED PLASMA WITH SOLID SURFACE

6.2.1 MODELLING OF PROCESSES OCCURRING IN THE SHOCK-COMPRESSED LAYER

Analysis of literature data and patent sources shows that the current practice of alloying surfaces of parts is by laser plasma [260–262] and/or plasma jet [263–265]. In this case the individual plasma jets may be of a different nature (gaseous, erosion plasma). Examination of the high-speed scan photos of the plasma jets reveals the shock waves present in them, periodic structure and formation of the shock-compressed plasma regions on a solid substrate (Chapter 3).

The plasma jet radiation spectra are characterized by the presence of lines belonging to the ions of nitrogen, oxygen and carbon with an excitation potential of 20 to 30 eV. It was established that the most intensive radiation in the central part of the jet was that of the atoms of hydrogen, oxygen, nitrogen, carbon and metals.

Distribution of alloying elements in the layer of parts modified by plasma-detonation treatment is affected mostly by the composition of the plasma jet. Composition of the radiating components of plasma with distance from the exit section of the plasma generator nozzle remains unchanged up to a distance of 15 mm. Examinations showed a marked increase in the intensity of line and continuous radiation of plasma near the sample surface.

As noted above, the energy characteristics of the plasma jets at the exit from the plasma generator (temperature, velocity, etc.) have a linear dependence upon the intensity of the magnetic field and length of the gap between the electrodes in the generator reaction chamber (Chapter 2).

Interaction of the supersonic plasma jet with a flat obstacle results in an isolated shock wave formed near the surface, behind which the physical properties of the jet change. It should be noted that velocity and temperature dramatically fall with distance from the nozzle exit section. Modification of the surface occurs in a layer of the shock-compressed plasma falling on the solid surface.

Therefore, to study capabilities of the technology, it is important to consider the processes occurring in the shock-compressed region. **Fig. 6.1** shows the diagram of interaction between the plasma jet and solid substrate.

Plasma of the hydrocarbon combustion products has a complex chemical composition and depends upon the temperature [266]. Therefore, we will use the averaged values of mass of plasma components and ionization potential. Within a plasma temperature range of 7,500 to 15,000 K, the averaged molar mass is $\mu = 11$ g/mole and ionization potential is $I = 14$ eV.

The Saha equation [267] for the plasma jet has the following form:

$$\frac{\tilde{n}_i \cdot \tilde{n}_e}{\tilde{n}_a} = 2 \cdot \left(\frac{2 \cdot \pi \cdot m_e \cdot k_b}{h^2} \right)^{\frac{3}{2}} \cdot \frac{g_i}{g_0} \cdot T_1^{\frac{3}{2}} \cdot \exp \left(- \frac{e \cdot I}{k_b \cdot T_1} \right), \quad (6.1)$$

where $h=6.626 \cdot 10^{-34}$ J·s – the Planck constant; $k_b=1.38 \cdot 10^{-23}$ J/K – the Boltzmann constant; $g_i=1$ and $g_0=2$ – the total statistical weights of internal axes of freedom of ions and atoms, respectively; $e=1.602 \cdot 10^{-19}$ C – the electron charge.

Let's determine the degree of ionization of plasma in the jet:

$$\alpha_1 = \frac{\tilde{n}_e}{\tilde{n}_0}, \quad (6.2)$$

where, $\tilde{n}_0 = \tilde{n}_a + \tilde{n}_i$ is the total concentration of neutral atoms and ions.

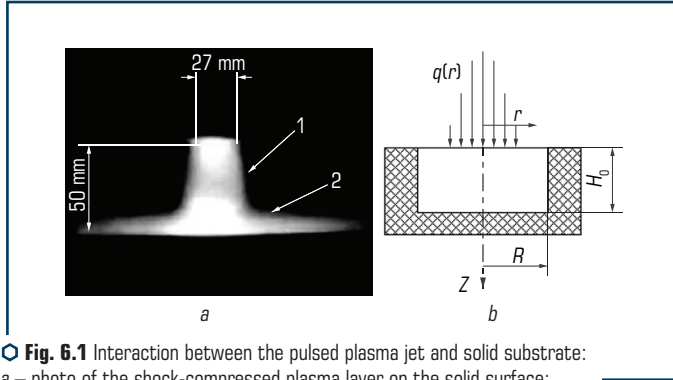


Fig. 6.1 Interaction between the pulsed plasma jet and solid substrate:
 a – photo of the shock-compressed plasma layer on the solid surface;
 b – calculation of energy parameters of the jet

Based on conditions of quasi-neutrality of plasma and single ionization of ions, assume that the concentration of electrons is equal to the concentration of ions, $\tilde{n}_e = \tilde{n}_i$.

Take into account that under the PDT conditions the pulsed plasma is in thermal equilibrium and temperatures of neutral atoms, ions and electrons are equal to each other ($\tilde{T}_a \approx \tilde{T}_e \approx \tilde{T}_i \approx \tilde{T}_1$).

Write down the expression for pressure in the plasma column:

$$P_1 = (1 + \alpha_1) \cdot n_0 \cdot k_b \cdot T_1. \quad (6.3)$$

For the PDT conditions the pressure of the pulsed plasma in the plasma column is $P_1 = 2 \cdot 10^5$ Pa [268].

Substitution of (6.2) and (6.3) to the Saha equation and transformation yield expression for the degree of ionization of plasma in terms of temperature and pressure:

$$\alpha_1 = \frac{1}{\sqrt{\frac{P_1}{k_b \cdot T_1 \cdot X}} + 1}, \quad (6.4)$$

where

$$X = 2 \cdot \left(\frac{2 \cdot \pi \cdot m_e \cdot k_b}{h^2} \right)^{\frac{3}{2}} \cdot \frac{g_i}{g_0} \cdot T_1^{\frac{3}{2}} \cdot \exp \left(-\frac{e \cdot I}{k_b \cdot T_1} \right).$$

Substitution of (6.2) to (6.3) yields expression for the concentration of electrons in the plasma column:

$$\tilde{n}_e = \frac{\alpha_1}{\alpha_1 + 1} \cdot \left(\frac{P_1}{k_b \cdot T_1} \right). \quad (6.5)$$

Physical properties of the plasma jet proper dramatically change behind an isolated shock wave. Change in the velocity and thermodynamic parameters can be evaluated from the adiabatic laws for the jet passing through the shock wave. In particular, the density of plasma behind the shock wave can be determined from the following equation [269]:

$$\rho_2 = \rho_1 \cdot \frac{\frac{\gamma + 1}{2} \cdot M_1^2}{1 + \frac{\gamma - 1}{2} \cdot M_1^2}, \quad (6.6)$$

where $\gamma = 1.2$ – the adiabatic exponent; $\rho_1 = P_1 / (R \cdot T_1)$ – the density of plasma ahead of the shock wave;

$$M_1 = V_1 / \sqrt{\gamma \cdot \frac{R_0}{\mu} \cdot T_1} \text{ – the Mach number;}$$

$R_0 = 8.3145 \text{ J} \cdot \text{mole}^{-1} \cdot \text{K}^{-1}$ – the universal gas constant.

Velocity behind the shock wave becomes lower than the local velocity of sound and equals [270]:

$$V_2 = V_1 \cdot \left(\frac{2}{\gamma + 1} \cdot \left(\frac{1}{M_1^2} - 1 \right) + 1 \right). \quad (6.7)$$

The Mach number behind the shock wave is determined from the following relationship [269]:

$$M_2 = \sqrt{\frac{1 + \frac{\gamma - 1}{2} \cdot M_1^2}{\gamma \cdot M_1^2 - \frac{\gamma - 1}{2}}}. \quad (6.8)$$

Then, directly at the obstacle the axial velocity becomes equal to zero, and plasma radially spreads over the surface. The stagnation region is a region of the shock-compressed plasma.

Estimate the density of plasma in the shock-compressed region from the equation for a fully stagnated gas flow [270]:

$$\rho_{20} = \rho_2 \cdot \left(1 + \frac{\gamma - 1}{2} \cdot M_2^2\right)^{\frac{1}{\gamma - 1}}. \quad (6.9)$$

This makes it possible to determine the concentration of neutral atoms and ions from the following relationship:

$$n_a + n_i = n_{20} = \rho_{20} \cdot \frac{N_a}{\mu}. \quad (6.10)$$

The Saha equation for the shock-compressed region can be written down as follows:

$$\frac{\alpha_{20}^2}{1 - \alpha_{20}} \cdot n_{20} = 2 \cdot \left(\frac{2 \cdot \pi \cdot m_e \cdot k_b}{h^2}\right)^{\frac{3}{2}} \cdot \frac{g_i}{g_0} \cdot T_{20}^{\frac{3}{2}} \cdot \exp\left(-\frac{e \cdot I}{k_b \cdot T_{20}}\right), \quad (6.11)$$

where T_{20} – the temperature of plasma in the shock-compressed region; α_{20} – the degree of ionization of plasma in the shock-compressed region.

The calculation of temperature from the equations for stagnated gas [269] gives overstated values. Realistically, the dissociation and ionization processes are intensive behind the shock wave and in the stagnated region of plasma. Taking into account an increase in the degree of ionization, as well as that the process under consideration is adiabatic, write down the equation of equality of enthalpies in the plasma column and in the shock-compressed region. In this case it is possible to ignore dissociation of molecules and radial spread of plasma over the surface:

$$\frac{M_a \cdot V_1^2}{2} + \frac{5}{2} \cdot k_b \cdot T_1 \cdot (1 + \alpha_1) + \alpha_1 \cdot I \cdot e = \frac{5}{2} \cdot k_b \cdot T_{20} \cdot (1 + \alpha_{20}) + \alpha_{20} \cdot I \cdot e, \quad (6.12)$$

where $M_a = M_i = 11.1.673 \cdot 10^{-27} \text{ kg} = 1.837 \cdot 10^{-26} \text{ kg}$ can be written down for the mass of atom and ion.

The temperature and degree of ionization in the shock-compressed region, T_{20} and α_{20} , can be determined from the system of equations (6.11) and (6.12):

$$\begin{cases} \frac{\alpha_{20}^2}{1 - \alpha_{20}} \cdot n_{20} = 2 \cdot \left(\frac{2 \cdot \pi \cdot m_e \cdot k_b}{h^2}\right)^{\frac{3}{2}} \cdot \frac{g_i}{g_0} \cdot T_{20}^{\frac{3}{2}} \cdot \exp\left(-\frac{e \cdot I}{k_b \cdot T_{20}}\right); \\ \frac{M_a \cdot V_1^2}{2} + \frac{5}{2} \cdot k_b \cdot T_1 \cdot (1 + \alpha_1) + \alpha_1 \cdot I \cdot e = \frac{5}{2} \cdot k_b \cdot T_{20} \cdot (1 + \alpha_{20}) + \alpha_{20} \cdot I \cdot e. \end{cases} \quad (6.13)$$

Pressure in the shock-compressed region can be determined from the following relationship:

$$P_{20} = n_{20} \cdot (1 + \alpha_{20}) \cdot k_b \cdot T_{20}. \quad (6.14)$$

The concentration of electrons in the shock-compressed layer is as follows:

$$n_e = n_{20} \cdot \alpha_{20}. \quad (6.15)$$

Plasma in the shock-compressed region is in thermal equilibrium, $T_{20} = T_i = T_e = T_a$, and is quasi-neutral, $n_e = n_i$.

To describe processes occurring in the shock-compressed plasma adjoining the metal surface, we will use a unified approach, within the framework of which the sub-surface layer is conditionally divided into three zones. The first zone directly adjoining the surface is the space charge layer. Conditions of quasi-neutrality of plasma are violated and the main potential drop between plasma and metal is formed in this layer. Thickness of this layer, commensurable with the Debye radius, is much smaller than characteristic lengths of the free path of plasma particles.

The second zone is the ionization region of a quasi-neutral plasma (or pre-sheath), where the intensive generation of charged particles takes place. Ions formed here are accelerated under the effect of the electric field in a direction to the metal surface and recombine near this surface. Therefore, the conditions of local ionization equilibrium are violated within the ionization region of plasma. A marked change in the plasma potential, commensurable with the potential drop in the space charge layer, takes place in this zone.

Boundary of the semiconducting layer goes at a distance from the metal surface equal to several lengths of the free path of the particles. The third zone begins outside this layer. This zone is the hydrodynamic region of plasma, where the local thermodynamic equilibrium is established. Thickness of the semiconducting (Knudsen) layer is $L_K \sim 10^{-2}$ cm [271].

Parameters of plasma at the boundary of the Knudsen layer and hydrodynamic region (concentration and temperature of particles, plasma pressure) are assumed to be equal to parameters of plasma in the shock-compressed region.

The workpiece in the plasma-detonation treatment can be anode or cathode, or can be electrically insulated. Consider the processes occurring on the workpiece surface depending upon the treatment conditions and electrical connection with the power supply.

6.2.2 WORKPIECE SURFACE SET AS CATHODE

The heat flow consumed for heating of a cathode workpiece, which is determined from the energy balance on the surface, is equal to:

$$q_{k\lambda} = q_i + q_{e-treat} + q_{r-pl} + q_e - q_{r-cath} - q_{emiss}. \quad (6.16)$$

Energy transferred to the cathode by ions is determined from the following formula:

$$q_i = j_i \cdot \left(\alpha_i \cdot \left(U_k + \frac{2 \cdot k_b \cdot T_i}{e} \right) + \alpha_n \cdot (I - \varphi_e) \right), \quad (6.17)$$

where $j_i = v_i \cdot e \cdot n_i$ – the density of the ion current on the cathode surface; $\varphi_e = 4.31$ eV – the electron work function;

$$v_i = \sqrt{\frac{2 \cdot e \cdot U_k}{M_i}}$$

– the velocity of ions acquired in the cathode potential drop.

The accommodation coefficient for ions with an energy of about 10 V can be assumed to be $\alpha_i = 1$ [272]. Coefficient α_n allows for the fact that not all the energy is transferred to the cathode, and that part of it can be emitted and transformed into the kinetic energy of a reflected atom. Let's assume that $\alpha_n = 0.5$ [272]. Here and below all the tabular data are given for Fe.

Energy transferred to the cathode by backscattered electrons is:

$$q_{e-treat} = j_{e-treat} \cdot \alpha_e \cdot \left(\varphi_e + \frac{2 \cdot k_b \cdot T_e}{e} \right), \quad (6.18)$$

where $\alpha_e = 0.5$ – the electron accommodation coefficient;

$$j_{e-treat} = \frac{e \cdot n_e}{4} \cdot \langle v_{e-treat} \rangle \cdot \exp \left(-\frac{e \cdot U_k}{k_b \cdot T_e} \right)$$

– the backscattered electron current density;

$$\langle v_{e-treat} \rangle = \sqrt{\frac{8 \cdot k_b \cdot T_e}{\pi \cdot m_e}}$$

– the mean thermal velocity of electrons.

Energy transferred to the cathode by neutral atoms is:

$$q_a = \frac{1}{4} \cdot n_a \cdot \langle v_a \rangle \cdot \frac{M_a \cdot \langle v_a^2 \rangle}{2} \cdot \alpha_a, \quad (6.19)$$

where

$$\langle v_a \rangle = \sqrt{\frac{8 \cdot k_b \cdot T_a}{\pi \cdot M_a}}$$

– the mean thermal velocity of atoms;

$$\langle v_a^2 \rangle = \frac{3 \cdot k_b \cdot T_a}{M_a}$$

– the root mean square velocity of atoms.

Determine the heat flow to the workpiece due to plasma radiation [191]:

$$q_{r-pl} = 2 \cdot \Delta z \cdot \sigma_{sb} \cdot T_a^4 \cdot \chi, \quad (6.20)$$

where $\Delta z = 5 \cdot 10^{-3}$ m – the thickness of the shock-compressed layer; $\sigma_{sb} = 5.67 \cdot 10^{-8}$ W·m⁻²·K⁻⁴ – the Stefan-Boltzmann constant; $\chi = 10^2 \cdot \rho^2 \cdot T_a^{4 \cdot \log(T_a)}$ – the Planck absorption coefficient [191].

Heat flow removed due to the surface radiation is:

$$q_{r-cath} = \varepsilon \cdot \sigma_{sb} \cdot T_k^4, \quad (6.21)$$

where $\varepsilon = 0.6$ – the integrated coefficient of heat radiation of the workpiece surface depending upon the kind of a material, surface condition and temperature level.

Let's assume in the calculations that surface temperature is $T_k = 1000$ K.

Energy removed by the emission electrons is:

$$q_{emiss} = j_e \cdot \left(\frac{2 \cdot k_b \cdot T_k}{e} + \Phi_e \right), \quad (6.22)$$

where $j_e = j_i \cdot S / (1 - S)$ is the emission current density.

Let's assume that the share of the emission current is $S = 0.6$ [267]. The electron current is formed due to the thermal autoelectronic mechanism [273].

Therefore, by substituting (6.17–6.22) to (6.16), it is possible to determine the heat flow to the cathode workpiece. Density of the electric current on the surface treated, i.e. cathode, can be determined from the following expression:

$$j = j_i + j_e - j_{e-treat}. \quad (6.23)$$

6.2.3 WORKPIECE SURFACE SET AS ANODE

As the plasma potential is as a rule higher than the anode surface potential [267], the movement of electrons is decelerated by the electric field in the layer set up as anode, and that of ions is accelerated towards the surface. To estimate plasma potential Φ_0 , assume that the current density at the anode workpiece is comparable with the current density at the cathode workpiece, the treatment conditions being identical. Density of the electric current at the anode is:

$$j = j_e - j_i, \quad (6.24)$$

where

$$j_e = \frac{e \cdot n_e}{4} \cdot \langle v_e \rangle \cdot \exp\left(-\frac{e \cdot \varphi_0}{k_b \cdot T_e}\right)$$

– the electron current density; $\varphi_0 = 1.2 \dots 2.5$ V;

$$\langle v_e \rangle = \sqrt{\frac{8 \cdot k_b \cdot T_e}{\pi \cdot m_e}}$$

– the mean thermal velocity of electrons at the external boundary of the semiconducting (Knudsen) layer.

Let's determine density of the ion current from the following relationship [271]:

$$j_i = \langle v_i \rangle \cdot e \cdot n_i \cdot \exp\left(-\frac{1}{2}\right),$$

where

$$\langle v_i \rangle = \sqrt{\frac{8 \cdot k_b \cdot T_i}{\pi \cdot m_i}}$$

– the mean thermal velocity of ions.

Energy transferred to the anode by electrons is determined as follows:

$$q_e = j_e \left(\varphi_e + \frac{2 \cdot k_b \cdot T_e}{e} \right). \quad (6.25)$$

Energy transferred to the anode by ions is as follows:

$$q_i = j_i \cdot \left(\alpha_i \cdot \left(\varphi_0 + \frac{2 \cdot k_b \cdot T_i}{e} \right) + \alpha_n \cdot (I - \varphi_e) \right). \quad (6.26)$$

And energy transferred to the anode by neutral atoms is as follows:

$$q_a = \frac{1}{4} \cdot n_a \cdot \langle v_a \rangle \cdot \frac{M_a \cdot \langle v_a^2 \rangle}{2} \cdot \alpha_a. \quad (6.27)$$

Heat flow to the anode due to plasma radiation can be described by the following relationship [191]:

$$q_{r-pl} = 2 \cdot \Delta z \cdot \sigma_{sb} \cdot T_a^4 \cdot \chi. \quad (6.28)$$

Heat flow removed due to surface radiation is as follows:

$$q_{r-an} = \varepsilon \cdot \sigma_{sb} \cdot T_{an}^4. \quad (6.29)$$

Therefore, substituteion of values of (6.25) through (6.29) yields the heat flow consumed for heating of the anode workpiece:

$$q_{a\lambda} = q_i + q_e + q_{r-pl} + q_a - q_{r-an}. \quad (6.30)$$

6.2.4 SURFACE OF INSULATED WORKPIECE

The heat flow to the surface of an insulated workpiece is determined in a similar way from formulae (6.25) through (6.30) for the anode. It should be taken into account that density of the electric current is $j = j_e - j_i = 0$. Therefore, plasma potential φ_0 relative to the workpiece surface can be determined from the following relationship [271]:

$$\varphi_0 = \frac{k_b \cdot T_e}{e} \cdot \ln \left(\frac{e \cdot n_e \cdot v_e}{4 \cdot \left(j + \langle v_i \rangle \cdot e \cdot n_i \cdot \exp \left(-\frac{1}{2} \right) \right)} \right). \quad (6.31)$$

Results of calculations of plasma parameters, heat flows to the workpiece surface and densities of the electric current for treatment conditions where a workpiece is insulated are given in **Table 6.5**. The calculations were made using formulae (6.11–6.31).

● **Table 6.5** Plasma parameters, heat flows and density of current to a workpiece depending upon the intensity of the electric current in the gap between electrodes

Parameters	E·10⁵, V/m	2.5	3	3.5	4
1		2	3	4	5
Temperature in plasma column, T_1 , K		$7.5 \cdot 10^3$	$9.4 \cdot 10^3$	$11.5 \cdot 10^3$	$13.3 \cdot 10^3$
Plasma jet velocity, V_1 , m/s		$2.72 \cdot 10^3$	$3.4 \cdot 10^3$	$4.1 \cdot 10^3$	$4.8 \cdot 10^3$
Degree of ionization in plasma column, α		0.001	0.012	0.063	0.23
Electron concentration in plasma, n_e , $1/\text{m}^3$		$1.9 \cdot 10^{21}$	$1.8 \cdot 10^{22}$	$7.7 \cdot 10^{22}$	$2.1 \cdot 10^{23}$

● Continuation of Table 6.5

1	2	3	4	5
Temperature in compressed region, T_{20} , K	$9.1 \cdot 10^3$	$11 \cdot 10^3$	$12.6 \cdot 10^3$	$15 \cdot 10^3$
Pressure in compressed region, P_{20} , Pa	$4.1 \cdot 10^5$	$4.5 \cdot 10^5$	$5.2 \cdot 10^5$	$6.63 \cdot 10^5$
Degree of ionization in region, α_{20}	0.006	0.032	0.1	0.29
Electron concentration in region, n_e , $1/m^3$	$1.9 \cdot 10^{22}$	$9.4 \cdot 10^{22}$	$2.7 \cdot 10^{23}$	$7.6 \cdot 10^{23}$
Density of current to workpiece, J_k, J_a , A/m^2	$9.2 \cdot 10^7$	$4.8 \cdot 10^8$	$1.35 \cdot 10^9$	$3.6 \cdot 10^9$
Value of potential at external boundary of Knudsen layer, ϕ_0 , V (anode workpiece)	1.2	1.45	1.8	2.2
Value of potential at external boundary of Knudsen layer, ϕ_0 , V (insulated workpiece)	3.24	3.89	4.51	5.32
Heat flow consumed for heating, cathode workpiece, q_{ka} , W/m^2	$7.2 \cdot 10^8$	$2.3 \cdot 10^9$	$6.4 \cdot 10^9$	$1.6 \cdot 10^{10}$
Heat flow consumed for heating, anode workpiece, q_{ka} , W/m^2	$9 \cdot 10^8$	$3.8 \cdot 10^9$	$1 \cdot 10^{10}$	$3 \cdot 10^{10}$
Heat flow consumed for heating, insulated workpiece, q_{ka} , W/m^2	$3.6 \cdot 10^8$	$8.4 \cdot 10^8$	$2.1 \cdot 10^9$	$5.7 \cdot 10^9$

It should be noted that the heat flow and current density substantially decrease as the distance of a workpiece from the nozzle exit section increases. This was confirmed by metallography and experimental studies of amplitude-time current characteristics.

6.3 THERMAL-PHYSICAL CHARACTERISTICS OF SURFACE

6.3.1 MODELLING

Interaction of the pulsed-plasma jet with a solid surface was studied on the basis of solution to the non-stationary equation of heat conduction, comprising variable coefficients, in the presence of a volumetric heat release:

$$C(T)\rho(T)\frac{\partial T}{\partial t} = \text{div}(\lambda(T)\overline{\text{grad}(T)}) + f, \quad (6.32)$$

where f – the term of the equation allowing for the volumetric heat source; $C(T)$, $\rho(T)$ and $\lambda(T)$ – the heat capacity, density and thermal conductivity of a material depending upon the temperature, respectively.

The equation of heat conduction was solved on cylindrical coordinates z and r (Fig. 6.1). To find the solution, it was assumed that the heat flow to a workpiece had distribution that followed the Gauss law. Boundary conditions were determined on this basis.

Heat exchange with environment was ignored. It was assumed that the surface was cooled due to removal of heat into the bulk of metal, as well as due to a radiant flow from the work-piece surface.

Heating of surface layers of a workpiece due to the electric current flow was determined using thermal-physical data for iron-base alloys [274].

The density amplitude and oscillation frequency of the electric current depend upon the treatment process parameters. They were determined experimentally using the Rogowski belts [210]. It was assumed in the calculations that density of an alloy treated was constant and independent of the temperature, $\rho(T) = \text{const}$.

High temperature gradient is formed in the sub-surface layers affected by the pulsed plasma. Therefore, the non-stationary equation of heat conduction should be solved by the method of finite differences on a non-uniform mesh, which makes the problem more difficult to solve.

Depending upon the frequency of pulses, the time of cooling of the surface layers in PDT may amount to 1 s. Therefore, to accurately describe the cooling process, the number of the time steps should be increased by three orders of magnitude, which will greatly increase the time of computation. The non-uniform time mesh was used to ensure efficiency of the diagram and reduce the number of the steps. The mesh was condensed in time interval of the intensive energy flow from the surface and extended in an interval of the low flow. Therefore, in cooling, the equation is solved by the method of finite differences using the mesh [275–277].

6.3.2 TEMPERATURE FIELD IN SURFACE LAYERS DURING PDT

Consider dynamics of variations of temperature field in sub-surface layers during PDT on samples made from steel U8 (0.8 % C). For this we will use results of the calculation of the heat flow at an intensity of the electric field in the gap between the electrodes equal to $E = 2.5 \cdot 10^5$ W/m.

The input data for the numeric calculation program are as follows: material – steel U8 (0.8 % C), heat flow – $q = 7.2 \cdot 10^8$ W/m², pulse duration – $\tau = 0.6$ ms, current amplitude – $I = 4.0 \cdot 10^3$ A, sample thickness – $H = 5.0 \cdot 10^{-3}$ m, sample radius – $R = 5.0 \cdot 10^{-3}$ m, quantity of pulses – $N = 6$, and pulse frequency – $n = 3$ Hz.

It can be seen from the calculation curves that fusion of the surface layer to a depth of 5.5 μm takes place under the given conditions of PDT (**Fig. 6.2**). It can also be seen that the rate of cooling of the melt at the surface at the initial time moment may amount to $8 \cdot 10^6$ K/s (**Fig. 6.3, 6.4**). As established, at the moment of martensitic transformations the cooling rate is $(1\text{--}3) \cdot 10^5$ K/s and depends upon the distance to the surface.

In this case, where overcooling amounts to several hundreds of degrees, the dendrite grain growth degenerates to form the flat grain front. Increase in the degree of dispersion of grains of the alloy on the surface treated provides the optimal combination of its strength and ductility. Refining of grains exerts the strongest effect on growth of creep resistance at increased tem-

peratures. The thermal energy input at a high heating rate exceeds the energy required for the crystalline lattice to restructure, $\alpha > \gamma$, while restructuring occurs at a finite velocity.

This leads to the fact that this restructuring takes place within a certain temperature range, rather than in an isothermal manner.

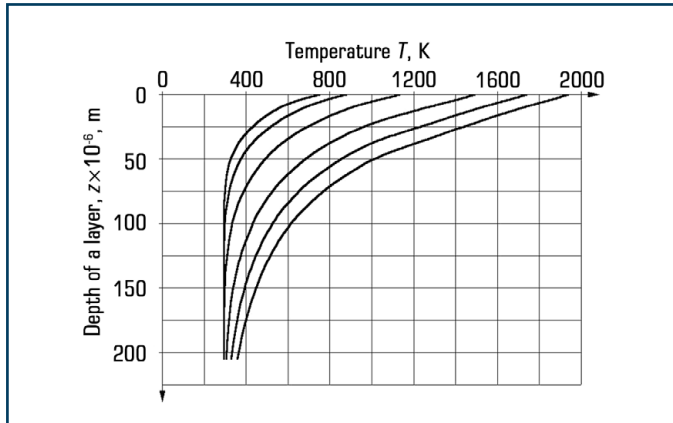


Fig. 6.2 Distribution of temperature through thickness of the surface layer at certain time moments t of heating: 1 – $t = 4.5 \cdot 10^{-5}$ s; 2 – $t = 7.5 \cdot 10^{-5}$ s; 3 – $t = 1.5 \cdot 10^{-4}$ s; 4 – $t = 3.0 \cdot 10^{-4}$ s; 5 – $t = 4.5 \cdot 10^{-4}$ s; 6 – $t = 6.0 \cdot 10^{-4}$ s

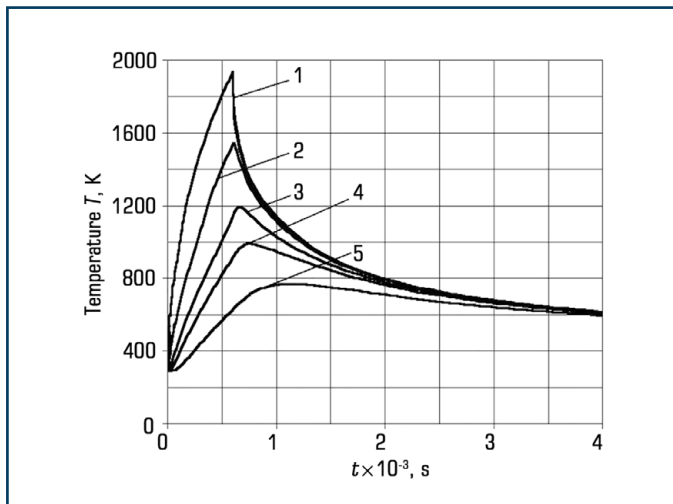


Fig. 6.3 Temperature change in the surface layers at different depths: 1 – $z = 0$ μm ; 2 – $z = 20$ μm ; 3 – $z = 40$ μm ; 4 – $z = 60$ μm ; 5 – $z = 100$ μm

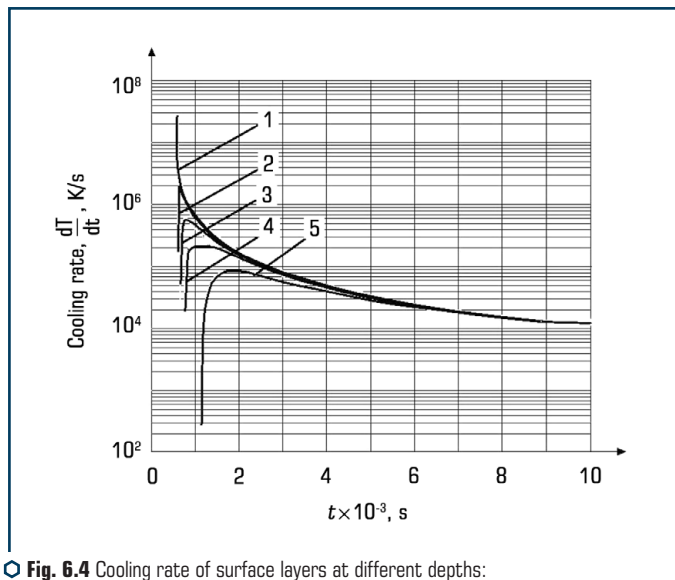


Fig. 6.4 Cooling rate of surface layers at different depths:
1 – $z=0 \mu\text{m}$; 2 – $z=20 \mu\text{m}$; 3 – $z=40 \mu\text{m}$; 4 – $z=60 \mu\text{m}$; 5 – $z=100 \mu\text{m}$

Shift of the critical points depending upon the heating rate and chemical composition of steel is 200°C [231]. Processes of diffusion re-distribution of carbon in austenite, i.e. homogenization of austenite, and processes of recrystallization of the wrought alloys shift to the regions of higher temperatures. Considering the shift of the critical points, it can be concluded that restructuring of the crystalline lattice at the set calculation parameters will occur in the surface layer equal to $50 \mu\text{m}$ (Fig. 6.3). It can be seen from the curves that the depth of fusion of the surface layer is $5.5 \mu\text{m}$.

Consider the calculation curves of variations of temperature through thickness of the surface layer of a workpiece in cooling to study in detail the cooling processes (Fig. 6.4).

As noted above, the rate of cooling of the surface from the melt is high at the initial time moment and equals $8 \cdot 10^6 \text{ K/s}$. After $96 \cdot 10^{-4} \text{ s}$ the cooling rate becomes equal to 10^4 K/s .

The higher cooling rate leads to increase in defectiveness of structures because of enhancement of phase hardening, slowing down of the recrystallization processes and a more complete inheritance of defects of the γ -phase. This is accompanied by refining of blocks, increase in the dislocation density and growth of stresses in the crystalline lattice.

Analysis of distribution of temperature along the radius of the treated sample surface at time moment $t=6.0 \cdot 10^{-4} \text{ s}$ shows that in a region limited by a radius of 4 mm , depending upon distance z , the surface temperature is higher than phase transformation point A_{c1} . This proves the fact that to modify the surface it should be subjected to multiple PDT. This is necessary to overlap the treatment spots.

The calculation curves for one pulse were considered above. **Fig. 6.5** shows the calculation curves for time variations of temperature at different distances from the surface under the effect of six pulses.

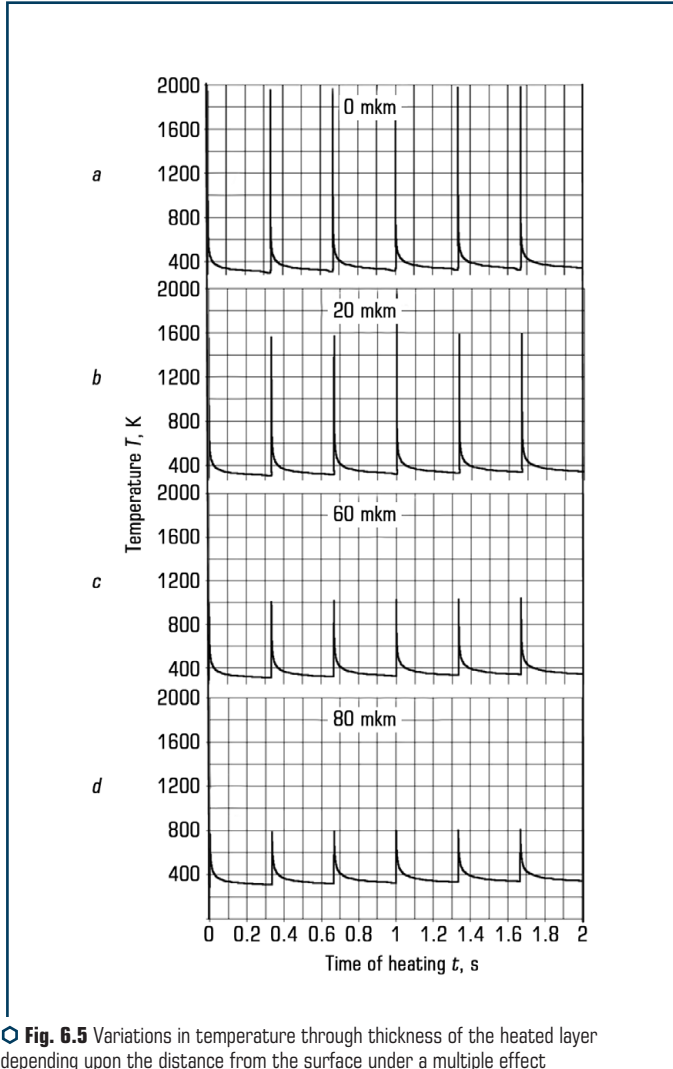


Fig. 6.5 Variations in temperature through thickness of the heated layer depending upon the distance from the surface under a multiple effect by pulsed plasma in PDT: *a* – $z = 0 \text{ } \mu\text{m}$; *b* – $z = 20 \cdot 10^{-3} \text{ } \mu\text{m}$; *c* – $z = 60 \cdot 10^{-3} \text{ } \mu\text{m}$; *d* – $z = 80 \cdot 10^{-3} \text{ } \mu\text{m}$

The character of distribution of temperature fields in heating after the second and subsequent pulses of the plasma treatment differs greatly from those seen after a single pulse. An intensive heat removal into metal takes place between the pulses. The surface layer has time to cool down. The temperature difference is not in excess of 10 °C. Therefore, PDT results in thermal cycling of the surface, leading to enhancement of phase hardening due to reversible α - γ transformations, increase in the dislocation density and decrease in the crystalline grain size. As noted above, this intensifies heat and mass transfer, thus raising the rate of the diffusion processes.

Realization of the so-called abnormal processes of mass transfer provides alloying of the surface layer and formation of an alloy layer with high and predictable service properties.

It can be seen from **Fig. 6.5** that, allowing for the shift of the critical points, thermal cycling is effective for layers up to 100 μm thick. In deeper layers, the amplitude of thermal oscillations is insignificant, but an elastic-plastic wave takes place, which also adds to increase in mass transfer.

6.4 MASS TRANSFER IN CARBON STEELS

6.4.1 STEEL 9KHS (0.9 % C, 1 % CR, 1 % SI)

During plasma-detonation treatment (PDT) the surface of the alloy experiences a complex effect, such as shock, acoustic, electromagnetic and heat effects. Each of them, taken separately, plays the role of initiator of the diffusion processes occurring during surface modification. In PDT a dramatic acceleration of mass transfer takes place as a result of mutual influence of the above factors.

The Auger spectroscopy method was used to determine the values of mass transfer of nitrogen, oxygen and oxygen. Examinations were conducted on samples of tool steel 9KhS (0.93 % C, 1.4 % Cr, 0.4 % Mn, 0.03 % S, 0.03 % P, 0.35 % Ni). The quantity of plasma pulses affecting the sample surface (10–30 pulses) was varied during the treatment. The pulse frequency was $n=1.5$ Hz. The pulse duration was $t=10^{-3}$ s. The distance from the nozzle exit section to a sample was $H=80$ mm. And the charge at the capacitors was $C=1200$ μF .

Distribution of the concentration of elements through thickness of the layer was examined on oblique sections at an angle of 8° to the surface using the LAS-2000 unit. Graphical interpretation of variations in the concentrations fixed by the Auger spectral elemental analysis is shown in **Fig. 6.6**.

Multiple plasma-detonation treatment results in decarburization of the workpiece surface (**Fig. 6.6, b**). Thickness of the layer depleted in carbon considerably increases with the pulse quantity. Increasing the pulse quantity to 30 pulses leads to saturation of the sample surface with carbon from plasma components. As the treatment was conducted in air atmosphere, an oxide film is formed on the surface during heating, which is caused by high reactivity of oxygen. With further repetition of plasma pulses the concentration of oxygen atoms near the surface remains high, despite a partial or full decomposition of oxides. This results in the formation of a surface layer that hampers saturation of the surface with alloying elements. So, this is the cause of a high

oxygen concentration distribution through thickness of the layer. On the other hand, the oxygen distribution curves are of a regular character, which allows estimation of the coefficient of mass transfer of light-weight elements in PDT from their appearance.

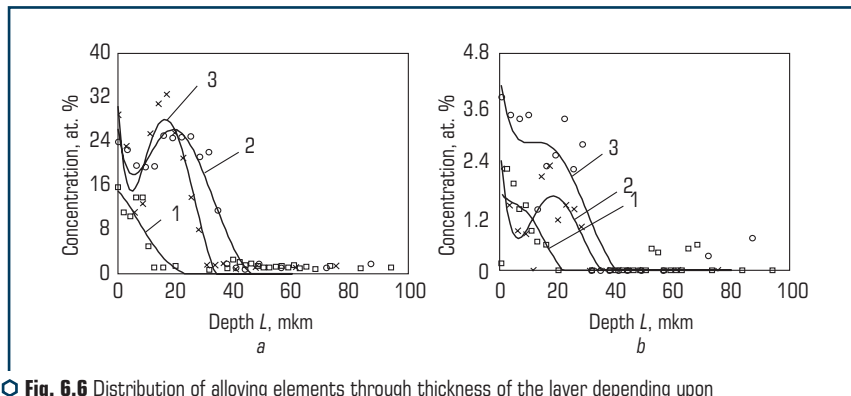


Fig. 6.6 Distribution of alloying elements through thickness of the layer depending upon the quantity of pulses: *a* – oxygen; *b* – nitrogen; 1 – 10 pulses; 2 – 20 pulses; 3 – 30 pulses

Estimate the coefficient of mass transfer, D , using the Fick law, $J = D \nabla N$ (where, J is the particle flow and ∇N is the particle concentration gradient). Go over to finite differences:

$$\frac{C_3 - C_1}{2} \cdot \frac{X_3 - X_2}{t_2 - t_1} = D \cdot \frac{C_2 - C_1}{X_2 - X_1},$$

then

$$D = \frac{C_3 - C_1}{2(C_2 - C_1)} \cdot \frac{(X_3 - X_2) \cdot (X_2 - X_1)}{t_2 - t_1}.$$

If to take two characteristic oxygen distribution curves at 20 and 25 pulses, we will have that $D \approx 1.5 \cdot 10^{-5} \text{ cm}^2/\text{s}$, which is by an order of magnitude higher than the coefficient of diffusion of, e.g., nitrogen in iron at $T = 1200 \text{ K}$.

The above coefficients of mass transfer are comparable with the coefficients fixed in the case of electromagnetic and deformation impacts on the surface. The authors of [155–158] consider such values of the coefficients abnormal and inexplicable from the standpoints of the current knowledge of diffusion.

As shown by experimental studies, during the pulsed plasma treatment process the coefficients of mass transfer of light-weight elements (N, O, C) amount to $K = 10^{-4} - 10^{-5} \text{ cm}^2/\text{s}$, which is in excess of the coefficients of thermal diffusion of nitrogen ($D = 1.5 \cdot 10^{-6} \text{ cm}^2/\text{s}$) at $T = 1000^\circ \text{C}$.

6.4.2 MODIFICATION OF α -Fe SAMPLES

Study of modification of metal surfaces was conducted on α -Fe samples [278]. In PDT molybdenum was introduced into the high-velocity plasma jet by placing a corresponding electrode set up as anode in the plasmatron.

The α -Fe sample surface after PDT (**Fig. 6.7**) has a characteristic roughness caused by its uniform fusion and rounding of all irregularity peaks.

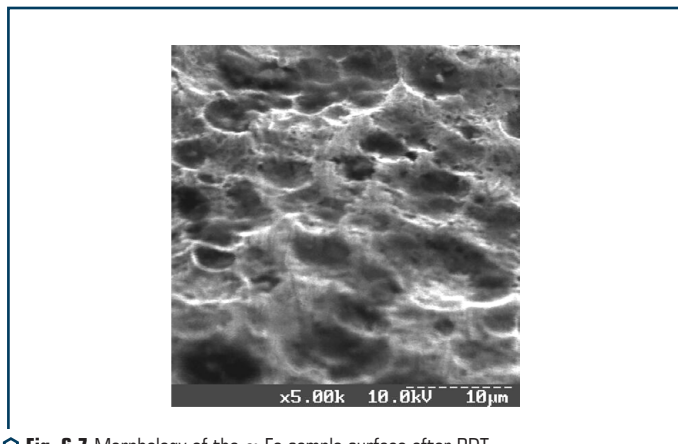


Fig. 6.7 Morphology of the α -Fe sample surface after PDT

Results of X-ray phase analysis of the α -Fe sample surfaces show that the main phase after PDT is bcc Fe (body-centred cubic crystalline lattice with $d=2.866$), Fe_7Mo_6 with lattice parameters of 2.157 (2.15), 2.086 (2.08) and 1.811 (1.80), and FeMo with lattice parameters of 2.157 (2.14) and 2.086 (2.09). Parameters of PDT of the samples are given in **Table 6.6**.

Table 6.6 PDT parameters

Sample No.	Quantity of pulses	Distance, mm	Frequency, Hz	Immersion of electrode, mm	Capacitance, μF
1	4	40	1.5	30	800
2	10				
3	15				
4	20				

The spectrum shows the boundary (kinetic factor) for Fe and Mo, the peak of the latter being on the right side. Formation of a small shoulder indicates to the formation of the compound with

a composition of FeMo_2 nears the surface in a layer about 300 nm thick. In addition, the spectrum recorded using the proton resonance shows a clearly defined carbon peak, **Fig. 6.8, 6.9**.

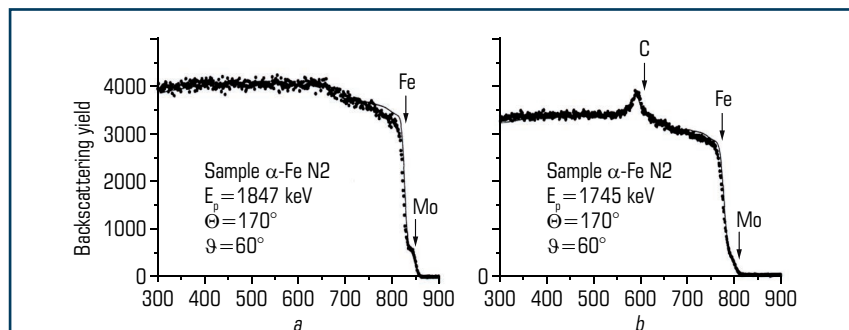


Fig. 6.8 Energy spectrum of Rutherford ion backscattering for the α -Fe sample after PDT (10 pulses) recorded by using ^4He : *a* – determination of molybdenum concentration; *b* – determination of carbon

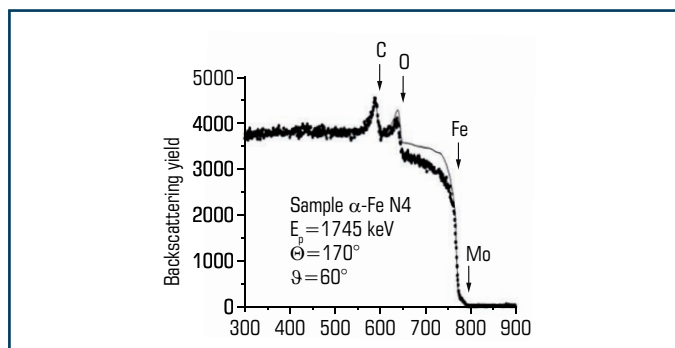


Fig. 6.9 Energy spectrum of Rutherford ion backscattering recorded by the method of elastic resonance of protons with an energy of 1.745 MeV to determine the concentration of carbon and oxygen on the α -Fe sample after PDT (20 pulses)

As can be seen from the spectrum, a high concentration of oxygen near the surface (about 40 at. %) is fixed in the surface layer, in addition to growth of the concentration of carbon and nitrogen. Further increase in the quantity of pulses leads to a still more intensive growth of oxygen on the surface.

Alloying elements have the following distribution through thickness of the modified layer (**Fig. 6.5**). The highest concentration of Mo was fixed near the surface (i.e. in a layer 10 μm thick). In PDT with 10 pulses the ultimate Mo concentration is about 8 at. %, while the maximum is located at a depth of about 7 μm from the surface.

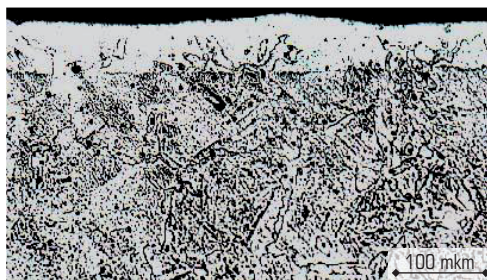
As shown by the studies, increasing the quantity of pulses leads to an insignificant increase in the concentration of carbon, whereas the concentration of oxygen is 40 at. % even after 15 pulses. Alloying the surface layer with molybdenum occurs with increasing the quantity of pulses from 4 to 20 and reaches a maximum concentration of 8 at. %. The maximum concentration is achieved after affecting the α -Fe sample surface with 10 pulses of the high-velocity plasma jet.

Analysis of structure of a transverse section of the α -Fe sample shows that thickness of the fused layer affected with 10 pulses of the plasma jet amounts to 50 μm and hardly changes with further increase in the quantity of pulses. Therefore, it is shown that the sub-surface layer can be alloyed with heavy metals (e.g. Mo) to a depth of more than 10 mm, and with nitrogen, carbon and oxygen to a depth of 5 μm by using the pulsed plasma generator with an eroding Mo electrode. As proved by metallography, the surface layer can be fused and alloyed in the melt to a depth of 50 μm .

6.4.3 MODIFICATION OF MEDIUM-CARBON STEEL SURFACE

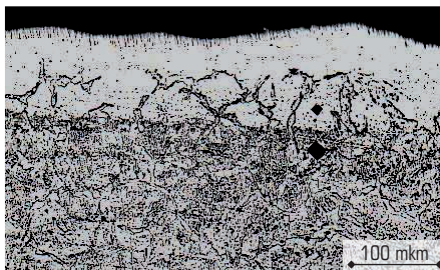
The studies were conducted on samples of medium-carbon steel (0.45 % C). PDT of the samples involved fusion of the sample surfaces. The use was made of the treatment conditions where the formed modified layer is not more than 50 μm thick.

Examinations of the transverse section of a sample showed that PDT resulted in an unetchable white layer formed on the surface (**Fig. 6.10**). The boundary between the white layer and structure of the metal substrate is indistinct and smeared. There is also some transient layer, but its thickness is smaller than that of the white layer. Thickness of the white layer may be different to some extent in different regions of a sample.



○ **Fig. 6.10** Surface layer of the steel 45 (0.45 % C) sample after PDT (3 pulses)

Hardening by PDT with 5 pulses results in a more distinct boundary between the white (nanocrystalline) and transient layers (**Fig. 6.11**).



○ **Fig. 6.11** Surface layer of the steel 45 (0.45 % C) sample after PDT (5 pulses)

The values of hardening and thickness of the hardened layer grow with increase in the intensity of PDT (decrease in D and h , and increase in N). In addition, they depend upon the electrode material. The trend to growth of hardening with increase in the atomic number of the electrode material is especially pronounced on steel U8 (**Fig. 5.2**). Hardening is higher in the case of the molybdenum and tungsten electrodes, compared with the stainless steel and titanium electrodes. This can be explained both by larger shifts of the substrate atoms bombarded by the plasma beam and by a higher hardening effect caused by the electrode elements introduced into solid solution of the sub-surface layer.

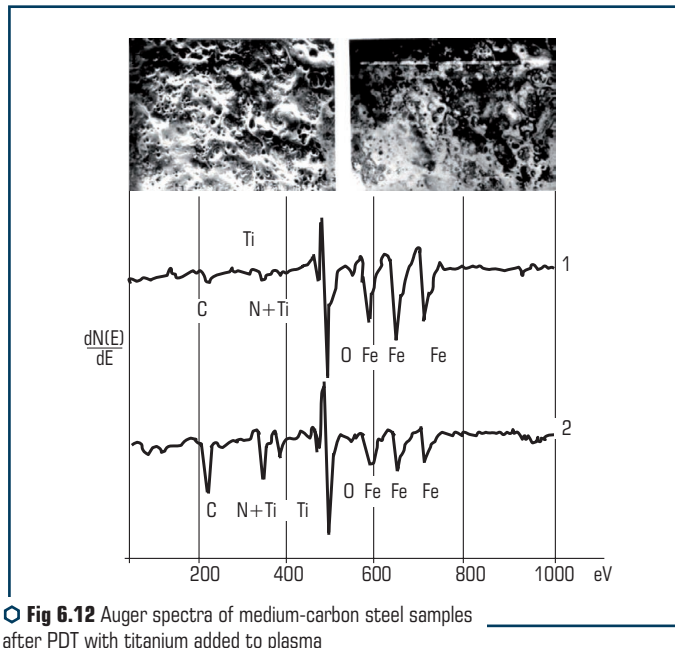
The pulsed plasma treatment takes place in local regions between cold volumes of the alloy. Therefore, α - γ transformations occur in a "restrained" layer and are accompanied by substantial deformation. It should be noted that the coefficients of mass transfer in deformation under the martensitic transformation conditions differ greatly from those under stationary conditions (without deformation).

Thus, carbon atoms during isothermal annealing and at a temperature of 613 K (temperature of the end of α - γ transformation) have a diffusion coefficient of 10^{-11} cm²/s, while iron and nickel atoms under the same conditions have a diffusion coefficient of $5 \cdot 10^{-21}$ cm²/s [279].

The highest effect in modification of carbon steels by PDT is achieved by using the plasma jet with a power of $1.8 \cdot 10^5$ W/cm², providing the ultimate temperature of the surface close to the melting point. The value of hardening and thickness of the hardened layer grow with increase in the intensity of PDT (decrease in D and h , and increase in N), and depend upon the electrode material. Modification is also affected by the quantity of treatment pulses, N . In addition, under comparable PDT conditions, modification is more pronounced in steel with higher carbon content.

Etching of the transverse section reveals an unetchable white layer near the surface subjected to PDT. Under certain conditions, this layer has an intermittent structure. The boundary between the white layer and structure of the metal substrate is indistinct and smeared. Besides, there is some transient layer, but its thickness is smaller than that of the white layer.

Alloying elements from the gas phase and metal electrode are always present in different regions of a sample. For example, after treatment of carbon steel with plasma containing titanium, carbon and nitrogen, the peaks of titanium and nitrogen can be seen in the Auger spectra of different regions of the treated surface (**Fig. 6.12**).



○ **Fig 6.12** Auger spectra of medium-carbon steel samples after PDT with titanium added to plasma

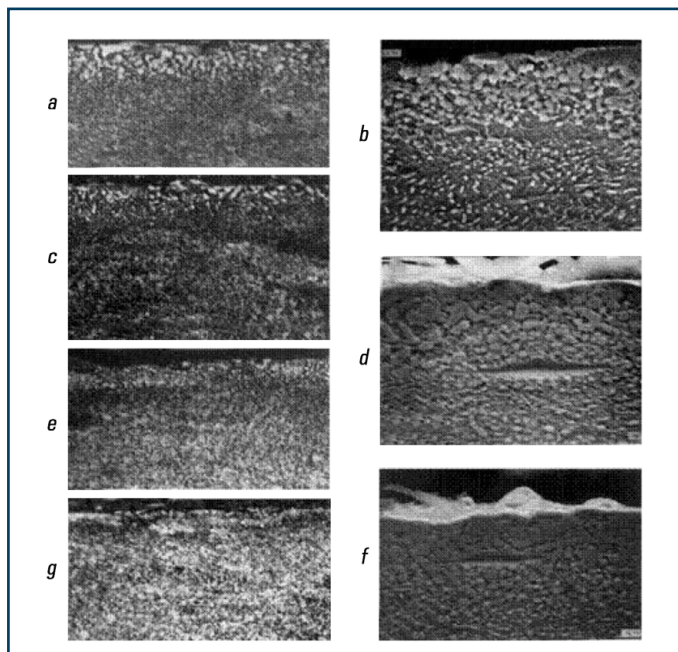
It can be seen that titanium is present in a combination with iron. Dark spots on the surface consist almost completely of carbon.

Results of examinations using the light microscope "Neophot-2" and scanning electron microscope T-20 fully coincide. It can be seen that the sub-surface layer of steel hardened by the pulsed plasma is characterized by the presence of a large number of white globules up to $3.5 \mu\text{m}$ in size (**Fig. 6.13**).

Microhardness of this layer ranges from 12 to 21 GPa, depending upon the treatment conditions. X-ray patterns of surfaces of the carbon steel samples hardened by plasma demonstrate the same phase composition as those of the structural steel samples. The $\gamma\text{-Fe}$ lines are most intensive, there is also a weak line of FeO. These lines are intensified with toughening of the treatment conditions and increase in the atomic number of plasma components.

X-ray patterns of hardened steel U8 feature splitting of the α -phase line caused probably by tetragonality of surface hardening martensite. This splitting is especially pronounced in lines $(110)\alpha$

and $(211)\alpha$. The amount of carbon contained in martensite can be estimated from splitting of the martensite lines. An increased carbon content of martensite after the pulsed plasma treatment, allowing for an extremely short duration of a plasma pulse, is attributable to an extra absorption of carbon from the plasma jet. Judging from the intensity of the austenite lines, the austenite content is lowest in the case of treatment with the chromium-containing plasma, and highest in the case of the tungsten electrode plasma (**Fig. 6.14**).

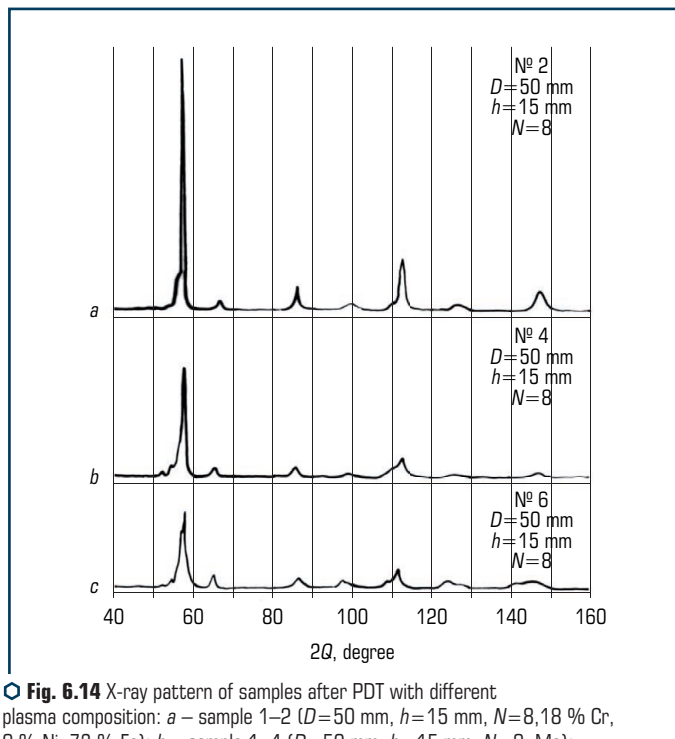


○ **Fig. 6.13** Microstructure of surface layer of the carbon steel sample after PDT using titanium electrode: *a, b* – sample 2-1 ($D=60$ mm, $h=15$ mm, $N=5$); *c, d* – sample 2-3 ($D=60$ mm, $h=35$ mm, $N=5$); *e, f* – sample 2-2 ($D=80$ mm, $h=15$ mm, $N=5$); *g* – sample 2-4 ($D=80$ mm, $h=35$ mm, $N=5$); *a, c, e* and *g* – light microscope images; *b, d, f* – scanning microscope images

This proves the assumption that the workpiece surface is heated to a higher temperature in the case of plasma containing elements with a higher atomic number.

The X-ray pattern of an initial sample shows weak lines of cementite, which vanish after plasma treatment. Physical widening of lines of retained austenite for steel U8 is identical to that for medium-carbon steels. This is in agreement with the conclusion that this widening is independent of the carbon content of alloy.

Characteristically, PDT is accompanied by a complex effect on the surface by a number of physical fields, which cause a high-rate deformation of local regions of the surface. The high-rate deformation results in a dramatic increase in the number of spot-like defects in a crystal, which are formed during the plastic deformation process. In this case the process of generation of defects is faster than the dynamic recrystallization process, which leads to acceleration of diffusion.



○ **Fig. 6.14** X-ray pattern of samples after PDT with different plasma composition: *a* – sample 1–2 ($D=50$ mm, $h=15$ mm, $N=8$, 18 % Cr, 9 % Ni, 73 % Fe); *b* – sample 1–4 ($D=50$ mm, $h=15$ mm, $N=8$, Mo); *c* – sample 1–6 ($D=50$ mm, $h=15$ mm, $N=8$, W). Records made in FeK α radiation

The dislocation velocities during the shock loading process amount to very high values even at low temperatures. The diffusion of atoms is likely to occur with moving dislocations. Therefore, the time of the effect has a strong influence on the coefficient of mass transfer. The pulsed treatment results in a dramatic heterogeneous hardening of metal, which is indicative of the formation of a clearly defined dislocation structure. The depth of the layer grows from 15–20 (1 cycle) to 30–35 μm (10 cycles) with an increased dislocation density and is a result of cyclic superposition of different physical fields in complex treatment.

ABSTRACT

The chapter presents the results of the study of the technology of pulsed plasma surfacing. The supply of metal in a liquid state to the plasma jet ensures its mixing with the material of the molten layer and the formation of a new alloy on the surface of the product. The high speed of the metal-containing plasma jet and the simultaneous exposure to a pulsed electromagnetic field ensures high quality mixing of the alloy being deposited with the melted surface of the product.

KEYWORDS

Metal-containing plasma jet, deposited alloy, gas-dynamic pressure, surfacing, productivity, alloying of the molten surface.

7.1 DESCRIPTION OF TREATMENT TECHNOLOGY AND ITS FEATURES

The pulsed plasma technology allows the surface layer 20–40 μm thick to be heated to a melting point. Feeding a molten metal to the plasma jet provides its mixing with material of a molten layer and formation of a new alloy on the workpiece surface. High velocity of the metal-containing plasma jet and a simultaneous impact by the pulsed electromagnetic field ensure a high quality of mixing of the deposited alloy with the fused workpiece surface. In PDT of porous materials, the deposited alloy may penetrate through pores to a depth of 40 μm . Fusion of the surface may be minimal. Treatment of the porous surface is accompanied by a gas-dynamic pressure of the combustion products, which leads to compaction of the fused surface and closing of the pores.

Device for microsurfacing (**Fig. 7.1**) consists of reaction chamber 1, internal electrode 2, small-size detonation device 3, systems 4 for feeding the material to be deposited and pulsed current source 5.

Filler material in the form of wire is fed to the reaction chamber. Feeding mechanisms are used to feed wire from semi-automatic surfacing devices. Filler (wire) is set up to the circuit as cathode. The workpiece surface is also set up as cathode.

After the plasma jet goes out from the channel of the reaction chamber (**Fig. 7.2**), region 4 filled with the electrically conducting gas is formed between the tips of electrode 1 and filler material 2 and workpiece surface 3. The pulsed electric current flows between the tip of electrode 1, workpiece surface 3 and tip of filler material 2 (wire or rod) fed into this gap.

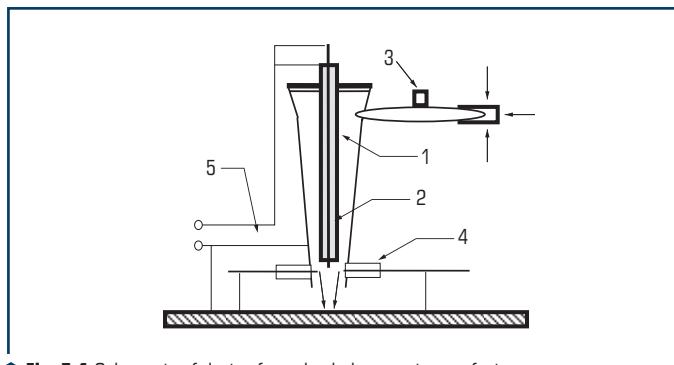


Fig. 7.1 Schematic of device for pulsed-plasma microsurfacing

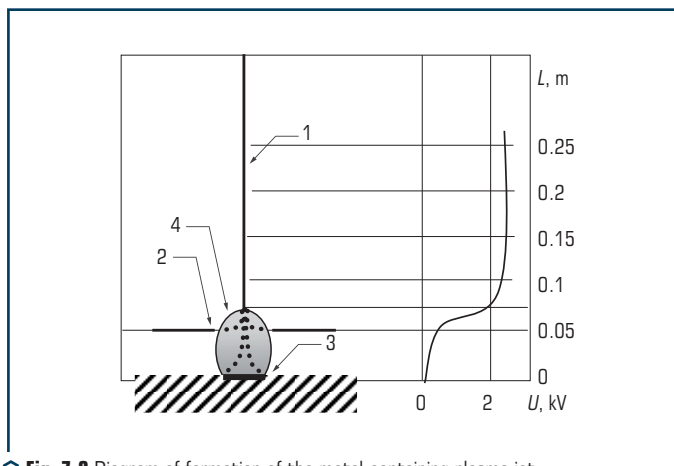


Fig. 7.2 Diagram of formation of the metal-containing plasma jet

Voltage in this region falls from 2.5 kV to 0. With the pulsed technology the plasma power density is known to depend upon the energy of the charge in a converter. A change in capacitance from 400 to 1200 mF allows achieving the plasma power density of 10^5 – 10^6 W/cm² at the cathode. The rate of heating of the electrode and workpiece surface at this power amounts to 10^6 – 10^7 K/s. The high-energy jet of the metal-containing plasma falling on the workpiece surface forms a shock-compressed layer on it. The electric current flows through the plasma jet with almost no losses at the tip of the filler material and workpiece surface, where it is converted into heat.

At an interaction time of 1 – $2 \cdot 10^{-3}$ s and current density of 3 kA/cm², the filler wire tips are overheated. Length of an overheated wire tip depends upon its diameter and amounts to 1.0 mm at a wire diameter of 2.5 mm. Dispersion of the overheated electrode material in its transition from

a meta-stable to stable state provides its introduction into the plasma jet in the vapor-drop state. The high-velocity plasma jet accelerates metal drops and presses them onto a fused workpiece surface (thickness of molten layer is up to 30 μm).

Calculations of the volume of molten metal on the workpiece surface and electrode tips showed that theoretical estimation can be made using formulae valid for the pulsed laser technology. The volume of molten metal at the electrode tip depends upon such factors as time, heat transfer coefficient, thermal-physical characteristics of metals and power density. The modification technology is implemented at a plasma jet velocity of 5–8 km/s, which forms a gas-dynamic component of the plasma effect on the workpiece surface.

The electric current forms a pulsed magnetic component with a magnetic field intensity of up to $4 \cdot 10^5$ A/m. The complex effect on the workpiece surface by the gas-dynamic and electromagnetic components provides mixing of the plasma components and filler metal with the substrate material, as well as its accelerated solidification.

Wires (rods) of Cu, Al, Cr, Mo, W and NiCr were used as a filler material. Distance D from the plasmatron chamber end to a sample was 50 mm, and distance h from the consumable wire (rod) to the electrode tip was 20 mm.

Heat flows to the cathode workpiece surface are estimated from analysis of the relationship (**Fig. 7.3**) having the following form:

$$q_c = U_{ac} \cdot J_{ac} - q_{nc} - q_l - q_{con}, \quad (7.1)$$

where q_l – the radiant energy losses on the side face of the shock-compressed layer; q_{con} – the losses due to convective heat exchange of the shock-compressed layer with the environment; J_{ac} – the current density; U_{ac} – the voltage of the electric field between anode and cathode.

Given that the area of interaction of the shock-compressed layer with the environment is by two orders of magnitude smaller than that with the heated surfaces of anode and cathode, losses q_l and q_{con} can be neglected. In this case formula (7.1) will have the following form:

$$q_c = U_{ac} \cdot J_{ac} - q_{nc}, \quad (7.2)$$

where $q_{nc} = J_{ac} / \sigma \varepsilon h$ – the Joule heat release; h – the length of the plasma column; $\sigma \varepsilon = n_e e^2 / m_e n_e$ – the electrical conductivity of the plasma column, $\text{Ohm}^{-1} \text{m}^{-1}$; n_e – the concentration of electrons, m^{-3} ; e – the electron charge, C; m_e – the electron mass, kg.

Calculations were made by the method described by Raizer [267]. It was assumed that the conductivity was of the electronic type. Also, it was assumed that $J_{ac} = 0.7 \cdot 10^7$ A/m², $U_{ac} = 3$ kV, $h = 42 \cdot 10^{-3}$ m, $n_e = (0.7-1) \cdot 10^{23}$ m⁻³, $m_e = 9 \cdot 10^{-31}$ and $e = 1.602 \cdot 10^{-19}$ C.

Numerical solution yielded a value of the heat power density on the workpiece surface equal to $q_c = 1.4 \cdot 10^9$ W/m². Allowing for energy consumption, efficiency of the electric energy consumed directly for heating of the cathode surface amounts to 65 %.

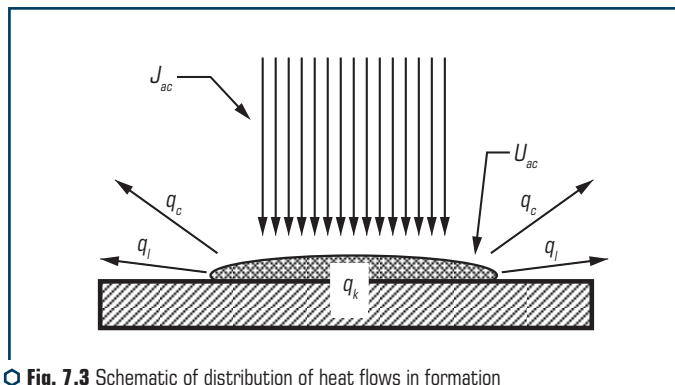


Fig. 7.3 Schematic of distribution of heat flows in formation of the shock-compressed layer

PDT is accompanied by high-power shock and sound waves, which interact with melt on the workpiece surface and generate short-wave acoustic phonons in an alloy. The main mechanism of establishing equilibrium in liquid metal alloys within a wide range of temperatures is interaction of conduction electrons with phonons.

Additional excitation of phonons increases their role in formation of thermal conductivity. In this case the efficiency of electron-phonon interaction is estimated through lattice constants, effective mass of an electron and mass of atoms. An extra factor allowing for frequency (50–20,000 Hz) and amplitude of phonons is also introduced into the calculations [186].

Long-wave acoustic phonons form a system of coherent waves, which are reflected during the process of collisions with atoms and molecules in a dense medium. The process of interference in the medium results in the formation of heterogeneities, which can act as unstable, rapidly disintegrating centres. High density of the acoustic centres compensates for their instability.

Under certain conditions, where, for example, acoustic waves transfer a high energy, or where the natural frequency of a medium coincides with a disturbing frequency, they can change physical properties of the medium in which they propagate. This causes smearing of cluster boundaries in a molten layer and fragmentation or rupture of coarse cluster formations [186].

Intensive treatment by sound waves at frequencies close or equal to frequencies of natural oscillations of a workpiece provides phonon disturbances at resonance phenomena, which enhances phonon-electron interactions and intensifies formation of defects of an interference nature.

PDT results in the formation of a liquid alloy layer with micro heterogeneous structure on the workpiece surface: clusters with closely packed atoms are surrounded by statistically packed (SP) atoms. Maximal hardening of the molten layer is achieved in partial dissolution of initial carbides and formation of a large number of zones with micro chemical heterogeneity of solid solutions in the irradiated layer. The peculiar effect is exerted by duration of a plasma pulse and structural state prior to deposition.

The presence in liquid metal of extra defects in the form of eddy magnetic currents (resulting from phonon-electron interactions), pressure loops and displacement of atoms caused by the impact by acoustic phonons, increases the number of clusters and smears their boundaries. This provides equality of energies in regions with clusters and statistically packed atoms, which is the necessary condition for formation of fine-grained structure during the process of solidification of a melt.

Migration of atoms after solidification can be intensified through increasing defectiveness of crystalline structure, taking place as a result of high-rate heating, phase transformation and plastic deformation. It is reported that value of plastic deformation in a range of $\Sigma \varepsilon = 10^{-7} - 10^{-3} \text{ s}^{-1}$ has a strong effect on diffusion. The coefficient of diffusion (mass transfer) grows within this range, which is attributable to a substantial increase in mean concentration of vacancies.

Acceleration of mass transfer is achieved also through deformation of metals and alloys during reversible martensitic transformations. The process of growth of a martensite crystal ($\alpha > \gamma$ transformation) induces substantial stresses, the relaxation of which leads to deformation of metal in micro volumes and increase in structure defectiveness. Each next event of $\alpha > \gamma$ transformation leads to increase in the dislocation density, as well as to increase in length of inter-phase and grain boundaries, which are the ways of accelerated diffusion.

In addition to the plastic deformation rate, the substantial effect on migration of atoms is exerted by energy of an electromagnetic field pulse.

In the case of pulsed compression [248], at 300 K and $\varepsilon = 1.7 \cdot 10^3 \text{ s}^{-1}$, depending upon the variations in energy of an electromagnetic field pulse, the coefficients of mass transfer vary for Cu from $D = 9.5 \cdot 10^{-3}$ to $D = 8.2 \cdot 10^{-5} \text{ cm}^2/\text{s}$, for Ni from $7.8 \cdot 10^{-3}$ to $D = 6.5 \cdot 10^{-5} \text{ cm}^2/\text{s}$, for Al from $D = 2.0 \cdot 10^{-2}$ to $D = 4.1 \cdot 10^{-5} \text{ cm}^2/\text{s}$, and for Fe from $D = 1.1 \cdot 10^{-2}$ to $D = 4.8 \cdot 10^{-5} \text{ cm}^2/\text{s}$.

7.2 MODIFICATION OF SURFACE WITH METALS BY THE PDT METHOD

7.2.1 PDT CONDITIONS AND INVESTIGATION RESULTS

Investigations were conducted on samples of steel 3 (C 0.3 %), steel 40X (C 0.4 %, Cr 1 %), cast irons and iron-graphite alloys (C 1 %, Cu 2 %, Fe – balance).

Experiments were carried out using the UN 138M plasma-detonation machine. Main parameters of PDT in plasma-detonation alloying of a melt (PDA) and solid-state plasma-detonation hardening (PDH), as well as results of measurements of thickness and hardness of a modified layer are given in **Table 7.1**.

Plasma-detonation treatment was performed using the fuel gas mixture of a stoichiometric composition. Alloying elements in the form of rods with a diameter of 4–8 mm were fed along the axis of the pulsed plasma generator through a hollow channel of electrode, or were fed laterally (**Fig. 7.1**).

● **Table 7.1** PDT modification parameters and results

Sample		Characteristics of surface after PDT				PDT conditions			
No.	Material	Hardness MPa	Thickness, μm		Hardness, MPa		Electrode	Q-ty of pulses	Distance, mm
			PDA	PDH	PDA	PDH			
149	Steel 3 (C 0.3 %)	1700	80	100	600	6000	Cu	1	30
149		1600	100	120	650	7000		5	30
150		1500	70	40	800	2500	Al	1	15
150		1500	250	45	800	2700		5	25
156		1600	80	30	7000	5000	Ti	1	15
157		1600	100	40	5000	5000		5	25
161		1100	45	30	4200	3300	W	1	15
160		1100	30	60	4500	3000		5	25
151		1500	40	30	7000	4300	Ni 40 %, Cr 60 %	1	40
159		1500	40	30	7000	4000		5	40
194	Steel 40X (C 0.4 %, Cr 1 %)	3100	10	45	–	3250	Ti	1	30
194		3100	40	50	6100	4700		5	40
193		3270	30	40	6000	6500	Al	1	30
193		3440	50	60	6100	5800		5	40
195		3500	30	50	6000	6700	Ni 40 %, Cr 60 %	1	30
195		3500	30	60	6000	6600		5	40
167	Iron-graphite (C 1 %, Cu 2 %)	1500	100	50	2100	4700	Ti	1	40
192		1500	40	–	5000	–	W	1	40
191		1500	39	–	5600	–	Mo	1	40
188		1500	90	–	7000	–	Al	1	40
180		2600	–	80	–	8500	–	8	60
181		2600	–	40	–	8000	–	4	60
182		2600	–	60	–	8500	–	5	60
184		2600	–	75	–	8500	–	10	60
185		2600	–	90	–	8750	–	15	60
241	Cast iron	1800	100	–	6800	–	Mo	3	40
243		3000	60	–	7800	–		3	40

Power density of the plasma jet was set by varying a distance from the exit section of the generator chamber to the workpiece surface, as well as by varying focusing of the plasma jet, which was made through immersing the electrode tip into the chamber from its exit section.

The pulse energy is determined by the total capacitance of the capacitors. The pulse energy of 2500 J was used for the experiments.

Alloying the melt on the sample surfaces was performed with single pulses. Alloying elements were added to the plasma jet in the form of gas and metal. The electrode consisting of alloying metal (rod or wire) is overheated, melted and partially evaporated under the effect of the electric current. The vapor-drop phases of this metal participate in microsurfacing. Intensification of this process is provided by the pulsed electric current, which is switched by the plasma jet (**Fig. 3.13**).

Amplitude values of the electric current depend upon the capacitance of a capacitor power supply and distance from the plasma generator exit section to a solid surface, i.e. cathode (**Fig. 3.13**).

7.2.2 MODIFICATION OF SURFACE WITH COPPER AND ALUMINIUM BY PDT

Microsurfacing with the vapor-drop phase of copper from the eroding electrode (copper rod 5 mm in diameter) forms a layer approximately 60 μm thick on the steel 3 sample surface (**Fig. 7.4, a**). X-ray phase analysis of the surface layer reveals the following phases: Cu, α -Fe, FeO and CuO. As shown by measurements of microhardness, the layer contains intermetallic inclusions with microhardness of up to 20,000 MPa.

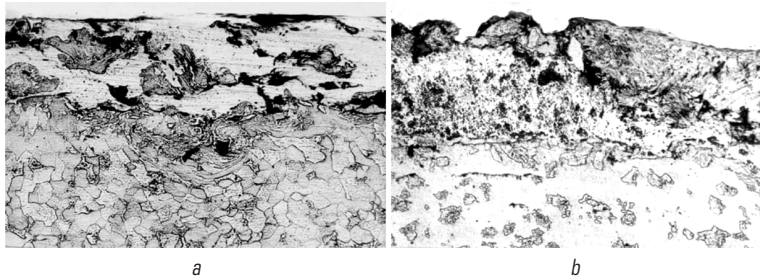


Fig. 7.4 Section of the surface layer of steel (0.3 % C) after one-pulse microsurfacing:
 a – with copper; *b* – with aluminium

The external layer of the coating contains a bluish monolithic phase with microhardness of about 800 MPa. Grains of the substrate mixed into the coating with a "vortex" structure have microhardness of 2000–2700 MPa. In addition, there are also numerous monolithic light-blue grains with microhardness of 6100 MPa, which are located within the interface zone of the substrate and in the grains mixed into the substrate. Microhardness of copper in the coating is 580 MPa. Microhardness of the substrate is 1700 MPa. Growth of grain of the substrate, caused by the thermal effect of the heat flows, is seen at a depth of about 100 μm from the sample surface.

Microsurfacing with aluminium results in a layer 40 to 100 μm thick formed on the sample surface.

The diffusion zone of light-grey monolithic intermetallic grains formed as a result of interaction of liquid aluminium with steel is located immediately under the deposited layer of aluminium. Below, there is the heat-affected zone about 40 μm thick, consisting of martensite (within prior pearlite grains) and structurally free ferrite. Some pearlite grains contain a clearly defined boundary of the heat-affected zone revealed by etching. This boundary divides the grains into the martensite (light portion of grain) and pearlite (dark portion of grain) regions. The substrate in an initial state, comprising pearlite and ferrite, is located beneath this layer.

X-ray phase analysis of the deposited layer reveals the following phases in the coating: Al, $\alpha\text{-Al}_2\text{O}_3$, $\alpha\text{-Fe}$, FeAl and FeAl_3 . Microhardness of the substrate ferrite is 1500 MPa, and that of the substrate pearlite is 2500 MPa.

7.2.3 MODIFICATION OF SURFACE WITH TITANIUM AND TUNGSTEN BY PDT

Microsurfacing with titanium and tungsten by fusion of the sample surface (1 pulse) forms a layer up to 80 μm thick (**Fig. 7.5**). Adjoining this layer is a heat-affected zone 15 mm thick. X-ray diffraction analysis reveals the following phases: $\alpha\text{-Ti}$, $\alpha\text{-Fe}$ and FeO. Values of microhardness of the deposited layer vary over wide ranges, i.e. from 4000 to 8000 MPa. Microhardness of the heat-affected zone is 4000–5000 MPa, and that of the substrate is 1000 MPa (**Fig. 7.5, a**). Increase in the number of pulses (up to 5) results in growth of the heat-affected zone to 60 μm , the microhardness value being unchanged. It should be noted that microhardness of the surface layer grows to 6,000–10,000 MPa. Phase composition of the coating is $\alpha\text{-Ti}$, Fe_3O_4 and $\alpha\text{-Fe}$.

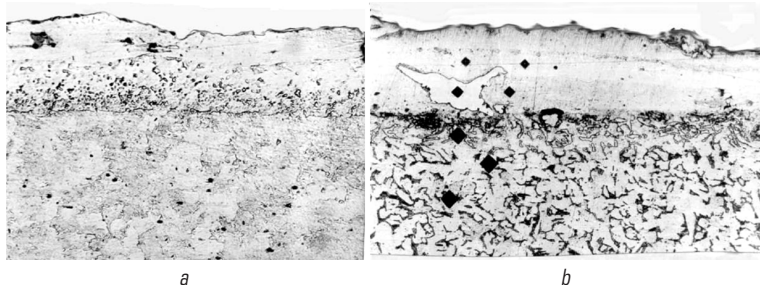


Fig. 7.5 Appearance of section of the surface layer of steel (0.3 % C) after one-pulse microsurfacing: *a* – with titanium; *b* – with tungsten

PDT by adding vapor-drop phases of tungsten into the plasma provides microsurfacing of the fused surface of a sample (**Fig. 7.5, b**). This results in the formation of a coating layer up

to 45 μm thick. Light tungsten and dark oxide inclusions can be seen in the coating. The heat-affected zone of the same thickness is located under this layer. This zone comprises martensite of eutectoid composition within the prior pearlite grains.

The substrate consists of pearlite and structurally free ferrite. X-ray diffraction analysis reveals the $\alpha\text{-Fe}$, $\gamma\text{-Fe}$ and W phases. Microhardness of the surface layer is 4100–4500 MPa, microhardness of light inclusions is 5400 MPa, that of the heat-affected zone is 3300–2500 MPa and that of the substrate is about 1100 MPa.

Different formations, looking like flattened metal drops flowing from the eroding electrode, are detected in the treated layer. A coarse (up to 20 μm thick) elongated particle of pure tungsten (100 % W) is seen at the interface with the substrate (**Fig. 7.5, b**). It is likely that this particle is in a quasi-liquid state, which allows it to deepen into the fused surface of a sample almost without diffusion and dilution with the sample material. No tungsten is detected in the substrate material near this particle. Thin tungsten interlayers with a tungsten content of about 3 % are located closer to the surface, while the content of tungsten in a layer adjoining the surface is 0.5 %.

Increase in the number of pulses to 5 leads to decrease in thickness of a light component of the surface layer and growth of the heat-affected zone to 60 μm (**Fig. 7.6**). X-ray phase analysis revealed the $\alpha\text{-Fe}$, $\gamma\text{-Fe}$ and W phases.

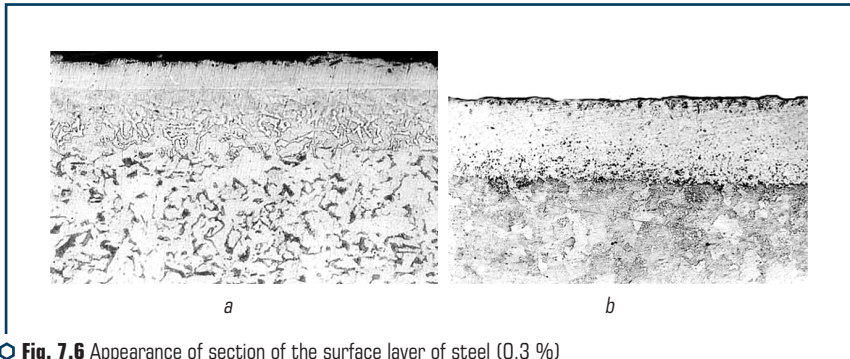


Fig. 7.6 Appearance of section of the surface layer of steel (0.3 %) after 5 plasma pulses containing: *a* – tungsten; *b* – titanium

Examinations of this layer showed a thin interlayer with increased tungsten content (up to 4 %) present at the interface with the substrate at a depth of 40 μm . A thin interlayer with increased tungsten content (up to 3 %) was seen at a distance of 18 μm from the interface with the substrate. The tungsten content between these layers is very low and equals 0.5 %.

PDT with a large number of plasma pulses results in the formation of surface layers with a uniform distribution of alloying elements, as well as interlayers with fine inclusions of a pure element. Analysis shows that a very thin interlayer enriched with tungsten is formed at the interface with the substrate.

It is followed by a layer with a tungsten content that gradually increases from 8 to 16 %. This layer is followed by a number of fine particle (98 % W), and then by a layer containing up to 18 % W. After that again a number of fine W particles can be seen, and the uniformly alloyed layer containing up to 20 % W adjoins the surface. This coincides with spectral analysis results, according to which the tungsten content of the surface layer after PDT is 11–20 %.

The surface layer subjected to one PDT pulse using a titanium filler metal was examined by the X-ray microanalysis method (**Fig. 7.5, a**). As shown by the examinations, the modified surface has a multi-layer structure. It consists of a thin interlayer at the interface with the substrate, containing up to 60 % Ti and 26–27 % Fe. It is followed by a layer of almost pure iron (98 % Fe and 1.7 % Ti). Above is the layer of almost pure titanium alloy containing up to 1.5 % Fe. A narrow diffusion zone is located between these layers. The external layer contains yellowish inclusions of a laminated structure with bluish boundaries (supposedly, these are intermetallics Fe-Ti and nitrides), as well as light-grey inclusions of iron oxides.

A more uniform alloying with titanium can be provided by multiple treatments with the titanium-containing pulsed plasma.

Fig. 7.6, b shows a layer alloyed with titanium, which consists of practically pure iron-base alloy (99 % Fe, 1 % Ti). Then follows a wide diffusion zone, i.e. interlayer, having a cast, finely crystalline structure. Dendrite axes are enriched with titanium (77–78 % Ti, 12–13 % Fe), while the spacing between dendrites contains less titanium (61–62 % Ti, 28–29 % Fe) than their axes. In addition, fine ($\ll 1 \mu\text{m}$) inclusions of a light-grey phase (71 % Ti, 12 % Fe) can be seen.

Surface alloying with molybdenum (molybdenum eroding electrode) provides a light alloy layer 9–33 μm thick formed on the sample surface. The heat-affected zone extends to a depth of 36–56 μm . It is characterized by an increased hardness of 5480–6740 MPa, compared with that of the substrate that is equal to 3000–3560 MPa. Increasing the number of pulses leads to growth of the heat-affected zone.

7.2.4 MODIFICATION OF SURFACE OF IRON-GRAPHITE ALLOY

Experiments were conducted on sleeves made from iron-carbon materials (Fe – substrate, C 1 %, Cu 3 %). Plasma-detonation treatment (PDT) conditions were unchanged, but different metals were used for alloying.

PDT with titanium leads to the formation of a dense coating with a uniform thickness of up to 100 μm on the sample surface. Microhardness of the titanium layer is 2100 MPa (**Fig. 7.7, a**). Titanium penetrates into the substrate material (mass transfer through pores and along grain boundaries) to a depth of up to 25 μm . The heat-affected zone is 50 μm thick. It is characterized by a much higher microhardness (4700 MPa) than the substrate (1500 MPa).

Tungsten forms a layer with a non-uniform thickness of 4 to 40 μm on the sample surface. The depth of penetration of tungsten through pores and along grain boundaries is 30 μm (**Fig. 7.7, b**).

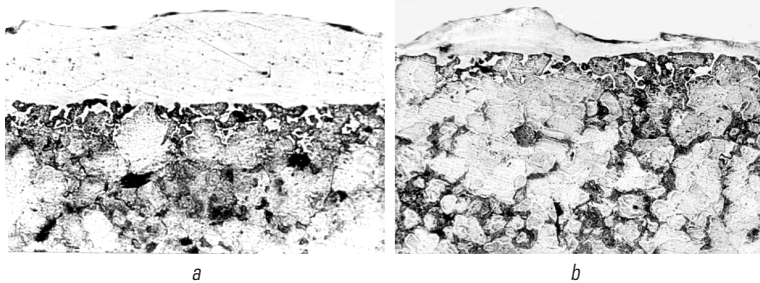


Fig. 7.7 Appearance of section of the surface layer of iron-graphite sample after treatment with one plasma pulse containing: *a* – titanium; *b* – tungsten

Molybdenum forms a dense, but non-uniform coating 6–39 μm thick (Fig. 7.9, *a*). The coating material penetrates into the substrate to a depth of 45 μm . Microhardness of the coating is 5000–7500 MPa, and that of the substrate is 1500 MPa.

Treatment of samples with plasma containing the vapor-drop chromium phase resulted in the formation of a uniform coating up to 45 μm thick (Fig. 7.9, *b*).

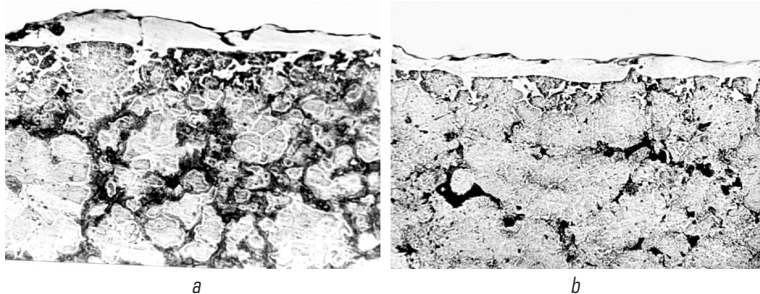


Fig. 7.8 Appearance of section of the surface layer of iron-graphite sample after treatment with one plasma pulse containing: *a* – molybdenum; *b* – chromium

PDT with plasma containing nickel-chromium leads to the formation of a non-uniform uneven coating from 4 to 45 μm thick on the surface. There are regions with a deep penetration of the coating material (NiCr) to the substrate. Microhardness of the coating is 5000 MPa.

Alloying of the sample surface with aluminium results in the formation on it of a two-layer coating with a continuous external layer and discontinuous light internal layer. Thickness of the external layer varies from 15 to 90 μm , and that of the internal layer – from 15 to 40 μm . The coating contains oxide inclusions. The coating material penetrates into the substrate through pores and

along grain boundaries. Microhardness of the external layer of the coating is 700 MPa, and that of the internal layer comprising intermetallic of the Fe-Al system is 5000–7000 MPa.

As shown by metallography of the samples, plasma-detonation alloying provides a dense layer strongly adhering to the substrate on the surface of the iron-graphite samples. Thickness of this layer depends upon the amount and temperature of metal in the plasma jet. Structure and phase composition of the modified layer depends upon the chemistry of the fused layer and its formation conditions.

After PDT without adding vapor-drop metal phases into plasma, a slightly etched layer with microhardness of 4600 MPa is formed on the sample surfaces (**Fig. 7.9**). In some places the layer is separated into two parts, the external part of which has hardness of 6400 MPa and internal part – 4600 MPa. Thickness of the hardened layer is up to 80 μm (**Fig. 7.9, a**). Microhardness of a light component of the substrate is 1700–2600 MPa (structurally free ferrite), and that of a grey component is 2300–5500 MPa (pearlite).

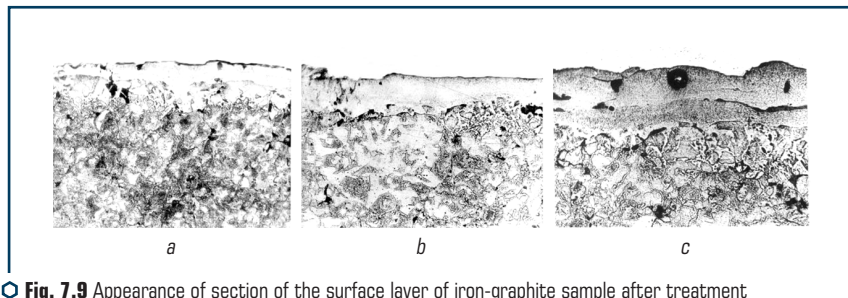


Fig. 7.9 Appearance of section of the surface layer of iron-graphite sample after treatment with plasma pulses containing no metal: *a* – one pulse; *b* – three pulses; *c* – five pulses

Toughening of the PDT conditions leads to increase in thickness of the light layer with microhardness of 8500 MPa to 80 μm (**Fig. 7.9, b**). At a large number of plasma pulses a thin layer of iron oxide is formed on the sample surface. Microhardness of the hardened layer varies from 7000 to 8000 MPa. Thickness of the layer is up to 100 μm . Microhardness of a light component of the substrate is 1650 MPa, and that of a grey component is 2040 MPa (**Fig. 7.9, c**).

7.3 MODIFICATION OF SURFACE WITH ALLOYING ELEMENTS CONTAINED IN COVERINGS

7.3.1 LASER ALLOYING

One of the methods of laser thermochemical treatment (LTCT) is laser alloying of metal surfaces. In this case composition of the surface layer can be changed through its combined alloying with filler elements. LTCT is performed by fusion of the coatings preliminarily deposited by this or

that method, or by fusion of powders added to the surface treatment zone [280–285]. Combined fusion of filler materials and surface layer, as well as super rapid solidification (10^4 – 10^7 K/s), allows formation of oversaturated solid solutions of alloying elements on the surface.

Laser alloying can be applied to improve service properties of parts, such as corrosion, wear and heat resistance and red hardness. In this case saving of alloying material may amount to 90–99 %, as laser alloying results in the formation of only thin layers of alloys on the surface of carbon or low-alloy steels.

Much information on laser surface modification can be found in domestic technical literature. As a rule, experiments were conducted by the following method. The first step comprises deposition of covering (paint) of a micro powder with a binder (sodium silicate – liquid glass) on the surface to be hardened. And the second step comprises fusion of the solidified covering (paint) together with the surface under the effect of the laser beam.

The paint is made from graphite and micro powders of hard alloys based on WC+Co. The liquid glass affected by the laser beam is evaporated and exerts no effect on microstructure of the substrate material. The use of the graphite-base paint leads to increase in the carbon content of metal to 3.3 %. Covering with the paint containing tungsten powders increases the tungsten content by a factor of 1.7 (up to 30 %).

Laser treatment of the surface with a preliminarily deposited layer of graphite powder provides the effect of alloying with carbon. Case-hardening in laser treatment can be provided both by surface fusion and by high-rate heating without fusion. The presence of activators (salmiac, borax) in the graphite-containing coverings enhances the case-hardening effect. Thickness of the case-hardened layer in the case of surface fusion may amount to 100–150 μm . deposition of carbon coverings leads to increase in the carbon content of the surface layer to 1.3–1.4 %.

Techniques employed for laser alloying are almost identical: first a layer of alloying elements or their mixture is deposited on the surface, and then this layer is fused together with the workpiece surface.

As proved by the cost effectiveness analysis, laser alloying has lower energy consumption, compared with traditional technologies, such as case-hardening, borating and nitriding.

In addition, laser treatment of borated layers decreases their brittleness (10–15 times) and allows widening of the borating technology application field [285]. The technology sequence is as follows. Coverings (paints) based on the BF-2 adhesive are deposited on the surface. Then they are dried at a temperature of 50–100 °C for 30 min. After drying of the paint on the workpiece surface, it is fused together with the surface by laser ("Quant-16"). The pulse energy is 520 J. As a result, boride layers 50–100 μm thick with microhardness of up to 21,000 MPa are formed on the surface.

Studies [20, 285] give data on alloying of surfaces from coverings containing such elements as Cr, W, Mo, V and Al. Alloying as it is with the above elements provides only insignificant increase in surface hardness. Nevertheless, investigation of saturation of the steel surface with nitride- and carbide-forming elements, taking place during laser heating, is of interest in terms of not only

increasing wear resistance and contact strength, but also in terms of preparation of the low-carbon steel surface for thermochemical treatment, such as nitriding, case-hardening and other hardening technologies, which are widely applied in industry. This combined surface treatment provides a higher wear resistance of surfaces of low-carbon steel parts than nitriding.

In study [281] the samples of structural steels 20 (0.2 % C), 40 (0.4 % C), 45 (0.45 % C), 20X (0.2 % C, 1 % Cr) and 40X (0.4 % C, 1 % Cr) were used as matrices. Treatment of the experimental samples was conducted using the gas-discharge CO₂-laser (of the LOK-2M type) with a power of up to 1 kW and laser beam velocity of 2 to 30 mm/s. Also the technological laser of the pulsed type "Quant-16" with energy of up to 240 J was employed.

The laser alloying process parameters include radiation power density q and amount m of the covering deposited on the surface. Thickness of the alloyed zone grows with increase in the radiation power. Thickness of the zone varies in a different way, depending upon the powder used in a covering. This is attributable to different thermal-physical properties of powder materials. Change in the amount of the saturating covering deposited on the surface treated has a substantial effect on thickness of the alloyed zone. An optimal amount of the covering deposited on the surface is $m=22\text{--}30\text{ mg/cm}^2$. Increasing velocity of movement of the laser beam from 2 to 30 mm/c leads to decrease in thickness of the alloyed layer from 800–900 to 200–300 μm . At a fusion treatment rate of $v=10\text{--}20\text{ mm/s}$, the LTCT zone has maximum of the concentration of alloying elements. Decrease in the concentration of elements at $v<10\text{ mm/s}$ is associated with large volumes of the fused zones. At $v>20\text{ mm/s}$, the concentration of elements decreases because of burning out of a large amount of the alloying covering before the beginning of fusion of the material treated.

Local X-ray microanalysis and filming in characteristic radiation of appropriate elements showed that alloying elements within the LTCT zone were distributed mostly uniformly both after pulsed and after continuous treatment. In the first case the content of alloying elements in the surface layer is 2–5 %, and in the second – 5–7 %, depending upon the type of an element added. Alloying of low-carbon steels with tungsten and molybdenum was performed at a minimal power of $q_{\min}=2.58\cdot10^6\text{ W/cm}^2$ and at $q_{\min}=1.6\cdot10^6\text{ W/cm}^2$, respectively [281–284].

Of interest is to deposit a covering directly ahead of the laser beam affected zone [285]. Coverings are usually made from a hard-alloy powder and appropriate binder. It should be taken into account in making of a covering that the binder must be evaporated within a short period of time during which the hard-alloy material still exists in a compact form, otherwise the powder particle will be blown out by a shielding gas. The heating process should provide evaporation of the binder and its derivatives. On the other hand, the binder should be made resistant to rapid drying, which is important for storing it under conventional conditions.

Proportion of the amounts of the binder and hard-alloy material has a strong effect on the coating deposition process. A high content of the binder leads to deceleration of evaporation and decrease in the efficiency. The optimal proportion of the binder and powder is 1:1. As shown by measurements, with the Co-Ni-Cr-W-B-Si mixture (Wallex 50) used as the powder, the value of microhardness of the coating ranges from 629 to 800 HV_{0.2}, depending upon the dilution degree.

Coating (Wallex 50) produced by laser fusion has a better wear resistance than a similar coating deposited by the plasma method [20].

7.3.2 MODIFICATION BY PDT USING COVERINGS

Analysis of experimental studies on laser modification using coverings (paints) shows that fusion of the coverings on the surface can be provided by pulsed plasma. Experiments were conducted on the basis of these studies to investigate plasma-detonation modification of surfaces with alloying elements contained in coverings (paints). Pulsed plasma treatment conditions and methods used to form the layer of filler materials were checked on the basis of the above results on LTCT.

Coverings were deposited on samples of St. 3 (0.3 % C) at $D=14$ mm and $h=7.96$ mm. Powder of the hard-alloy material VK15 (80 % W, 14.20 % Co, 5.12–0.045 % C, 0.039 % Fe) with a particle size of less than 10 μm was used as the covering base. The BF-2 adhesive served as the binder. Proportion of the hard alloy powder and binder was 2:1. The mixture was diluted with alcohol to provide a uniformly deposited layer. Covering layers 30–150 μm thick were deposited on the samples. Preliminary drying was performed in a drying box at a temperature of about 150 °C for 20 min. Distance from the plasma generator nozzle exit section to sample, H , electrode extension h and quantity of pulses were varied during plasma-detonation treatment.

As proved by the experiments, coverings more than 50 μm thick were not fused and not sintered during treatment with the pulsed plasma jet. The covering layer was partially destroyed after multiple treatments with plasma pulses. Fusion took place on the surface of a sample cleaned from the covering layer. The covering layer less than 50 μm thick was fused with a single plasma pulse. The treatment distance was 50 mm, the electrode extension was 15 mm and capacitance of the capacitors was 1200 μF .

Examinations of samples showed that the coating was formed not as a continuous layer, but as a number of small isolated regions (10–30 μm in size). Fusion of base metal and its splash over the surface of the deposited layer take place within the zone of the direct impact by pulses. This effect was not seen with distance from the sample centre.

Electrolytic etching reveals that the fused region of base metal under the coating has a cast structure. Here the values of microhardness vary from 1430 to 1810 MPa, and those of the white region vary from 4290 to 5720 MPa.

Examinations of phase composition of the modified layer by X-ray diffraction analysis showed that the main phase was $\alpha\text{-Fe}$. The lines next in intensity to the above one corresponded to the $\text{Co}_6\text{W}_6\text{C}$ and WC phases.

PDT by sintering the covering of binary titanium-chromium carbide was performed on samples of steel 40X (0.4 % C, 1 % Cr). The synthetic adhesive of the BF-2 grade was used as a binder. Treatment was performed with 5 plasma pulses using the molybdenum electrode. Metallography revealed two layers on the sample surface (**Fig. 7.10**).

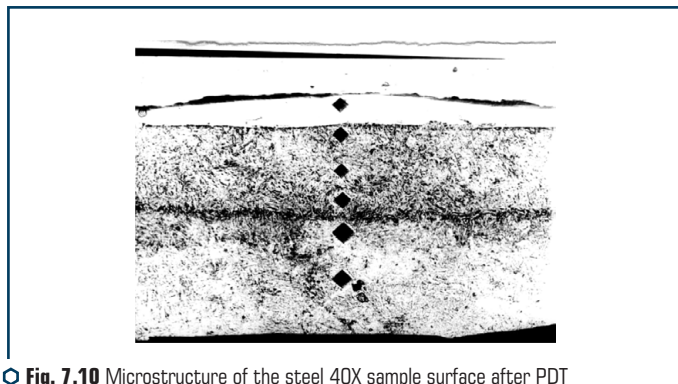


Fig. 7.10 Microstructure of the steel 40X sample surface after PDT by fusion of the binary titanium-chromium carbide with the BF-2 adhesive binder

The first is the external layer up to $35\text{ }\mu\text{m}$ thick. This layer is light, non-etched, having microhardness of $700\text{--}8000\text{ MPa}$. And the second layer is the internal layer up to $70\text{ }\mu\text{m}$ thick. This layer has an acicular structure, which is likely to consist of a bainite and martensite mixture. Microhardness of this layer is $4600\text{--}6700\text{ MPa}$.

The substrate is a sorbite of tempered steel 40X with microhardness of 4000 MPa . As proved by technical-economic analysis of the efficiency of the two technologies, i.e. LTCT and PDT, PDT is characterized by energy consumption which is 5–10 times lower, as well as by a reduced cost of the equipment involved. Pulsed plasma surfacing has power consumption of up to 10 kW/h per 0.3 m^3 of the surface. Productivity of microsurfacing depends upon the consumed electric power and is $0.2\text{--}0.5\text{ m}^2/\text{h}$. The surface modification technology is based on using high-velocity plasma jets formed by the overcompressed detonation waves. Duration of pulses is $1\cdot 10^{-3}\text{ s}$, frequency is $2\text{--}6\text{ Hz}$ and pulse energy is 4 kJ . Velocity of the plasma jet is $5\text{--}8\text{ km/s}$, and plasma temperature is $25,000\text{--}30,000\text{ K}$. The electric current of $1\text{--}3\text{ kA}$ is passed through the plasma jet.

The set of energy parameters of the pulsed plasma is sufficient for high-efficiency alloying of surfaces of parts using coverings. Results of investigation of metallurgical processes occurring in alloying of the fused surface of a part are of interest in terms of formation of layers of new alloys with predictable properties.

ABSTRACT

The efficiency of pulse-plasma processing of various metals and alloys is considered. The results of the structural-phase analysis, as well as the physical and mechanical characteristics of the hardened layers are presented.

KEYWORDS

Cast iron, steel, hard alloy, titanium alloys, metallographic analysis, efficiency of pulse-plasma treatment.

8.1 PLASMA TREATMENT OF HIGH-STRENGTH CAST IRON

Cast iron is widely applied in many industries. It is used for manufacturing such parts as machine slideways, cam- and crankshafts, forming rolls, etc.

Traditional methods of volumetric heat treatment and surface hardening (e.g. with high-frequency currents) do not allow potentially high operating properties of cast iron to be realized to a sufficient degree. Therefore, development of new hardening methods is a topical area of current R&D efforts.

Much experience has been accumulated in the field of laser, electron beam and plasma [286–290] hardening of different grades of cast irons. Plasma holds high promise for treatment of cast iron, which is provided by the possibility of not only hardening local surfaces, but also producing surface layers in the nano-crystalline or even amorphous state. This opens up new areas for practical application of plasma technologies to achieve a high level of performance of cast iron parts. In addition, plasma hardening of cast iron can be effectively employed also in combination with other surface treatment methods [291].

Comprehensive volumetric plasma hardening of cast iron parts is of industrial interest [292]. This technology is efficient for hardening of high-strength cast iron containing a pearlite-cementite base and globular graphite. Studies were conducted to investigate peculiarities of phase and structural transformations, dynamic crack resistance and character of fracture of high-strength cast iron, which is extensively applied, for example, for manufacture of forming rolls.

High-strength cast iron (2.64 % C, 1.41 % Si, 0.36 % Mn, 0.35 % Cr, 0.88 % Ni, 0.132 % P, 0.009 % S) in the initial state contains up to 10 % of free cementite and up to 8 % of graphite. Samples measuring 10×10×55 mm were subjected to plasma treatment across

one of their lateral faces. Hardening conditions were as follows: total thermal power of the plasma jet – 32 kW, specific thermal power – $1.14 \cdot 10^5$ W/cm², and plasmatron travel speed – 25 and 40 m/h in treatment with and without fusion, respectively. Some of the samples were subjected to preliminary volumetric oil quenching from 900 °C or finish volumetric tempering at 300 °C (holding for 2 h, furnace cooling). The plasma hardening process parameters and investigation results are given in **Table 8.1**.

● **Table 8.1** Properties of high-strength cast iron after plasma hardening

Sample No.	Variant of treatment	H_v before hardening, MPa	H_v after hardening, MPa	KC , MJ/m ²	KC_3 , MJ/m ²	KCP , MJ/m ²	P_{oc} , kN	K_{Hv} , MPa* (m) ^{1/2}
1	I	240–270	–	0.099	0.087	0.012	3.36	–
2	I+PH	240–270	740–810	0.051	0.039	0.012	2.97	–
3	I+PHF	240–270	790–835*	0.024	0.012	0.012	2.11	–
4	I+PHF+VT	240–270	815–860*	0.028	0.016	0.012	2.29	–
5	I	240–270	–	0.036	0.024	0.012	2.75	7.1
6	I+PH	240–270	740–810	0.031	0.019	0.012	2.42	6.2
7	I+PH+VT	240–270	675–720	0.033	0.021	0.012	2.92	7.5
8	VQ	530–590	–	0.015	0.011	0.004	1.87	4.8
9	VQ+PH	530–590	755–800	0.023	0.019	0.004	2.10	5.4
10	VQ+PH+VT	485–520	690–725	0.027	0.021	0.006	2.57	6.6

Note: * – hardness of the fused zone. Designations: I – as-cast condition; PH and PHF – plasma hardening without and with fusion, respectively; VQ – volumetric quenching; VT – volumetric tempering

As shown by the investigations [292–294], plasma treatment forms a hardened layer (plasma-affected zone – PAZ) with a circle segment shape on the cast iron surface. PAZ formed after treatment without fusion is 2.4 mm deep and 12 mm wide, and after treatment with fusion it is 3.2 mm deep (depth of the fused layer is 0.5 mm) and 14 mm wide. No transition zone between PAZ and initial structure is formed in plasma treatment of cast iron, which is attributable to a high concentration of heat input. Similar structures are formed also in cases of laser hardening [293–295].

Experimental studies show that plasma treatment without fusion leads to transformation of the pearlite matrix into a finely dispersed martensite, which is caused by heating of the surface to an austenization temperature and rapid cooling. According to the data of X-ray diffraction analysis, PAZ contains retained austenite (up to 10 %). Also, it retains the total graphite content. Hardness of cast iron after plasma treatment grows more than 3 times. It becomes much in excess of that achieved with volumetric quenching. This is provided primarily by a high degree of dispersion of martensite formed during plasma treatment. At the same time, plasma treatment causes decrease

of almost 2 times in crack resistance characteristics (impact toughness) of cast iron. Decrease in crack resistance results from decrease in energy of crack initiation in a more brittle PAZ metal, compared with the initial one. Globular graphite particles in high-strength cast iron, both in its initial structure and in PAZ, do not act as centres of secondary micro fractures, as no cracking of these particles was detected.

Plasma treatment involving surface fusion leads to realization of the effect of chilling of cast iron. Free graphite transfers to liquid solution, and a layer of ledeburite is formed during solidification. Crystalline grains of ledeburite are oriented in a direction of heat removal, i.e. from surface of the fused layer to base metal. At the same time, individual coarse graphite particles remain non-melted and act as a cold wall in solidification of ledeburite. Investigations showed similarity of the main structure and phase features of ledeburite in plasma [292] and laser fusion. These are a high degree of dispersion of structure, high hardness and increased austenite content (about 50 %). Another distinctive feature of ledeburite as a structural component of high-strength cast iron is its high brittleness. The character of crack propagation in a fused layer between grains is attributable to high brittleness of the eutectic phase between dendrites. This structure leads to a still greater decrease in impact toughness (2 times, compared with treatment without fusion), which is caused by decrease in energy of crack initiation.

Volumetric quenching of high-strength cast iron results in a dramatic decrease in its crack resistance. Martensitic structure of cast iron, quenched in the bulk, has coarse needles, which causes crack propagation by the mechanism of cleavage outside the crystalline grains (between the grains). Secondary microcracks propagating normal to the fracture surface are contained in regions adjoining the graphite particles.

Plasma hardening of cast iron results in refining of grains (needles) in structure, which provides substantial increase in its crack resistance due to increase in the crack initiation energy. Like in treatment in the initial state, the martensitic base of PAZ is characterized by high hardness and high degree of dispersion, i.e. almost by an order of magnitude higher than after volumetric quenching. Increased fracture toughness at a higher hardness provides the efficiency of highly concentrated (plasma) surface heating used instead of volumetric heat hardening.

The feasibility of realizing "multiple" fracture and retardation of cracks was proved through dynamic loading of parts of high-strength cast iron with globular graphite treated by the plasma jet. This makes it appropriate, in terms of cost effectiveness and properties achieved, to widely apply plasma surface treatment of cast iron parts in the initial state without fusion.

Comprehensive treatment, including volumetric quenching, plasma hardening and subsequent tempering, can be recommended only in special cases. In such cases, it is necessary to take into account decrease in crack resistance of cast iron. In turn, surface plasma treatment is undoubtedly effective for cast iron parts subjected to volumetric quenching, as it leads to simultaneous increase in hardness and crack resistance.

Plasma treatment provides PAZ with the properties that can be regarded as properties of a laminated composite material with the hard surface layer and relatively soft internal layer.

8.2 PLASMA-DETONATION HARDENING OF CAST IRON

Plasma-detonation hardening of cast iron samples was performed with the pulsed plasma containing a vapor-drop phase of molybdenum. The eroding molybdenum electrode was installed in the plasma generator. Distance from the nozzle exit section of the generator was $D=30$ mm, and immersion of the electrode tip was $h=20$ mm. The number of pulses, N , and capacitance of the capacitors discharged per pulse were varied.

The following characteristics were determined as a result of the studies: character of variations in structure, thickness and microhardness of the heat-affected zone (HAZ), quantity of plasma pulses affecting the surface, and their energy.

As shown by metallography, PDT results in the formation of an electrode material layer on the sample surfaces. The surface layer of cast iron has a microcrystalline acicular structure, which is characterized by the presence of non-dissolved globules of the electrode material.

The chilled cast iron layer (white layer) with hardness of 8,000–11,000 MPa, depending upon the PDT conditions, is located immediately beneath the fused layer.

The surface of the samples has roughness (round drops of solidified metal) characteristic of the high energy density treatment conditions, which hardly changes under conditions with a low energy density.

In the case of using copper + zinc alloy electrodes the surface acquires a yellowish color, which is caused by the deposited electrode material, whereas in the case of using chromium electrodes it has a silver color. Color of the surface is also affected by the fuel mixture composition. Excess of the fuel gas (propane – butane) paints the surface of the samples in a dirty-grey color, independently of the electrode material.

Modification of the surface of grey pearlitic cast iron (with a low content of ferrite) results in the formation of two layers. Total thickness of these layers is 90–100 μm (**Fig. 8.1**). The external light layer 30–50 μm thick has a slightly etchable acicular structure with microhardness of 5000–8000 MPa. The internal layer has a fine-acicular bainitic-martensitic structure with microhardness of 7000–9000 MPa, and contains individual soft regions of ferrite.

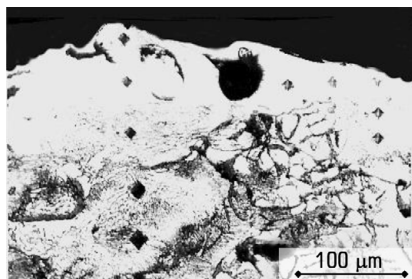
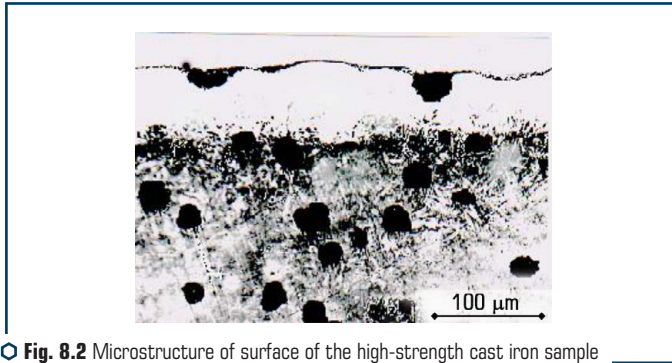


Fig. 8.1 Microstructure of surface of the grey cast iron sample after PDT

The modified layer contains flaky graphite inclusions, which can act, on the one hand, as stress raisers in a material and, on the other hand, as a solid lubricant in sliding friction assemblies. The similar result was obtained with cast iron containing inclusions of spherical graphite particles (**Fig. 8.2**). In this case these spherical graphite inclusions remained undissolved and persisted in the modified layer. Microhardness of the pearlitic component is 2700–3000 MPa, and that of the ferritic component is 1700–2300 MPa.



○ **Fig. 8.2** Microstructure of surface of the high-strength cast iron sample with spherical graphite particle inclusions after PDT

Pulsed plasma treatment of high-strength pearlitic cast iron causes the formation of a layer 45–60 μm thick on its surface. This layer consists of a structureless and acicular martensite with microhardness of 8000–9000 MPa. The cast iron samples were heat treated prior to PDT. The substrate has an acicular bainitic structure with microhardness of 4500–4700 MPa (**Fig. 8.3**). Auger spectroscopy revealed molybdenum, carbon, iron, oxygen and small amounts of copper and zinc present in the sample surfaces modified by PDT (**Fig. 8.4**). PDT was performed with plasma (containing carbon, nitrogen and oxygen) by adding a vapor-drop molybdenum phase. Copper and zinc were added to plasma from the electrode material used to fix the molybdenum rod. It should be noted that the modified layer, which is located closer to the surface, contains no graphite inclusions. It is very likely that carbon of these inclusions was dissolved in the surface layer, which provided its additional alloying with molybdenum and increased the hardening efficiency. Maximal microhardness fixed at a depth of 10–80 μm is 14,000–15,000 MPa. The formed layer seems to be very brittle, which is responsible for cleavages and spalls formed under the impact by the diamond pyramid.

Molybdenum and carbon are also contained in the bulk, under the modified layer. Their concentration lines dominate even over the iron lines. It can be seen from the SEM photo that the modified layer of cast iron (alloyed with the plasma components) is practically a different alloy. This alloy is formed, i.e. inoculated, on the substrate material surface, copying its relief and healing, in some cases, the surface defects (**Fig. 8.5**).

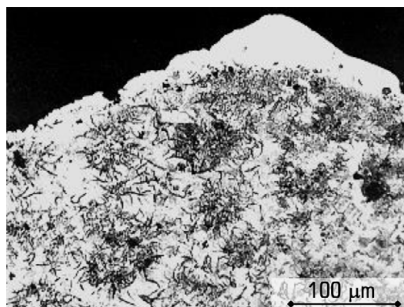


Fig. 8.3 Microstructure of surface of the high-strength cast iron sample after PDT

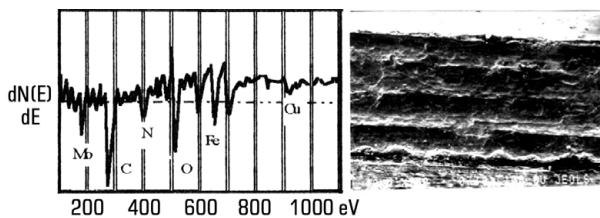


Fig. 8.4 Auger spectrum and appearance of surface of the high-strength cast iron sample after plasma treatment by adding molybdenum to plasma (SEM photo)

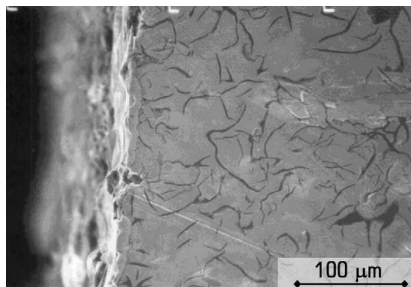


Fig. 8.5 Transverse section of modified layer on surface of the cast iron sample (SEM photo)

The efficiency of surface modification of cast iron parts depends upon the power density of the plasma jet and its composition. Introduction of molybdenum to plasma allows a layer of products of plasma-chemical synthesis of compounds of elements constituting the plasma to be deposited on the part surfaces (**Fig. 8.5**). Hardness of this coating is up to 14,000 MPa, its thickness being 10–20 μm . The chilled cast iron layer with hardness of up to 14,000 MPa and thickness of 60–90 μm is formed under the coating. An addition of tungsten allows hardness of the layer to be increased to 20,000 MPa, its thickness being unchanged.

Copper and zinc added to plasma decrease hardness of the surface to 700 MPa, hardness of the chilled cast iron layer being 11,000–14,000 MPa, and total thickness of the hardened layer being up to 100 μm .

Analysis of the results of literature survey shows that similar layers (without alloying) can also be formed in hardening of surfaces of cast iron parts by using technological lasers.

PDT conditions and some investigation results are given in **Table 8.2**.

● **Table 8.2** Conditions for modification of cast iron sample surfaces by PDT and investigation results

No.	PDT conditions		Hardened layer		Fused layer		Heat-affected zone (HEZ), μm
	C, μF	N of pulses	Thickness, μm	Hardness, MPa	Thickness, μm	Hardness, MPa	
1	400	1	0–7	–	23	10,200	24–30
2		3	0–7	–	24	11,000	24–32
3		5	14–17	8,600	25	10,000	30–45
4		10	13–17	8,000	32	9,000	45–90
6	800	1	14–18	9,000	36	11,000	55–105
7		3	15–20	9,000	34	11,000	54–100
8		5	15–19	8,500	36	10,500	55–100
9		10	17–21	8,000	42	10,000	56–95
10	1,200	1	16–20	9,500	47	11,500	60–90
12		4	18–22	9,000	48	10,500	60–120

PDT of the surface of cast iron parts without addition of alloying elements is of practical interest. As shown by the investigation results, thickness of the modified layer increases with growth of power of a plasma pulse at the identical quantity of the PDT pulses. Thickness of the layer also increases with growth of the quantity of the plasma pulses, which is indicative of accumulation of energy of the pulses in the surface layer of a part (**Table 8.2**).

The surface of cast iron parts after PDT (**Fig. 8.6**) is a system of fused regions chaotically distributed in this surface. At a higher magnification, round inclusions of the electrode material and microcracks can be seen on the modified (fused) surface of a cast iron part.

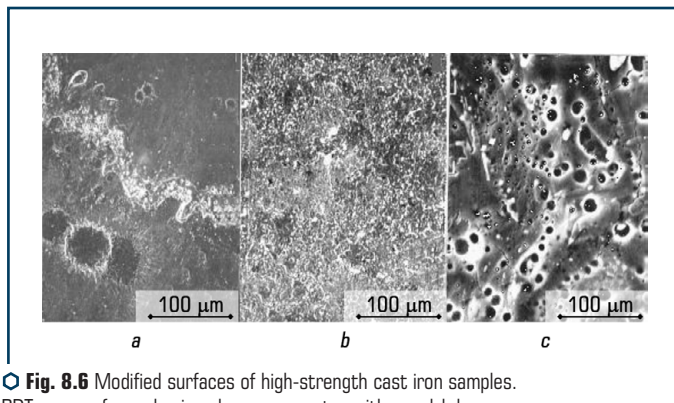


Fig. 8.6 Modified surfaces of high-strength cast iron samples. PDT was performed using plasma generator with a molybdenum electrode (SEM photo)

PDT is effective for modification of surfaces of cast iron parts. For example, modification of wearing surfaces of cast iron rings (**Fig. 8.3**) used in internal combustion engines, compressors and pumps provides their high wear resistance combined with retained strength and elastic properties of the rings.

Foreign and domestic experience of application of laser cladding for treating wearing surfaces of piston rings indicates that their performance in this case is higher by a factor of 1.53 than performance of chromium plated rings. Our rig tests showed that wear resistance of a cast iron sample hardened by pulsed plasma is 3 times as high as that of the chromium plated one.

Comparative studies of wear resistance of surfaces of cast iron samples were conducted under the sliding friction conditions. The type of contact in friction was plane over the cylindrical surface (roller). The samples measuring $10 \times 10 \times 12$ mm were made from cast iron SCh 21–40. The roller (40 mm in diameter and 12 mm thick), i.e. mating sample, was made from the same cast iron.

The tests were conducted in friction without lubrication and in a bath of motor oil M-1032, according to GOST 858178. The following samples were tested: samples with non-hardened surfaces, samples with galvanic chromium coatings, samples with vacuum-plasma coatings, and samples treated by the pulsed plasma containing molybdenum.

As indicated by analysis of the results of the comparative studies, the maximal wear was exhibited by the non-hardened samples, which were tested without lubrication. Chromium plating, vacuum-plasma coating and pulsed plasma treatment provide tens of times increase in wear resistance of the surfaces. It is interesting to note that the mating sample surfaces have the lowest wear in friction on a sample treated by the molybdenum-containing plasma. The chromium plated samples wear the mating sample surfaces 2–3 times more intensively than the samples treated by the pulsed plasma.

8.3 PLASMA-DETONATION HARDENING OF DIE STEEL

Experiments on surface modification were carried out with die steel of the H13 type (base – Fe, 5.0 % Cr, 1.7 % Mo, 1.0 % Si, 1.0 % V, and 0.37 % C), which is used to manufacture tools operating under long-time thermal cycling to temperatures of 600–630 °C, such as compression rams, needles for pipe piercing, hammer and press inserts, tools for upsetting of billets, etc. To improve heat resistance of the working layer of a die, it is suggested increasing the content of tungsten, silicon, nitrogen and carbon in the surface layer, and change structure of the surface layer material to that close to the nanocrystalline one.

The samples studied were not subjected to prior heat treatment. The following process parameters were set: inductance of the discharge circuit – $L=30\text{ }\mu\text{H}$, capacitance of the capacitor bank – $C=800\text{ }\mu\text{F}$, and voltage at the capacitor bank plates – $U=3\text{ kV}$. The effect of distance to the surface treated and electrode penetration depth on the modification process was investigated. Parameters of treatment of the samples are given in **Table 8.3**.

● **Table 8.3** Parameters of treatment

No. sample	Distance to the surface H , mm	Electrode penetration depth h , mm	Quantity of treatment zone overlapping
1	45	25	3.4
2	35	25	5.2
3	40	18	5.7
4	50	18	5.7
5	60	18	5.7

As noted above, a change in value of the consumable electrode penetration depth leads to a change in diameter of the treatment spot and, accordingly, density of the heat flow into the workpiece. The $h=25\text{ mm}$ value was set for samples 1 and 2. Diameter of the visible treatment zone was 12–14 mm. Optical metallography revealed no visible traces of hardening on sample 1 (**Fig. 8.7, a**). Decrease in the distance to $H=35\text{ mm}$ and increase in the quantity of overlaps provided a modified (white) layer up to $15\text{ }\mu\text{m}$ thick (**Fig. 8.7, b**).

Samples of the next series (3, 4, 5) were treated at $h=18\text{ mm}$. This allowed increasing the power density and producing thicker hardened layers. Sample 3 was treated at a distance of $H=40\text{ mm}$. This mode of treatment provided a sufficiently high power density, causing fusion and evaporation of material from the sample surface. A modified layer 30–40 μm thick was formed on the sample surface (**Fig. 8.8, a**). This layer has a clearly defined interface with the base metal.

Measurement of surface hardness showed that hardness increased by a factor of 6, up to 996 HV_{1000} (initial hardness of the alloy was 168 HV_{300}), and hardness of the sample material at a depth of $50\text{ }\mu\text{m}$ increased to 512 HV_{300} .

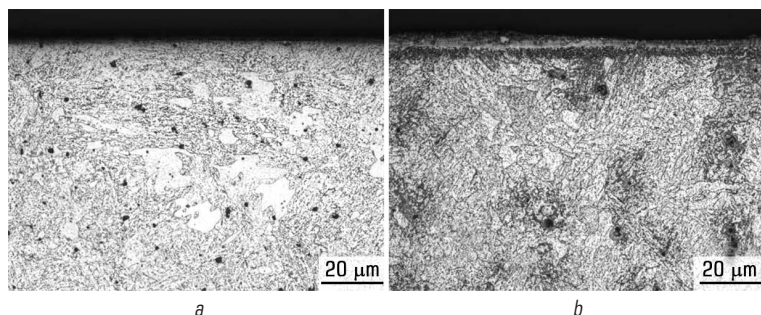


Fig. 8.7 Microsections of samples: *a* – No. 1; *b* – No. 2

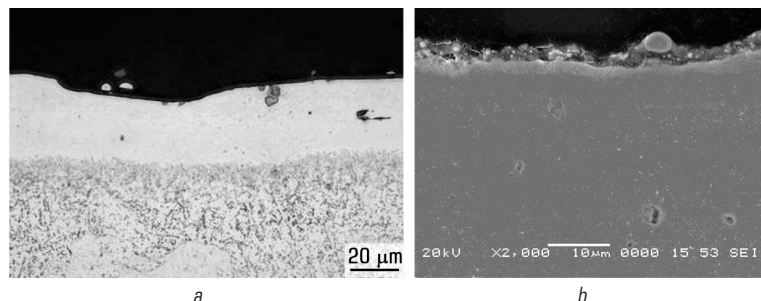


Fig. 8.8 Modified layer of the sample No. 3:
a – layer image on the optical microscope; *b* – layer image on the SEM

High power density provided refinement of structure of the surface layer due to high temperature gradients, but elemental analysis revealed no plasma component elements in the layer. Most probably, this was caused by a high temperature, evaporation and destruction of a thin surface layer, which was proved by the presence of drops and beads of the material on the sample surface (Fig. 8.8, *b*). The sample surface was rough and had the traces of melting and spattering of the material.

X-ray diffraction analysis (Fig. 8.9) revealed considerable oxidation of the surface. In addition, the surface contained carbon, which was condensed from the combustion products. Alloying elements under such conditions were oxidised and removed from the surface together with the destructed layer of the base metal.

Next sample 4 was treated in a mode which provided fusion of a thin layer on the sample surface, erosion of the consumable electrode and alloying in the melt with plasma component elements.

Pulse-plasma treatment resulted in formation of a modified layer 13–20 μm thick on the sample surface (Fig. 8.10). This layer had a clearly defined interface with the base metal.

Measurement of surface hardness showed that hardness increased by a factor of 6, up to 831 HV_{1000} , and hardness of the sample material at a depth of $50\text{ }\mu\text{m}$ increased to 315 HV_{300} .

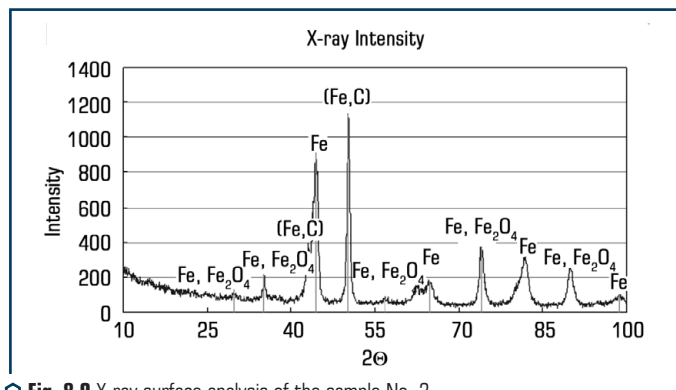


Fig. 8.9 X-ray surface analysis of the sample No. 3

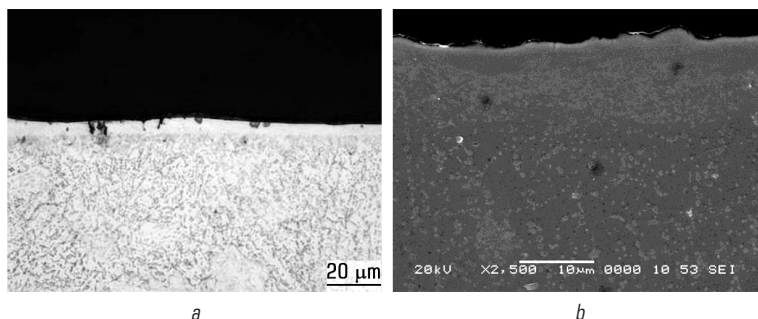


Fig. 8.10 Modified layer of the sample No. 4:

a – layer image on the optical microscope; *b* – image of the analyzed zone on the TEM

Examination of the sample with a transmission electron microscope equipped with the energy-dispersive microanalysis system allowed determining that the fused layer (point 4, **Fig. 8.10, b**) had a high tungsten content equal to 38 at. %, and an oxygen content of up to 13.8 at. %. No oxygen was detected at point 2, and the tungsten content there was 19.38 at. %. Further on the tungsten content gradually decreased to 4 at. % at a depth of $1\text{ }\mu\text{m}$ (point 5).

Crystalline structure of the modified layer is close to the nanocrystalline one. Surface of the modified layer is characterized by low roughness. Heterogeneities can be seen in a thin "white" layer (point 1 in **Fig. 8.10, b**). Most probably, these heterogeneities are caused by oxidation (the oxygen content is up to 13.8 %).

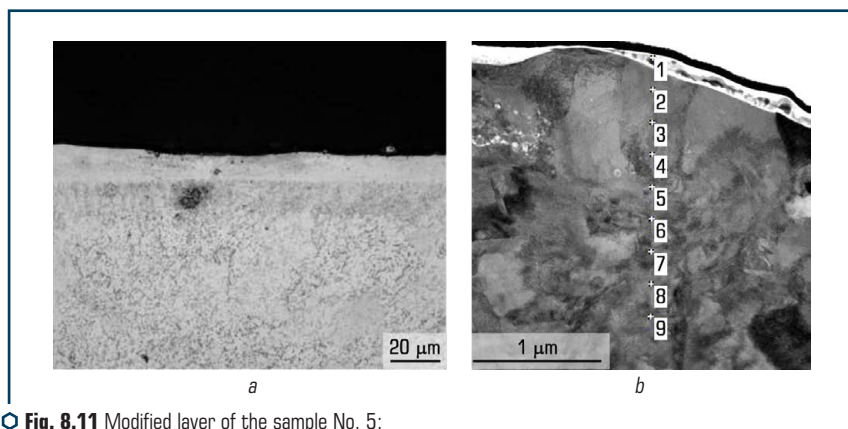
Increase in the distance to $H=60$ mm led to decrease in the heat flow and, as a result, provided formation of the modified surface layer to a depth of $10\text{ }\mu\text{m}$ (**Fig. 8.11**).

Microhardness of the surface was 730 HV_{1000} . Considering that thickness of the layer is small, and it is pressed through by the indenter under a load of 1000 g, this hardness measurement method is inaccurate and gives underestimated characteristics. There were no visible traces of changes in the alloy structure at a depth of $50\text{ }\mu\text{m}$, but hardness there was 451 HV_{300} , which was almost three times as high as hardness of the base metal. Roughness of the surface did not change.

Results of analysis of the samples using a scanning electron microscope with the energy-dispersive detector showed the carbon content of the surface layer equal to 7 at. %. X-ray patterns of samples 3 and 5 (**Fig. 8.12**) were different. The surface layers of sample 5 were less oxidised, and had a lower degree of deformation of the crystalline lattice.

X-ray diffraction analysis of the pulse-plasma hardened surface layers of the samples revealed broadening of α -Fe lines with decrease in their intensity, and appearance of lines of retained austenite in Fe. Intensity of the austenite lines grew with intensification of treatment. As shown by the examinations, broadening of the X-ray diffraction lines of both α -Fe and γ -Fe is indicative of heterogeneous elastic distortions of the lattice. These distortions may be related both to elastic deformations caused by dislocations and coherent bond of particles of different phases, and to heterogeneous distribution of alloying elements.

Samples of a new series were treated by using the treatment mode corresponding to that applied to sample 4. It was planned to increase the concentration of main elements affecting the surface layer heat resistance, i.e. tungsten, nitrogen and silicon, in the surface layer. Nitrogen and tungsten were introduced into the plasmatron in the form of metal electrode (rod) erosion products and in the form of detonation mixture components (propane, nitrogen), while silicon was added to the reaction chamber in the form of suspension.



○ **Fig. 8.11** Modified layer of the sample No. 5:
a – layer image on the optical microscope; *b* – layer image on the SEM

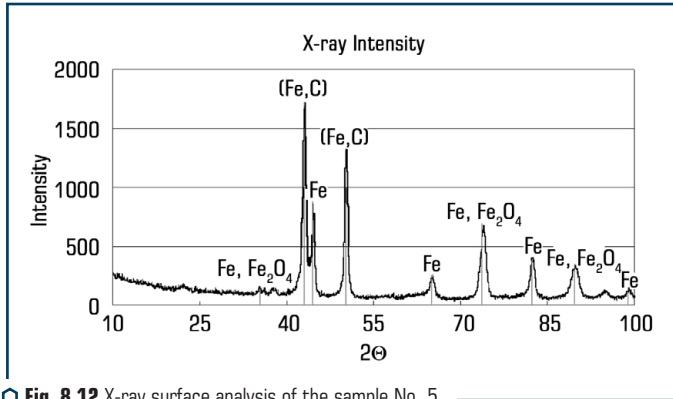


Fig. 8.12 X-ray surface analysis of the sample No. 5

Considering that the alloy contained the sufficient amount of chromium, it was planned to produce a chromosiliconized nanocrystalline layer on the workpiece surface through increasing the concentration of silicon. It is a known fact that chromosiliconizing is a high-temperature process of thermochemical treatment (950–1100 °C). Parts subjected to chromosiliconizing have increased scale and acid resistance, as well as increased erosion resistance within a high-temperature range of up to 800–1000 °C. Chromosiliconizing is a simultaneous saturation of the workpiece surface with chromium and silicon (Fig. 8.13). The temperature of chromosiliconizing is 900–1200 °C, depending upon the composition of a material treated and chromosiliconizing method.

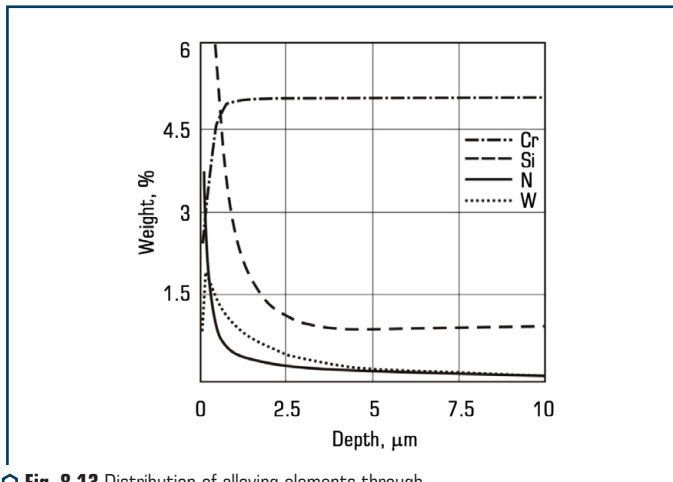


Fig. 8.13 Distribution of alloying elements through thickness of the modified layer

Distribution of alloying elements through thickness of the modified layer was found by using the glow-discharge atomic emission spectrometer. Precision quantitative layer-by-layer analysis of the die steel after the pulse plasma treatment with tungsten, silicon and nitrogen added to plasma showed the alloying elements located at a depth of 5 μm . The concentration of iron and chromium at this depth decreases accordingly. A new material with a high content of alloying elements is formed in the surface layer of the die steel. This material has a structure close to the nanocrystalline one.

8.4 MODIFICATION OF SURFACE OF HARD ALLOY

Consider first the mechanism of wear of hard alloys under conditions of treatment of metal parts.

Three processes are known to lead to wear of hard alloy tools used in treatment of steels [12, 101–104, 150–152]. These are dissociation of tungsten carbide and dissolution of WC grains in iron, micro fracture of carbide grains, as well as iron weakening of the cobalt phase binder with entrainment of partially dissolved tungsten carbides and non-dissolved (W, Ti)C grains by the moving volumes of steel.

The main cause of smoothing out of carbides is their dissolution by diffusion. In this case it is more logical to assume the mechanism of intensive dissolution and smoothing out of WC grains, rather than (W, Ti)C grains, as the temperature of dissociation of carbide (W, Ti)C is much higher than that of carbide WC. This results in smoothing out of the WC grains in contact with steel.

The established principles of changes in mechanical characteristics of hard alloys depending upon their structure and structural components favour development and practical implementation of methods intended for hardening of hard alloy parts.

Below we consider efficiency of the known methods used for surface hardening of hard alloys. The first example is explosion hardening [23]. As shown by investigations, explosion hardening causes only an insignificant change in physical-mechanical properties of alloy VK16.

The second example is plasma-chemical synthesis and deposition of coatings [28, 29], which are performed, as a rule, in vacuum. These technologies provide deposition of strong thin films of nitrides, carbides and oxides on the surface, and it is these films that take a fracture load on a hard alloy. Versatility of these technologies allows selection of a coating composition depending upon the service requirements.

According to the literature data, the most effective technology among those known in the art is hardening by the effect of concentrated energy flows. As a result of the treatment the heat-affected zone (HAZ) 30–60 μm deep is formed in the surface layer of a sample. This zone differs from the initial, untreated material in a higher microhardness.

Investigations [150–152] show that the light, radiation treatment of samples results in a substantial decrease in the content of the cobalt binder and refining of the carbide grain in the HAZ. New phases WC and W_2C are formed in hard alloys based on tungsten carbide. At the same time, no new phases were revealed in hard alloys based on TiC.

Characteristic peculiarities of alloy structure in the HAZ include refining of the carbide grain, dissolution of tungsten carbide in the cobalt binder and increase of porosity in the recrystallization zone. Formation of pores in the modified layer of a hard alloy is attributable to burning out and re-distribution of the binder. Porosity of the hardened layer depends upon the time of the effect exerted by the light flow on a sample. The fusion zone grows with increase in time of the effect of the light flow on a material. Depth of the HAZ in alloys VK2 and VK20 is 1.5–2.0 times larger than in alloys TK and TTK. This depends upon the difference in thermal conductivity coefficients of hard alloys VK and TK.

Treatment of alloys based on tungsten carbide WC and cobalt by laser radiation [153, 154] and concentrated solar energy [296] is of high interest. Hardening provides increase in microhardness of the surface layer of a hard alloy to 35,000 MPa. This is attributable to formation of carbides of the W_2C type, which have an increased hardness (10,000–14,000 MPa) compared with carbides of the WC type. In addition, hardening leads to a change in fine structure and composition of the binding alloy.

Analysis of the investigation results shows that if a density of the energy is not in excess of 80 J/cm², this leads to saturation of the binder with the WC monocarbide elements. At an energy density of 80–100 J/cm² complex carbides Co_3W_3C are formed in the binder. These carbides have a negative effect on strength of the surface of an alloy, which is caused by decrease in the content of cobalt metal in the binder. Complex carbides with a disturbed stoichiometry (of the $Co_xW_yC_z$ type) are formed, and the amount of semi-carbides W_2C and cubic carbide WC markedly grows at an energy density of 140–280 J/cm².

The energy density should not exceed 80 J/cm² to increase wear resistance of hard alloys based on tungsten carbides with a cobalt content of 8–10 %, 100 J/cm² for alloys with a cobalt content of 3–6 %, and 120 J/cm² for alloys with a cobalt content of 10 %. The aggregate state of an alloy hardly changes in low-energy irradiation.

The plasma hardening technology was studied on cutting plates. These are the cutters with plates brazed on them and with non-resharpened plates of hard alloys of the WC-Co (of the VK type) and WC-TiC-Co (of the TK type) systems with a differing content of carbides and a binding phase. Composition of the alloys studied, their initial hardness and hardness after hardening treatment are given in **Table 8.4** [218].

Structure of the VK type alloys in the initial state consists of free and contacting particles of tungsten carbides immersed in solid solution of tungsten and carbon in cobalt. Alloys of the TK type in the initial state (after sintering) have a three-phase structure and consist of oval crystals (Ti, W)C formed as a result of diffusion in dissolution of W and C in TiC during sintering of the WC carbide grains. Increase in the binding phase content is accompanied by decrease in hardness of the VK and TK type alloys.

Variations in thermal power during plasma heating from 20 to 150 kW/cm² (depending upon the composition, shape and size) can provide treatment of cutting edges of the plates with full surface fusion of molten composition, partial fusion (of only the binding phase), or without fusion with transformations occurring in carbides and binder or with transformations occurring only in the binder.

● **Table 8.4** Properties of hard alloys in the initial and hardened conditions

Alloy grade	Composition %			Hardness H_v after plasma treatment				
	WC	TiC	Co	Initial hardness, H_v	Fused alloy	Fused Co-phase	Transformations	
							in alloy	in Co-phase
VK4	96	–	4	1,420–1,470	1,530–1,675	1,570–1,590	1,680–1,725	1,420–1,470
VK6	94	–	6	1,380–1,445	1,515–1,635	1,550–1,565	1,645–1,695	1,380–1,445
VK8	92	–	8	1,405–1,450	1,515–1,670	1,520–1,545	1,590–1,620	1,405–1,450
VK15	85	–	15	1,290–1,320	1,530–1,640	1,400–1,440	1,535–1,575	1,290–1,320
T5K10	85	5	10	1,420–1,475	1,600–1,685	1,580–1,610	1,660–1,700	1,420–1,475
T15K6	79	15	6	1,455–1,500	1,600–1,685	1,600–1,625	1,705–1,725	1,455–1,500

Plasma treatment with full fusion of the composition leads to an intensive formation of pores and a network of microcracks, which is associated with burning out of the binder and super rapid (at a rate of about 10^4 – 10^5 °C/s) solidification of the fused layer. Strength of the tools with such a treatment is not increased, despite increase in hardness. The cause is brittleness of the hardened cutting edge.

Plasma heating with partial fusion of the binding phase also leads to formation of pores and microcracks on the surface. However, in this case they are smaller in size and much smaller in number than in treatment with full fusion. Hardness of the surface of hardened alloys increases but insignificantly, while the presence of defects (cracks, micropores) on their working surfaces does not allow utilization of the hardening effect to increase strength of the tools.

The highest values of hardness of the alloys studies are achieved by using plasma treatment without fusion of the binder, i.e. by heating the surface to temperatures of about 1,300–1,495 °C [151]. In this case the main process that determines structure and properties of the hardened zone is contact fusion of the carbide – binder interfaces.

Contact fusion of the interfaces between the phases under conditions of good wetting of the components (contact angle $\Theta=0^\circ$) for alloys WC-Co favours division of dense groups of carbides into fine particles, i.e. single crystals. This is one of the factors that increase the degree of dispersion of structure during hardening. Under conditions of high-rate heating and extremely short time of holding in a heated state, the process of re-grouping is not accompanied by growth of the carbide particles both by the mechanism of recrystallization through the binder (dissolution – deposition) and by the mechanism of coalescence.

The degree of transformation in carbides under conditions of contact fusion is not the same and depends upon their sizes. The final structure of alloys of the WC-Co system is formed in plasma treatment under non-equilibrium conditions of high-rate cooling. Dissociation of oversaturated solid solution of W and C in Co, accompanied by precipitation of dispersed secondary carbides, occurs in

this case. Along with refining of the carbide phase, the positive effect on properties of the hardened alloys is also exerted by a change in the shape of grains, i.e. initial rectangular shape is distorted and grains take an irregular shape and "loose" ends.

Plasma treatment of the surface of alloys of the WC-TiC-Co system without surface fusion also leads to a substantial increase in hardness. These alloys are characterized by an incomplete wetting of components ($\Theta > 0^\circ$) under the contact fusion conditions, which does not allow comprehensive realization of precipitation hardening of the binder. Increase in hardness of the TK type alloys after the plasma effect is associated with refining of grains and strengthening of the binder, which is saturated with tungsten and carbon as a results of diffusion and dissociation of the oversaturated solid solution of (Ti, W)C.

Plasma hardening without fusion with transformations only in the Co-phase (heating to a temperature below 1200 °C) does not lead to a marked increase in hardness and structural changes. This is caused by a short time of the effect. So, the carbide grains and interfaces remain unchanged [151].

Therefore, in plasma treatment under optimal conditions an increase in hardness of sintered hard alloys is caused by the effect of the mechanism of precipitation hardening of the binding phase and increase in the degree of dispersion of the carbide phase. As a result, this provides grain-boundary hardening of an alloy with increase in the specific surface of the carbide – carbide and carbide – binder interfaces [150–153].

The positive feature of plasma hardening of hard alloy tools, unlike laser hardening, is a large size of the hardened zone: it is up to 2 mm deep and up to 10 mm wide. There is a gradual transition of structure of the hardened layer to the initial structure with distance from the heating location. Depth of the transition zone is 0.3–0.6 mm, depending upon the alloy grade and treatment conditions. Absence of a clearly defined boundary with an initial alloy makes plasma treatment advantageous over the methods of application of hardening coatings of carbides and nitrides by condensation or deposition. Strength and absence of separation of the hardened layer are provided owing to a substantial depth of the modified layer and gradual transition to the initial structure.

The effect of plasma treatment on the character of fracture of sintered hard alloys of the WC-Co and WC-TiO-Co systems of the medium-grained grades with a mean size of carbide grains equal to 2–3 μm was studied. Plasma treatment of each of the alloys was performed under two optimal conditions, i.e. with fusion of the binder and without fusion with transformations in carbides and binder. Mean values of the investigated parameters are given in **Table 8.5**.

Plasma hardening of hard alloys under optimal conditions does not lead to decrease in their crack resistance, despite a substantial increase in hardness. Increase in coefficient K_{Ic} by 20 % is achieved in a number of cases, compared with the initial state. Among the recommended treatment conditions the most efficient treatment is hardening without fusion of the composition with realization of phase and structural transformations in carbides and binder.

Plasma treatment of alloy WC-Co provides refining and re-grouping of the initial carbide phase, as well as saturation of the binder with dispersed secondary carbides. This leads to a change in size

of the specific mating surfaces (interfaces between phases) carbide – carbide and carbide – binder, which are the weakest links of the composition. The binding phase retains its initially high ductility and, at the same time, is saturated with dispersed carbides, which in turn causes a considerable increase in strength. These factors taken together provide simultaneous increase in hardness and crack resistance of alloys of the VK type (WC-Co) in plasma treatment.

● **Table 8.5** Hardness H_V and crack resistance of the surface of hard alloys in plasma hardening (values for treatment with fusion of the binder are given in numerator, and values for treatment without fusion are given in denominator)

Alloy grade	$F_b, \text{ N}$	H_V		$K_{Ic}, \text{ MPa/m}^2$	
		In hardened layer	In initial alloy	In hardened layer	In initial alloy
VK6 (WC-Co 6 %)	490	1,560/1,670	1,410	12.6/14.1	11.8
VK15 (WC-Co 15 %)	588	1,420/1,565	1,305	13.6/14.4	12.9
T5K10 (WC-TiC 5 %–Co 10 %)	588	1,595/1,680	1,450	9.1/10.0	8.4
T15K6 (WC-TiC 15 %–Co 6 %)	490	1,610/1,715	1,480	7.9/8.6	7.2

Crack resistance of alloys of the TK type (WC-TiO-Co) is also increased as a result of hardening, although to a lesser degree than that of alloys of the VK type (WC-Co). This is associated both with the initially low crack resistance and with the insufficiently complete realization of the effect of contact fusion of the interfaces (because of incomplete wetting of components) and, hence, absence of precipitation hardening of the binder at high-speed treatment.

While leading to refining of carbide grains (decrease in d_g), plasma treatment provides increase in hardness and crack resistance. At the same time, the role of the binding phase grows. Its saturation with tungsten and carbon and precipitation of ultra dispersed secondary carbides in plasma treatment lead to strengthening of the binder.

It is an established fact that plasma treatment of hard alloys leads to a qualitative change in the mechanism of their fracture. Refining of the initial carbide phase and precipitation of sub-microscopic particles of secondary carbides provide realization of primarily inter-granular fracture along the interfaces between the phases. A large amount of tough fracture of the binding phase persists, despite its saturation with tungsten, carbon and dispersed secondary carbides. A hardened hard alloy retains its properties of a composite material. The positive effect on increase in crack resistance of the alloys is also exerted by a wavy path of a crack, which is caused by a substantial refining of carbide grains and, particularly, by formation of fine secondary cracks normal to an avalanche crack. This is indicative of formation of an additional field of internal stresses in the binder and dissipation of the fracture energy.

8.5 MODIFICATION OF TITANIUM BASE ALLOYS

8.5.1 ALLOY VT-22

Light titanium-base alloys are finding an increasingly wide commercial application. Despite high strength properties, these alloys have substantial drawbacks caused by high reactivity of titanium. First of all, this is a low wear resistance of the surface of titanium parts in friction. Technologies that receive a large development effort now are those that provide modification of surfaces of titanium parts [297, 298].

Plasma-detonation treatment (PDT) provides a complex effect on the workpiece surface. The Chapter considers some investigation results on PDT of titanium alloys, e.g. VT-22 (6 % Al, 5 % Mo, 5 % V, 1 % Cr, 1 % Fe) and VT-6 (6 % Al, 4 % V).

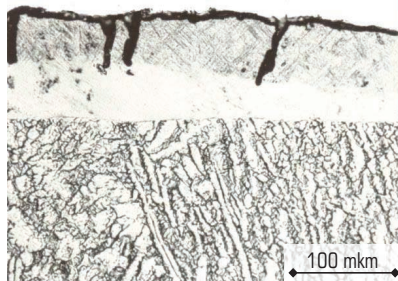
Alloy VT-22 has a coarse-grained structure oriented normal to the surface. PDT was performed using a plasma generator that forms the pulsed plasma jet with a power density of 10^5 – 10^6 W/cm², velocity of 5–8 km/s, plasma temperature of 15,000 K and generation frequency of 2–4 Hz. The electric current of 1–3 kA was passed through the jet, which provided formation of the pulsed magnetic field.

Alloying elements were added to the plasma jet in the form of gas (propane + butane + nitrogen) and vapors of Ni, W, Ti, Cr and Mo metals. The vapors were formed from a rod, the tip of which was evaporated under the effect of the electric current flowing through the plasma jet. The alloying elements participated in surface modification. Treatment was performed in air and nitrogen atmospheres. Productivity of the treatment was up to 1 m²/h.

Metallographic analysis of samples was conducted using the Neophot-32 optical microscope. Microhardness of structural components was determined using the LECO hardness meter M-400 equipped with the automatic load increment system under a load of 25 g. X-ray phase analysis of the samples was conducted using the DRON-UM1 diffractometer in copper anode radiation (CuK α).

Metallography of the samples of two-phase titanium alloy VT-22 shows that structure of the alloy consists of lamellae of the α - and β -phases (with close-packed hexagonal and body-centered cubic lattices, respectively) oriented mostly normal to the surface treated. The structure is coarse-grained with interlayers of the α -phase located along the primary grain boundaries. Inside the grains, the α -phase lamellae alternate with the β -phase ones (high-temperature phase of Ti). Microhardness of the base is 2000–2500 MPa ($HV_{mean} = 2.3 \cdot 10^3$ N/mm²).

The modified layer 30–40 μ m thick is formed on the surface of alloy VT-22 after single-pulse PDT. The layer consists of two interlayers (**Fig. 8.14**). The external layer (darker one) has a fine acicular structure. Transverse channels (extending from the surface to a white internal layer) are revealed in this layer by etching. These layers cannot be seen on the non-etched samples. Most probably that this is caused by formation of electrical breakdown channels on the sample surface, which propagate through the shock-compressed layer of plasma along the boundaries of both primary grains and coarse lamellae of the α -phase. It is likely that the channels are formed due to coincidence of energy fluctuations, where plasma has a maximal power density, with grain boundaries.

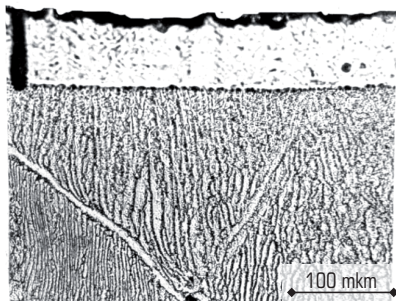


○ **Fig. 8.14** Characteristic microstructure of the layer modified by PDT (single-pulse treatment) on the surface of alloy VT-22

The internal, unetchable and structureless layer constitutes 30–70 % of total thickness of the hardened zone. It is characterized by a structureless state, which proves theoretical prediction of formation of the meta-stable state caused by high cooling rates and "freezing" of clusters in the internal layers. The diffraction pattern is of the amorphous-crystalline character.

The single-pulse plasma treatment in air atmosphere results in formation of a heat-hardened layer up to 50–60 μm thick on the sample surface (**Fig. 8.15**).

The layer has a fine acicular structure, which can be etched only slightly in the $\text{HF} + \text{HNO}_3$ solution, and microhardness of 4500–6500 MPa ($4.5\text{--}6.5 \cdot 10^3 \text{ N/mm}^2$). This metal layer overheated to above the β -temperature underwent martensitic transformation as a result of rapid cooling. The formed hardened layer is heterogeneous. It can be etched but poorly at the interface with the base, which is most probably caused by an increased cooling rate in this region and formation of the amorphous phase.



○ **Fig. 8.15** Characteristic microstructure of the surface of alloy VT-22 modified by PDT (treatment with three pulses)

Increase in microhardness of the base material to 2800 MPa ($2.8 \cdot 10^3 \text{ N/mm}^2$) is detected under the hardened layer at a depth of 50 to 100 μm .

PDT with six pulses provides the highest modification of the surface of alloy VT-22. **Fig. 8.16** shows distribution of hardness through the hardened layer. Mean hardness of the hardened layer amounts to 7000 MPa, hardness of the metal base being 2300 MPa. Microhardness of the base of a sample grows to 3000 MPa at a depth of 90 μm . X-ray phase analysis reveals (**Fig. 8.17**) the presence of the amorphous phase and titanium nitride (Ti_2N), in addition to solid solution of alloying elements in the martensite α -phase of titanium.

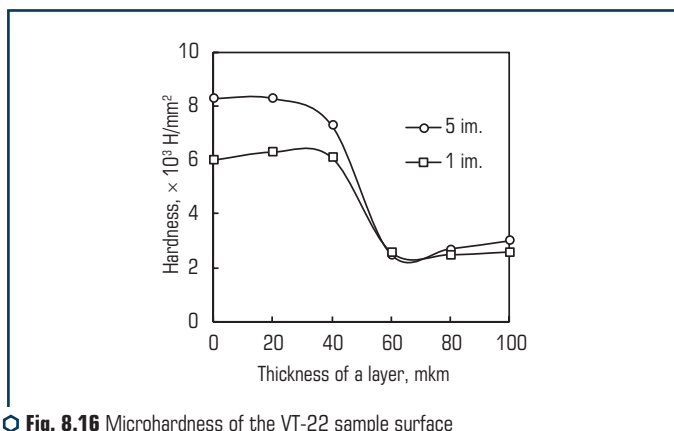


Fig. 8.16 Microhardness of the VT-22 sample surface modified by PDT

Auger spectroscopy shows that metals added to plasma from the eroding electrode are present on the surface of all samples, independently of their composition.

The cementite lines persisted after the plasma treatment (PDT), and two very intensive lines were formed in a region of low reflection angles ($Q=7.2^\circ$, $d=0.714 \text{ nm}$; $Q=14.5^\circ$, $d=0.244 \text{ nm}$). The last line is a strong line of titanium nitride TiN.

The next strong line is that of TiN with $d=0.714 \text{ nm}$ and $Q=14.5^\circ$, $d=0.358 \text{ nm}$, and then goes a weak line with $Q=21.5^\circ$ and $d=0.244 \text{ nm}$. The last line is a strong line of titanium nitride TiN. The strong line at $Q=14.5^\circ$ may correspond to a modification of titanium oxide TiO_2 , i.e. anatase ($d=0.352 \text{ nm}$). The hypothesis of formation of channels in the hardened surface layer was checked on samples of two-phase ($\alpha+\beta$)-alloy VT-3. This alloy has a structure with finer grains than alloy VT-22. The α -phase dominates in this alloy. Microhardness of the alloy is 2000–2700 MPa.

Continuous unetchable layer with microhardness of up to 4600 MPa and thickness of 30–35 μm is formed on the sample surface as a result of the pulsed plasma treatment (distance $L=40 \text{ mm}$ and quantity of pulses $N=3$).

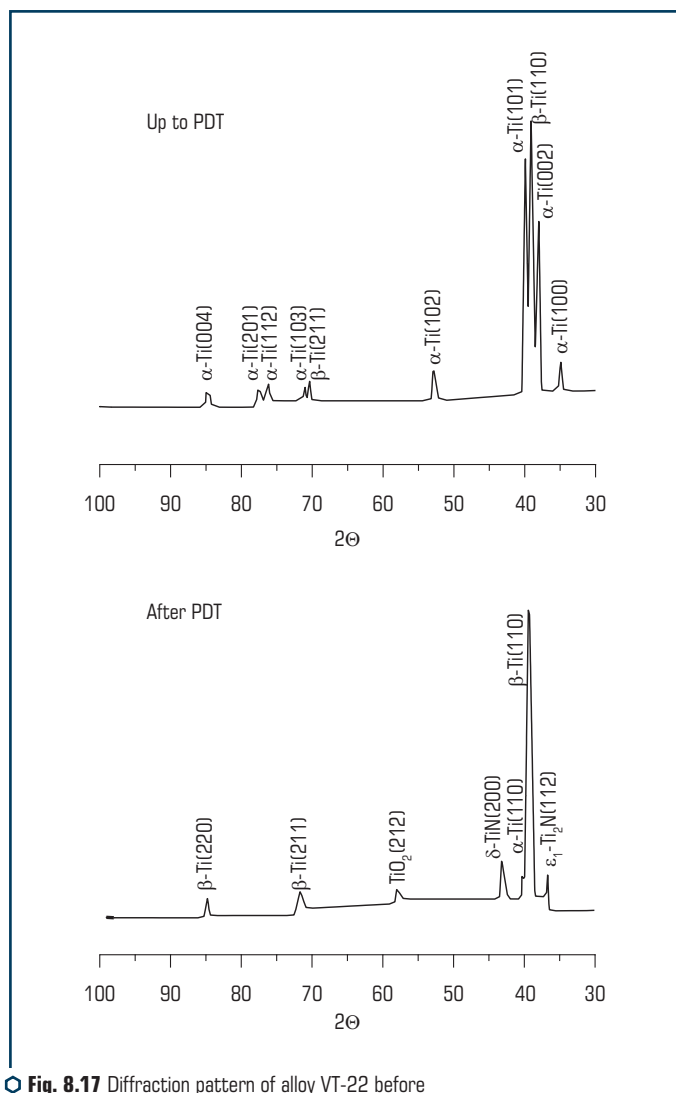


Fig. 8.17 Diffraction pattern of alloy VT-22 before and after pulsed plasma treatment

According to the data of X-ray phase analysis, the hardened layer on the alloy has a structure of the martensite type with inclusions of nitrides, oxides and a small amount of the amorphous phase. The inclusions are located primarily on the sample surface.

8.5.2 ALLOY VT-6

Alloy VT-6 (6 % Al, 4 % V) has a favourable combination of mechanical and operational properties. This is achieved through its alloying with vanadium, which is the only element that raises ductility of Ti ($\sigma_t=1000$ MPa, $\sigma_y=900$ MPa, $\delta=10$ %, $\psi=30$ %, $KCU=40-80$ J/cm²). The alloy has a two-phase structure ($\alpha+\beta$), where the α -phase is dominant. Microhardness of the base is 2100–3300 MPa.

Alloy Vt-6 was subjected to PDT in nitrogen atmosphere. The studies showed that structure of the hardened zone changed with increase in the quantity of the PDT pulses. After 20 treatment pulses it becomes of a two-layer character at thickness 35–40 μm (**Fig. 8.18**).

The upper layer about several microns thick consists mostly of titanium nitride (carbonitride), and the lower layer consists of alloyed acicular martensite. Microhardness of the hardened layer amounts to 11,000 MPa, mean values of microhardness being 8,100 MPa (**Fig. 8.19**).

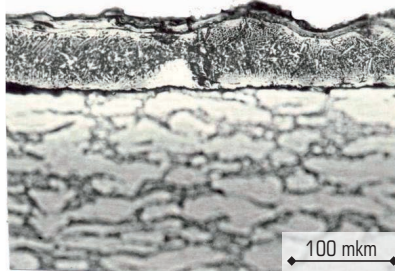


Fig. 8.18 Characteristic microstructure of the surface of alloy VT-6 modified by PDT with 20 pulses in nitrogen atmosphere

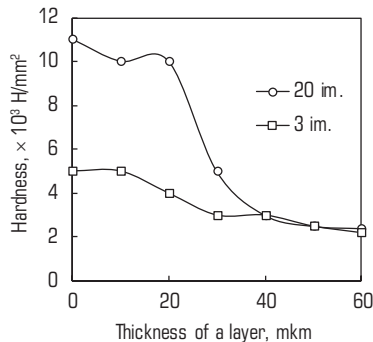
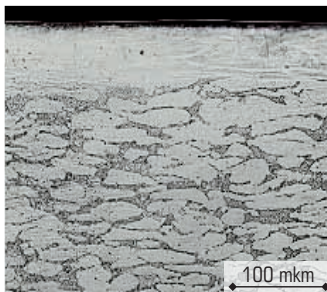


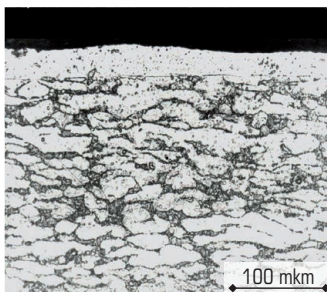
Fig. 8.19 Microhardness of the surface of alloy VT-6 modified by PDT

The surface of the titanium alloy samples undergoes changes as a result of PDT. Poorly etchable layers of a goldish color, up to 60 μm thick and having increased hardness are formed on the surface. Thickness of a layer depends upon the quantity of the treatment pulses. In PDT at a distance of 40 mm (three pulses) the hardened layer is light in color and 35–55 μm thick, its microhardness is 4200–4600 MPa. Etching in reagents intended for titanium failed to reveal the structure, as it consisted of the α -phase with TiN , TiC and TiO_2 inclusions (**Fig. 8.20**).



○ **Fig. 8.20** Characteristic microstructure of the surface of alloy VT-6 modified by PDT with three pulses in nitrogen atmosphere at a distance of 40 mm

Increase in the PDT distance to 70 mm (15 pulses) results in a substantial increase in hardness of the surface layer (**Fig. 8.21**). Thickness of the layer is up to 30 μm . It consists of two sub-layers. The sub-layer on the sample surface has microhardness of 7250 MPa, and the sub-layer lying closer the base has microhardness of 5700 MPa.



○ **Fig. 8.21** Characteristic microstructure of the surface of alloy VT-6 modified by PDT with three pulses in nitrogen atmosphere at a distance of 70 mm

As revealed by X-ray microanalysis, the hardened layer has an increased nitrogen content. Its amount in the surface layer is up to 8.44 at. %, in the sub-layer adjoining the base it is 6.73 at. %, and at the interface with the base it is 2.24 at. %.

No nitrogen was detected in the base. These data explain the character of distribution of hardness through thickness of the hardened layer. Thus, the higher the nitrogen content of the hardened metal, the higher the hardness of this metal. Hardening is provided by formation of titanium nitrides and saturation of martensite with nitrogen (formation of nitrous martensite).

The maximum hardening was achieved on the samples treated by PDT at a distance of 70–120 mm with 15–20 pulses. This results in formation of a hardened layer 20–30 μm thick. Microhardness of this layer amounts to 5800–1100 MPa (**Fig. 8.22**).

According to the data of X-ray phase analysis and X-ray microanalysis, structure of the layer consists of martensite with an increased nitrogen content, in which the very fine needles of TiN can be seen. A brittle nitride layer (TiN, Ti – 55.6–48.1 at. %, N – 39.7–49.3 at. %) is formed on top of the nitrous martensite layer. Titanium carbide was also detected, in addition to titanium nitride and nitrous martensite (**Table 8.6**).

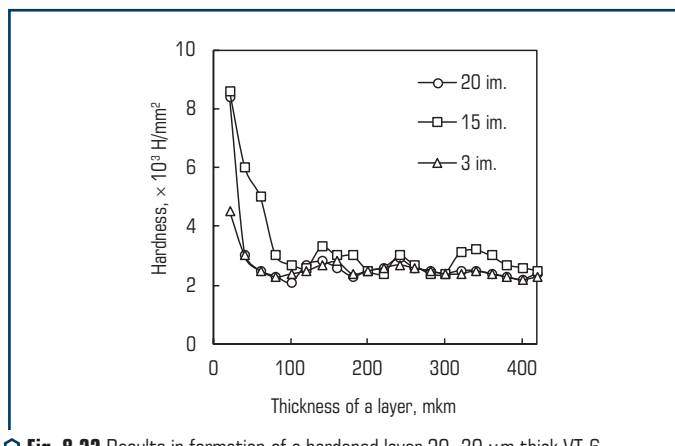


Fig. 8.22 Results in formation of a hardened layer 20–30 μm thick VT-6

Table 8.6 Conditions of PDT in nitrogen atmosphere and characteristic of modified surface of alloy VT-6

Sampl No.	PDT distance mm	Quantity of pulses	Layer thickness, μm	Layer hardness, MPa	Phase composition (data of X-ray phase analysis and X-ray micro-analysis)
5	40	3	25–35	4300	α – Ti, TiN layer, TiC, TiO ₂ , β – Ti
7	70	15	20–50	5700–7250	α – Ti, TiN layer, TiC, TiO ₂ , β – Ti
18	120	20	20–25	8500	α – Ti, TiN layer, TiC

As shown by the analysis, there is a trend to enhancement of the hardening effect on alloy VT-6 with increase in the quality of pulses and distance of PDT in nitrogen atmosphere. It is likely that increase in the distance allows a good access of nitrogen to the surface treated. All these factors provide conditions for formation of phases with a high hardness (e.g. TiN and nitrous martensite).

For example, the examinations showed that increase in the PDT distance (40, 70 and 120 mm) with increase in the quantity of the treatment pulses (4, 15 and 20, respectively) provided increase in hardness compared with the base material by a factor of 1.5, 2–2.5 and 3.35. The examination results prove that modification of alloy by PDT should be conducted at an optimal distance selected experimentally using a series of plasma pulses. The maximal hardening effect and averaging of qualities of the hardening layer through thickness are achieved under these conditions.

Appearance of the surface of a titanium-base alloy after pulsed plasma treatment is characterized by bright yellow and dark blue regions present on the surface. Roughness of the surface depends upon the intensity of the effect. No increase in roughness is seen at a low power density ($D=70\text{--}120\text{ mm}$), whereas after treatment of rough surfaces, e.g. with roughness of class 5, it reduces to class 6. At a high power density, where treatment is accompanied by fusion of the surface layer, roughness increases. Traces of metal spatters, elongated drops, radial valleys and periodic surface depressions (plateaus) are formed on the surface.

8.5.3 X-RAY DIFFRACTION ANALYSIS

Studies [299, 300] give results of investigations of the efficiency of pulsed plasma treatment (PDT) on samples of commercial titanium VT-1-0 and its alloys VT-6, VT-23 and VT-22. The following methods were used for the investigations: X-ray diffraction analysis, scanning electron microscopy (SEM) and secondary-ion mass spectrometry (SIMS). Microhardness was measured using the Vickers diamond pyramid.

X-ray phase analysis shows that titanium of the VT-1-0 grade in the initial state contains only the α -phase of titanium, while titanium alloys VT-6, VT-22 and VT-23 contain, in addition, also the β -phase. All the alloys have an oxide film on the surface, which consists of natural oxide TiO_2 (rutile). Such films act as a barrier for further diffusion of oxygen into an alloy. The secondary-ion mass spectrometry (SIMS) fixes clear peaks of TiO^+ and TiO in these films.

PDT of commercial-purity titanium in the fusion mode using six pulses with a specific power of about 1 MW/cm^2 led to substantial structural changes in the sub-surface layer. Comparison of diffraction patterns of samples of titanium of the VT-1-0 grades in the initial state and after PDT proves the substantial changes. Firstly, this is appearance of interference lines of $\delta\text{-TiN}$, $\epsilon_1\text{-Ti}_2\text{N}$, $\epsilon_3\text{-Ti}_3\text{N}$ and TiC , which is indicative of formation of nitride and carbide phases. The presence of titanium carbides and nitrides was also fixed by the SIMS method. Considering that the interference lines are smeared and that $\delta\text{-TiN}$ and TiC are present in large quantities, it can be suggested that the solid solution of nitrogen and carbon was formed in $\alpha\text{-Ti}$.

Secondly, treatment by the pulsed plasma containing molybdenum (product of erosion of consumable molybdenum electrode) resulted in introduction of molybdenum and molybdenum nitride Mo_2N into the surface of a titanium sample. Being β -stabilizer, molybdenum was not dissolved in titanium, but remained in the form of individual inclusions, which is evidenced by formation of peaks of Mo and Mo_2N in the diffraction pattern. Supposedly, compounds of molybdenum with nitrogen, carbon and oxygen are formed in the plasma jet as a result of plasma-chemical synthesis.

Thirdly, the intensity of the peaks of TiO_2 (anatase) doubled, and that of TiO_2 (rutile) grew insignificantly.

Compared with the initial state, PDT of alloy VT-6 (in the fusion mode) led to disappearance of a peak corresponding to the β -phase, which is indicative of saturation of the matrix material with α -stabilizers N, C and O, which are plasma components.

PDT of alloy VT-6 also led to saturation of the surface layer of a sample with elements contained in plasma (N, O). Mass transfer of these elements was intensified by the electromagnetic field, which provided formation of sufficiently thick layer (up to 10 μm thick) containing carbide and nitride phases. Non-uniform cooling of a sample through thickness favoured formation of martensite α' - and α'' -phases. δ -Ti of two types is formed on the surface: the first type is dark and porous, and the second type is continuous and goldish-yellow, up to 1 μm thick (**Table 8.7**).

An interlayer of the $\varepsilon_1\text{-Ti}_2\text{N}$ phase is located beneath this layer. Total thickness of the modified layer under such conditions of plasma treatment is not in excess of several microns. Such structure-phase transformations caused an insignificant increase in microhardness of alloy VT-6 (about 1.1 times).

Peaks of α -Ti almost vanished and the intensity of peaks of the β -phase increased in alloy VT-22 after PDT (with one pulse). PDT in the mode of fusion of the surface of this alloy led to formation of almost 100 % β -phase, unless the interstitial phase is taken into account. This is not surprising, as stabilization coefficient K_β is equal to:

$$K_\beta = C/C_m,$$

where C – the concentration of the β -stabilizer in the alloy; C_m – the minimum concentration at which the alloy can be quenched from the β -region to 100 % β -structure.

C_m is 1.05 for this alloy [297]. In this case peaks of the β -phase became more smeared, which is also indicative of saturation of alloy Vt-22 with alloying elements from plasma. The medium-intensity peaks (200) of δ -TiN and the low-intensity peaks (112) of $\varepsilon_1\text{-Ti}_2\text{N}$ were formed as well.

● **Table 8.7** Phase composition of alloy VT-6 after PDT

h, mm	TiN (δ -phase)	$\varepsilon_1\text{-Ti}_2\text{N}$	$\alpha\text{-Ti}$
0	+	+	+
5	–	+	+
10	–	–	+

The diffraction pattern obtained for the surface of alloy VT-23 modified by PDT comprises the increased-intensity peaks of α -Ti, δ -TiN, ε_1 -Ti₂N and TiC. The layer-by-layer X-ray diffraction analysis of an angle lap conducted by using the scanning electron microscope showed that the modified surface had a laminated structure (**Fig. 8.23**). A layer of δ -TiN with thickness of up to several microns was formed on the surface. This layer has a fine-grained structure. Located beneath is a narrow interlayer of ε_1 -Ti₂N, as well as a zone of solid solution of nitrogen in titanium. This zone consists of oval grains both for pure α -Ti and for $(\alpha + \beta)$ -Ti (alloys VT-6, VT-23 and VT-22). Thickness of the nitrified zone depends upon the alloy grade. The higher the β -phase content of an alloy in the initial state, the smaller the thickness of the modified layer. It can be seen from the SEM results that, unlike commercially pure titanium (VT-1-0), the $(\alpha + \beta)$ -alloys (VT-6, VT-22, VT-23) have a transition zone consisting of grains with a laminated morphology, formed between the gas-saturated layer and base metal.

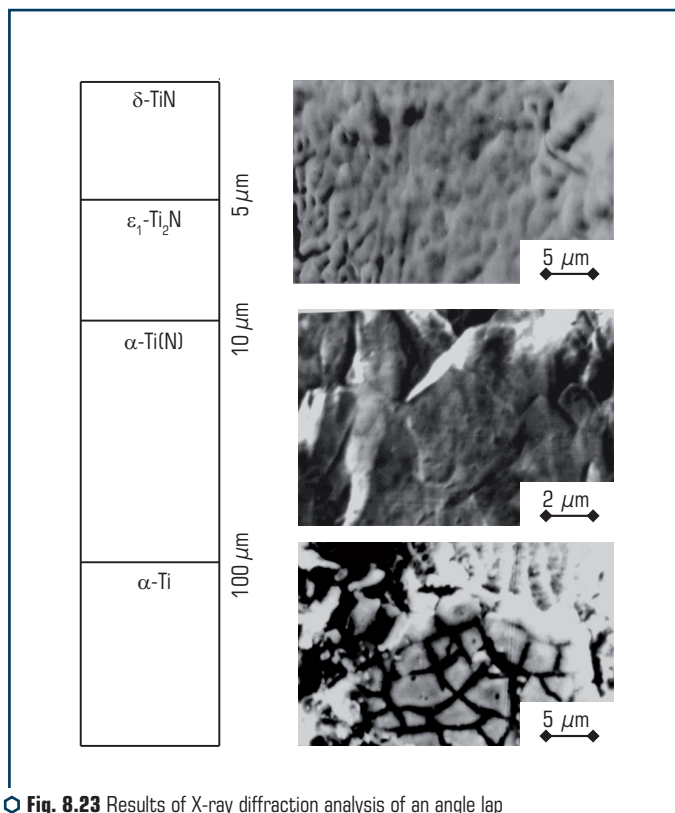


Fig. 8.23 Results of X-ray diffraction analysis of an angle lap of the surface of a titanium sample modified by PDT (SEM)

Considering the laminated morphology of grains of this zone, which is characteristic of the α -phase of titanium, and presence of martensite detected in alloy VT-6 after PDT in the mode without surface fusion, the authors of [298] think that the transition zone can be a martensite phase.

The effect of the quantity of the PDT pulses on the processes of phase formation was determined on samples of alloy VT-6, which were treated with a different quantity of pulses (1, 5, 10 and 15). Smearing of maxima of the interference lines decreases with increase in the quantity of pulses. The intensity of lines of the α -phase decreases, and the intensity of lines of δ -TiN and TiC increases. Decrease in smearing of the α -Ti lines and increase in the intensity of maxima of the interference lines of δ -TiN and TiC with increase in the quantity of the treatment pulses is attributable to transition of nitrogen and carbon from the "free" state into the fixed one, i.e. formation of titanium nitride and carbide. The ϵ_3 -Ti₃N phase in alloy VT-6 was formed only after treatment with 15 pulses.

Growth of the amount of nitrides and carbides on the surface depends, most probably, upon the rate of diffusion of a saturating element and is determined, primarily, by the temperature, duration and quantity of pulses. The total content of nitrogen in a sub-surface layer in the fixed state (δ -TiN) with increase in the quantity of pulses grows to 40 at. %. Hardness of the modified layer changes accordingly.

8.5.4 FORMATION OF SURFACE GEOMETRY

The surface of alloy VT-23 was subjected to PDT with 2 and 6 pulses. Examination of the morphology of alloy VT-23 by the SEM method shows that the resulting surface geometry has a characteristic morphology with ordered peaks and valleys oriented primarily across the direction of the spreading plasma. This can be explained by the fact that under the effect of the high-energy plasma flow and its spreading over the surface of a solid the shock waves are reflected from a solid boundary and collide inside the liquid substrate layer to form local centres of increased pressure.

Examination of the geometry of the surface of titanium VT-1-0 and its alloys (VT-6, VT-23, VT-22) after PDT using a different quantity of pulses shows that micro geometry of the surface is determined both by the experimental conditions and by the type of an alloy treated. For example, whereas the surface of alloy VT-23 after PDT with 2 pulses has a wavy character with an insignificant amount of gas bubbles, the surface of titanium VT-1-0 after PDT with 2 pulses is loose, porous and has a large amount of gas bubbles (**Fig. 8.24**).

Therefore, geometry of the surface of titanium alloys may vary from wavy to porous, and may even contain spattered drops of the electrode material. Depending upon the type of a titanium alloy, quantity and intensity of pulses, formation of a wavy geometry causes considerable stresses, which may lead to formation of cracks.

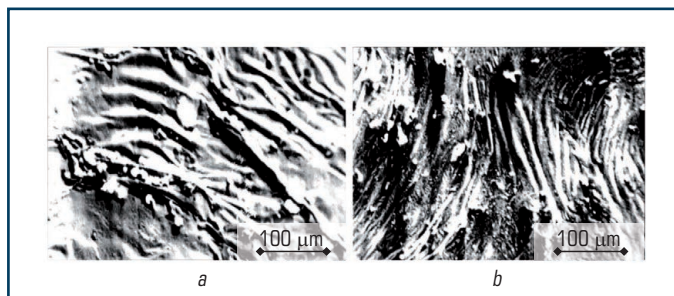


Fig. 8.24 Appearance of the surface of a titanium sample modified by PDT with 2 pulses: *a* – alloy VT-23; *b* – alloy VT-1-0

8.5.5 LASER HARDENING OF TITANIUM-BASE ALLOYS

Pulsed laser plasma treatment [134–136] of alloy of the Ti-V system, containing 2, 4 and 6 at. % vanadium, was conducted at a radiation intensity of $5 \cdot 10^8 \text{ W/cm}^2$. Pulse duration was $0.7 \cdot 10^{-3} \text{ s}$. The treatment resulted in a high-rate fusion and hardening of the alloy surface. Hence, microhardness of the surface of alloy Ti-6 % V grew to 3690 MPa, compared with initial 2760 MPa.

Investigations showed that pulsed plasma fusion of the surface of titanium alloys in air led to formation of a martensitic structure, whereas after treatment in vacuum no such structure was detected. Hardening of the molten layer results in formation of an oversaturated titanium-base single-phase α -solution, instead of initial two-phase $(\alpha + \beta)$ -melts. Microhardness of this layer is higher than in the initial state, and grows with growth of the vanadium content of the alloys. Formation of the surface layer of titanium oxides and nitrides takes place in air. Distortions and local heterogeneities in lattice of the α -solution, more pronounced than in the initial alloys, take place within the solidification zone of the melts, and a decrease in the lattice parameter in a direction normal to the irradiation plane occurs. These effects are associated with oversaturation of the α -solutions of titanium with vanadium, and with an influence by a non-uniform temperature field and thermal-elastic stresses on the mass transfer and solidification processes. The effects are enhanced with growth of the vanadium concentration of the alloys and increase in residual stresses.

The pulsed effect on alloys VT-8M and VT-6 by electron flows was studied [301]. Treatment was performed under the following conditions: maximal electron energy $E = 20\text{--}30 \text{ keV}$, and pulse duration $t = 0.7\text{--}2.5 \text{ } \mu\text{s}$. The energy density was about $2.5\text{--}5.0 \text{ J/cm}^2$. The quantity of pulses was varied from 5 to 100.

It is reported that the electron treatment resulted in a modified layer about $10 \text{ } \mu\text{m}$ thick. Examinations showed that this layer provided extension of cyclic fatigue life of an alloy at least by an order of magnitude. This is caused by two factors: change of a mechanism of fatigue crack initiation and dramatic decrease (2–3 times) in fatigue grooves within the limits of one grain. It is a known

fact that the surface fracture mechanism is characteristic of the initial state of an alloy, while the sub-surface fracture mechanism is characteristic of parts having a modified surface.

Thicker modified layers on an alloy were produced by using laser alloying [302]. Coatings of such metals as Ni, Cr, Mn and Cu, as well as their compositions (Ni+Mo, Ni+Cr, Cr+Cu, Cu+Ni, Mn+Cu) were deposited by a galvanic method on surfaces of samples made of a titanium-base alloy. Subsequent fusion of a coating allowed layers up to 400 μm thick with a content of alloying elements at a maximum depth equal to 5 at. % to be formed on the sample surface. At a depth of 5 μm the content of alloying elements was 20 at. %. Investigations showed that this treatment led to an increase of 2–3 times in surface hardness.

The effect by a high-energy pulse on the surface of molten metal leads to its saturation with the coating and gas atmosphere components. This is accompanied by dilution of the melt and transfer of alloying elements by the mechanism of convective mass transfer in the melt. Modelling of heating and melting of titanium plates during the laser-plasma effect process showed that the maximal value of thickness of the molten layer equal to 24 μm was achieved in 300 μs after beginning of the treatment [302].

8.5.6 MICROHARDNESS TITANIUM BASE ALLOYS AFTER PDT

Hardness of the surface of samples of a titanium-base alloy modified by PDT was measured under a load of 50 g. The measurements showed no traces of pyramid indentations. This is indicative of high microhardness of the sub-surface carbide and nitride layer. Therefore, further measurements of microhardness in the initial state and after PDT were made under a load of 200 g. Thin carbide and nitride layers are indented under this load, and microhardness of the initial material changes, although the carbide and nitride layers contribute to the integrated value of microhardness.

Investigations showed that the surface of samples made from commercial-purity titanium VT-1-0 modified by PDT had maximal microhardness. The treatment was performed with six plasma pulses in the surface fusion mode. The surface of samples of alloy VT-22 had minimal microhardness. The efficiency of hardening of the alloys in a region of homogeneous α -solid solutions normally decreases with increase in the content of a solute. It is likely that this effect is associated with the fact that dependence of strength properties of β -alloys upon the concentration of alloying elements is of a parabolic character, rather than of a linear one. So, an increased content of alloying elements leads to exhaustion of the hardening ability of β -alloys. Increase in microhardness of titanium alloys as a result of PDT is most probably caused by formation of meta-stable martensite phases and titanium nitrides and carbides, as well as by increase in the density of defects in a modified layer.

Investigations of microhardness (**Table 8.8**) showed that samples of alloy VT-22 had a maximal microhardness in the initial state and samples of commercial-purity titanium VT-1-0 had a minimal microhardness.

● **Table 8.8** Microhardness of the surface of samples of titanium alloys

Alloy	Alloy composition	State of alloy and PDT conditions		Microhardness, MPa
VT-1-0	99.46 % Ti	Initial		2,600
		PDT with fusion	2 pulses	6,600
			6 pulses	9,100
VT-6	90 % Ti, 6 % Al, 4 % V	Initial		3,700
		PDT without fusion	6 pulse	4,000
		PDT with fusion	1 pulse	5,000
			5 pulses	6,300
			6 pulses	7,700
			5 + 5 pulses	7,300
			5 + 5 + 5 pulses	8,200
VT-23	86 % Ti, 5.5 % Al, 2 % Mo, 4 % V, 1 % Cr, 1 % Fe	Initial		3,400
		PDT with fusion	6 pulses	6,800
VT-22	83 % Ti, 5 % Al, 5 % Mo, 5 % V, 1 % Cr, 1 % Fe	Initial		4,200
		PDT with fusion	1 pulse	4,900
			3 pulses	5,000
			6 pulses	5,100

In our opinion, increase in microhardness of titanium alloys as a result of PDT is caused mainly by 5 factors: formation of meta-stable martensite phases, formation of titanium nitrides and carbides, increase in the density of defects and thickness of the modified layer. The main contribution to increase in microhardness of the modified surface is made by formation of high-strength titanium carbide.

The effect by a plasma pulse on the workpiece surface leads to its saturation with coating and plasma components. Transfer of alloying elements to the surface layer occurs by the mechanism of convective mass transfer in the melt and effective mass transfer in solid and liquid phases. Also, this is caused by the fact that PDT leads to overheating of local regions on the surface of a massive sample and superposition of deformation on phase transformations. In addition, substantial acceleration of migration of atoms causes a strong impulse of the electromagnetic field.

The process of growth of a martensite crystal induces substantial stresses, the relaxation of which leads to deformation of metal in micro volumes and increase in defectiveness of a structure. The dislocation density and length of the phase and grain boundaries, which are the ways of accelerated diffusion, increase with each next transformation event.

As indicated by analysis of the investigation results, PDT has wider technological capabilities than laser treatment. The surface thermochemical treatment of parts during the PDT process provides a combination of high performance (wear, heat and corrosion resistance), ductility and strength of the base (titanium-base alloy).

ABSTRACT

The chapter presents the results of studies of the fine structure of the steel 40X surface layers after PDT. An analytical assessment of the yield strength, strength h , internal stresses and plastic properties is carried out.

KEYWORDS

Transmission electron microscopy, structure formation, strength, plasticity, destruction.

9.1 MATERIALS AND METHODS OF RESEARCH

The nature of the heating source, heat flux, time of exposure to the surface affect the properties of the heat-strengthened layer (thickness, physical and mechanical characteristics, phase composition and its dispersion). High heating (cooling) rates and temperature gradients of more than 10^7 m/K make it possible to obtain hardened layers with a previously unattainable level of performance properties. The whole range of performance properties depends on the structure of the surface-hardened layer of the material.

We investigated the effect of the pulsed action of a plasma jet on the modification of the surface layers of samples made of 40Kh steel (%: C 0.36–0.44; Si 0.17–0.37; Mn 0.50–0.80; Cr 0.8–1.10, the rest is iron). The samples were subjected to preliminary heat treatment: isothermal quenching for bainite in oil (at $T=850$ °C) to obtain at the level of 1500–1800 MN/m² and to maintain satisfactory impact strength (600–700 KJ/m²). The samples were treated with 5 pulses per point. In this case, the specific heat flux was $Q=6.5 \cdot 10^8$ W/m². Used electrode: W.

Metallographic research. Chemical etching of the material under study was carried out in a 4 % solution of nitric acid (HNO₃), the samples were viewed on an optical microscope "Versamet-2" at a magnification of 300 ($\times 300$). The microhardness H_{μ} (MPa) of the samples was measured on a Leko microhardness tester with a load of 50 g on the indenter.

Quantitative metallography was used to analyze changes in grain sizes. It is known that the grain size and the degree of its homogeneity are very important characteristics of metals and alloys, which determine the level of their structurally sensitive mechanical and physical properties. Therefore, it is no coincidence that the parameters characterizing the grain size (D_g), the form factor (∂e), the grain growth rate (G), and the change in these parameters in the course of thermal deformation processes are of interest.

The value of D_g was determined by the formula (9.1):

$$D_{-p} = \frac{\sum D_i \cdot N_i}{N}, \quad (9.1)$$

where D_i – the size (diameter) of the grain in the i -th group; N_i – the number of grains in the i -th group; N – the total number of grains measured.

When studying samples under various thermal deformation conditions, the methods of quantitative metallography, namely the secant method, were used to determine the average size of recrystallized grains, as well as the density of twin boundaries. The average grain growth rate (G) at different stages of recrystallization was determined from the dependence:

$$G = \frac{D_{mas}^k - D_{mas}^h}{t}. \quad (9.2)$$

X-ray structural phase analysis was performed on a DRON-UM 1 unit using monochromatic CuK_α – radiation.

A direct transmission study of the fine structure was carried out on a JEM-2000CX device (Jeol) at an accelerating voltage of 200 kV. Direct transmission studies were carried out with the aim of a deeper and more detailed analysis of the features of the structure, morphology and distribution of finely dispersed phase formations of various types, their composition, as well as the nature of the distribution of crystal lattice defects, the formation of dislocation inhomogeneities, incl. local concentrators of internal stresses.

Foils for electron microscopic studies were prepared using electrical erosion cutting, followed by mechanical thinning on sanding papers with different grain sizes, electrolytic polishing in a PTF installation, and final ion thinning.

The phase composition of the resulting dispersed and ultradispersed precipitates, the distribution of chemical elements in different parts of the sample during electron microscopic studies of the fine structure were determined in accordance with the standard methods of microdiffraction, micro-microdiffraction microscopy when examined in a JEM-200 CX transmission electron microscope (this allowed it possible to obtain more detailed information on the structural-phase composition of very local regions and the sizes of dispersed phases). At the same time, a special configuration of the electron microscope provides a quick transition from bright-field to dark-field images.

To estimate the size of ultrafine crystalline inclusions, a special measurement method was used. The essence of the technique is as follows. If thin foils cannot be obtained during the thinning process, then an electron diffraction pattern can be obtained. After counting the spots on the diffraction rings and using the formula to determine the grain size from the number of spots on the X-ray diffraction pattern, determine the average volume of the binder phase, which accounts for one inclusion (V_{br}). Further, according to the known volumetric composition (P), the average volume of the ultrafine particle is determined $V_p = PV_{br}$.

In this work, let's determine the volume fraction of the forming dislocation substructures (DSS) – sizes of cells, fragments, strip structures, etc.

Due to the fact that the size of the structural element in the forming type of DSS is larger or comparable with the thickness of the foil, it is possible to work with their images in the foil with random sections on the thin section. In this regard, the work used a method for determining the volume fraction by random sections, based on measuring the fraction of the foil area P_s occupied by a certain type of DSS (planimetric method). In this case:

$$P_v = \frac{V}{L^3} = P_s = \frac{S}{L^2}, \quad (9.3)$$

where S and V – the area and volume occupied by the corresponding type of DSS in the sample element, which is a cube with an edge L . In fact, the applied method is similar to quantitative phase analysis. The results of quantitative measurements of the volume fraction of DSS types were used to construct diagrams of dislocation substructures in the coordinates " $P_v - \epsilon(\epsilon^\circ)$ ".

The measurement of the scalar dislocation density was carried out in various ways. The first of them, the secant method, was used with a fairly uniform distribution of dislocations. The cutting lines formed a rectangular grid. The dislocation density ρ in the micrographs was determined using the formula:

$$\rho = \frac{M}{t} \left(\frac{n_1}{L_1} + \frac{n_2}{L_2} \right), \quad (9.4)$$

where M – magnification in the micrograph; t – foil thickness; n_1, n_2 – the number of intersections with horizontal and vertical lines, respectively; L_1, L_2 – total length of horizontal and vertical lines.

The foil thickness was measured by the width of the slip track, by the number of extinction thickness contours.

Measurements for calculating ρ were carried out using micrographs with a magnification of at least 30,000. This magnification was chosen for the reason that it is large enough to resolve individual dislocations, and still small enough for the dislocation density in the micrograph to correspond to the average dislocation density, and not to the local density in the walls of the cells.

At high degrees of deformation, when the dislocation density is high, micrographs were used with direct magnification in the microscope column of at least 40,000 and subsequent double enlargement.

This method for determining the scalar dislocation density was used for sufficiently isotropic dislocation structures. The average dislocation density in this micrograph was determined using the average distances between dislocations l in the slip plane parallel to the foil surface according to the formula:

$$\rho = \frac{\delta(1 + \Delta) \cdot M}{l \cdot t}, \quad (9.5)$$

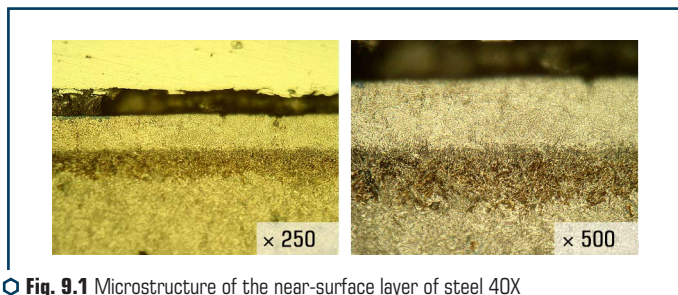
where δ – the fraction of dislocations in this micrograph belonging to a slip plane parallel to the foil surface; Δ – the number of other planes in the given microphotography.

Fractographic studies were carried out to study the nature of destruction (structure) in the investigated zone of the fracture surface using analytical scanning electron microscopy. The studies were carried out using a SEM-515 scanning electron microscope from Philips (Holland) equipped with LINK energy dispersive spectrometers.

Raster images of structures make it possible to obtain microimages with a large depth of field of view, which allows one to study structures at high magnifications and obtain clearer pictures of the details of these structures.

9.2 RESULTS OF METALLOGRAPHIC STUDIES AND X-RAY PHASE ANALYSIS

The results of studying samples of steel 40X by optical metallography methods show that as a result of pulse-plasma treatment, a layered structure is formed on the alloy surface, consisting of: a weakly etched strip (**Fig. 9.1**) finely dispersed with an indistinct (optically) pronounced structure of martensite (M), depth up to 70 microns from the surface, with an integral microhardness $HV=6550-5160$ MPa; and a transition layer with troostomartensitic ($Tr-M$) structure ($d \sim 70-100 \mu m$ from the surface) with an integral microhardness of 3860–3760 MPa. In this area, the process of heating and subsequent cooling can be considered as a kind of "tempering".



○ **Fig. 9.1** Microstructure of the near-surface layer of steel 40X during pulsed plasma treatment

The base metal (depth $\geq 100 \mu m$) is characterized by a structure (**Fig. 9.2**) of upper and lower bainite (B_u, B_l) and an insignificant amount of martensite. Volume fraction ($V \%$) of the above structures: $B_u \sim 58 \%$, $B_l \sim 40 \%$, $M \sim 2 \%$. The grain size of the structural components (D_g^B) is $12-25 \mu m$. Integral microhardness $HV=4120-5090$ MPa, which is 1.2–1.4 times less than the HV of the treated surface.

The results of measurements on the Leco device, with a load on the indenter of 50 g, of the integral microhardness after pulsed plasma treatment of steel 40X are shown in **Fig. 9.3**. In the plasma-treated surface, the microhardness increases on average \sim by 25 % in comparison with the base metal. And at a depth of 70–100 μm from the surface in the transition layer with

troostomartensite ($Tr-M$) structure, the microhardness drops to 3860–3760 MPa, which indicates a high temperature gradient along the depth of the material and structural tempering.

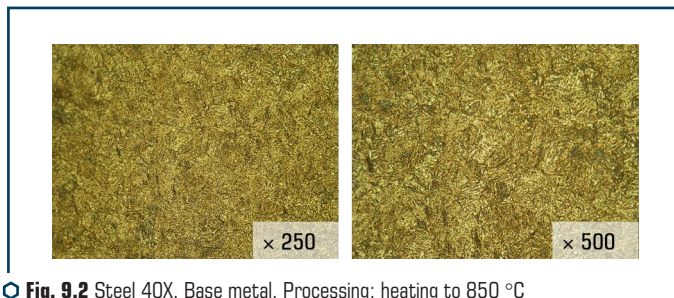


Fig. 9.2 Steel 40X. Base metal. Processing: heating to 850 °C and quenching in oil

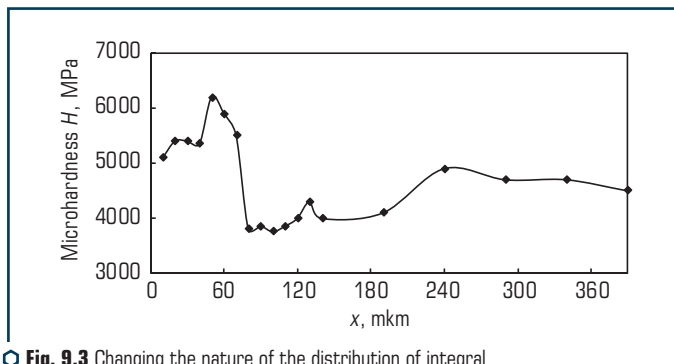


Fig. 9.3 Changing the nature of the distribution of integral microhardness from the outer surface to be treated to the base metal

It was established by X-ray diffraction phase analysis that the lattice parameter (a) of the α -Fe annealed sample made of steel 40X is: $a=2.8686 \text{ \AA}$; for 40X steel after quenching in oil, lattice parameter (a) α -Fe: $a=2.8706 \text{ \AA}$. In a sample of steel 40X treated by pulsed plasma, the following phase composition and lattice parameters are:

α -Fe (69.17 %), $a=2.8634 \text{ \AA}$;

γ -Fe (14.77 %), $a=3.6079 \text{ \AA}$;

Fe_4N (8.07 %), $a=3.7538 \text{ \AA}$;

FeO (3.11 %), $a=4.2719 \text{ \AA}$;

Fe_3O_4 (4.89 %), $a=8.3916 \text{ \AA}$.

The presence of oxides and iron nitrides is associated with the nature of the pulse-plasma treatment (treatment in air).

9.3 TRANSMISSION MICRODIFFRACTION ELECTRON MICROSCOPY

Studies by transmission electron microscopy made it possible to determine additional structural factors that were not detected using the method of optical metallography.

The analysis of the studies showed that a layered structure is formed on the surface of the samples after the pulse-plasma treatment, consisting of:

- a weakly etched band of fine martensite (M) – $\delta \sim 0\text{--}70\text{ }\mu\text{m}$ from the surface. A typical image of a fine structure is shown in **Fig. 9.4**. The structure is represented by clearly pronounced dispersed martensite needles (**Fig. 9.4, e, f**). The width of the martensite laths: $h_{\min} \sim 0.16\text{--}0.33\text{ }\mu\text{m}$, $h_{\max} \sim 0.56\text{--}0.81\text{ }\mu\text{m}$. The dislocation density is $\rho \sim 2 \cdot 10^{11}\text{--}4 \cdot 10^{11}\text{ cm}^{-2}$. The size of substructural elements is in the range: $d_c \sim 0.03\text{--}0.13$ (minimum) and $d_c \sim 0.1\text{--}0.3$ (maximum).

- transition layer with troostomartensite ($\text{Tr}\text{--}M$) structure ($\delta \sim 70\text{--}100\text{ }\mu\text{m}$ from the surface) (**Fig. 9.5**). The fine structure is represented by acicular structures (M , Tr) $h \sim 1.8\text{ }\mu\text{m}$ with enlarged lath sizes in martensite – $1.2\text{--}2\text{ }\mu\text{m}$; at a significant (up to $\rho \sim 6 \cdot 10^{10}\text{--}10^{11}\text{ cm}^{-2}$), relative to the surface structure, a decrease in the density of dislocations. There is a "blur" of boundaries (strips). In some areas, the formation of a substructure is observed ($d_c \sim 0.25\text{--}0.5\text{ }\mu\text{m}$). The latter indicates a high temperature gradient, i.e. the flow of structural tempering.

The base metal (depth $\geq 100\text{ }\mu\text{m}$) is characterized by the structure of the upper and lower bainite (B_u , B_l) and an insignificant amount of martensite. The fine structure (**Fig. 9.6**) of this zone is characterized by a slight increase (in comparison with the transition zone) in the dislocation density up to $\sim 10^{11}\text{ cm}^{-2}$, which, however, is lower than ρ in the surface. The lath width is $h_{\min} \sim 0.1\text{--}0.3\text{ }\mu\text{m}$, $h_{\max} \sim 0.7\text{--}1\text{ }\mu\text{m}$. A variegated structure and an increase in the size of the equiaxed substructure are observed.

Thus, based on the description of the structure by transmission electron microscopy, it can be concluded that a fine-dispersed martensite structure with a uniform distribution of increased dislocation density without dislocation density gradients is observed in the surface layer, which predetermines the absence of local internal stresses and cracking in this zone. The nature of the dislocation structure should contribute to the provision of crack resistance.

In the transition layer, there is an increase in the width of the laths of needle-like structures and a significant decrease in the dislocation density in comparison with the previous layer. This structure indicates a high temperature gradient, i.e. the flow of structural tempering. Structural changes of this type should lead to a decrease in the strength characteristics (in comparison with the values in the surface layer).

The base metal (depth $\geq 100\text{ }\mu\text{m}$) is characterized by a different grain size of the structure (upper and lower bainite (B_u , B_l), martensite). There is a slight increase in the density of dislocations ρ

up to $\sim 10^{11} \text{ cm}^{-2}$, which, however, is lower than the value of ρ in the surface. An increase in the size of the equiaxed substructure is observed.

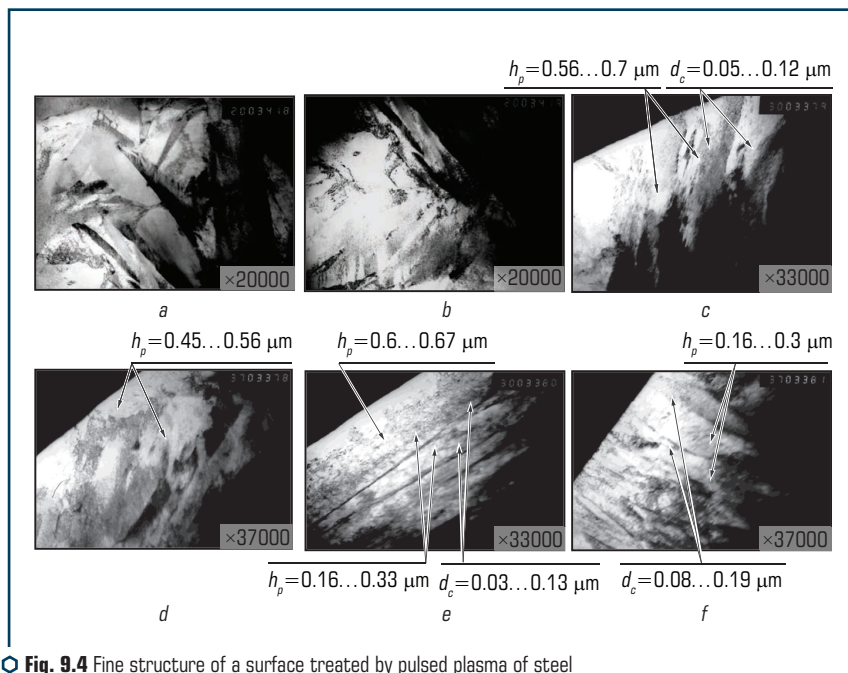


Fig. 9.4 Fine structure of a surface treated by pulsed plasma of steel samples at a distance of 10 μm from the surface

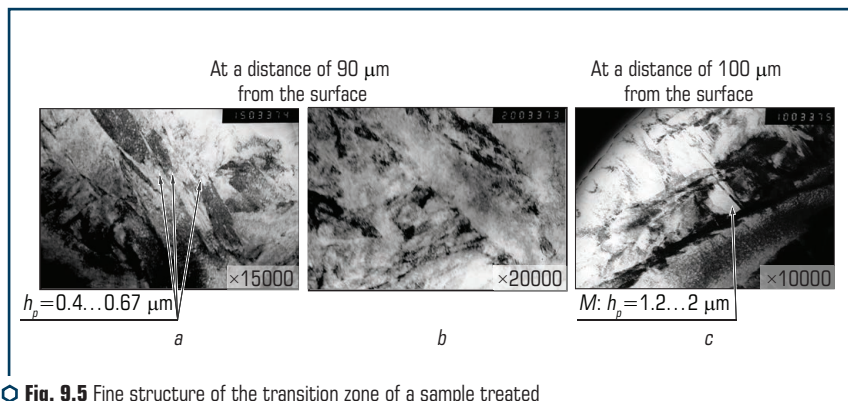


Fig. 9.5 Fine structure of the transition zone of a sample treated with pulsed plasma at a distance of 90 μm and 100 μm from the surface

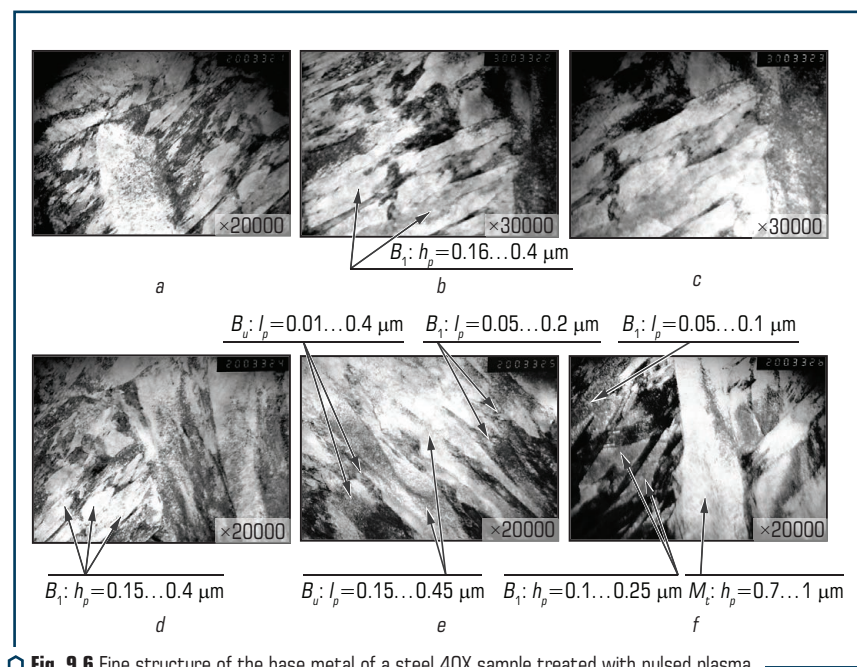


Fig. 9.6 Fine structure of the base metal of a steel 40X sample treated with pulsed plasma

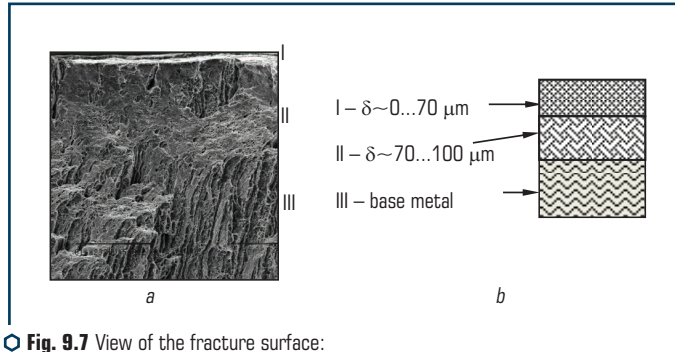
9.4 FRACTOGRAPHIC STUDY OF THE FRACTURE SURFACE OF THE MODIFIED LAYER

The general view of the fracture is shown in **Fig. 9.7**, where characteristic fracture zones I, II, III and their sizes are marked. Studies have shown that the microrelief of the fracture surface is different for the characteristic fracture zones and has its own characteristics.

Fig. 9.8–9.12 show fragments of the investigated fracture surface at various magnifications.

Detailed studies of zone I at a depth of $\delta \sim 0\text{--}70\text{ }\mu\text{m}$ from the treated surface have established the following. The area adjacent to the treated surface at $\delta \sim 0\text{--}30\text{ }\mu\text{m}$ is characterized mainly by intragranular quasi-brittle fracture (**Fig. 9.8**), the volume fraction of which is $\sim 70\%$ (the size of the quasi-cleavage facets $D_p^q \sim 5\text{--}13\text{ }\mu\text{m}$), intragranular viscous (**Fig. 9.9**) $\sim 25\%$ (the size of the pits $D_p \sim 1\text{--}6\text{ }\mu\text{m}$) and a small fraction of brittle fracture (**Fig. 9.10, a**) $\sim 5\%$ (the size of the cleavage facets $D_p^{cl} \sim 15\text{--}20\text{ }\mu\text{m}$).

Areas of quasi-brittle fracture are characterized by a relief of a quasi-cleavage of a complex configuration – with viscous elements, which indicates the presence of a plastic zone in front of the crack tip during fracture, and the size of the microrelief elements is small pits (about $d_p \sim 0.5\text{--}1.3\text{ }\mu\text{m}$) and tear-off ridges (**Fig. 9.8, b, d**) – on the dispersion of the structure in this area.



○ **Fig. 9.7** View of the fracture surface:
a – along the destruction zones; *b* – schematic illustration

In this case, single secondary cracks along the boundaries of structural components with a length (L) of the order of $\sim 10\text{--}30\text{ }\mu\text{m}$ (**Fig. 9.8, c, d**) and delamination characteristic of the martensitic structure (**Fig. 9.12, c**) in this region are located perpendicularly in the direction from the processed surface and their main distribution is blocked (by $\delta \sim 30\text{--}50\text{ }\mu\text{m}$) by the dispersed intragranular viscous component (the size of the pits is $d_p \sim 1\text{--}2\text{ }\mu\text{m}$). In the direction from top to bottom (**Fig. 9.8, b**), a transition to a dimple relief is visible. In local near-surface layers, characterized by a brittle transcrystalline cleavage (which share is $\sim 5\%$), the length of these cracks is somewhat longer (L of the order of $\sim 50\text{ }\mu\text{m}$, **Fig. 9.10, a**).

In the transition region at a depth of $\delta \sim 70\text{--}100\text{ }\mu\text{m}$ from the treated surface (zone II), the nature of fracture is predominantly viscous intragranular (the characteristic size of the pits is $D_p \sim 1\text{--}8\text{ }\mu\text{m}$), secondary microcracks and delamination are not observed, **Fig. 9.10, b**, **Fig. 9.11**. This zone is characterized by a change in the fracture mechanism from quasi-brittle cleavage to ductile fracture by merging micropores and, accordingly, a change in the structural-phase state, for example, such parameters as grain and subgrain sizes, dislocation density, etc. and a decrease in the density of dislocations, and the viscous micromechanism of destruction - on an increase in plasticity and a decrease in strength. Zone III (the region of the base metal) is also characterized by ductile fracture. However, the morphology of the microrelief of the fracture surface differs markedly from the ductile fracture in zone II and is a combination of dispersed pits (the characteristic pits size $d_p \sim 1\text{--}3\text{ }\mu\text{m}$), which characterizes the refinement of the structure (substructure), as well as large elongated pits ($D_p \sim 10\text{--}40\text{ }\mu\text{m}$) containing small particles of phase precipitates characteristic of bainite components, **Fig. 9.12**.

Microrelief parameters (most typical) for all zones of the fracture surface, including the size of brittle and quasi-brittle facets – D_F^{br} ; $D_F^{q/br}$, respectively; the average length of secondary microcracks (L_{cr}) and viscous fracture pits D_p , including dispersed type (d_p), as well as the volume fractions of the nature of fracture (brittle, quasi-brittle and viscous) are presented in the form of histograms and sector diagrams in **Fig. 9.13**.

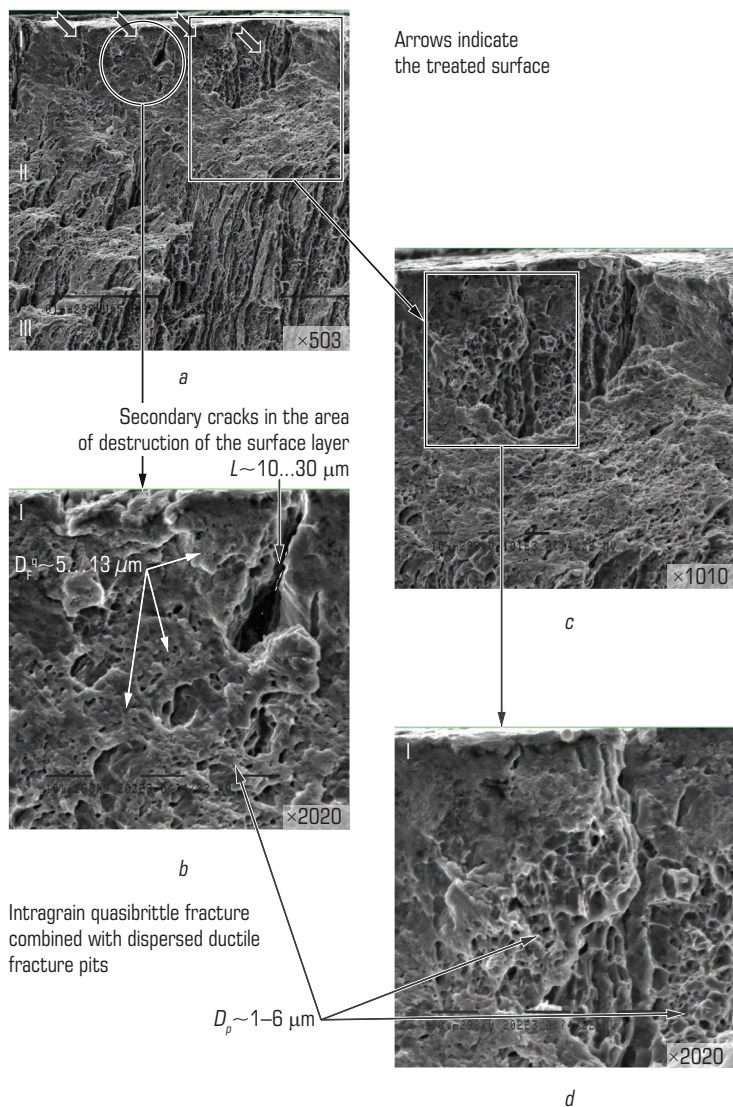


Fig. 9.8 Fragments of the fracture microstructure in the area of the treated surface at different magnifications

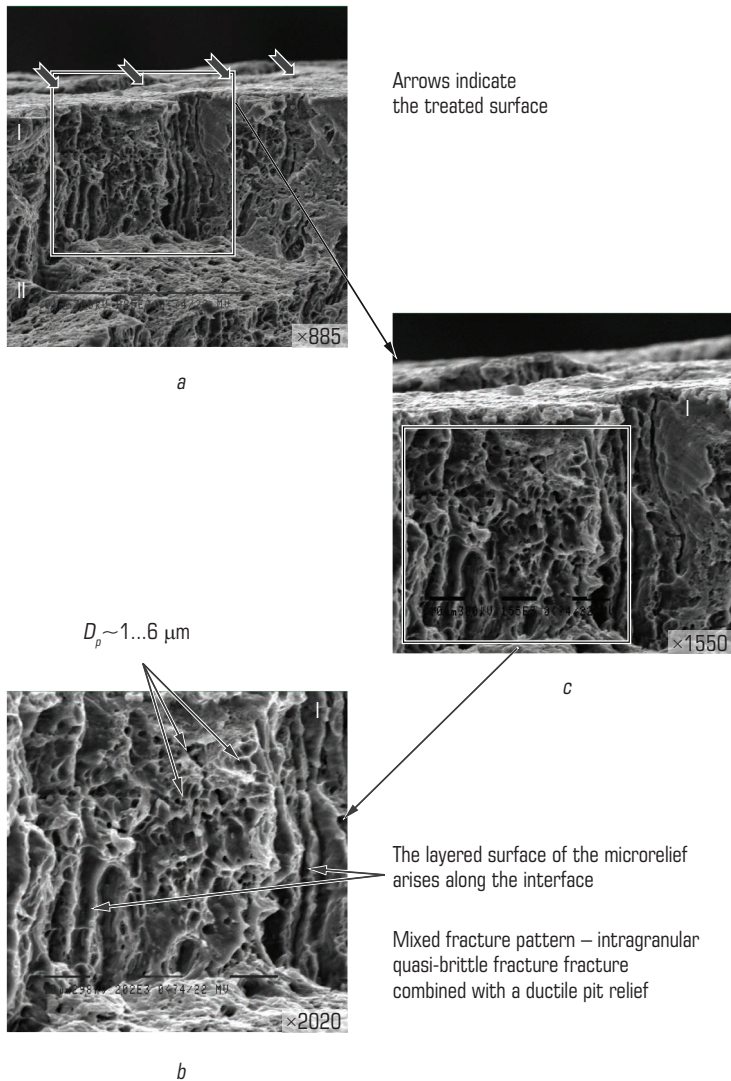


Fig. 9.9 Fragments of the microstructure of the fracture in the adjacent area to the machined surface at different magnifications

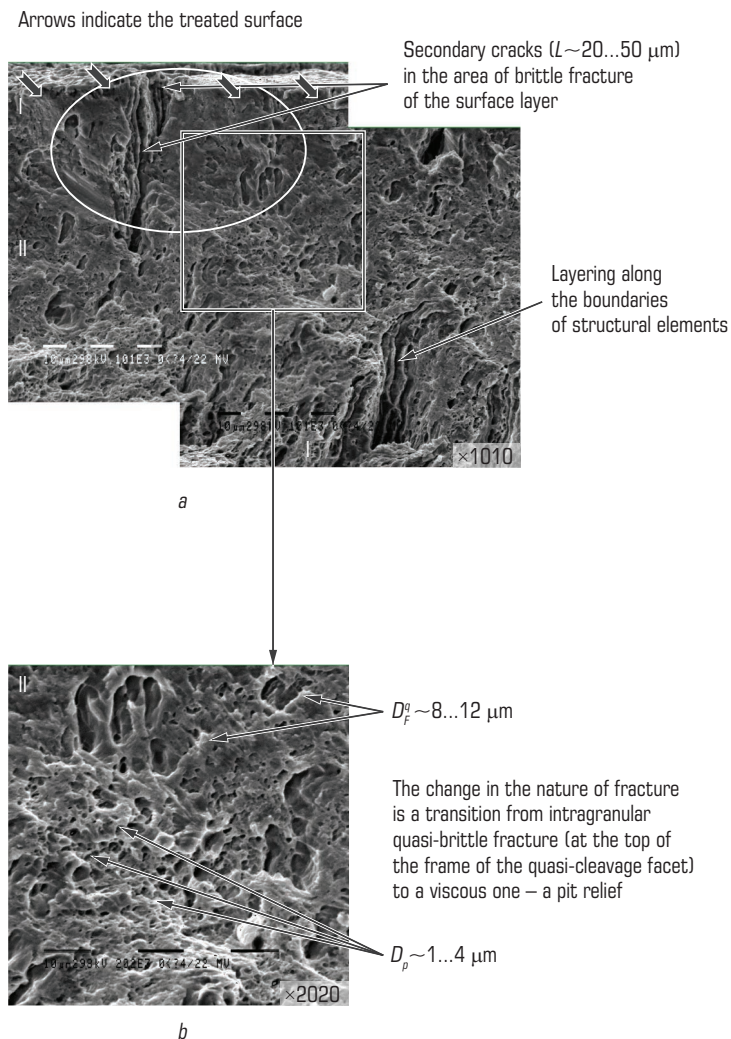


Fig. 9.10 Fragments of the microstructure of a fracture in the area of brittle fracture of surface layers at various magnifications

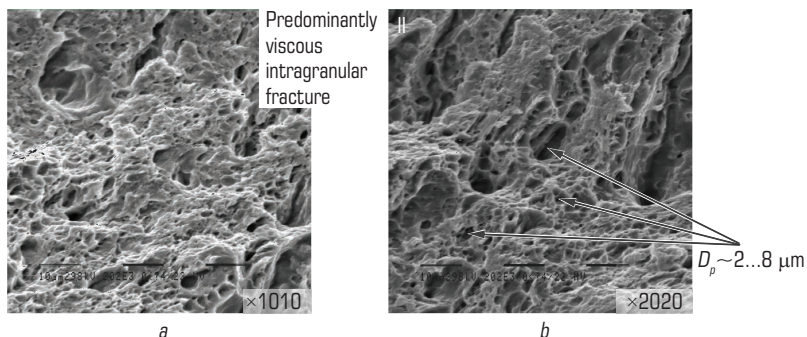


Fig. 9.11 Fragments of the fracture microstructure in the region of the transition fracture zone at various magnifications

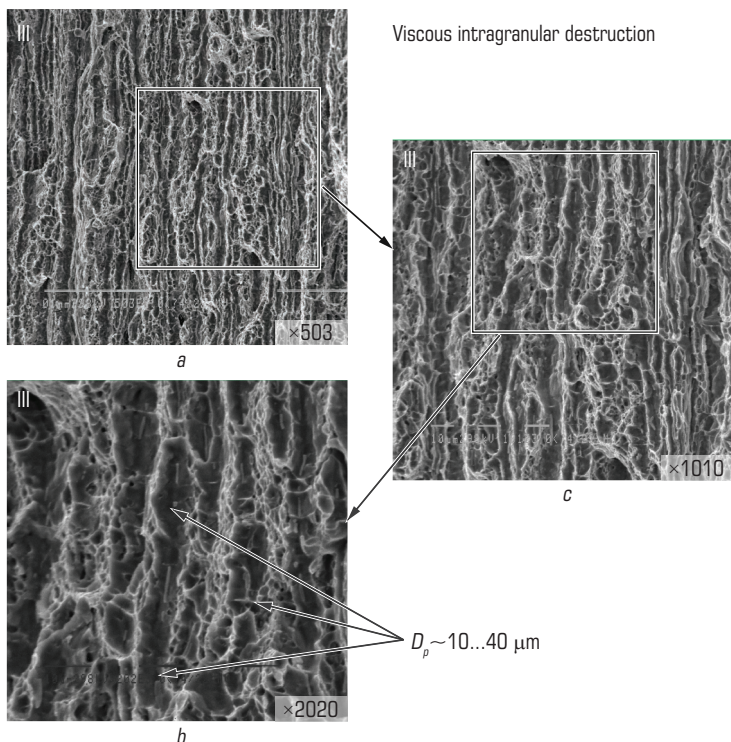


Fig. 9.12 Fragments of the microstructure of a fracture in the area of destruction of the base metal at various magnifications

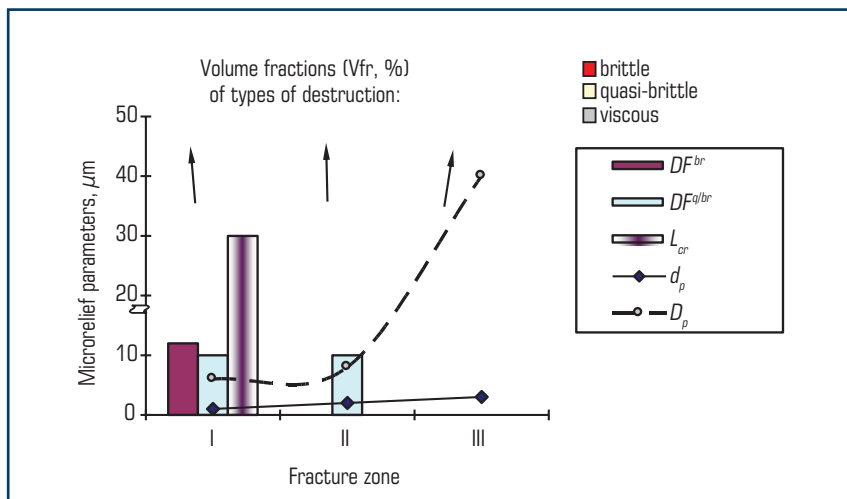


Fig. 9.13 Change in the volume fraction (V fr, %) of all types of fracture: brittle, quasi-brittle and viscous (pie diagrams) and characteristic parameters of the micro-relief of the fracture surface (histograms) – the size of the facets of the brittle and quasi-brittle type (D_F^{br} ; $D_F^{q/br}$); secondary microcracks (L_{cr}); viscous fracture pits (D_p ; d_p – dispersed) along the fracture zones

Studies of the nature of the change in brittle fracture and its movement along the destruction zones have established the following. The most dangerous zone prone to embrittlement is the first zone of the fracture surface – the area adjacent to the treated surface. Judging by the sector diagrams of the types of destruction in **Fig. 9.13**, (brittle, quasi-brittle, viscous) and their volume fraction, for the 1st fracture zone (surface layer), the viscous fraction is minimal (~20–25 %). This zone is characterized by a decrease in ductility and an increase in strength compared to the base metal. From the point of view of brittle fracture, this character is less pronounced for the II-nd fracture zone. The histograms show that the volume fraction of the quasi-brittle type of fracture decreases markedly (from 70 % to 5 %). Accordingly, when passing from zone I to zone II, the micromechanism of destruction changes (from quasi-brittle cleavage to viscous) and, accordingly, the properties of strength (decrease) and plasticity (increase) change.

9.5 ANALYTICAL ASSESSMENT OF THE RELATIONSHIP BETWEEN STRUCTURAL PARAMETERS IN PULSED PLASMA TREATED LAYERS AND THEIR MECHANICAL PROPERTIES

On the basis of a comprehensive study (optical microscopy, analytical scanning and transmission electron microscopy), a structural approach was used to assess the mechanical properties

in the working surfaces of products made of steel 40X after hardening pulse-plasma surface treatment, which made it possible to determine the differentiated (specific) contribution of each structural factor (grain size, subgrains, dislocation density, phase composition, etc.) into the total (integral) value of the strength characteristics ($\sigma_{0.2}$, σ_B) and plasticity (K_{lc}) of the surfaces relative to the properties of the base metal, which was the basis for adjusting the technology in order to form the optimal (in terms of properties) the structural state of the surface layers.

9.5.1 ASSESSMENT OF THE YIELD STRENGTH OF THE SURFACE LAYERS OF STEEL 40X AFTER PDT

The considered approach to predicting the quality of products made of steel 40X treated with pulsed plasma is based on assessing the effect of experimentally determined specific structural parameters on the most important mechanical characteristics: strength and plasticity, including the flow stress σ_f , the ultimate strength σ_B , and the fracture toughness parameter – the stress intensity factor K_{lc} .

At the same time, the experimentally determined structural-phase parameters include: chemical composition, grain size, subgrains, dislocation density, size and distribution of phase formations, etc., the data on which were obtained using a set of research methods at various structural levels, and namely, optical metallography, analytical scanning and transmission electron microscopy.

The quantification of the hardening (increase in the yield stress) due to each of the structural parameters was carried out as follows [303–306]. The yield point of metallic materials was considered as the sum of the following components:

- σ_0 – resistance of the metal lattice to the movement of free dislocations (lattice friction stress or Peierls – Nabarro stress);
- $\Delta\sigma_{s.s.}$ – hardening of a solid solution with alloying elements and impurities (solid solution hardening);
- $\Delta\sigma_g$, $\Delta\sigma_{sg}$ – hardening due to a change in the size of the grain and subgrain, according to the Hall – Petch relationship (grain boundary and substructural hardening);
- $\Delta\sigma_p$ – hardening due to pearlite;
- $\Delta\sigma_d$ – dislocation hardening due to interdislocation interaction;
- $\Delta\sigma_{d.h.}$ – hardening due to dispersed particles according to Orowan (dispersion hardening).

Thus, in accordance with the principle of linear additivity, the yield point is the sum of the following components:

$$\sigma_y = \sigma_0 + \Delta\sigma_{s.s.} + \Delta\sigma_g + \Delta\sigma_{sg} + \Delta\sigma_p + \Delta\sigma_d + \Delta\sigma_{d.h.}$$

The components that determine the main hardening mechanisms were calculated according to the dependencies:

$$\sigma_0 = 2 \cdot 10^{-4} G, \text{ MPa},$$

where G – the shear modulus: for steel – 84,000 MPa;

$$\Delta\sigma_{s,s} = \Sigma k_i c_i, \text{ MPa},$$

where k_i – the hardening factor; c_i – the concentration of the alloying element in the solid solution;

$$\Delta\sigma_g = k_g D_g^{-1/2}, \Delta\sigma_{sg} = k_{sg} d_{sg}^{-1} \text{ MPa},$$

where k_g, k_{sg} – coefficients that take into account the barrier effect of sub-borders and boundaries; D_g, d_{sg} – grain size and subgrain, respectively;

$$\Delta\sigma_p = 2.4 \cdot P, \text{ MPa},$$

where P – the content of the pearlite component, %;

$$\Delta\sigma_d = \alpha G b \rho^{1/2}, \text{ MPa},$$

where α – coefficient for steel – 0.5; b – Burgers vector for steel – $2.5 \cdot 10^{-7}$ mm;

$$\Delta\sigma_p = 0.81 \frac{Gb}{4\pi} \varphi \ln \frac{1 \cdot 2r}{2b} \frac{2}{1 - 2r}, \text{ MPa},$$

where φ – the coefficient characterizing the type of dislocations interacting with particles; r – the radius of the particles; 1 – the distance between particles.

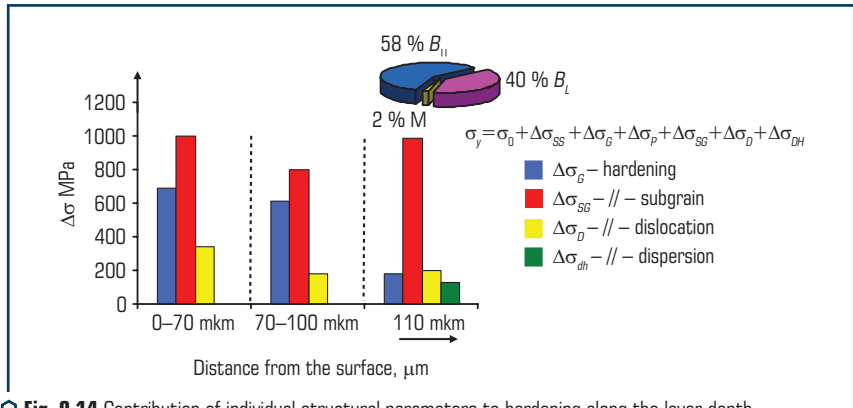
Changes in structural parameters and their contribution to hardening σ_y for steel 40X treated with pulsed plasma are shown in **Table 9.1** and **Fig. 9.14**.

It is shown that in the treated surface the total hardening ($\Sigma\sigma_{0,2}$) is ~ 2086 MPa (at 1551 MPa in the base metal), and the greatest contribution to the overall level of strength is made by the refinement of the acicular (martensitic) and lath substructure ($\Delta\sigma_{a/lm} \sim 1000$ MPa; $\Delta\sigma_g \sim 693$ MPa and dislocation hardening ($\Delta\sigma_d \sim 342$ MPa), due to a significant increase in the density of dislocations in surfaces during their processing.

In the transition zone, a decrease in hardening is due to a slight increase in the size of the lath structure (due to relaxation processes) and a decrease in the density of dislocations ($\Delta\sigma_d \sim 178$ MPa). For the base metal (in comparison with the first zone), the proportion of substructural hardening in bainite (up to 882 MPa) and dislocation hardening ($\Delta\sigma_d \sim 199$ MPa) increases.

● **Table 9.1** Changes in structural parameters and their contribution to hardening (σ_y) for steel 40X treated with pulsed plasma

Structural parameters	Surface ($\delta \sim 0\text{--}70\text{ }\mu\text{m}$ from the suface); finely dispersed M	Transition zone ($\delta \sim 70\text{--}100$ from the suface); TR/M structure	Base metal ($\delta \geq 100\text{ }\mu\text{m}$ from the suface); BL, B_L , M		
$D_g, \mu\text{m}$	min/mean/max $h_a = 0.32/1.1/1.8$	min/mean/max $h_a = 1.2/1.4/2$	min 12	mean 16	max 25
$(h_{peak}), \mu\text{m}$	016/0.45/0.73 (M)	0.25/0.56/1.0 (M)	0.075/0.17/0.53 (B_L); 0.07/0.13/0.4 (B_L)		
ρ, cm^{-2}	$2 \cdot 10^{11}\text{--}4 \cdot 10^{11} \text{ cm}^{-2}$	$6 \cdot 10^{10}\text{--}10^{11} \text{ cm}^{-2}$	10^{11} cm^{-2}		
$\lambda_p, \mu\text{m}$			0.05/0.27/0.5 (B_L); 0.03/0.15/0.25 (B_L)		
$V, \%$			58 % (B_L); 40 % (B_L); 2 % M)		
Strengthening due to structural parameters					
σ_0, MPa	16.8	16.8	16.8		
$\sigma_{s.s}, \text{MPa}$	34	34	34		
$\Delta\sigma_g, \text{MPa}$	542/693/1286	542/614/1286	145/182/211		
$\Delta\sigma_{sg}, \text{MPa}$	616/1000/2813	450/803/1800	300/882/2000 (B_L); 375/1154/2143 (B_L); 409/500/643 (M)	from V_r 174/512/1160 (B_L); 150/466/857 (B_L); 8/10/13 (M); $\Sigma 322/988/2030$	
$\Delta\sigma_d, \text{MPa}$	283/342/400	154/178/199	199		
$\Delta\sigma_p, \text{MPa}$			49/120/327 (B_L); 89/152/484 (B_L)	28/70/190 (B_L); 36/61/194 (B_L); $\Sigma 64/131/384$	
$\Sigma\sigma, \text{MPa}$	1492/2086/4550	1170/1646/2714	781/1551/2875		



● **Fig. 9.14** Contribution of individual structural parameters to hardening along the layer depth

9.5.2 ANALYTICAL ASSESSMENT OF PLASTICITY PROPERTIES

Based on the data of fractographic studies, an assessment was made of the tendency of the metal to brittle fracture in all fracture zones (**Table 9.2**), based on the calculation of the plasticity depending on the specific characteristics of the metals, where the parameter K_{1C} is the critical stress intensity factor, usually considered as a material constant at a given temperature – high-speed test conditions.

● **Table 9.2** Calculation of the stress intensity factor (K_{1C})

	Surface			Transition zone			Base metal		
$D_p, \mu\text{m}$	min	mean	max	min	mean	max	min	mean	max
	1.0	5	13.3	1.7	7	18	2.5	10	20
$\Sigma\sigma_y^{\text{calc}}, \text{MPa}$	2086			1728			1551		
$\Sigma\sigma_y^t, \text{MPa}$							1560		
$K_{1C}, \text{MPa}\cdot\text{m}^{1/2}$	24.7	52.5	90.2	29.2	56.5	94.9	32	63.9	90.5

To determine the plasticity properties of the metal, an estimate was chosen based on the Krafft dependence [307, 308] linking K_{1C} with the value of the critical crack opening (δ_t), taking into account the mechanism of its propagation:

$$K_{1C} = (2\sigma_y \delta_t E)^{1/2},$$

Fig. 9.15 shows a diagram of the structural strength of the metal (as an example of the combination of strength and ductility properties). In this case, the assessment of the K_{1K} value was carried out according to the dependence, based on the criteria of linear fracture mechanics, taking into account the contribution of the strengthening mechanisms that affect the increment of σ_y and the micromechanisms of crack propagation in each specific case, based on the analysis of the structural and fractographic features of the metal. At the same time, to assess K_{1C} , let's use the experimental data of fractographic analysis of fractures, in particular, the size of facets or pits on the fracture surface d_p , the value of which is equal to the value of the critical crack opening δ_t .

Based on the analysis of the structural strength diagram, it can be seen that the viscosity in the surface layers (fracture zone I) is on average $K_{1C} = 58 \text{ MPa}\cdot\text{m}^{1/2}$, which is 3 % lower compared to the transition zone (fracture zone II) and 10 % less base metal (fracture zone III).

The figure shows the achievable combinations of K_{1C} and σ_y , which indicate a significant influence on the structural strength indicators of structural parameters that determine the implementation of the micromechanism of crack propagation.

Thus, the transition zone from the surface to the base metal is characterized by a change in the nature of fracture from quasi-brittle to viscous, which is due to the structural – phase state of the metal, namely, a decrease in the volume fraction of the finely dispersed martensitic component, an increase in the proportion of bainite, a decrease in the density of dislocations, and an increase in the proportion of subgrained structural component.

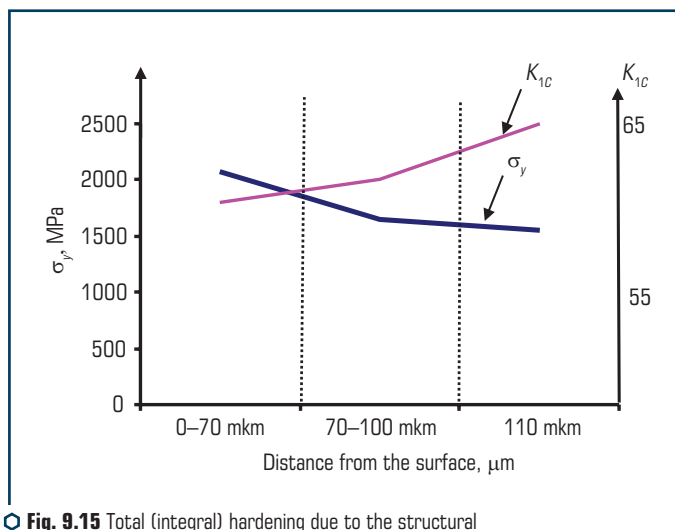


Fig. 9.15 Total (integral) hardening due to the structural state and stress intensity factor K_{1C}

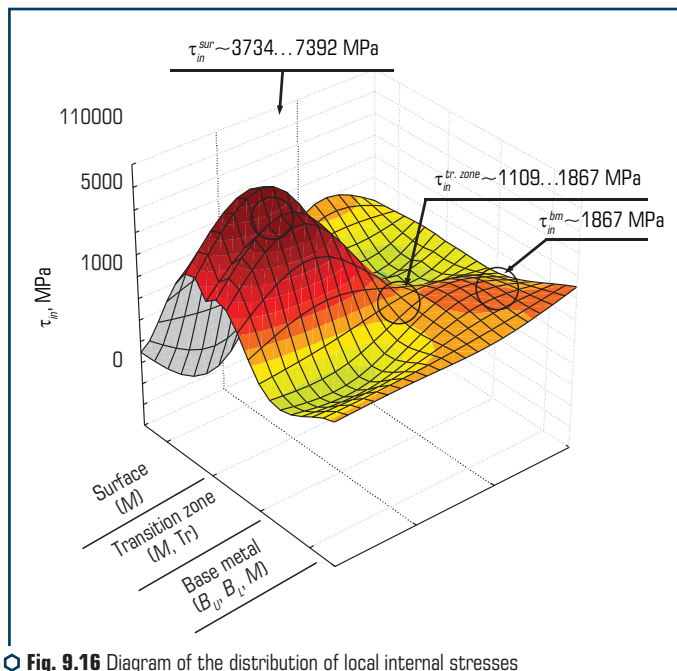
General and detailed analysis of the fracture – the structural components of the microrelief of the fracture surface, as well as the analytical assessment of the tendency of the metal to brittle fracture in all fracture zones showed that pulse-plasma treatment of the surface hardens the surface layers (maximum hardening) while the plasticity index in this area decreases slightly, which at the structural level is ensured by an increase in the density of dislocations and the formation of a finely dispersed martensitic structure.

9.5.3 CALCULATION OF LOCAL INTERNAL STRESSES (TIN) ACCORDING TO THE DEPTH OF PRODUCTS FROM STEEL 40X TREATED WITH PULSED PLASMA

Using the experimental data on the change in the density of dislocations (ρ), the nature of their distribution in the metal structure during the pulse-plasma treatment of surfaces, an analytical assessment of local internal stresses (τ_m) in depth was carried out. The results are shown in **Table 9.3** and **Fig. 9.16**.

● **Table 9.3** Calculation of internal stresses (τ_m) of steel 40X after PDT

	ρ, cm^{-2}	τ, MPa
Surface (M) ($\delta \sim 0\text{--}70 \mu\text{m}$)	$2 \cdot 10^{11}\text{--}4 \cdot 10^{11}$	3734–7392
Transition zone ($M + \text{Tr}$) ($\delta \sim 70\text{--}100 \mu\text{m}$)	$6 \cdot 10^{10}\text{--}10^{11}$	1109–1867
Base metal B_U, B_L, M ($\delta \geq 100 \mu\text{m}$ from the surface)	10^{11}	1867



○ **Fig. 9.16** Diagram of the distribution of local internal stresses over the depth of a 40X sample treated with pulsed plasma

The assessments were carried out according to the dependence:

$$T_{IN} = Gbh\rho/\pi(1-\nu), \quad (9.4)$$

where G – the shear modulus (84,000 MPa); b – Burgers vector ($2.5 \cdot 10^{-8}$ cm); h – foil thickness ($2 \cdot 10^{-5}$ cm); ν – Poisson's ratio (0.28); ρ – dislocation density showed that the maximum level ($\tau_m \sim$ up to 7,400 MPa) is observed on the surface, up to 0–70 μm deep (up to the transition layer with a partial tempering structure). In the transition zone (δ 70–100 μm from the outer surface) the level (τ_m) decreases and amounts to ~ 1500 MPa. A slight increase (τ_m) to ~ 1900 MPa is typical for the structure of the base metal ($\delta \geq 100 \mu\text{m}$).

ABSTRACT

The industrial use examples of plasma detonation technology are given. The efficiency of pulse-plasma treatment is shown. As a result of pulsed plasma processing, the performance of products increases by 2–4 times.

KEYWORDS

Industrial implementation, operability, cutting tool, rolling rollers, punches, dies.

High performance of alloys used to manufacture tools is known to be provided by alloying them with tungsten, molybdenum and vanadium. The chromium content of alloys is 3.0–4.5 %.

Dies for hot forming of machine parts are made from alloys containing 2–6 % W (of the 4KhNV and 4Kh5V2FS type), 6–9 % W (of the 3Kh2V8F type) and 12–18 % W.

Molybdenum is an element that efficiently improves properties of alloys. It increases toughness with no loss in heat resistance and raises fire crack resistance. Molybdenum alloys (5–6 % Mo) are very sensitive to decarburization. Therefore, surface alloying of alloys with molybdenum is accompanied by alloying with carbon, or performed in a gas atmosphere with an excess fuel gas coefficient ($\alpha < 0.7$). For more details, see Chapters 1 and 5.

Plasma exerts thermochemical and thermomechanical effects on a workpiece material, which activates plasma-chemical synthesis and formation of new compounds of elements that are components of plasma and workpiece surface.

Treatment of the surface by the pulsed plasma [309–322] is more efficient than treatment with a continuous plasma flow, which is attributable to a 1–2 orders of magnitude higher heating and cooling rate, as well as to the effect exerted by the electromagnetic and shock waves. Because of propagation of a heat wave, heating of the internal layers of a workpiece material continues also after the end of a pulse, which increases the efficiency of treatment of the workpiece surface with a series of alternate pulses.

Analysis was conducted on a number of studies, where the ambient pressure was varied, thus causing variations in density of the plasma jet and, finally, concentration of dissolved alloying elements in the workpiece surface and microhardness. A high ambient pressure restricts scattering of plasma, which extends the time of its interaction with the workpiece surface.

Pulsed plasma treatment of parts made from high-speed alloys R9M5, R9M4K8F, R10K5F5, R12F5M and R12F2K8M3 should be performed without fusion of the surface. With treatment in this mode the performance of tools grows 3–5 times. For example, in pulsed laser treatment an

increase in surface hardness and wear resistance of tools of high-speed steel is achieved only in the case where the specific power of pulses is within a range of $1 < W_p < 5 \cdot 10^5 \text{ W/cm}^2$ and the time of the effect is $t = 5 \cdot 10^{-3} \text{ s}$. These treatment conditions are used also for the pulsed plasma modification. They provide ultimate temperature of the surface close to the melting point.

Experiments show that introduction of molybdenum and/or tungsten to plasma through using corresponding electrodes raises the treatment efficiency. Hardness of the treated surface is higher in the case that in introduction of chromium and titanium. The trend to growth of the efficiency of PDT with increase in the atomic number of alloying elements is especially pronounced in modification of steel with a carbon content of up to 0.8 %. This is attributable both to large displacements of atoms of the substrate bombarded by heavy ions of the plasma beam and a hardening effect of the elements introduced into the workpiece surface. In addition to rapid heating and cooling, phase hardening also takes place at an energy density of $10^5\text{--}10^6 \text{ W/cm}^2$.

Maximal hardness of the surface layer was achieved in modification by plasma containing tungsten or molybdenum vapors at the presence of excess nitrogen and carbon. In addition to the above technological parameters, the value of microhardness is affected also by the quantity of plasma pulses. Increasing the quantity of pulses leads to increase in thickness of the hardened layer and its uniformity. For more details see Chapters 1 and 6.

10.1 HARDENING OF METAL CUTTING TOOLS

PDT was applied to treat metal cutting tools. Prior to hardening, the tools were subjected to standard heat treatment and machining. Pulsed plasma treatment was used as a final operation. Hardening was performed only on surfaces of cutting edges of the tools. Productivity of hardening was up to 0.5 m^2 of the surface per hour, which, when re-calculated to actual tools, is up to 100 punches per hour. The surface of a tool requires no cleaning or any other preparatory operation before hardening.

The power density insufficient for fusion and rounding of cutting edges was selected to harden metal cutting tools, such as taps, rams and broaches. A molybdenum consumable electrode was used in this case, and the plasma gas contained excess propane and nitrogen ($\alpha = 0.6$). Treatment of mills, drills, cutters, etc. was conducted using a titanium electrode. The treatment was performed with a 5- to 10-fold effect by plasma pulses on the surface to be hardened.

Industrial tests of the tools subjected to PDT were conducted at enterprises of Ukraine, Russia, Czechia and Finland. The tests showed that the efficiency of hardening was especially high on the re-sharpened tools, where sharpening of the cutting face exposes the hard-modified layer formed by PDT on the clearance face.

This applies, for example, to hardening of knives for cutting rolled metal stock (**Fig. 10.1**) (sections, plates and profiles), or to PDT of metal cutting tools, (broaches, taps (**Fig. 10.2**), mills, shaped cutters, etc.). Analysis of operation of the tools subjected to PDT in industry showed that their performance is as a rule 3–6 times higher, compared with untreated tools.



Fig. 10.1 Hardened knives for cutting rolled stock: *a* – steel sheets; *b* – sections

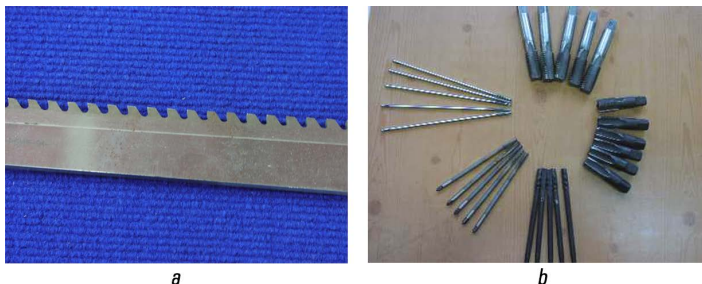


Fig. 10.2 Metal cutting tools hardened by PDT: *a* – flat broach; *b* – taps M4-M16

PDT was performed with plasma generators using the tungsten rod electrodes 6 mm in diameter. As a rule, the treatment of tools is carried out with a wide plasma flow (up to 30 mm wide) having a low power density (10^3 – 10^5 W/cm²), which provides hardening of only the cutting edges, with no loss in their roughness.

Given that the PDT technology requires no surface preparation, is performed in air and does not cause heating of a workpiece in the bulk, it can be used almost at any metal working enterprise. The productivity of hardening is sufficiently high to meet the demand of a machine building plant workshop with a staff of up to 800 people. As shown by experience of commercial operation, performance of the tools after PDT increases 3–6 times.

10.2 PDT OF BLANKING DIES AND PUNCHES

Examination of wearing surfaces of blanking (slotting) dies and punches for cold forming of holes shows that their performance depends upon the score resistance of rubbing surfaces, strength and hardness of the cutting (forming) edge and structural strength of a die.

PDT influences the first three parameters, but has no effect on structural strength of the dies, which limits its applicability. For example, analysis of the results of tests of blanking dies at the Gorky Motor-Car Plant revealed that failure of the dies was caused by fatigue of a structural material, rather than by wear of cutting surfaces. The reason was that the cutting surfaces of the dies were hardened by PDT and had a 3–4 times higher performance compared with the untreated dies. Peculiarity of PDT of blanking tools (**Fig. 10.3**) and punches is treatment with the plasma jet having a high power density (10^5 – 10^7 W/cm).



○ **Fig. 10.3** Appearance of hardened blanking die

This is achieved by focusing the plasma jet and passing the electric current through the jet. Contraction of the jet to a diameter of 8–10 mm and the electric current flow provide a 2–3 orders of magnitude increase in power density of the jet. In addition, molybdenum in the form of a rod 6 mm in diameter is used as an electrode.

Erosion of the electrode provides introduction of the vapor and drop phase of molybdenum to the plasma. Fusion of the working surfaces of parts with a high-density plasma jet containing ions, vapors and small drops of molybdenum, as well as carbon and nitrogen, leads to formation of a layer with new strength properties (Chapter 6). This layer protects the working surfaces of dies from fracture.

10.3 PDT OF TOOLS FOR HOT TREATMENT OF METALS

In contrast to metal cutting tools of high-speed steels, melting of the surface is permitted for the forming tools. The selected technological parameters of treatment for different types of punches, blocks and dies are characterized by a minimal power density, sufficient for heating of the surface to melting. These parameters provide alloying of the molten surface of a part with elements

contained in the plasma jet. A tungsten consumable electrode is used for hardening, and plasma gas contains excess propane ($\alpha=0.7$). The treatment was performed with a three-fold effect by the pulsed plasma on the surface treated.

The object of investigations was a press tool for hot forming of bearing rings in operation at a ball bearing plant. Pushers and punches made from steel 3Kh3M3F (0.3 % C, 3 % Cr, 3 % Mo, 1 % V) are subjected in forming to an intensive thermocycling effect, which is caused by contact with a hot deformed billet, and to rapid water cooling. Failure of the tools was caused by formation of a network of deep fire cracks.

Punches and dies for hot forming of steering connections were tested at an automated precision forming line. Punches were also tested on a press for half-hot extrusion moulding of piston rings. The tests were conducted at a motor-car plant. In addition, punches for precision hot forming of gears were also tested.

Dies for hot forming of complex-configuration cutters used in cleaning machines in mining industry were hardened (**Fig. 10.4**). Only the projecting parts of a die, which wear out during operation, were subjected to hardening.

It should be noted that, as shown by the studies, the two-layer hardening treatment proved to be most efficient. In this case the first layer is formed using a high-density plasma containing titanium, and the second layer is formed using the molybdenum-containing plasma.

Performance of the parts hardened only with as titanium-containing plasma is 2–3 times higher than that of the untreated parts made by a standard technology, while performance of the parts hardened with two layers is 3–6 times higher.

Experience accumulated in hardening of punches and dies shows that it is necessary to locate zones of maximal wear on the working surface prior to PDT. This allows only the wearing surfaces to be subjected to PDT. In addition, it is necessary to strengthen structure of the dies, allowing for the possibility of extending their life.



Fig. 10.4 Hardened die for hot forming of cleaning machine cutters

The PDT technology and equipment are efficient also for hardware manufacture and mass production of metallurgical parts. Experience of commercial application of PDT shows it provides a 2–3 times decrease in the tool production costs.

For example, dies for hot forming of metal (**Fig. 10.5**) are made from alloys containing 2–6 % W (of the 4KhNV and 4Kh5V2FS types), 6–9 % W (of the 3Kh2V8F type), or from alloys containing 12–18 % W.

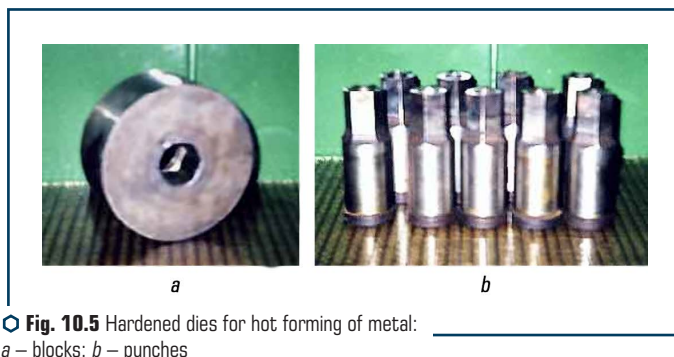


Fig. 10.5 Hardened dies for hot forming of metal:
a – blocks; b – punches

Tungsten may have a different effect on heat and fire resistance of die steels. Increase in the tungsten content of an alloy to 7–8 % leads to an almost proportional increase in heat resistance. Further increase in the tungsten content (to 12 %) causes almost no increase in heat resistance. Toughness and hardenability of an alloy are increased by adding 2–3 % Ni, although this fails to provide a substantial effect. Application of such alloys to manufacture massive parts is inefficient, which is caused by their high cost, difficult heat treatment and, what is most important, low impact toughness.

We suggested using low alloy 3Kh3M3F (GOST 5950-73), containing 0.27–0.34 % C, 0.1–0.4 % Si, 0.2–0.5 % Mn, 2.8–3.5 % Cr, 0.4–0.6 % V, 2.5–3.0 % Mo, 0.35 % Ni and 0.3 % Cu, for the manufacture of dies and punches (**Fig. 10.6**) for hot forming of metals, as well shaving and blanking punches.

Integrated treatment of working surfaces (duplex technology) was used to compensate for low hardness and heat resistance of the alloy. The duplex technology included case-hardening of the working surfaces of the tools, quenching, tempering and then alloying of the surfaces and hardening by PDT.

As a result, the tools have low hardness of the substrate equal to 49–50 HRC and high impact toughness of the material. Depending upon the cross section, the alloy may have the following values of impact toughness: 10 mm – KCU 24 J/cm², 120–200 mm – KCU 7 J/cm². Heat resistance of alloy 3Kh3M3F is not high, and at a temperature of 590 °C the alloy can resist heat only for 2 h (at 47 HRC). Hardness of the surface after case-hardening is 60–62 HRC. To increase heat resistance and hardness of the working surface of a part, PDT was used as a second (duplex technology) hardening operation. The choice of technological conditions of the treatment was based

on the need to ensure a minimum power density of the pulsed plasma sufficient to heat the surface to melting. These conditions provide alloying of the molten surface of a part with elements that are components of the plasma jet. A consumable electrode of tungsten carbides + cobalt and plasma gas containing excess carbon and nitrogen were used to introduce alloying elements. The treatment was performed by the three- to five-fold effect by the pulsed plasma on the surface hardened. The treatment spot diameter in this case was 15 mm. The pulse frequency was 1.5 Hz.



Fig. 10.6 Hardened punch for hot forming of metal

The effect by the pulsed plasma jet on a case-hardened and quenched working surface of a part resulted in formation of a modified layer 40–80 μm thick with high microhardness (up to 20 GPa) and high content of refractory elements (W + Co, 15–20 at. %).

Control tests of the hardened batches of tools showed that after the duplex technology their performance increased 3–7 times. The results of tests of the tools made from standard alloys and hardened by the duplex technology are given in **Table 10.1**.

As indicated by analysis of the results of the tests, the tools hardened by the duplex technology had no failures caused by brittle fracture or rupture. The only cause of failure of the tools was fire cracking of the working surface. Treatment of the tools with the pulsed plasma increased the content of refractory alloying elements in the tool surfaces, which extended life of the tool surface to formation of fire cracks, while the use of alloy with high impact toughness eliminated failures because of brittle fracture.

The developed duplex technology allows resolving a contradiction between high requirements to working surfaces (fire crack resistance, hardness) and not less high requirements for strength (impact toughness) of components of dies for hot forming of metals. Application of two efficient technologies to one part provides a substantial increase in performance of the part (**Table 10.1**). In addition, components of the dies are characterized as a rule by a large mass, and replacement of high alloys with high tungsten content by low alloys is very topical.

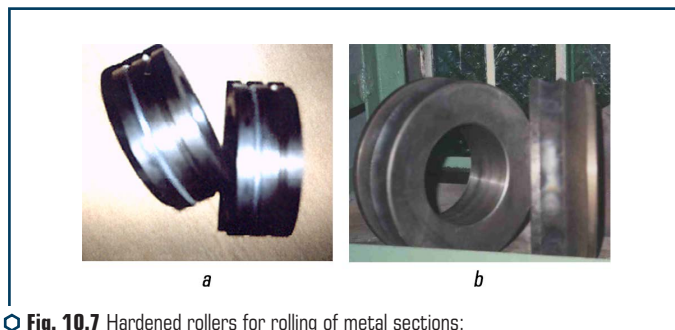
● **Table 10.1** Results of industrial tests of tools made from high-alloy and low-alloy steels after the duplex technology

No.	Tools	Resistance, t/pc		
		Standard	Before hardening	After hardening
1	Cutting knife	4.5	11.0	52.9
2	Cutting die	6.47	24.4	79.35
3	Bearing die	2.5	4.5	29.23
4	Slotting punch	0.85	1.8	7.08
5	Deformation punch	4.0	10.85	22.5
6	Bearing die	20.4	26.7	177.75
7	Forming die	5.0	18.0	54.0
8	Cutting die	9.2	20.8	32.0

Given that dies have complex configuration and are usually metal consuming, it is of practical interest to harden them in air using no shielding atmosphere. In addition, wear of dies is of a local character, it occurs only on cutting edges. So, PDT allows hardening of only the cutting edges of tools, thus saving materials and power usually consumed for hardening of the entire surface of a tool, which is the case of thermochemical treatment by standard technologies in salt baths or furnaces.

The industrial tests showed that surface modification of hard alloy rollers (**Fig. 10.7**) and rolls applied in metallurgy decreased the intensity of wear and eliminated wear by setting.

Treatment of saw disks for pipe rolling mill (**Fig. 10.8**) using a titanium containing plasma provided a 3–4 times increase in their performance. The saw disks were made from high-speed steel of the R6M5 type (6 % W, 5 % Mo) by standard technology.



● **Fig. 10.7** Hardened rollers for rolling of metal sections:
a – made from hard alloy; b – made from cast iron

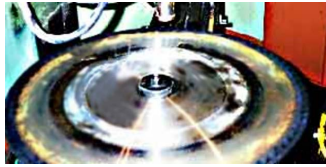


Fig. 10.8 Hardened saw disk

Pulsed plasma treatment of the surfaces of rolls for rolling car sheets is of an industrial interest. Examination of the surfaces of samples by scanning electron microscopy showed that individual hard drops consisting mainly of the anode electrode material were formed on the roll surface even under the softest treatment conditions. The quantity of the drops grows with growth of the treatment intensity. They spread over the workpiece surface to form a developed geometry with peaks having high hardness. Accumulation of carbon in the surface layer and valleys between the peaks takes place in this case. The peaks of oxygen and carbon are most intensive in the Auger spectra of all regions of the hardened surface. Introduction of molybdenum to plasma causes its mass transfer to a sample. X-ray spectroscopy using the "Superprobe" unit revealed about 5 % molybdenum in the matrix at a depth of about several microns. Such surfaces have consistent and uniform roughness, and are resistant to fire cracking.

Industrial tests of plasma hardened cast iron rollers of "tribe-apparatus", conducted in hot rolling of a rod 6.5 mm in diameter showed that the intensity of its wear decreased 4 times.

10.4 PDT OF WOOD WORKING KNIVES, SAWS AND MILLS

There is a class of parts applied in wood working, such as shaving and crushing knives, profiled and shaped mills, band, circular and frame saws, saw chains, etc.

The mechanism of wear of all these parts is almost the same. It consists of mechanical, thermal and chemical components. Low thermal conductivity of wood causes the concentration of heat at tips of the cutting blades of tools. As a result, their temperature grows to 200–700 °C. At such a temperature the processes of thermal-mechanical destruction of wood and thermal-diffusion displacement of the destruction products (as a rule, hydrogen) deep into a material take place at the blade surface.

The process of hydrogen pickup on the surface of a cutting blade is accompanied by decarburization and decrease in hardness. But the main result of this wear mechanism is hydrogen embrittlement, which is accompanied by fracture of entire conglomerates of grains and formation of cracks.

In this case a competing wear process is an abrasive wear using a free abrasive or abrasive fixed in wood. Considering a fracture effect of hydrogen, the process of abrasive wear under service conditions is often more intensive than under laboratory conditions in tests using abrasive

cloth. The intensity of these processes can be decreased through alloying of tool alloys. Volume alloying has certain limitations caused by increased requirements imposed on tools for safety factor for ductility in bending and fatigue under alternating loads. In addition, high-alloy steels are more expensive and more labour-consuming in machining. Selective surface alloying of only a cutting edge and formation of hard nano-crystalline layers on it is of a practical interest. Such technologies are well developed and applied using high-power laser or electron beam systems.

Metallography of samples of tool steels after PDT shows (see Chapter 6) that it is not inferior, and in the case of simultaneous alloying with different elements is even superior in efficiency to the laser technology.

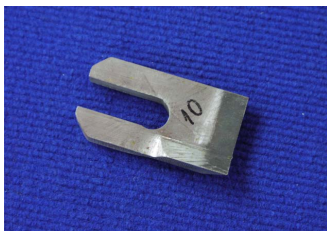
The results of the PDT tests were applied for hardening of commercial batches of wood crushing knives of the DS-57 type (**Fig. 10.9**).

The tests were conducted at wood working enterprises. The results of the tests showed that performance of the knives doubled after PDT. It should be noted that a relatively low efficiency of hardening is attributable to severe service conditions, presence of mineral inclusions in a wood pulp and ingress of stones and metal into a knife roll.

Shaving knives were tested (**Fig. 10.10**) in shaving of parquet using the DS-7 machine. The industrial tests showed that performance of the knives increased 5–7 times. The effect of hardening persisted after re-sharpening, which provides a many times increase in the efficiency of PDT.



○ **Fig. 10.9** Hardened knife for wood crushing



○ **Fig. 10.10** Hardened knife for wood working

The tests of circular (**Fig. 10.11**) and frame saws showed that their performance after hardening increased 6–8 times. The efficiency of hardening of the saws is provided by the fact that after standard quenching the saws have hardness of 40–45 HRC. Low hardness of the saws is determined by service conditions under alternating loads and stresses close to tensile strength of metal. After hardening, the surface hardness of a saw tooth was 11,000–19,000 MPa, which is more than twice as high as after volume quenching (4,500–6,000 MPa).



○ **Fig. 10.11** Hardened circular saw

10.5 PDT OF HARD ALLOY TOOLS

Variations in a hard alloy are attributable to the fact that the pulsed plasma energy is consumed for excitation of elastic oscillations of individual groups of atoms to cause dramatic increase in temperature in small volumes, crushing of grains, extra dissolution of tungsten in cobalt, etc. (see Chapter 8). As a result of the pulsed plasma effect, tungsten semi-carbide with hardness 1200–1400 MPa higher than that of initial tungsten carbide is formed in structure of an alloy.

Results of investigation of structure of the tool surface showed that melting of a periphery of the tungsten carbide grains, their fusion and formation of a characteristic structure of a carbide network occurred after PDT. Healing of microcracks and formation of finely dispersed carbides with a mean size of up to 0.5 μm at a mean size of initial carbide equal to 5 μm were found to take place.

The saws with a diameter of 300 mm, made from hard alloy VK15 (WC+15 % Co), were subjected to PDT (**Fig. 10.12**).

The saws were tested under industrial conditions when sawing wood chip plates at a furniture plant. The tests showed that the saws after PDT had a 3 times higher performance than the untreated ones. The hardening effect persists after re-sharpening, which is provided by the fact that hardening is performed on a rear face, and sharpening of the saw – on a front face.

Batches of drawing dies for calibration of 3.5 mm wire and rolling washers for wire diameter of 6.5 mm were treated by the pulsed plasma. These parts are made from hard alloys based on tungsten carbides (WC+12–15 % Co). Industrial tests under metallurgical production conditions showed that performance of the drawing dies increased 1.5–2 times after PDT.



○ **Fig. 10.12** Hardened saw with hard alloy regions formed on its surface

10.6 PDT OF TOOLS USED IN PROCESSING INDUSTRY

Parts widely applied in processing industry are knives for cutting beet (**Fig. 10.13**), potato, meat, straw, tobacco (**Fig. 10.14**) and other agricultural products.

These parts are made as a rule from low-alloy carbon steel. For example, knives for cutting sugar beet are made from steel with 0.5 % C, and scooter knives for cutting meat are made from steel with 0.7 % C.



○ **Fig. 10.13** Hardened knife for cutting of sugar beet



○ **Fig. 10.14** Hardened knife for cutting of tobacco leaves

Tests of the sugar beet knives after PDT were conducted at sugar beet processing plants. The tests showed that performance of the knives increased 3 times, and quality of crushing of sugar beet was also improved.

10.7 PDT OF CAR COMPONENTS

Working surfaces of piston rings were hardened. Initial structure of cast iron SCh 14–20 is a lamella pearlite with graphite inclusions and secondary cementite.

Hardening of the surface of piston rings was performed under the chosen conditions, where heat hardening was accompanied by alloying of the surface with molybdenum, nitrogen and carbon. Quenching from a liquid state at high cooling rates favours oversaturation of matrix with alloying elements, dramatic refining of secondary phases and even amorphization of alloys of the FeMo(Cr,V) type.

Two quenching zones are formed after PDT: zone of quenching from the melt and zone of quenching from a solid state. The first zone has a dendritic structure and contains dispersed ledeburite located in inter-dendrite spacings. The distance between dendrites was decreased 4 times, diameter of the dendrite axes being reduced more than 60 times (0.33–23 μm). Long thin dendrites surrounded by dispersed ledeburite increase strength of cast iron. The quenching zone consists of dispersed martensite saturated with carbon, which leads to a marked increase in hardness and strength of cast iron.

Two variants of PDT were performed on piston rings. A thick layer (up to 200 μm thick) is formed with the first variant of PDT. This is the PDT mode that involves surface fusion and alloying with molybdenum, carbon and nitrogen. The resulting layer is characterized by high hardness and poor workability, which is inadmissible in mass production.

The second variant provided for maintaining of roughness of the ring surface. Modification included deposition of the product of plasma-chemical synthesis of molybdenum and plasma components (oxides, nitrides and carbides of molybdenum), in addition to heat hardening (to a depth of 70 μm). The deposited layer has thickness of up to 50 μm .

Industrial tests oil-arresting piston rings subjected to PDT showed that as to performance they met requirements imposed on rings with a galvanic chromium coating.

10.8 PDT OF HYDRAULIC DRIVE AND END SEAL COMPONENTS

Most wearing surfaces of parts of hydraulic equipment are characterized by the boundary friction conditions. This applies to the following parts and components: piston rings of positive-displacement machines, side load discharge assemblies of piston sets, spherical joints, different types of dispensing devices (slide, plate, pin), regulators, and end seals.

According to service conditions, these parts do not need a high mechanical strength, but very stringent requirements are imposed on them as to wear resistance of their surfaces. Friction and wear of active surfaces of these parts occur in aggressive and abrasive environments. Parts of hydraulic equipment are made from high alloys and non-ferrous metals.

Industrial tests of a number of hydraulic drive components, such as valves and seats of dispensing devices, cross-arms of hydraulic motors, pump pistons and valve seats, showed that their performance after PDT increased 3–5 times.

Tests of end seals (**Fig. 10.15**) subjected to PDT were conducted under excavating machine service conditions. End seals of bearing compactor rollers were also subjected to tests. The tests showed a 3 times increase in performance of the end seals after PDT.



○ **Fig. 10.15** The end seals subjected to PDT

10.9 PDT OF PRINTING MACHINE PARTS

Fast wearing parts of wire stitching machines and knives for cutting paper and cardboard were subjected to hardening. Tests of the hardened parts were conducted under industrial conditions. The tests showed that performance of pulling rollers, wire cutting knives, stop plates for bending of wire ends, cross-arm guides, cams, bearing rollers and plain bearings after PDT was 3–5 times higher than that of the parts made by standard technology.

Tests of cardboard cutting knives were conducted at a folding carton plant. Performance of the knives after PDT increased 5 times. The hardening effect persisted after re-sharpening of the knives.

CONCLUSIONS

The book presents data on one of the most advanced and promising areas of metal physics, materials science and engineering. This is the effect by pulsed high-power density plasma jets on a solid metal substrate with a simultaneous stimulation of structural transformations and diffusion of alloying elements. Scientific and application aspects of these data are considered. When preparing the book, the authors used results of their own research and results obtained by other researchers. Structural-phase transformations causing the observed modifications of properties of solid materials are analysed on the basis of a unified concept of transformation of energy under the effect of the plasma jet in a material. They are determined mainly by the following three factors:

- kind and energy parameters of the plasma jet;
- initial characteristics of metals and alloys;
- parameters of treatment environment.

Despite a wide variety of materials studied, types and conditions of treatment, we can distinguish some features shared by the observed processes and effects:

1. Treatment of the workpiece surface is realized by pulsed plasma flow having temperature of up to 15,000 K together with the pulsed electric discharge having a current density of up to 10,000 A/cm², that produce a manifold impact on the surface including the thermal impact with power density of up to 10⁶ W/cm², chemical impact, electromagnetic impact (strength of magnetic field up to 4·10⁵ A/m) and mechanical impact. Pulse duration is up to 10⁻³ s. Intense short-time heating of the metal surface creates areas with a high temperature gradient (10⁷ K/m) near the surface, where stress and strain are produced due to the expansion of the heated metal and its subsequent compression while cooling. It causes the reduction of the metal structure close to the surface. Modification of the surface layer takes place at the depth of up to 80 microns and includes the following processes:

- 1) recrystallization with the formation of submicron structures;
- 2) alloying of the surface with the elements present in the ionized gas flow (W, Mo, Co, Ti, N, etc.);
- 3) chemical reactions with the formation of new phases. Alloying elements are added into plasma in the form of products of erosion of a metal electrode (rod) and in the form of gas (propane, nitrogen).

2. The suggested pulsed plasma technology is a resource-saving technology, which is provided by a low consumption of alloying elements and power, combined with high productivity (up to 0.5 m²/h). The technology allows treatment (heating) of only the working surfaces of parts, which solves the problems related to increase in wear resistance with no changes in structural state of material of the entire part.

3. PDT is efficient for modification of surfaces of almost all metal alloys. With different combinations of technological treatment conditions, PDT can be applied for modification of surfaces of iron, titanium or aluminium base alloys and parts made by the powder metallurgy methods.

4. Commercial application of the pulsed plasma technology shows that it provides increase in performance of different parts: disk knives – 2–4 times, saws – 3–4 times, rolls and rollers – 1.5–2.0 times, knives for cutting of rolled metal products – 5 times. The intensity of wear of cast iron "tribe" rollers decreases 4 times after the pulsed plasma hardening. Batches of drawing dies for calibration of 3.5 mm wire and rolling washers were hardened. These parts are made from hard alloys based on tungsten carbides (VK-8 and VK-15, respectively). The hardening treatment increased their performance 1.3–1.6 times.

5. Special consideration in the book is given to the experience of application of the described technologies, which makes it valuable for scientists and production engineers.

REFERENCES

1. Zhuravel, V. M., Bukhanova, I. F., Ilina, A. S. (1983). Povyshenie iznosostoikosti stalei s pomoschiu lazernogo izlucheniia. Proizvodstvenno-tekhnicheskii biulleten, 12, 34–44.
2. Urshanskii, A. I., Anikaev, V. A., Kilin, I. G. (1984). Lazernoe uprochnenie instrumenta dlia prokatki stalei. Moscow, 45.
3. Pamfilov, E. A., Severin, V. D. (1985). Tekhnologicheskoe obespechenie kharakteristik kachestva i iznosostoikosti izdelii pri lazernoi uprochniaiuschei obrabotke. Briansk, 62.
4. Kovalenko, B. C., Golovko, L. F., Merkulov, G. V., Strizhak, A. I.; Kovalenko, V. S. (Ed.) (1981). Uprochnenie detalei luchom lazera. Kyiv: Tekhnika, 241.
5. A. S. No. 396060 (SSSR). Sposob termicheskoi obrabotki detalei mashin OKG v srede azota i SO_2 .
6. Menin, R., Ramos, E., Magrini, M. (1981). Laser surface treatment of carbon and alloy steels. Proc. 4. Int. Coft. Rapid Quench. Metals. Sendai, 1, 193–196.
7. Medvedovskaia, L. A., Shur, N. F. (1983). Oborudovanie i tekhnologii lazernoi termicheskoi obrabotki (obzor). Metallovedenie i termicheskaia obrabotka metallov, 4, 34.
8. Mordike, B. L., Bergmann, H. W., Groß, N. (1983). Gaseous alloying with Laser Heating. Materialwissenschaft Und Werkstofftechnik, 14 (8), 253–257. doi: <http://doi.org/10.1002/mawe.19830140803>
9. Kogan, Ia. D. (1985). KHimiko-termicheskaia obrabotka splavov s primeneniem lazernogo nagreva. 4. Int. Congress of Heat. Treatment of Materials. Berlin, 2, 1393–1402.
10. Moorep, I., McCafferty, E. (1984). Corrosion resistant surface alloys prepared by laser processing. Proc. Conf. International Congress on Metallic Corrosion. Toronto, 2, 636–638.
11. Steffen, N., Erich, K. (1985). Oberflächenbehandlung von thermisch gespritzten Schichten mittels CO_2 – Laser zur Verbesserung des Verschleißverhaltens. Wiss. Z. Hochsch. Verkehrsw. Friedrich List Dresden, 1, 32–41.
12. Pamfilov, E. A., Borzenkova, T. G. (1983). Lazernoe uprochnenie tverdospalvnykh poverkhnostei. Mashinostroitel, 11, 44–46.
13. Soni, P. R., Rajan, T. V. (1985). Laser Beam Machining of High Temperature Ceramic Products. Transactions of the Indian Ceramic Society, 44 (2), 42–47. doi: <http://doi.org/10.1080/0371750x.1985.10822731>
14. Steen, W. M. (1985). Surface engineering with a laser. Metals and Materials, 1 (12), 730–736.
15. Vainerman, A. E., Kalganov, B. D., Popov, V. O. (1995). Osobennosti sozdaniia i perspektivy primeneniia materialov s osobymi svoistvami poverkhnostnykh sloev. Voprosy materialovedeniia, 1, 116–125.
16. Cordier-Robert, C., Crampon, J., Foct, J. (1998). Surface alloying of iron by laser melting: microstructure and mechanical properties. Surface Engineering, 14 (5), 381–385. doi: <http://doi.org/10.1179/sur.1998.14.5.381>

17. Chudina, O. V., Borovskaia, T. M. (1994). Uprochnenie poverkhnosti stalei legirovaniem pri lazernom nagreve s posleduiushei khimiko-termicheskoi obrabotkoi. Metallovedenie i termicheskaja obrabotka metallov, 12, 2–7.
18. Chudina, O. V. (1997). Poverkhnostnoe legirovanie zhelezouglerodistykh splavov s ispolzovaniem lazernogo nagreva. Metallovedenie i termicheskaja obrabotka metallov, 7, 11–14.
19. Ritter, U., Kahrman, W., Kipfer, R., Glardont, R. (1992). Laser coating proven in practice. Surface Engineering, 8 (4), 272–274. doi: <http://doi.org/10.1179/sur.1992.8.4.272>
20. Lugscheider, E., Bolender, H., Krappitz, H. (1991). Laser Cladding of Paste Bound Hardfacing Alloys. Surface Engineering, 7 (4), 341–344. doi: <http://doi.org/10.1179/sur.1991.7.4.341>
21. Navara, I., Bengtsson, B., Wen-Bin, L. (1983). Surface treatment of steel by laser hardening. VTsP N-L-02747, 8.
22. Sultanov, M. A. (1984). Ob adekvatnosti protsessa abliatsii metallov pri deistvii lazernogo izlucheniia i udarno-szhatoi plazmy. Fizika i khimii obrabotki materialov, 4, 17–21.
23. Popova, N. V., Fedorova, I. P., Popov, E. G. (1980). Deistvie plazmy vzryva na zhelezouglerodistye splavy. Fizika gorenii i vzryva, 4, 23–28.
24. Kaunov, A. M. (1985). O nekotorykh novykh napravleniiakh KHTO s ispolzovaniem udarnykh voln. Penza, 89.
25. Nosarev, P. S., Dikunov, Iu. G., Tkhai, V. (1985). O vozmozhnosti polucheniia pokrytii pri vozdeistvii bystrykh heterogennykh puchkov. Problemy zashchity metallov ot korrozii. Kazan, 45–49.
26. Safonov, A. N. (1997). Osnovnye napravleniia effektivnogo ispolzovaniia lazernoi tekhniki dlia termicheskoi obrabotki splavov. Metallovedenie i termicheskaja obrabotka metallov, 7, 18–21.
27. Ustanovka dlia poverkhnostnoi zakalki valkov s pomoschiu elektricheskogo razriada (1980). Japan. Zaiavka No. 55-36249.
28. Sposob poverkhnostnogo uprochneniia vysokoenergeticheskim puchkom (1980). Great Britain. Zaiavka No. 2027752.
29. A. S. No. 1092959 (SSSR). Sposob obrabotki metallicheskih detalei impulsnoi plazmoi v vakuume.
30. A. S. No. 1092960 (SSSR). Sposob poverkhnostnoi zakalki produktami sgoraniia v kamere pod davleniem.
31. A. S. No. 634569 (SSSR). Sposob poverkhnostnoi zakalki stalnykh detalei plazmennoi pushkoi s kapiliarom.
32. Pogrebniak, A. D., Vasiliuk, V. V., Alontseva, D. L., Kravchenko, Iu. A., Ruzimov, Sh. M., Tyurin, Yu. N. et. al. (2004). Struktura i svoistva pokrytii iz nikelovogo splava posle plavlennia elektronnykh puchkom. Pisma v Zhurnal tekhnicheskoi fiziki, 30 (4), 78–85.
33. A. S. No. 867040 (SSSR). Sposob termicheskoi obrabotki izdelii puchkom elektronov.
34. A. S. No. 1010875 (SSSR). Ustroistvo dlia poverkhnostnoi zakalki stali primeneniem uskoritelei relativistskikh elektronov.
35. A. S. No. 1048796 (SSSR). Sposob uprochneniia stalei potokom elektronov.
36. Kumanin, V. I., Livshin, V. B., Platitsin, A. V. (2002). Povyshenie stoikosti press-form pri elektronno-luchevoi obrabotke. Metallurg, 7, 50–51.

-
37. Tuli, M., Ctrutt, P. R. (1981). Property enhancement in rapidly quenched alloy surfaces. *Rapidly Solidified Amorphous and Cryst. Alloys. Proc., Mater. Res., Annu., Meet., Boston*, 456–460.
 38. A. S. No. 801627 (SSSR). Sposob obrabotki stalnykh izdelii azotirovaniem pered obrabotkoi elektronami.
 39. A. S. No. 867040 (SSSR). Sposob termicheskoi obrabotki izdelii elektronnoi pushkoi.
 40. A. S. No. 1176605 (SSSR). Sposob poverkhnostnogo uprochneniia izdelii elektronami.
 41. Ivanov, S. V., Salmanov, N. S., Salmanov, M. N. (2002). Borosulfokarbonitrirovanie rezhushchego instrumenta v elektrolitnoi plazme. *Metallovedenie i termicheskaiia obrabotka metallov*, 9, 42–43.
 42. Arzamastseva, E. P., Zinchenko, V. M. (1980). Elektronno-luchevaia obrabotka – novyi ekonomichnyi metod poverkhnostnogo uprochneniia detalei. *Tekhnologiiia avtomobilestroeniia*, 5, 23–26.
 43. Gusev, O. A., Lazarenko, A. V., Ivanov, B. A. et. al. (1984). Ispolzovanie impulsnogo elektronno-puchka dlia termicheskoi obrabotki metallov. *Metallovedenie i termicheskaiia obrabotka metallov*, 9, 35–39.
 44. Goldenberg, A. A., Polikarpov, V. I. (1984). Vliianie elektronno-luchevoi i lazernoi obrabotki na strukturu i svoistva mashinostroitelnykh materialov (obzor). *Vestnik mashinostroeniia*, 8, 67.
 45. Gonser, T. K. (1981). Computer sharpens EB hardening. *Amer. Mach.*, 11.
 46. Hutctings, R. (1986). The improvement of wear resistance by ion implantation. *Journal of Southern African Institute of Mining and Metallurgy*, 86 (3), 77.
 47. Pat. No. 215923 (GDR) (1984). Ustroistvo dlia ionnogo naneseniia tverdykh pokrytii.
 48. Picraux, S. T., Peercy, P. S. (1985). Ion Implantation of Surfaces. *Scientific American*, 252 (3), 102–113. doi: <http://doi.org/10.1038/scientificamerican0385-102>
 49. Vasileva, E. V., Fedorov, A. V., Savicheva, S. M. (1986). Vliianie ionnoi implantatsii na svoistva izdelii iz stali 30KHGSNA. *Vestnik mashinostroeniia*, 1, 21–25.
 50. Vasileva, E. V., Savicheva, S. M., Kriukova, I. V. (1987). Povyshenie iznosostoikosti stali ShKh15 ionnoi implantatsiei. *Metallovedenie i termicheskaiia obrabotka materialov*, 1, 17–23.
 51. Kustas, F. M., Misra, M. S. (1984). Application of ion implantation to improve the wear resistance of 52100 bearing steel. *Thin Solid Films*, 122 (4), 279–286. doi: [http://doi.org/10.1016/0040-6090\(84\)90028-2](http://doi.org/10.1016/0040-6090(84)90028-2)
 52. Poletika, M. F., Vesnovskii, O. K., Kulkov, S. N. (1986). Povyshenie stoikosti rezhushchego instrumenta putem izmeneniia ego kristallicheskoi struktury ionnoi implantatsiei. *Poverkhnostnyi sloi, ekspluatatsionnye svoistva detalei mashin i priborov. Moscow*, 127–232.
 53. Dillish, S. A., Bolster, R. N. (1983). Friction and wear reduction of 440-C stainless steel by ion implantation. *Mater. Symp. Boston*, 56–59.
 54. Dillish, S. A., Bolster, R. N., Singer, I. L. (1983). Friction and wear behavior of a cobalt-based alloy implanted with Ti or N. *Ion Implantant and Ion Beam Process. Mater. Symp. Boston*, 23–29.
 55. Hohmuth, K., Kolitsch, A., Rauschenbach, B., Richer, E. (1984). Beel N flussing mechanischer Eigenschaften durch Ionenimplantation. *Neue Hutte*, 5, 174–178.
-

56. Bolster, R. N., Singer, I. L. (1983). The reduction of wear and wear variability under lubricated sliding by ion implantation. Ion Implantation and Ion Beam Process. Mater. Symp. Boston, 145–148.
57. Singer, I. L. (1983). Tribomechanical properties of ion implanted metals. Ion Implanted and Ion Beam Process. Mater. Symp. Boston, 111–115.
58. Goltsev, V. P., KHodasevich, V. V., SHpilevskii, E. M. (1985). Puti povysheniia iznosostoikosti metallicheskih poverkhnostei metodami ionnoi implantatsii i ionno-plazmennoi obrabotki. Trenie, iznos i smazochnye materialy. Trudy konferentsii. Tashkent, 56–59.
59. Gurov, V. M., Korneev, A. A., Liapin, A. I. (1985). Tekhnologicheskie aspekty primeneniia ionno-implantirovannykh materialov v tribotekhnike. Iznos v mashinakh i metody zashchity ot nego. Briansk, Moscow, 78–83.
60. Kaunov, A. M., Burminskaia, L. N., Bukin, V. M., Riadinskaia, I. M. (1985). Formirovanie pokrytii iz smesi poroshkov khroma i grafita pri udarno-volnovoi obrabotke. Poroshkovaia metallurgii, 15, 25–28.
61. A. S. No. 554690 (SSSR). Sposob obrabotki metallorazruschego instrumenta iz bystrore-zhushchei stali putem obrabotki impulsnym magnitnym polem.
62. A. S. No. 940328 (SSSR). Sposob obrabotki izdelii impulsnym magnitnym polem.
63. UTRC Laser Systems (1977). United Technologies Research Center, 45.
64. Mason, I. H., Wisko, I. H. (1974). Spot and continuous Welding with solid state lasers. SME, MR-74, 955. Technical Paper, 79–83.
65. HLP Lasers (1977). AVCOE verett Pesarch Laboratory, 17.
66. Carstens, G. P. (1976). Material Processing with Multikilowatt Lasers. UTPS, 12–18.
67. Kotsiubinskii, O. Iu. (1980). Otsenka tekhnologicheskikh vozmozhnostei zakalki s ispolzovaniem gazovogo lazera nepreryvnogo deistviia. Metallovedenie i termicheskaiia obrabotka metallov, 5, 24–26.
68. Borodina, G. G., Kraposhin, V. S., Romanov, Iu. A. et. al. (1983). Struktura tekhnicheskogo zheleza v zone vozdeistviia izlucheniia nepreryvnogo SO₂-lazera. Metallovedenie i termicheskaiia obrabotka metallov, 4, 32–34.
69. Moriashev, S. F., Kisilitsyn, A. A., Kosyrev, F. K. (1984). Optimizatsiia parametrov protsesa zakalki stali izlucheniem SO₂ –lazera. Fizika i khimiia obrabotki materialov, 1, 23–29.
70. Dubrovskaiia, E. A., Kopetskii, I. V., Kraposhin, V. S. et. al. (1986). Vybor parametrov lazernogo nagreva uglerodistykh stalei dlia polucheniia zadannoi glubiny zakalki. Metallovedenie i termicheskaiia obrabotka metallov, 9, 23–26.
71. Bondoruk, O. F., Seits, S. E. (1981). Povyshenie iznosostoikosti shtampov oblucheniem OKG. Elektrofizicheskie i elektrokhimicheskie metody obrabotki. Moscow, 2.
72. Kornev, V. V., Kosyrev, F. K., Moriashev, S. F. et. al. (1980). O nekotorykh zavisimostiakh termoobrabotki lazerom. Fizika i khimiia obrabotki materialov, 3, 3–6.
73. Gustav, V. A. et. al. (1986). Vliianie lazernogo oblucheniia na strukturu shtampovoi stali KH12M. CHernaia metallurgii, 6, 28–29.

-
74. Tverdokhlebov, T. N., Diachenko, V. S. (1980). Vlianie uslovii lazernoi obrabotki na stoikost instrumenta iz bystrorezhuschei stali. Metallorezhuschee oborudovanie i instrument. Moscow, 17–21.
 75. Grechikhin, A. I. (1982). Issledovanie vlianiia izlucheniia nepreryvnogo i impulsnogo lazerov na strukturu i svoystva chugunov. Moscow, 19.
 76. Chekanov, N. G. (1981). Vlianie moschnogo izlucheniia SO₂-lazera na strukturu i svoystva chugunov, primeniayemykh v avtomobilestroenie. Moscow, 18.
 77. Abislov, G. A., Golubev, V. S. (1981). Osnovnye problemy lazernoi tekhnologii i tekhnologicheskikh lazerov. NIUTP. Troitsk, 3–39.
 78. Lazernaia obrabotka materialov (1977). Ref. Obzor. Riga: LatINTI, 43.
 79. Akulina, G. A., Tsyrlin, E. S. (1984). Lazernaia zakalka detalei mashin. Moscow: NIIMash, 64.
 80. Lakiza, Iu. V. et. al. (1984). Povyshenie effektivnosti lazernoi obrabotki. LDNTP, 1, 23–28.
 81. Travkina, N. T., Nikitin, A. A. (1985). Primenenie lazernoi tekhnologii dlia uprochneniia poverkhnosti metallov i splavov. Chernaia metallurgiya, 18–21.
 82. Roitenburg, D. I., Grishko, V. F., Nikitina, A. V. et. al. (1985). Lazernoe uprochnenie flantsa poluosi avtomobilia Kraz-255. Avtomobilnoe proizvodstvo, 8, 32–35.
 83. Zhuravel, V. M., Bukhanova, I. F., Maksimov, V. D., Nadirians, L. R. (1983). Lazernoe uprochnenie detalei. Proizvodstvenno tekhnicheskii biulleten, 10, 10–13.
 84. Sedunov, V. K., Kokin, S. D., Stises, G. I. (1984). Metody poverkhnostnogo uprochneniia golovok tsilindrov iz aluminievogo splava AL4. Avtomobilnoe proizvodstvo, 12, 13–14.
 85. Konig, W., Meis, F. I., Schmitz-Justen, C. (1986). Harten mit dem Laserstrahl. VDI – Zeitschrift, 128 (192), 27–31.
 86. Lasers in manufacturing (1983). Wilson Michaels "Production", 92 (2), 30–35.
 87. Kitani, M., Hiroyaki, K. (1985). Application of industrial robots in machine building. Oe Kakai Kogaku, 26 (8), 118–125.
 88. Koelsch, J. (1985). Industrial Lasers – Putting Light to Work. Product. Engineering, 32 (9), 50–54.
 89. Kawasumi, H. (1985). New Laser Machining Technology in Japan. Technocrat, 18 (6), 18–24.
 90. Tower, S., Ehiering, G. (1984). Laser Technology for Industry. 2nd Bien. Int. Mach. Tool Techn. Conf. Chicago, 111 (4), 12/57–12/69.
 91. Akulina, G. A., Mechetner, B. Kh., Shnyepkin, A. G. (1985). Lazernaia zakalka detalei stankov. Stanki i instrument, 6, 27–29.
 92. Brekhovskii, V. F. et. al. (1968). O poverkhnostnoi zakalki stalei izlucheniem OKG. Fizika i khimiia obrabotki materialov, 4, 35–43.
 93. Dubniakov, V. N. (1985). Povyshenie iznosostoikosti konstruksionnykh materialov pri fretting-korrozii. Trenie, iznos i smazochnye materialy. Tashkent, 123–126.
 94. Kovalenko, V. S. et. al. (1984). Lazernoe uprochnenie reztsov ugledobyvayushchikh mashin. Tekhnologiya i organizatsiya proizvodstva, 3, 34–39.
-

95. Kichigin, A. F., Terentev, O. M., Sergienko, N. I. (1986). Lazernoe uprochnenie detalei gidroprivoda gornyykh mashin. *Ugol*, 2, 22–25.
96. Velikikh, V. S., Goncharenko, V. P., Romanenko, A. V. et. al. (1983). Vliianie lazernoi zakalki na mekhanicheskie svoystva stali 45. *Fizika i khimiia obrabotki materialov*, 3, 32–34.
97. Velikikh, V. S., Kartantsev, V. S., Romanenko, A. V. (1984). Vliianie lazernoi zakalki na mekhanicheskie svoystva stali 45 s razlichnoi predvaritelnoi termicheskoi obrabotkoi. *Fizika i khimiia obrabotki materialov*, 2, 15–19.
98. Obnischenko, L. I., Mikhin, N. G., Degobuzov, D. A. et. al. (1983). Vliianie struktury poverkhnostnogo sloia, poluchennogo metodom lazernogo uprochneniia na iznosostoikost stali 40KH. *Metallovedenie i termicheskaiia obrabotka metallov*, 5, 21–28.
99. Edneral, N. V., Lokshiev, V. A., Skakov, Iu. A. (1981). Mikrostruktura stali U10 posle oblucheniia OKG i zakalki iz zhidkogo sostoiianiia. *Fizika i khimiia obrabotki materialov*, 4, 8–15.
100. Betaneli, A. I., Danilenko, L. P., Loladze, T. N. et. al. (1972). Issledovanie vozmozhnosti dopolnitelnogo legirovaniia poverkhnosti stali R18 s pomoschiu luchia lazera. *Fizika i khimiia obrabotki materialov*, 6, 27–32.
101. Pamfilov, E. N., Borzenkova, T. G. (1982). Povyshenie iznosostoikosti tverdykh splavov lazernym uprochneniem. *Vestnik mashinostroeniia*, 3, 61–63.
102. Kolganov, E. A., Beliaev, G. IA. (1985). Issledovaniia vozmozhnosti uprochneniia tverdykh splavov pri skorostnom nagreve. *Mashinostroenie*, 10, 73–86.
103. Kardapolova, M. A., Spiridonov, N. V., Stankevich, O. I. (1985). Vliianie rezhimov lazernoi obrabotki na mikrostrukturu samofliusiushchikhsia splavov. *Mashinostroenie*, 10, 36–41.
104. Nagano, Yu. (1985). Laser treatment of ceramic materials. *Kikai to kogu. Too ep*, 5, 29.
105. Spiridonov, N. V., Lutsko, I. I. (1985). Primenenie obrabotki lazerom dlia uvelicheniia iznosostoikosti keramicheskikh pokrytii. *Mashinostroenie*, 10, 47–50.
106. Obischenko, L. I., Dergozubov, A. A., Gantimirov, B. M. et. al. (1986). Lazernoe termouprochnenie osevoi opory turbobura. *Vestnik mashinostroeniia*, 1, 26–29.
107. Kremnev, L. S., Vladimirova, O. V., Sagadeeva, T. G. (1985). Uprochnenie rabochikh poverkhnostei plosko-paralelnykh kontsevykh mer dlin lazernym izlucheniem. *Fizika i khimiia obrabotki materialov*, 3, 14–18.
108. Diachenko, V. S. (1986). Vliianie rezhimov impulsnoi lazernoi obrabotki na strukturu i svoystva bystrozrezhuschikh stalei. *Metallovedenie i termicheskaiia obrabotka metallov*, 9, 3–7.
109. Diachenko, V. S. (1985). Osobennosti stroeniia i svoystva bystrozrezhuschikh stalei posle lazernoi obrabotki. *Metallovedenie i termicheskaiia obrabotka metallov*, 8, 7–11.
110. Gureev, D. M. (1984). Poverkhnostnaia zakalka stali KhVG impulsnym i nepreryvnyim lazernym izlucheniem. *Struktura i svoystva deformirovannykh materialov. Kuibyshev*, 127–132.
111. Vasilev, V. Iu., Edneral, N. V., Kuzmenko, T. T., Chekanova, N. T. (1982). Vliianie lazernoi obrabotki na korrozionnye svoystva chuguna SCH 24-44 i stali U10. *Zaschita metallov*, 3, 18–20.
112. Grechin, A. N. (1985). Issledovanie vliianiia izlucheniia nepreryvnogo i impulsnogo lazerov na strukturu i svoystva kovkikh chugunov. *Moscow*, 19.

-
113. Velikh, V. S., Gonchareko, V. P., Zverev, A. F. (1984). Vliianie koeffitsienta perekrytiia "piaten" zakalki na ostatochnye napriazheniia posle lazernoi obrabotki. *Metallovedenie i termicheskaja obrabotka metallov*, 9, 24–26.
 114. Mordike, B. L. (1983). Trends in the development of the application of CO₂-Lasers in materials technology. *Materialwissenschaft Und Werkstofftechnik*, 14 (7), 221–228. doi: <http://doi.org/10.1002/mawe.19830140704>
 115. Konig, W., Meis, F. U., Willerscheid, H., Schmitz-Justen, C. (1985). Problemstellungen beim Laserstreichharten von Bauteilen. *Laser/Optoelectron. Techn. Vortr.* 7. Int. Kongr. Laser Optoelectron. Munchen, Berlin, 427–436. doi: http://doi.org/10.1007/978-3-642-82638-2_83
 116. Demian, T., Dontu, O. (1984). Asupra durificarii superficiale locale cu laser pentru elemente constructive de mecanica fina. *Bul. inst. politehn. Gh.Gheorghin-Dej. Bucuresti. Ser.mec.*, 70–73.
 117. Biriukov, V. P. (1985). Uprochnenie poverkhnosti treniia skaniruiuschim lazernym luchom. *Iznos v mashinakh i metody zaschity to nego*. Briansk, Moscow, 93–94.
 118. Voinov, S. S., Schur, E. A., Kraposhin, V. S. (1986). Lazernaia obrabotka poverkhnosti metallov i splavov. *Fizika i khimiia obrabotki materialov*, 7, 7–11.
 119. Kaiukov, S. V., laresko, S. I. (2003). Lazernoe uprochnenie instrumentalnykh stalei profilirovannym impulsnym izlucheniem. *Fizika i khimiia obrabotki materialov*, 4, 13–18.
 120. Rykalin, N. N., Uglov, A. A., Zuev, I. V. (1984). Poluchenie plenok i pokrytii s ispolzovaniem kontsentririrovannykh istochnikov energii. *Fizika i khimiia obrabotki materialov*, 1, 32–35.
 121. Burakov, V. A., Kozakov, V. K., Malinina, E. R. (1997). Priroda i tekhnologicheskie perspektivy lazernogo uprochneniia tverdykh splavov. *Progressivnye metody termicheskoi obrabotki v traktornom i selskokhoziaistvennom mashinostroenii*. Rostov na Donu, 78–83.
 122. Burakov, V. A., Baryshevskaja, B. A. (1981). Lokalnaia tsementatsiia stali v usloviakh lazernogo nagreva i skorostnoi zakalki. *Khimiko-termicheskaja obrabotka metallov i splavov*. Minsk, 51–53.
 123. Bunep, J., Da, K., Haus-loachim (1982). Roloff Lasermaterialbearbeitung-technologien mit zukunft. *Schweisstechnik*, 4, 21–25.
 124. Sepold, G., Bekker, R. (1984). Lazernaia zakalka i legirovanie poverkhnosti. *Chernye metally i metallurgija*, 5, 13–19.
 125. Suslov, A. G., Kolesnikov, Iu. V., Iniotin, V. P. (1985). Issledovanie vozmozhnostei povyschenie dinamicheskoi poverkhnostnoi prochnosti stalei s pomoschiu lazernogo legirovaniia. *Trenie i iznos*, 5, 34–39.
 126. Burakov, V. A., Brovech, G. I. (1985). Povyschenie teplostoikosti bystrorezhuschikh stalei lazernym legirovaniem. *Metallovedenie i termicheskaja obrabotka metallov*, 11, 6–13.
 127. Zemskii, S. V., Andriakhin, V. M., Chekanova, N. T. (1983). Nanesenie zaschitnykh pokrytii s pomoschiu lucha lazera. *Diffuzionnoe nasyschenie i pokrytiia na metallakh*. Kyiv, 8–12.
 128. Grigorov, P. K., Stepanov, M. S. (1985). Rezultaty issledovaniia uprochneniia slozhnolegировannykh stalei karbonitrirovaniem s posleduiuschim lazernym nagrevom. *Nadezhnost i kontrol kachestva*, 10, 6–8.
-

-
129. Sepold, G., Becker, R. (1984). Oberflahenveredlung durch Laserharten und Einlegieren. Stahl und Eisen, 104 (5), 41–43.
 130. A. S. No. 910835 (SSSR). Sposob plazmennogo khromirovaniia stali pri toke cherez plazmu.
 131. A. S. No. 1026487 (SSSR). Sposob poverkhnostnogo uprochneniia OKG s diffuzionnym legirovaniem i povtoriauschiisia nagrevom poverkhnosti.
 132. Gorlenko, O. A., Chistov, V. F., Frolov, E. N. (1984). Ekonomii materialov i energii pri lazernom uprochnenie. Metallovedenie i termicheskaiia obrabotka metallov, 5, 29–32.
 133. Devoino, O. G., Iakovlev, G. M. (1985). Vliianie skorostnogo nagreva na khрупkost boridnykh pokrytii. Mashinostroenie, 10, 89–96.
 134. Lakhtin, Iu. M., Kogan, I. A. D. (1983). Poverkhnostnoe uprochnenie stali izlucheniem lazera. Poverkhnostnye metody uprochneniia metallov i splavov. Moscow, 65–67.
 135. Lakhtin, Iu. M., Kogan, I. A. D., Teplova, L. A. (1984). Uprochnenie poverkhnosti titanovykh splavov lazernym legirovaniem. Metallovedenie i termicheskaiia obrabotka metallov, 5, 24–28.
 136. Troitskii, V. N., Grebtsov, B. M. (1980). Fiziko-khimicheskie svoistva karbonitridov titana, sintezirovannykh v nizkotemperaturnoi plazme. FiTOM, 2, 21–23.
 137. Uglov, A. A., Galiev, A. L. (1981). O pogloscheniia azota rasplavom metalla v zone vozdeistviia lazernogo izlucheniia. Fizika i khimiia obrabotki materialov, 4, 27–31.
 138. Rykalin, N. N., Uglov, A. A., Kokora, A. N. (1975). Lazernaia obrabotka materialov. Moscow: Mashinostroenie, 296.
 139. Shoroshorov, M. Kh. (2001). Ultradispersnoe strukturnoe sostoiianie metallicheskh splavov. Moscow: Nauka, 155.
 140. Morokov, I. D., Trusov, L. I., Chizhik, S. P. (1977). Ultradispersnye metallicheskie sredy. Moscow: Atomizdat, 264.
 141. Diachenko, V. S., Tverdokhlebov, A. A., Korosteleva, A. A. (1984). Osobennosti lazernoi termicheskoi obrabotki instrumenty iz bystrorezhushchei stali. Metallovedenie i termicheskaiia obrabotka metallov, 9, 36–39.
 142. Mironov, V. M., Mazanko, V. F., Gertsriken, D. S., Filatov, A. V. (2001). Massoperenos i fazoobrazovanie v metallakh pri impulsnykh vozdeistviakh. Samara: Izd-vo "Samarskii universitet", 232.
 143. Isakov, V. V., Medres, B. S., Solovov, A. A. (1983). O teplostoikosti instrumentalnykh stalei, obrabotannykh lazernym izlucheniem. Metallovedenie i termicheskaiia obrabotka metallov, 4, 34–39.
 144. Burakov, V. V., Fedoseenko, S. S. (1983). Formirovanie struktur povyshennoi iznosostoikosti pri lazernoi zakalke metalloobrabatyvaiushchego instrumenta. Metallovedenie i termicheskaiia obrabotka metallov, 5, 4–9.
 145. Volkhin, S. A. (1990). Vliianie struktury instrumentalnykh stalei posle zakalki i otpuska na parametry lazerno-uprochnennykh sloev. Sudostroitelnaia promyshlennost, 23, 44–48.
 146. Dahotre B. (1989). Laser melting of surface and alloying of steel with chromium. Laser Mater. Process. 3: Proc. 3rd Symp. TMS Fall Meet, Chicago, Warrendale, 3–19.
-

-
147. Babushkin, V. B. (1990). Osobennosti strukturoobrazovaniia v bystrozrezhuschikh i vysokokhromistykh shtampovykh staliakh pri lazernom nagreve. *Izvestiia vysshikh uchebnykh zavedenii. Chernaia Metallurgii*, 4, 68–70.
 148. Sobusiak, T., Sokolov, K. N. (1991). Vliianie lazernoi termicheskoi obrabotki na strukturu i svoistva bystrozrezhuschei stali. *Problemy mashinostroeniia i avtomatizatsii*, 5, 45–53.
 149. Korotaev, A. D., Tiumentsev, A. N., Sukhovarov, V. F. (1989). *Dispersnoe uprochnenie tugoplavkikh metallov*. Novosibirsk: Nauka, 211.
 150. Poduraev, V. N., Divaev, A. V., Senchenko, A. E. (1990). Uprochnenie tverdosplavnogo rezhushchego instrumenta lazernym i radiatsionnym izlucheniem. *Stanki instrumenty*, 9, 18–20.
 151. Blinovskii, V. A., Brover, G. I., Tsyrbii, I. K. (1991). Sostoianie poverkhnostnykh sloev lazerno-legirovannogo tverdogo splava VK8. *Fizika i khimii obrabotki materialov*, 4, 111–115.
 152. Mokritskii, B. Ia., Kabaldin, Iu. G. (1991). Kombinirovannoe uprochnenie tverdosplavnogo instrumenta. *Fizika i khimii obrabotki materialov*, 5, 153–154.
 153. Gureev, D. M., Lamtin, A. P., Chulkin, V. N. (1990). Vliianie impulsnogo lazernogo izlucheniia na sostoianie kobaltovoi prosloiki tverdykh splavov. *Fizika i khimii obrabotki materialov*, 1, 51–54.
 154. *Kombinierte Wärmebehandlungsverfahren* (1987). *Technologier Wärmebehandlung*. Leipzig: Grundstoffindustrie, 190–205.
 155. Gertsriken, D. S., Mazanko, V. F., Tyshkevich, V. M., Falchenko, V. M. (2001). *Mas-sopereenos a metallakh pri nizkikh temperaturakh v usloviiax vneshnego vozdeistviia*. Kyiv: RIO IMF, 438.
 156. Sliadnikov, E. E. (2000). Kotsentratory napriazhenii – istochnik mikroplasticheskoi deformatsii v nagruzhennom kristalle. *Fizicheskaia mezomekhanika*, 3 (5), 53–57.
 157. Badaeva, V. F., Kaminskii, P. P., Khon, Iu. A. (2000). Avtovolnovye protsessy i lineinaia stadiia plasticheskoi deformatsii poverkhnostno uprochnennoi khromistoi stali. *Fizicheskaia mezomekhanika*, 3 (5), 47–53.
 158. Krasulin, Iu. L. (1981). Ob "anomalnoi" diffuzii v materialakh pri impulsnom nagruzhении. *Fizika i khimii obrabotki materialov*, 4, 34–37.
 159. Schneider, J. M., Hjärvarsson, B., Wang, X., Hultman, L. (1999). On the effect of hydrogen incorporation in strontium titanate layers grown by high vacuum magnetron sputtering. *Applied Physics Letters*, 75 (22), 3476–3478. doi: <http://doi.org/10.1063/1.125301>
 160. Levinskii, Iu. V., Petrov, A. P., Namango Saul, S. (2000). O raspredelenii legiruiuschiikh metallov pri poverkhnostnom azotirovanii titanovykh splavov. *Metally*, 4, 92–96.
 161. Bekrenev, A. I., Kirilenko, Iu. N. (1984). Azotirovanie titanovogo splava VT9 posle obrabotki udarnymi volnami. *Fizika i khimii obrabotki materialov*, 1, 27–29.
 162. Gaiduk, V. V., Volodin, T. V., Zuev, L. B., Volodin, V. L. (2003). Issledovanie vliianiia impulsnykh vozdeistvii na prochnost metallicheskiikh materialov. *Stal*, 12, 71–72.
 163. Borovskii, I. B., Gorodskii, D. D., Sharafiev, I. M., Moriashev, S. F. (1984). O poverkhnostnom legirovanii metallov s pomoschiu nepreryvnogo lazernogo izlucheniia. *Fizika i khimii obrabotki materialov*, 1, 37–41.
-

164. Averin, V. I., Avrov, A. I., Erofeev, M. V., Kalin, A. A. (1984). Rezhimy vozbuzhdeniia i parametry voln napriazhenii v metalle pri vozeistvii lazernykh mono impulsov. *Fizika i khimiia obrabotki materialov*, 2, 25–28.
165. Lysenko, A. B., Kozina, N. N., Mirkin, L. I. (1988). Struktura i svoystva evtekticheskikh splavov v zone lazernogo plavleniia. *Metallovedenie i termicheskaiia obrabotka metallov*, 10, 30–34.
166. Matthews, A., Leyland, A. (1995). Hybrid techniques in surface engineering. *Surface and Coatings Technology*, 71 (2), 88–92. doi: [http://doi.org/10.1016/0257-8972\(94\)01004-3](http://doi.org/10.1016/0257-8972(94)01004-3)
167. Patentschrift DE 42 05 647 C 2 (1996). Verfahren zur ther-mochemisch-thermischen Behandlung von Einsatzstählen, 1. 8.
168. Bell, T., Sun, Y., Cote, S. J. (1992). Duplex surface engineering. *Proc. Heat & Surface '92, Japan Techn. Inform. Cent. Tokyo*, 1–6.
169. Sun, Y., Bell, T. (1992). Combined Plasma Nitriding and PVD Treatments. *Transactions of the IMF*, 70 (1), 38–44. doi: <http://doi.org/10.1080/00202967.1992.11870939>
170. Zlatanović, M. (1991). Deposition of (Ti,Al)N coatings on plasma nitrided steel. *Surface and Coatings Technology*, 48 (1), 19–24. doi: [http://doi.org/10.1016/0257-8972\(91\)90124-f](http://doi.org/10.1016/0257-8972(91)90124-f)
171. Soki, M. H., Bell, T.; Sudarsham, T. S.(Ed.) (1991). Eleccron beam and PVD duplex treatment of Al-Si based alloys. *Surface Mod. Technol IV. The Minerals, Mecats & Materials Soc.*, 795–809.
172. Borger, M.; Henserer, F. (Ed.) (1992). PVD-Schichten fur Zahnrad und Walzlager. *Randschichtermudung irn Walzkontakt. Berichtsband. AWT Suhl 1992*, 163–171.
173. Leyland, A., Bin-Sudin, M., James, A. S., Kalantary, M. R., Wells, P. B., Matthews, A. et. al. (1993). TiN and CrN PVD coatings on electroless nickel-coated steel substrates. *Surface and Coatings Technology*, 60 (1-3), 474–479. doi: [http://doi.org/10.1016/0257-8972\(93\)90135-b](http://doi.org/10.1016/0257-8972(93)90135-b)
174. Kobayashi, M., Katsutoshi, J. (1990). Effect of shot peening on the pitting fatigue strength of carburized gears. *Proc. 4th Int. Conf. Shot Peening 1990. Tokyo*, 1345–1349.
175. Zenker, R., Frenkler, N., John, W., Günther, U. (1992). Flüssigphasen-Randschichtbehandlung mit dem Elektronenstrahl. *HTM Journal of Heat Treatment and Materials*, 47 (3), 153–159. doi: <http://doi.org/10.1515/htm-1992-470306>
176. Dingremont, N., Bergmann, E., Collignon, P. (1994). Anwendung von Duplexschichten fur Druckg formen. *Proc. 9. Int. Congr. Heat Treatment and Surface Eng. Nizza*, 131–137.
177. Prokhorov, A. M. (1982). *Fizicheskie printsipy obrabotki materialov impulsnoi lazernoi plazmoi. Nauchnye osnovy progressivnoi tekhnologii*. Moscow: Mashinostroenie, 123–130.
178. Belianin, V. A., Zhukov, A. A., Kokura, A. N. et. al. (1967). Struktura i tverdost poverkhnostnykh sloev stali posle obrabotki luchom lazera. *Fizika i khimiia obrabotki materialov*, 2, 115–116.
179. Andriiaxhin, V. M., Fishkis, M. M. (1980). *Lazery i perspektivy ikh primeneniia v avtomobilestroenii*. Moscow: NIIAvtoprom, 47.
180. Drapkin, B. M., Rudenko, V. A. (1882). Ob opredelenie energii sublimatsii metallov. *Zhurnal tekhnicheskoi fiziki*, 62 (6), 125–138.
181. Uglov, A. A., Kokora, A. N. (1977). Teplofizicheskie i gidrodinamicheskie iavleniia pri obrabotke materialov luchom lazera. *Kvantovaiia elektronika*, 4 (6), 7–12.

-
182. Golub, A. P., Loseva, T. V., Nemchinov, I. V. (1981). Teoreticheskie otsenki vzaimodeistviia impulsov izlucheniia lazera s pregradoi, okruzhennoi gazom vysokogo davleniia v usloviakh ploskoi geometrii. *Fizika i khimiia obrabotki materialov*, 1, 51–52.
 183. Mirkin, L. I. (1975). *Fizicheskie osnovy obrabotki materialov luchami lazera*. Moscow: Izdatel'stvo Moskovskogo universiteta, 384.
 184. Rykalkin, N. N., Zuev, I. V., Uglov, A. A. (1976). *Osnovy elektronoluchevoi obrabotki materialov*. Moscow: Mashinostroenie, 231.
 185. Vaisburg, D. I., Semin, B. N., Gavanov, E. G. (1982). Vysokoenergeticheskaiia elektronika tverdogo tela. Novosibirsk: Izd. "Nauka", Sibirskoe otdelenie, 173.
 186. Lifshits, K. M., Pitaevskii, L. P. (1979). *Fizicheskaiia kinetika*. Moscow: Nauka, 528.
 187. Martens, V. Ia. (1996). Sloi mezhdu plazmoi i otritsatel'nykh elektrodom pri nalichii potokov zariazhennykh chastits. *Zhurnal tekhnicheskoi fiziki*, 66 (5), 70–79.
 188. Brekhovskii, V. D., Zhukov, A. A., Kokora, A. N., Uglov, A. A. (1968). O poverkhnostnoi lokalnoi zakalke stalei izlucheniem OKG. *Fizika i khimiia obrabotki materialov*, 4, 47–48.
 189. Iudaev, B. N. (1981). *Teploperedacha*. Moscow: Vysshiaia shkola, 234.
 190. Uglum, J. R., Bacon, J. L., Davis, D. G., Polizzi, R. J., Sledge, R. L., Zowarka, R. C. (1997). Scaling Analysis of the Electromagnetic Powder Deposition (EPD) Gun. *Thermal Spray 1997: Proceedings from the United Thermal Spray Conference*, 373–391. doi: <http://doi.org/10.31399/asm.cp.itsc1997p0385>
 191. Lebedev, A. D., Uriukov, B. A. (1990). *Impulsnye uskoriteli plazmy vysokogo davleniia*. Novosibirsk, 280.
 192. Levin, V. A. (1975). Rasprostranenie udarnykh i detonatsionnykh voln v goriuchikh gazakh. Moscow, 320.
 193. Katushev, A. G., Tatosov, A. V. (1998). Matematicheskoe modelirovanie vybrosa gazovzvesi iz kanala udarnoi trubyy pod deistviem szhatogo gaza. *Fizika goreniia i vzryva*, 34 (3), 107–116.
 194. Chernyi, G. G. (1988). *Gazovaia dinamika*. Moscow: Nauka, 415.
 195. Demutskii, V. P., Polovin, R. V. (1961). Ob udarnoi ionizatsii i detonatsii i magnitnoi gidrodinamike. *Zhurnal tekhnicheskoi fiziki*, 31 (2), 17–21.
 196. Larit, E., Shekhtman, I. (1959). Rasprostranenie detonatsionnoi volny v prisutstvii magnitnogo polia. *Zhurnal tekhnicheskoi fiziki*, 8 (1), 87–90.
 197. Liubimov, G. A. (1960). Vliianie elektromagnitnogo polia na detonatsionnyi rezhim. *DAN SSSR*, 4 (1), 52–61.
 198. Helliwell, J. B. (1962). Gas-ionizing shock and combustion waves in magnetogasdynamics. *Journal of Fluid Mechanics*, 14 (3), 405–419. doi: <http://doi.org/10.1017/s0022112062001329>
 199. Helliwell, I. B. (1963). Magreto gas dynamic defloration and detonation waves with ionization. *I. Fluid Mech*, 16, 243.
 200. Kelly, J. R., Toong, T. Y. (1967). Detonation wave in electromagnetic field. *Symposium (International) on Combustion*, 11 (1), 657–664. doi: [http://doi.org/10.1016/s0082-0784\(67\)80190-5](http://doi.org/10.1016/s0082-0784(67)80190-5)
-

201. Salamandra, G. D., Venttsel, N. M., Fedoseeva, I. K. (1976). Vlianie poperechnogo elektricheskogo polia na raspredelenie skorosti gaza vblizi fronta plameni. *Fizika gorenii i vzryva*, 2, 229–233.
202. Burenin, Iu. A., Shvetsov, G. A. (1977). Issledovanie koaksialnogo MGD – generatora vzryvnogo tipa. *Fizika gorenii i vzryva*, 13 (1), 130–132.
203. Plett, E. G., Toong, T. Y. (1969). Electromagnetic effect on flow behind gaseous detonations. *AIAA Journal*, 7 (6), 1127–1133. doi: <http://doi.org/10.2514/3.5285>
204. Soloukhin, R. I., Iakobi, Iu. A., Iakovlev, V. I. (1977). Issledovanie ravnovesnoi zony za frontom ioniziruiushei UV. *Fizika gorenii i vzryva*, 13 (3), 481–483.
205. Kulikovskii, A. G., Liubimov, G. A. (1962). *Magnitnaia gidrodinamika*. Moscow: Izd. fiz. mat. lit., 248.
206. Fay, J. A. (1959). Two-Dimensional Gaseous Detonations: Velocity Deficit. *Physics of Fluids*, 2 (3), 283. doi: <http://doi.org/10.1063/1.1705924>
207. Vatazhin, A. B., Liubimov, G. A., Regirer, S. A. (1970). *Magnitogidrodinamicheskie techeniia v kanalakh*. Moscow: Nauka, 672.
208. Uizem, Dzh. (1977). *Lineinye i nelineinye volny*. Moscow: Mir, 604.
209. Shi-i, B. (1960). *Teoriia strui*. Moscow: Gosud. izd-vo fiziko-matemat. literatury, 328.
210. Andelfinger, K. (1971). *Metody issledovaniia bystroprotekaushchikh protsessov v fizike plazmy. Fizika bystroprotekaushchikh protsessov v fizike plazmy*. Moscow: Mir, 360.
211. Lokht-Kholgreven, V. (Ed.) (1971). *Metody issledovaniia plazmy*. Moscow: Mir, 552.
212. Kasabov, G. A., Eliseev, V. V. (1973). *Spektroskopicheskie tablitsy dlia nizkoteraturnoi plazmy*. Moscow: Atomizdat, 160.
213. Grim, G. (1978). *Ushirenii spektralnykh linii v plazme*. Moscow: Mir, 491.
214. Minko, I. Ia. (1979). *Poluchenie i issledovanie impulsnykh plazmennyykh potokov*. Minsk: NiT, 181.
215. Sultanov, M. A. (1981). *Udarnoszhataia plazma v moschnykh impulsnykh razriadakh*. Dushanbe: Donish, 281.
216. Voloshin, M. N., Gasin, D. A., Korableva, I. R., Skliarenko, N. N. (1994). Osobennosti uprochneniia stali U8 s pomoschiu impulsno-plazmennoi obrabotki. *Fizika i khimiia obrabotki materialov*, 1, 16–20.
217. Gurev, V. A., Tesker, V. I. (1996). Primenenie lazernoi obrabotki dlia formirovaniia poverkhnostnogo sloia normalizovannoi stali s vysokimi tribotekhnicheskimi i viazkimi svoistvami. *Fizika i khimiia obrabotki materialov*, 1, 14–19.
218. Leschinskii, L. K., Smotugin, S. S., Pirch, I. I. (1990). *Plazmennoe poverkhnostnoe uprochnenie*. Kyiv: Tekhnika, 109.
219. Dong, C., Wu, A. M., Hao, S. Z., Zhang, A. M., Xu, T., Xu, J. et. al. (2003). High-current pulsed electron beam: rapid surface alloying and wear resistance improyement. *Acta Metallurgica Sinica*, 16 (14), 276–282.
220. Lebedev, V. K., Kaleko, D. M. (1998). Impulsnaia dugovaia termicheskaiia obrabotka poverkhnosti metallov. *Metallovedenie i termicheskaiia obrabotka metallov*, 6, 8–12.

-
221. McCay, M. N., Dahofre, N. B., Hopkins, J. A., McCay, T. D. (1999). The influence of metals and carbides during laser surface modification of low alloy steel. *Journal of Materials Science*, 34 (23), 5789–5802. doi: <http://doi.org/10.1023/a:1004762319012>
222. Suminov, I. V., Klopikov, E. B., Semenikhin, N. A., Pentiuk, S. A., Zasetskii, Iu. A. (1991). Issledovanie strukturno-fazovykh prevraschenii v uglerodistykh staliakh pri sovместnom vozdeistvii lazernogo izlucheniia i magnitnogo polia. *Fizika i khimiiia obrabotki materialov*, 3, 44–47.
223. Bolesta, A. V., Golovnev, I. F., Fomin, V. M. (2000). Issledovanie protsessa soudareniiia sfericheskogo klastera medi s zhestkoi stenкой metodom molekuliarnoi dinamiki. *Fizicheskaiia mezhomekhanika*, 3, 39–46.
224. Gertsriken, D. S., Skripnichenko, A. L., Tishkevich, V. M., Falchenko, V. M., CHachin, V. N. (1987). Vliianie impulsnogo magnitnogo polia i rastiagivaiuschikh napriazhenii na podvizhnost atomov nikelia i medi. *Vestsi AN BSSR*, 4, 45–49.
225. Gertsriken, D. S., Kostiuhenko, V. G., Tishkevich, V. M., Falchenko, V. M. (1997). Vliianie plasticheskoi deformatsii v impulsnom magnitnom pole na migratsiiu atomov v metallakh. *Dok. NAN Ukrainy*, 3, 78–81.
226. Gertsriken, D. S., Mazanko, V. F., Falchenko, V. M. (1991). Impulsnaia obrabotka i massopereenos v metallakh pri nizkikh temperaturakh. *Kyiv: Naukova Dumka*, 208.
227. Tyurin, Yu. N. (1999). Sovershenstvovanie oborudovaniia i tekhnologii detonatsionnogo naneseniia pokrytii. *Avtomaticheskaia svarka*, 5, 13–18.
228. Iuschenko, K. A., Borisov, Iu. S., Tyurin, Yu. N. (1994). Teoriia i praktika impulsno-plazmennogo modifitsirovaniia poverkhnosti detalei mashin i instrumenta. *Svarochnoe proizvodstvo*, 5, 23–25.
229. Borisov, Iu. S., Tyurin, Yu. N. (1992). Uprochniaiuschaia obrabotka detalei vysokoenergeticheskoi plazmoi. *Kyiv*, 37.
230. Kidin, I. N. (1969). *Fizicheskie osnovy elektrotermicheskoi obrabotki metallov i splavov*. Moscow: Metallurgiiia, 376.
231. Gridnev, V. N., Meshkov, Iu. A., Oshkaderov, S. P., Trefilov, V. I. (1973). *Fizicheskie osnovy elektrotermicheskogo uprochneniia stali*. Kyiv: Naukova dumka, 335.
232. Efimov, N. A., Korzhova, N. P., Lotsko, D. V., Tyurin, Yu. N. (1994). *Zaschitnye pokrytiiia na metallakh*. Kyiv: Naukova dumka, 1994, 28, 14–18.
233. Mordovets, N. M., Borisov, Iu. S., Rachev, A. P., Tyurin, Yu. N. (1994). Struktura, kristallograficheskaiia tekstura i mikrotverdost v pripoverkhnostnom sloe uglerodistoi stali, modifitsirovannoi impulsno-plazmennym metodom. *Kyiv: Naukova dumka*, 28, 50–57.
234. Borisov, Iu. S., Kolisnichenko, O. V. (2003). Vliianie uslovii nagreva poverkhnosti izdeliia na strukturu uprochnennykh sloev stali U8 pri plazmenno-detonatsionnoi obrabotke. *Avtomaticheskaia svarka*, 3, 31–35.
235. Pogrebnik, A. D., Tyurin, Yu. N. (2003). Impulsno-plazmennaiia modifikatsiia svoistv poverkhnosti i nanesenie pokrytii. *Uspekhi fiziki metallov*, 4 (1), 1–66.
236. Kovalenko, V. S. (Ed.) (1985). *Spravochnik po tekhnologii lazernoi obrabotki*. Kyiv: Tekhnika, 167.
-

-
237. Kikin, P. Iu., Pchelintsev, A. I., Rusin, E. E. (2003). Povyshenie teplostoikosti i iznosostoikosti bystrorezhushchikh stalei lazernym udarno-volnovym vozdeistviem. *Fizika i khimiia obrabotki materialov*, 5, 15–17.
238. Kovalenko, V. S., Golovko, L. F., Chernenko, V. S. (1990). Uprochnenie i legirovanie detalei mashin luchom lazera. Kyiv: Tekhnika, 192.
239. Samotugin, S. S., Muratov, V. A., Kovalchuk, A. V. et. al. (1995). Plazmennoe uprochnenie rabochnykh organov selskokhoziaistvennykh mashin. *Vestnik PGU*, 1, 173–175.
240. Samotugin, S. S. (1996). Plazmennaiia obrabotka instrumentalnykh materialov. *Avtomaticheskaia svarka*, 8, 48–51.
241. Leschinskii, L. K., Samotugin, S. S., Goritskii, V. M. et. al. (1996). Struktura i treschinostnoi-kost naplavlennogo metalla 18KH6GMFS posle plazmennogo uprochneniia. *Avtomaticheskaia svarka*, 8, 31–35.
242. Leshchinsky, L. K., Samotugin, S. S. (2001). Mechanical properties of plasma-hardened 5 % – chromium tool steel deposited by arc welding. *Welding Journal*, 1, 25–30.
243. Samotugin, S. S., Lavrik, V. P., Leschinskii, L. K., Solianik, N. Kh. (2001). Plazmennaiia obrabotka ekonomnolegirovannogo teplostoikogo naplavlennogo metalla. *Problemy spetsialnoi elektrometallurgii*, 2, 26–31.
244. Molian, P. A. (1987). Fatigue Characteristics of Laser Surface-Hardened Cast Irons. *Journal of Engineering Materials and Technology*, 109(3), 179–187. doi: <http://doi.org/10.1115/1.3225961>
245. Rie, K.-T. (1999). Recent advances in plasma diffusion processes. *Surface and Coatings Technology*, 112 (1-3), 56–62. doi: [http://doi.org/10.1016/s0257-8972\(98\)00747-6](http://doi.org/10.1016/s0257-8972(98)00747-6)
246. Grigoriants, A. G., Safonov, A. N., Ivashov, G. P. et. al. (1987). Issledovanie impulsnoi lazernoi zakalki shtampovoi osnastki. *Kuznechno-shtampovochnoe proizvodstvo*, 12, 22–23.
247. Vinokurov, A. V. (2001). Osobennosti protsessa plazmenno-dugovogo oplavlennia gazotermicheskikh pokrytii. Voronezh: Voronezh. gos. lesotekhn. akad, 37–42.
248. Ivanov, Iu. F., Lychagin, D. V., Gromov, V. E., Tsellermaer, V. V., Sosnin, O. V. et. al. (2000). Mezoskopicheskaia substruktura i elektroimpulsnoe podavlenie ustalostnogo razrusheniia. *Fizicheskaiia mezomekhanika*, 3 (1), 103–108.
249. Sorokin, V. M., Shetulov, D. I. (1983). Fiziko-mekhanicheskie svoistva pokrytii i stalei osnovy posle udarno-impulsnogo vozdeistviia. *Fizika i khimiia obrabotki materialov*, 3, 43–46.
250. Ilinskii, V. A., Zhukov, A. A., Kostylev, L. V., Loktiushin, V. A. (1998). Sverkhbystroe perezraspredelenie ugleroda v tsementovannykh sloiakh stalnykh izdelii. *Metally*, 3, 46–50.
251. Pogrebniak, A. D., Tyurin, Yu. N., Vasiliuk, V. V. et. al. (2004). Dupleksnaia obrabotka nikel-evogo splava, nanesennogo na podlozhku iz stali 3. *Trenie i iznos*, 25 (1), 71–77.
252. Vasilev, M. A., Kozlov, A. V., Prokopenko, G. I., Mordiyuk, B. N. (1995). Massoperenos pri UZ udarnoi obrabotke pary Cu-Al. *Metallfizika i noveishie tekhnologii*, 11, 34.
253. Bekrenev, A. N., Vasilev, M. A. (1996). Diffuziia v kristallicheskikh tonkikh plenkach pod deistviem millisekundnykh lazernykh impulsov. *Fizika i khimiia obrabotki materialov*, 6, 14–19.
-

-
254. Varavka, V. N., Dombrovskii, Iu. M., SHabarinov, A. V. (2003). O strukturnykh effektakh v zone obrabotki materialov kontsentrirovannymi potokami energii. Vestn. Don. gos. tekhn. un-ta, 3 (4), 445–452.
255. Maning, D. R. (1971). Kinetika diffuzii atomov v kristallakh. Moscow: Mir, 278.
256. Volosevich, V. P., Pogorelov, A. E. (1986). Osobennosti strukturnykh izmenenii v armko zheleze posle vozdeistviia dokriticheskikh potokov impulsnogo izlucheniia OKG. Poverkhnost, 9, 47–58.
257. Mazanko, V. F., Pogorelov, A. E. (1984). Migratsiia atomov tseziia v zheleze pri impulsnom vozdeistvii izlucheniia OKG. Metallofizika, 4, 46–52.
258. Prokopenko, G. I., Liutun, T. A. (1977). Issledovanie rezhimov poverkhnostnogo uprochneniia s pomoschiu ultrazvuka. Fizika i khimiia obrabotki materialov, 3, 27–29.
259. Konstantinov, E. G., Tarachenko, E. A., Mikhailov, Iu. V. (2003). Issledovanie vliianiia termotsiklicheskoi obrabotki na strukturu i svoistva kremnistoi stali 60S2. Sovremennye tekhnologii i materialovedenie. Magnitogorsk: Izd-vo MGTU, 119–125.
260. Bekrenev, A. N., Filina, E. A. (1991). Vliianie lazernogo legirovaniia na izmenenie fiziko-mekhanicheskikh svoistv poverkhnostnykh sloev titana. Fizika i khimiia obrabotki materialov, 4, 32–26.
261. Voss, A., Funken, J., Alunovic, M., Sung, H., Kreutz, E. W. (1992). Removal and transfer of material in laser-assisted physical vapour deposition of ceramics. Thin Solid Films, 220 (1-2), 116–121. doi: [http://doi.org/10.1016/0040-6090\(92\)90558-s](http://doi.org/10.1016/0040-6090(92)90558-s)
262. Modelling of Laser Hard-Facing of Steels with Carbide Powder Injection (1990). BRITE/EURAM Programme. Luxemb: OPEC, 337.
263. Kharaev, Iu. P. (2002). Predvaritelnaia termotsiklicheskaia obrabotka litogo instrumenta. Problemy i perspektivy razvitiia liteinogo, svarochnogo i kuznechno-shtampovochnogo proizvodstv. Barnaul: Izd-vo AltGTU, 254–255.
264. Yuschenko, K. A., Borisov, Y. S., Tyurin, Yu. N. (1992). Coating and Surface Modifying International with the Help of Advances in Plasma-Detonation Coating Treatment Deposition Thermal Spray. Technology. Orlando, 78–81.
265. Verkhoturov, A. D., Podchernyayeva, I. A., Linkina, L. D. (1990). Formation of hardening coatings made of powder components based on mineral raw material under affect of concentrated energy flows/CEE. 7th Int. Congr. Heat Treat. Mater. Moscow, 368–375.
266. Petrov, S. V., Karp, I. N. (1993). Plazmennoe gazovozdushnoe napylenie. Kiev, Naukova dumka, 490.
267. Raizer, Iu. P. (1992). Fizika gazovogo razriada. Moscow: Nauka. Gl. red. fiz.-mat. lit., 536.
268. Tyurin, Yu. N. (1997). Osnovy tekhnologii poverkhnostnogo uprochneniia izdelii plazmoi elektricheskogo razriada. Kyiv, 485.
269. Povkh, I. L. (1969). Tekhnicheskaiia gidromekhanika. Leningrad: Mashinostroenie, 524.
270. Loitsianskii, L. G. (1978). Mekhanika zhidkosti i gazov. Moscow: Nauka. Gl. red. Fiz.-mat. lit-ry., 736.
-

-
271. Krivtsun, I. V. (2001). Model isparenii metalla pri dugovoi, lazernoi i lazerno-dugovoi svarke. *Avtomaticheskaia svarka*, 3, 3–10.
272. Gordeev, V. F., Pustogarov, A. V. (1988). *Termoemissionnye dugovye katody*. Moscow: Energoatomizdat, 192.
273. Ekker, G. (1982). *Voprosy teorii vakkumnoi dugi. Vakuumnnye dugi*. Moscow: Mir, 267–384.
274. Babichev, A. P., Babushkina, N. A., Bratkovskii, A. M. et. al.; Grigoreva, I. S., Meilikhova, E. Z. (Eds.) (1991). *Fizicheskie velichiny*. Moscow: Energoatomizdat, 1232.
275. Anderson, D., Tannehill, Dzh., Pletcher, R. (1990). *Vychislitelnaia gidromekhanika i teploobmen*. Vol. 1. Moscow: Mir, 384.
276. Samarskii, A. A. (1987). *Vvedenie v chislennye metody*. Moscow: Nauka. Gl. red. fiz.-mat., lit., 288.
277. Samarskii, A. A., Gulin, A. V. (1989). *Chislennye metody*. Moscow: Nauka. Gl. red. fiz.-mat., lit., 432.
278. Pogrebnyak, A. D., Tyurin, Y. N., Kobzev, A. P. (2001). High-speed plasma jet modification and doping of α -Fe. *Technical Physics Letters*, 27 (8), 619–621. doi: <http://doi.org/10.1134/1.1398947>
279. Pogrebnyak, A. D., Kul'ment'eva, O. P., Kobzev, A. P., Tyurin, Y. N., Golovenko, S. I., Boiko, A. G. (2003). Mass transfer and doping during electrolyte-plasma treatment of cast iron. *Technical Physics Letters*, 29 (4), 312–315. doi: <http://doi.org/10.1134/1.1573301>
280. Lumei, W., Liyan, D. (1998). Laser alloying on chromium-coated surface of nodular cast iron. *Trans. Nonferrous Metals Soc*, 8 (3), 496–499.
281. Grigoriants, A. G. (1989). *Osnovy lazernoi obrabotki materialov*. Moscow: Mashinostroyeniye, 300.
282. De Rességuier, T., Hallouin, M. (1998). Stress relaxation and precursor decay in laser shock-loaded iron. *Journal of Applied Physics*, 84 (4), 1932–1938. doi: <http://doi.org/10.1063/1.368322>
283. Tsukamoto, F., Uchiyama, F., Fons, P., Yanagisawa, T., Kaga, Y., Okuo, T. (1995). A micro laser spray technique for depositing extremely fine patterns. *Proceedings of ITSC'95. Kobe*, 345–349.
284. Draper, C. W., Poate, J. M. (1983). Surface modification and alloy by laser, lin and electron beams. *Proc. NATO adv. Study inst. New York, London*, 385–404.
285. A. S. No. 1557193. *Sposob lazernogo legirovaniia poverkhnosti*.
286. Berdnikov, A. A., Demin, V. S., Serebriakova, E. D. et. al. (1995). Uprochnenie chugunnykh valkov metodom plazmennoi zakalki. *Stal*, 1, 56–59.
287. Kraposhin, V. S., Kurochkin, Iu. V., Mukhanov, G. V. (1989). Skorostnoe rasplavlenie poverkhnosti vysokoprochnogo chuguna plazmenno-dugovym razriadom. *Fizika i khimiia obrabotki materialov*, 3, 65–70.
288. Stavrev, D. S., Nikov, N. Ia. (1985). Uprochnenie serykh chugunov pri poverkhnostnom oteble nizkoterperaturnoi plazmoi. *Metallovedenie i termicheskaiia obrabotka metallov*, 4, 15–18.
-

-
289. Ishida, T. (1983). Local melting of nodular cast iron by plasma arc. *Journal of Materials Science*, 18 (6), 1773–1784. doi: <http://doi.org/10.1007/bf00542074>
290. Shepelev, N. S., Selivanov, M. V., Chepyzhev, I. S. et. al. (1988). Uprochnenie rabochikh poverkhnostei chugunnykh detalei avtomobiley metodom plazmennogo oplavleniia. *Metallovedenie i termicheskaiia obrabotka metallov*, 12, 34–36.
291. Zhukov, A. A., Shilina, E. N., Bron, D. I. et. al. (1985). Plazmennoe oplavlenie poverkhnostnogo sloia chuguna posle elektroiskrovogo legirovaniia. *Elektronnaia obrabotka metallov*, 3, 25–33.
292. Samotugin, S. S., Kovalchuk, A. V., Solianik, N. Kh., Puiko, A. V. (1996). Struktura i viazkost razrusheniia vysokoprochnogo perlitno-tsementitnogo chuguna posle plazmennoi obrabotki. *Metallovedenie i termicheskaiia obrabotka metallov*, 4, 2–6.
293. Molian, P. A. (1987). Fatigue Characteristics of Laser Surface-Hardened Cast Irons. *Journal of Engineering Materials and Technology*, 109 (3), 179–187. doi: <http://doi.org/10.1115/1.3225961>
294. Gureev, D. M. (1998). Strukturoobrazovanie pri lazerno-ultrazvukovom rasplavlenii poverkhnosti bystrorezhuschikh stalei. *Fizika i khimiia obrabotki materialov*, 2, 41–44.
295. Girzhon, V. V., Anpilogov, D. I. (1997). Vliianie impulsnoi lazernoii obrabotki na strukturu legirovannogo chuguna. *Metallovedenie i termicheskaiia obrabotka metallov*, 4, 11–13.
296. Bloshchanevich, A. M., Kovalchenko, M. S., Paustovskii, A. V., Pasichnyi, V. V. (1989). Sravnitelnyi analiz vozeistviia kontsentrirovannoi solnechnoi energii i lazernogo izlucheniia na svoistva tverdykh splavov. *Poroshkovaia metallurgiiia*, 9, 71–82.
297. Brover, G. I., Pustovoit, V. N., Brover, A. V., Komissarov, A. V. (2002). Lazernoe uprochnenie titanovykh splavov. *Nauka – tekhnika – tekhnologii. Nakhodka: Izd-vo In-ta tekhnol. i biznesa*, 9–10
298. Stratton, P. F. (2003). Surface hardening of titanium. *Heat Treatment of Metals*, 30 (1), 8–12.
299. Pogrebniak, A. D., Sokolov, S. V., Bazyl, E. A., Tyurin, Yu. N., Kshniakin, V. S. (2001). Modifikatsiia poverkhnostnogo sloia titanovykh splavov impulsno-plazmennoi obrabotkoi. *Fizika i khimiia obrabotki materialov*, 4, 49–55.
300. Tyurin, Yu. N., Adeeva, L. I. (1999). Impulsno-plazmennoe uprochnenie splavov na osnove titana. *Avtomaticheskaiia svarka*, 3, 43–47.
301. Valiaev, A. N., Pogrebniak, A. D., Plotnikov, S. V. (1998). Radiatsionno-mekhanicheskie efekty v tverdykh telakh pri obluchenii vysokoenergeticheskimi impulsnymi elektronnyimi i ionnymi puchkami. *Almaty: Gylym*, 245.
302. Uglov, A. A., Smurov, I. Iu., Gorbach, A. F. (1989). Teplovyie protsessy pri lazerno-plazmennom sinteze karbidov tugoplavkikh metallov. *Poverkhnost. Fizika, khimiia, mekhanika*, 9, 36–42.
303. Eshbi, I. F. (1972). O napriazhenii Orovanna. *Fizika prochnosti i plastichnosti*. Moscow: Metallurgiiia, 88–107.
-

-
304. Petch, N. J. (1953). The cleavage strength of polycrystalline. The Journal of the Iron and Steel Institute, 173 (1), 25–28.
305. Orowan, E. (1954). Dislocation in Metals. New York: AIME, 103.
305. Ashby, M. F. (1983). Mechanisms of deformation and fracture. Advances in Applied Mechanics, 117–177.
307. Romaniv, O. N. (1979). Viazkost razrusheniia konstruktsionnykh stalei. Moscow: Metallurgiiia, 176.
308. Konstantinova, T. E., Primisler, V. B., Dobrikov, A. A., Volkova, G. K., Liafer, E. I. (1991). Mekhanizmy plasticheskoi deformatsii vysokoprochnoi martensitno-stareiuschei stali. Metallofizika, 13 (5), 62–68.
309. Tyurin, Yu. N., Kolisnichenko, O. V., Tsigankov, N. G. (2001). Impulsno-plazmennoe uprochnenie instrumenta. Avtomaticheskaiia svarka, 1, 38–44.
310. Pogrebniak, A. D., Tyurin, Yu. N., Kulmenteva, O. P., Kshniakin, V. S., Kolisnichenko, O. V. (2002). Uprochnenie i massoperenos pri impulsnoi plazmenno-detonatsionnoi obrabotke stalei. Fizika i khimiia obrabotki materialov, 2, 40–48.
311. Tyurin, Yu. N., Zhadkevich, M. L., Kolisnichenko, O. V. (2003). Impulsno-plazmennoe uprochnenie instrumenta i detalei mashin. Doklad. Materialy v avtomobilstroenie. Toliati-Samara, 234–238.
312. Tyurin, Yu. N., Kulkov, S. N., Kolisnichenko, O. V. (2009). Impulsno-plazmennoe uprochnenie kalibrov tverdosplavnykh prokatnykh shaib. Chernye metally, 10, 10–14.
313. Tyurin, Yu. N., Kulkov, S. N., Kolisnichenko, O. V., Duda, I. M. (2009). Impulsno-plazmennoe modifitsirovanie poverkhnosti izdeliia iz splava WC + 20 % Co. Fizichna inzheneriia poverkhni, 7 (3), 262–267.
314. Nekoz, O. I., Tyurin, Yu. M., Kolisnichenko, O. V., Batrachenko, O. V. (2010). Impulsno-plazmove zmitsnennia nozhiv kutera. Suchasni problemy trybolohii. Kyiv, 180.
315. Tyurin, Yu. N., Kolisnichenko, O. V., Duda, I. M., Khong, K. CH., Chzhun, K. Kh. (2010). Legirovanie i nanostrukturirovanie poverkhnosti shtampovoi stali. Chernye metally, 11, 11–16.
316. Tyurin, Yu. N., Kolisnichenko, O. V., Duda, I. M., Khong, K. CH., Chzhun, K. Kh. (2010). Iznosostoikost valkovykh chugunov posle impulsno-plazmennoi obrabotki. Chernye metally, 12, 14–17.
317. Nekoz, O. I., Kolisnichenko, O. V., Zdislav, K. Z., Batrachenko, O. V.; Kindrachuk, M. V. (Ed.) (2010). Impulsno-plazmove zmitsnennia nozhiv miasorizalnykh vovchkiv. Problemy tertia ta znoshuvannia, 54, 172–180.
318. Tyurin, Yu. N., Kolisnichenko, O. V., Duda, I. M. (2011). Impulsno-plazmennoe uprochnenie poverkhnosti vysokoprochnykh chugunov. Svarschik, 2 (78), 20–23.
319. Tyurin, Yu. N., Kolisnichenko, O. V., Tishenko, A. N., Kovaleva, M. G., Prozorova, M. S., Arsenko, M. lu., Smoliakova, M. lu. (2013). Struktura i svoistva modifitsirovannogo plazmoi sloia na rabochei poverkhnosti nozhei dlia rezki prokata v metallurgicheskomo proizvodstve. Uprochniaiuschie tekhnologii i pokrytiia, 3, 28–33.
-

- 320. Markashova, L. I., Tyurin, Yu. N., Kolisnichenko, O. V., Valevich, M. P., Bogachev, D. G. (2013). Effect of structure parameters on mechanical properties of steel R6M5 under conditions of strengthening surface treatment. *Avtomaticheskaia svarka*, 12, 18–23.
- 321. Tyurin, Yu. N., Markashova, L. I., Kolisnichenko, O. V., Duda, I. V., Valevich, M. L., Bogachev, D. G. (2014). Impulsno-plazmennoe modifitsirovanie rabochei poverkhnosti instrumenta iz bystrorezhuschei stali. *Svarschik*, 4, 30–32.
- 322. Tyurin, Yu. N., Zhadkevich, M. L. (2008). *Plazmennye uprochniaiuschie tekhnologii*. Kyiv: Naukova dumka, 216.

Edited by
Volodymyr Korzhyk

THEORY AND PRACTICE OF PLASMA-DETONATION TECHNOLOGY
OF SURFACE HARDENING METAL PRODUCTS

Volodymyr Korzhyk, Yuriy Tyurin, Oleg Kolisnichenko

Monograph

Technical editor I. Prudius
Desktop publishing T. Serhiienko
Cover photo Copyright © 2021 V. Korzhyk

PC TECHNOLOGY CENTER
Published in December 2021
Enlisting the subject of publishing No. 4452 – 10.12.2012
Address: Shatyl'ova dacha str., 4, Kharkiv, Ukraine, 61165
